



BRNO UNIVERSITY OF TECHNOLOGY

VYSOKÉ UČENÍ TECHNICKÉ V BRNĚ

FACULTY OF MECHANICAL ENGINEERING

FAKULTA STROJNÍHO INŽENÝRSTVÍ

INSTITUTE OF AEROSPACE ENGINEERING

LETECKÝ ÚSTAV

FORMULA SAE AERODYNAMIC OPTIMIZATION

AERODYNAMICKÁ OPTIMALIZACE MONOPOSTU FORMULE SAE

MASTER'S THESIS
DIPLOMOVÁ PRÁCE

AUTHOR
AUTOR PRÁCE

Bc. Lukáš Fryšták

SUPERVISOR
VEDOUCÍ PRÁCE

Ing. Robert Popela, Ph.D.

BRNO 2016

Master's Thesis Assignment

Institut: Institute of Aerospace Engineering
Student: **Bc. Lukáš Fryšták**
Degree programm: Mechanical Engineering
Branch: Aircraft Design
Supervisor: **Ing. Robert Popela, Ph.D.**
Academic year: 2015/16

As provided for by the Act No. 111/98 Coll. on higher education institutions and the BUT Study and Examination Regulations, the director of the Institute hereby assigns the following topic of Master's Thesis:

Formula SAE aerodynamic optimization

Brief description:

Performance of racing car is strongly determined by its aerodynamic characteristics. Aerodynamic optimization is currently integral part of design of racing cars. TU Brno Racing team is for years developing Formula Student cup vehicle. For further development there is necessary to perform testing and aerodynamic optimization of car.

Master's Thesis goals:

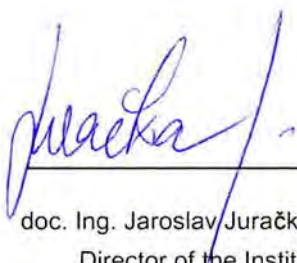
Determine the basic aerodynamic characteristics of monopost in its current configuration. Perform analysis, and identify gaps and determine areas for improvement in aerodynamic characteristics (increase downforce, optimal distribution of downforce, reduce drag). Optimization by sophisticated method using either the experimental or computational monopost model.

Bibliography:

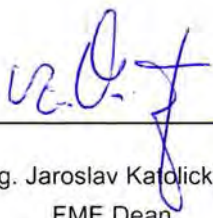
- Hucho, W. H.: Aerodynamics of Road Vehicles, ISBN: 978-0-7506-1267-8.
Barlow, J. B., Rae, W. H., Pope, A.: Low-Speed Wind Tunnel Testing, ISBN: 978-0-471-55774-6.
Katz, J.: Race Car Aerodynamics: Designing for Speed (Engineering and Performance), ISBN-13: 978-0837601427.

Students are required to submit the thesis within the deadlines stated in the schedule of the academic year 2015/16.

In Brno, 30. 11. 2015



doc. Ing. Jaroslav Juračka, Ph.D.
Director of the Institute



doc. Ing. Jaroslav Karolický, Ph.D.
FME Dean

ABSTRACT

This work focuses on wind tunnel testing of a 25% scale model of a Formula SAE race car. In the first part, Formula SAE is introduced and role of aerodynamics within this competition is described. That is followed by review of the theoretical background that is relevant to the presented experiment. In the second part, the experiment itself is described and results presented. As part of this work, a six component strain gauge force balance was designed, manufactured, and calibrated. Wind tunnel testing was done in four different configurations to determine the influence of inverted wings and floor with diffuser on aerodynamic performance of the car.

KEYWORDS

Formula SAE, Formula Student, Wind tunnel, aerodynamics, force balance

ABSTRAKT

Tato práce se zabývá měřením aerodynamických charakteristik modelu závodního vozu Formula SAE v aerodynamickém tunelu, v měřítku 1:4. V první části je představen projekt Formula SAE a popsána role aerodynamiky v rámci této soutěže. Následuje přehled teoretického pozadí, které je relevantní k provedenému experimentu. Ve druhé části práce je popsán samotný experiment a prezentovány jeho výsledky. Součástí je návrh, výroba a kalibrace šestikomponentní tenzometrické váhy pro měření aerodynamického zatížení. Testy v aerodynamickém tunelu byly provedeny ve čtyřech konfiguracích, aby bylo možné určit vliv přítlačných křídel a podlahy s difuzorem na výsledné aerodynamické charakteristiky vozu.

KLÍČOVÁ SLOVA

Formula SAE, Formula Student, aerodynamický tunel, aerodynamika, tenzometrická váha

FRYŠTÁK, Lukáš *Formula SAE aerodynamic optimization*: master's thesis. Brno: Brno University of Technology, Faculty of Mechanical Engineering, Institute of Aerospace Engineering, 2016. 181 p. Supervised by Ing. Robert Popela, PhD.

DECLARATION

I declare that I have written my master's thesis on the theme of "Formula SAE aerodynamic optimization" independently, under the guidance of the master's thesis supervisor and using the technical literature and other sources of information which are all quoted in the thesis and detailed in the list of literature at the end of the thesis.

As the author of the master's thesis I furthermore declare that, as regards the creation of this master's thesis, I have not infringed any copyright. In particular, I have not unlawfully encroached on anyone's personal and/or ownership rights and I am fully aware of the consequences in the case of breaking Regulation § 11 and the following of the Copyright Act No 121/2000 Sb., and of the rights related to intellectual property right and changes in some Acts (Intellectual Property Act) and formulated in later regulations, inclusive of the possible consequences resulting from the provisions of Criminal Act No 40/2009 Sb., Section 2, Head VI, Part 4.

Brno
.....
author's signature

ACKNOWLEDGEMENT

I would like to express a huge thank you to everyone that helped me with this work. Mainly, to my advisor, Ing. Robert Popela, PhD., whose help and guidance played an elemental role in the successful completion of this thesis.

Největší poděkování však patří mé rodině, za neúnavnou podporu během celého studia.

Brno
.....
author's signature

CONTENTS

Introduction	23
I Introduction, Theoretical background	24
1 Formula SAE	25
1.1 About FSAE	25
1.2 Aerodynamics in FSAE	27
1.2.1 Wind tunnel tesing in FSAE	27
1.3 Aerodynamics of Dragon cars	28
1.3.1 Dragon 4	29
1.3.2 Dragon 5	32
1.3.3 Dragon 6	33
2 Current State-of-the-art	35
2.1 Aerodynamics in automotive industry	35
2.2 Various aspects of on-road driving	37
2.3 Tools of the trade	39
2.3.1 Road testing	39
2.3.2 Wind tunnel testing	39
2.3.3 Computational methods	40
3 Wind tunnel testing	41
3.1 Wind tunnel nomenclature	41
3.2 Types of wind tunnels	41
3.3 Types of test sections	43
3.4 Facility characterization	44
3.4.1 Flow uniformity	44
3.4.2 Longitudinal static pressure gradient	45
3.4.3 Angular flow variation in a jet	45
3.4.4 Turbulence	46
3.4.5 Surging	46
3.4.6 Acoustics	46
3.5 Representation of the road	46
3.5.1 Wheel-road contact, wheel rotation	48
3.6 Wind tunnel corrections	50
3.6.1 Closed test section	52
3.6.2 Further comments on blockage	53

3.6.3	Boundary layer effects	55
3.7	Tests with reduced-scale models	56
3.7.1	Details of model construction	56
3.7.2	Reynolds number effects	56
3.8	Model mounting	59
3.9	Wind tunnel balances	60
3.9.1	Deflections	62
3.9.2	Measurement of the aerodynamic coefficients	62
II	Experimental testing	66
4	Introduction to Part II	67
5	Experimental setup	69
5.1	Facility	69
5.1.1	Wind tunnel	69
5.1.2	Test section and its equipment	69
5.2	Description of the experimental setup	71
5.2.1	Model scale	71
5.2.2	Measured quantities	72
5.2.3	Model mounting	72
5.2.4	Final experimental setup	73
6	Model	75
7	Balance design and calibration	81
7.1	Basic definitions	81
7.1.1	Coordinate system	81
7.1.2	Aerodynamic loads	81
7.2	Balance design	83
7.3	Balance calibration	90
7.3.1	Test case	96
8	Experiment results	101
8.1	Measurement procedure	101
8.2	Aerodynamic load	103
8.2.1	Evaluation of acquired data	103
8.2.2	Results – Cases 1-4	105
8.2.3	Results – comparison of all cases	112
8.3	Pressure coefficient distribution	113

8.3.1	Results – Cases 1-4	113
8.3.2	Results – comparison of all cases	119
8.4	Wake traversing	119
8.4.1	Prandtl probe	119
8.4.2	Hot wire probe	122
8.5	Review of Reynolds number during the experiment	122
8.6	Comparison with numerical simulations	123
8.6.1	Aerodynamic coefficients	123
8.6.2	Wake	124
8.7	Load distribution	124
9	Conclusion	127
Bibliography		129
List of symbols and abbreviations		133
List of appendices		137
A	Reynolds number and blockage calculation	139
B	Balance – further information	141
B.1	Balance drawings	141
B.2	Balance – calibration graphs	150
C	Aerodynamic load evaluation	157
C.1	Loads on balance	157
C.2	Load on model	161

LIST OF FIGURES

1.1	Some aspects of Formula SAE project	26
1.2	Full scale symmetrical test, Monash Motorsports [27]	28
1.3	LUMotorsport scaled wind tunnel test [twitter.com/LUMotorsport]	29
1.4	Schematic sketch of G-G diagram [6]	30
1.5	Dragon 4 aerodynamic package [23]	31
1.6	Comparison of CFD results and measured data [21] (modified)	32
1.7	Dragon 5 aerodynamic package [24]	33
2.1	Aspects of vehicle aerodynamics [4]	36
2.2	1996 Chaparral 2E Chevrolet (picture taken in 2005, Retrieved from: http://www.ultimatecarpage.com/img/1553/Chaparral-2E-Chevrolet.html)	37
2.3	Real environment in which a vehicle operates [4]	38
2.4	Comparisson of various crosswind profiles [4]	38
2.5	Illustrative picture – CFD. Total pressure coefficient displayed in several planes along the car's x axis to trace vortices that are shed from front and rear wing's end plates.	40
3.1	Wind tunnel nomenclature [18]	41
3.2	Types of wind tunnels [1]	42
3.3	Main geometric characteristics of a wind tunnel test section [4]	43
3.4	The different types of wind tunnel test sections [5]	44
3.5	Variation in the test section freestream velocity [6]	45
3.6	Generic shape of the boundary layer [6]	47
3.7	Various possibilities of road simulation [4]	48
3.8	Drag and lift coefficients of isolated stationary and rotating wheel versus ground clearance. The range of C_L shown for zero ground clearance indicates the range of resutls obtained with a variety of ground-to-wheel seals. [6]	49
3.9	Pressure distribution on the floor beneath a wheel for different ground clearances [4]	50
3.10	Schematic sketch of flow separation and horseshoe vortex forming under a stationary wheel [4]	51
3.11	Wind tunnel testing of a passanger car, using flow visualisation paint. This test was conducted with stationary wheels. The horseshoe vortex is clearly visible. [17]	51
3.12	Simulation of wheel rotation by attachment of trip molding[4]	51
3.13	Streamlines around a body in a closed test section [4]	53
3.14	Wall effects in closed test section [4]	54

3.15 Example of a detailed scaled model (1:4) of a passenger car [17]	57
3.16 Drag coefficient versus Reynolds number for a 1:5 model and a real car [4]	58
3.17 Mounting a model through the tyre patches, while using elevated ground plane [6]	59
3.18 Model mounted on a sting from behind [6]	60
3.19 Sauber F1 Team – wind tunnel testing of 60% scale model mounted from above [22]	61
3.20 Model mounted on a sting from below	61
3.21 Overview of wind tunnel balance types after Hucho [4]	63
3.22 Internal balance schema [6]	64
3.23 Off-the-shelf internal balance, as sold by Aerolab [aerolab.com]	64
5.1 Wind tunnel at the Institute of Aerospace Engineering (IAE) [9]	69
5.2 Test section used for wind tunnel testing [9]	70
5.3 Wind tunnel freestream velocity and test section blockage versus model scale. Based on Reynolds number calculation.	72
5.4 Final experimental set up used for wind tunnel tests in this work	74
6.1 Overall model dimensions	75
6.2 Geometry simplification – engine compartment; rear wing with the additional fin in the symmetry plane	76
6.3 Geometry simplification – upright assembly, suspension	76
6.4 Detailed view of the pressure taps	77
6.5 Pressure taps connected to rubber hoses inside of the model	78
6.6 Floor with diffuser	78
6.7 'Simple' floor – cut around sidepods, without a diffuser	79
6.8 Detailed view of the floor versions	79
6.9 Model used for the experiment	80
7.1 Aerodynamic loads on a vehicle acting in the reference coordinate system [4]	81
7.2 Sketch of the force balance in the test section with model – left view .	84
7.3 Sketch of the force balance in the test section with model – front view	85
7.4 Schematic picture of force balance	86
7.5 Sketch of balance's rectangular cross-section	88
7.6 Data logger used to log strain gauge responses (during both calibration and wind tunnel testing)	91
7.7 Load cell used for applying load during calibration	91
7.8 Schematic sketch of moment application on the balance	92
7.9 Moment application on balance (1)	93
7.10 Moment application on balance (2)	94

7.11	Data used for calibration of bridge B2, plotted with approximated moment	96
7.12	Balance calibration; test case – sketch	97
7.13	Balance calibration; test case. Comparison of values calculated based on balance calibration and values based on load cell log – moments at points of respective strain gauge bridges.	98
7.14	Balance calibration, test case. Comparison of values calculated based on balance calibration and values based on load cell log – resulting load at the model attachment point	99
8.1	Tyre contact patch treatment	103
8.2	Case 1 – aerodynamic forces (left) and moments (right) versus velocity	107
8.3	Case 1 – aerodynamic coefficients versus velocity	107
8.4	Case 2 – aerodynamic forces (left) and moments (right) versus velocity	108
8.5	Case 2 – aerodynamic coefficients versus velocity	108
8.6	Case 3 – aerodynamic forces (left) and moments (right) versus velocity	109
8.7	Case 3 – aerodynamic coefficients versus velocity	109
8.8	Case 4 – aerodynamic forces (left) and moments (right) versus velocity	110
8.9	Case 4 – aerodynamic coefficients versus velocity	110
8.10	Positive rake angle [30]	112
8.11	Resulting aerodynamic coefficients for all cases	114
8.12	Resulting aerodynamic coefficients for all cases, multiplied by models reference area A	114
8.13	Pressure coefficient distribution, Case 1 – foam used to seal tyre contact patch	116
8.14	Pressure coefficient distribution, Case 1 – rubber strip used to seal tyre contact patch	116
8.15	Pressure coefficient distribution, Case 1. (a) stands for foam used to seal tyre contact patch; (b) stands for rubber strip used to seal tyre contact patch	117
8.16	Pressure coefficient distribution, Case 2	117
8.17	Pressure coefficient distribution, Case 3	118
8.18	Pressure coefficient distribution, Case 4	118
8.19	Pressure coefficient distribution, All cases, 30 m/s	120
8.20	Distance from the rearmost point of the model to the traversing plane	120
8.21	Case 3, $U_\infty = 25 \text{ m/s}$. Velocity distribution behind a car – prandtl probe traversing.	121
8.22	Case 4, $U_\infty = 25 \text{ m/s}$. Velocity distribution behind a car – prandtl probe traversing.	121

8.23	Case 3, $U_\infty = 25 \text{ m/s}$. Turbulence intensity distribution behind a car – hot wire probe traversing.	122
8.24	CFD – full scale, $U_\infty = 16.7 \text{ m/s}$, velocity distribution behind a car [25]	124
8.25	Velocity contour plot – CFD	125
8.26	Velocity contour plot – experiment (case 3)	125
8.27	Load transfer vs. speed from Dragon 4 on track testing [21]	126
B.1	Raw data recorded when a single component of load was applied – F_x	151
B.2	Raw data recorded when a single component of load was applied – F_y	151
B.3	Raw data recorded when a single component of load was applied – F_z	152
B.4	Raw data recorded when a single component of load was applied – M_x (after subtraction of zero values)	152
B.5	Raw data recorded when a single component of load was applied – M_y (after subtraction of zero values)	153
B.6	Raw data recorded when a single component of load was applied – M_z (after subtraction of zero values)	153
B.7	Data used for calibration of bridge B1, plotted with approximated moment	154
B.8	Data used for calibration of bridge B2, plotted with approximated moment	154
B.9	Data used for calibration of bridge B3, plotted with approximated moment	155
B.10	Data used for calibration of bridge B4, plotted with approximated moment	155
B.11	Data used for calibration of bridge B5, plotted with approximated moment	156
B.12	Data used for calibration of bridge B6, plotted with approximated moment	156
C.1	Measurement of forces acting on balance, zero values	157
C.2	Measurement of forces acting on balance, strain gauge response to loads	158
C.3	Measurement of load acting on balance. Resulting forces on balance	161
C.4	Measurement of load acting on balance. Resulting moments on balance	162
C.5	Transformation of aerodynamic load to default coordinate system	163
C.6	Case 1 – measured strain gauge responses for all measured velocities	167
C.7	Case 1 – measured strain gauge responses – zero values	168
C.8	Case 1 – measured forces corrected – loads acting on the balance subtracted	168
C.9	Case 1 – transformation of the reference coordinate system	169
C.10	Case 1 – resulting forces acting on the model	169
C.11	Case 1 – resulting moments acting on the model	170

C.12 Case 1 – resulting aerodynamic coefficients of the model	170
C.13 Case 2 – measured strain gauge responses – zero values	171
C.14 Case 2 – measured strain gauge responses for all measured velocities .	171
C.15 Case 2 – measured forces corrected – loads acting on the balance subtracted	172
C.16 Case 2 – transformation of the reference coordinate system	172
C.17 Case 2 – resulting forces acting on the model	173
C.18 Case 2 – resulting moments acting on the model	173
C.19 Case 2 – resulting aerodynamic coefficients of the model	174
C.20 Case 3 – measured strain gauge responses – zero values	174
C.21 Case 3 – measured strain gauge responses for all measured velocities .	175
C.22 Case 3 – measured forces corrected – loads acting on the balance subtracted	175
C.23 Case 3 – transformation of the reference coordinate system	176
C.24 Case 3 – resulting forces acting on the model	176
C.25 Case 3 – resulting moments acting on the model	177
C.26 Case 3 – resulting aerodynamic coefficients of the model	177
C.27 Case 4 – measured strain gauge responses – zero values	178
C.28 Case 4 – measured strain gauge responses for all measured velocities .	178
C.29 Case 4 – measured forces corrected – loads acting on the balance subtracted	179
C.30 Case 4 – transformation of the reference coordinate system	179
C.31 Case 4 – resulting forces acting on the model	180
C.32 Case 4 – resulting moments acting on the model	180
C.33 Case 4 – resulting aerodynamic coefficients of the model	181

LIST OF TABLES

1.1	Overall aerodynamic characteristics of Dragon 4 and Dragon 5, data from CFD simulations	31
5.1	Wind tunnel parameters	69
5.2	Test section parameters	70
7.1	Maximum estimated load on the force balance	84
7.2	Balance geometry values	87
7.3	Dimensions of balance's cross-section at points of strain gauge bridges	90
8.1	Description of measured cases	101
8.2	Maximum wind tunnel velocity achieved for all cases	102
8.3	Test cases measured – force balance	103
8.4	Test cases measured – pressure reading	103
8.5	Test cases measured – traverser	104
8.6	Case 1 – drag and lift forces, pitching moment and aerodynamic coefficients	111
8.7	Case 2 – drag and lift forces, pitching moment and aerodynamic coefficients	111
8.8	Case 3 – drag and lift forces, pitching moment and aerodynamic coefficients	111
8.9	Case 4 – drag and lift forces, pitching moment and aerodynamic coefficients	111
8.10	Resulting aerodynamic coefficient for all cases	113
8.11	Resulting aerodynamic coefficients for all cases, multiplied by models reference area A	113
8.12	Comparison of experimental and numerical results – aerodynamic coefficients	123
8.13	Load transfer based on measured aerodynamic load	126
C.1	Density used for calculation of aerodynamic coefficients – case 1	165
C.2	Density used for calculation of aerodynamic coefficients – case 2	165
C.3	Density used for calculation of aerodynamic coefficients – case 3	165
C.4	Density used for calculation of aerodynamic coefficients – case 4	165
C.5	Model reference dimensions for dimensionless coefficient computation	165
C.6	Forces and moment acting on the model – case 1	166
C.7	Forces and moment acting on the model – case 2	166
C.8	Forces and moment acting on the model – case 3	166
C.9	Forces and moment acting on the model – case 4	166

INTRODUCTION

Formula SAE is a student design competition with a motorsport theme. As part of this project, a team of students is presented with a task – design and build a single-seat open-wheel racecar. The car has to comply with a given set of regulations. Since its inception in 1981 in the USA it has become a world wide competition, and arguably, the largest student project in the world. Teams are not judged only by the car's performance but also in off-track, so called, static disciplines. In total, there are eight disciplines, for which points are awarded. In the end, a team with the highest score wins the competition.

In the beginning of 2000s, some teams started to explore effects of downforce inducing devices, i.e. inverted wings and undertray with diffuser, with the aim of lowering lap times. Previously, inverted wings made an appearance around 1990. Although the two cars using them were extremely fast in the dynamic disciplines, it was believed, that the benefits did not outweigh the negatives. [31] In 2006 Wordley and Saunders published their four year work in this area. [26] [27] They mention a considerable debate in the Formula SAE community as to the benefit of using wings on FSAE cars with respect to the low speeds. Although they concluded that "the 'wing' package described would significantly benefit the car's dynamic event performance.", the aforementioned debate went on for some more years. Ultimately, downforce inducing aerodynamic packages became a standard on FSAE cars.

Many papers, reports and theses were published in the last few years regarding aerodynamic development and performance of FSAE cars. However, most of this work relies on numerical simulations as a primary tool with little or no validation of results. Although it is known that both full scale and subscale wind tunnel experiments were conducted, there is not a lot of data available. Full scale wind tunnel test of two FSAE cars were described and results published in Racecar Engineering magazine. [11] – [15] In these articles, overall aerodynamic coefficients are measured for different wing setups and also for different yaw angles.

The presented study takes aim at conducting a subscale wind tunnel measurement and investigate if the data can be used to fill the gap between numerical simulations and track testing. That is for two reasons. Firstly, CFD computations, unless properly validated, give results with a high degree of uncertainty. And secondly, designing, manufacturing, building, testing and competing with a FSAE car is a one year process. Therefore reducing the time requirement for specifically aerodynamic on-track testing would be a considerable advantage.

Part I

Introduction, Theoretical background

1 FORMULA SAE

Formula SAE was briefly described in the Introduction. This chapter aims to provide more detailed information on the competition, present what role does aerodynamics play in FSAE car development and introduce family of cars that is connected to this work.

1.1 About FSAE

Formula SAE is a student design competition. It is organized by SAE International¹ as one of its Collegiate Design Competitions². It was introduced in 1979 in the US to provide undergraduate and graduate engineering students a real-life engineering challenge. Since then it has spread into Australia, Asia, South America and in 1998 the project got into Europe under a different name – Formula Student.

A team entering the competition is presented with a task to form a hypothetical company. Such a company would operate on an amateur weekend racing market. It would develop, build and *sell* a single-seat open-wheel racecar.

In reality, every year a team has to design and build a racecar. With this racecar teams meet at competitions. There, a car is not only judged by its performance. A team also has to present its engineering design, cost analysis and a hypothetical business plan. These three areas form what is called static disciplines. Then there are four so called dynamic disciplines, where cars are actually run on track. For each of these disciplines a team is awarded points, maximum being 1000. A team with highest cumulative total wins the competition.

For a given year there is a set of regulations that the car has to comply with. They define only basic specifications of a car and specifications to ensure safety of everyone involved. Other than that, it is specifically desired to give students as much freedom in their design as possible.

Formula SAE is a very complex (and demanding) project. It runs through all of an academic year. In this time a team has to form itself, design a car, collect sufficient

¹"SAE International is a global association of more than 138,000 engineers and related technical experts in the aerospace, automotive and commercial-vehicle industries. SAE International's core competencies are life-long learning and voluntary consensus standards development. SAE International's charitable arm is the SAE Foundation, which supports many programs, including A World In Motion and the Collegiate Design Series." [28]

²Other student design competitions under the SAE Collegiate Series's roof are SAE Baja (off-road vehicles), SAE Aero Design (radio-controlled airplanes), SAE Clean Snowmobile and SAE Supermileage (single-person fuel-efficient vehicle). [28]

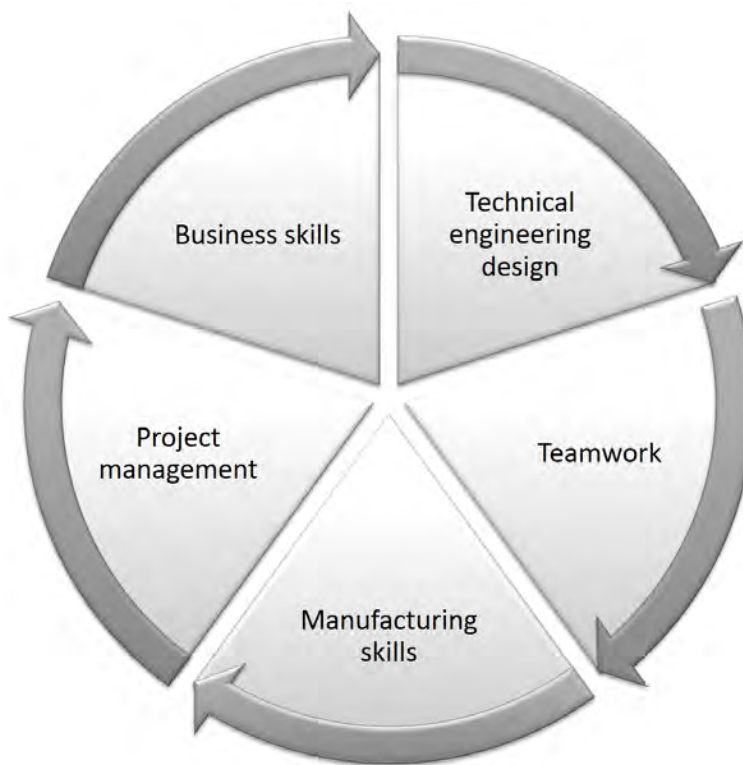


Fig. 1.1: Some aspects of Formula SAE project

budget, manufacture the car, test the car and learn how to operate it and attend competition(s).

Some aspects of Formula SAE are shown in a circular flow diagram in fig. 1.1. A student usually wants to join a team to improve his/her engineering skills. In order to be able to do that he/she is forced to work in a team. Then, to finish the project, the team has to master manufacturing skills. All of this has to be done in a given time period, therefore project management is of utmost importance. "Formula SAE is firstly a program management exercise and secondly an engineering exercise, not the other way around!" [19]. And last, but not least, the team has to find all the resources it needs/wants to be able to take part in the competition in the first place.

Currently, there are almost 600 teams taking part in Formula SAE, who can attend around 15 races all around the world.

In 2010 a team was established at Brno University of Technology – TU Brno Racing. Since its establishment the team took part in the competition every year. In 2016, this team is in its sixth season and constructs its sixth car.

1.2 Aerodynamics in FSAE

As was mentioned in the Introduction, first attempts to utilize inverted wings on a FSAE car were made in 1991. However, it was not until around 2005 that teams started to seriously implement them into their design. In both 2010 and 2011, number of winged cars attending Formula Student Germany³ was still less than five. A significant turning point came in 2012. That year there were twelve winged cars and in 2013 there were thirty-seven of them [3]. In 2015 there were 70 winged cars, which makes it 76% of all cars.

With such a vast majority of teams spending time on aerodynamic development, a lot of publications on the topic can be found. Generally speaking, Formula SAE teams usually have no or rare access to wind tunnels. Therefore, the bulk of aerodynamic development is done using numerical simulations. In the publications available, there is usually not much information regarding validation of the simulations. This can be perceived three ways – validation is done after the publications (which can be the case for bachelor's and master's theses), or teams keep information about accuracy of their simulation to themselves (for engineering design presentation purposes at competitions), or there is no validation done.

From experience, it can be anticipated, that at least half of the teams do not validate their numerical results. That is inconvenient for two reasons: (a) it leaves a high degree of uncertainty in the results, and (b) when a team presents numerical simulation results without proper validation, it loses points at the engineering design presentation.

1.2.1 Wind tunnel testing in FSAE

There are teams that have access to wind tunnels. Firstly, Monash Motorsport (University of Melbourne) – as pioneers of inverted wings in FSAE – were validating their numerical simulations in a full scale wind tunnel from the beginning of their development. This work was later published by Wordley and Saunders in [26] and [27]. Their work included numerical simulations, wind tunnel testing and also track testing. Interesting is their attempt to simulate ground motion by mounting symmetrical models (see fig. 1.2)

Other well documented full-scale tests are those of UH Racing (University of Hertfordshire) and Bath Racing (University of Bath). Both of these teams got access for half a day to MIRA wind tunnel⁴. These tests were focused on measuring

³Largest and most prestigious race in the world

⁴ UK's only full-scale wind tunnel facility [[http://www.horiba-mira.com/our-services/full-scale-wind-tunnel-\(fswt\)](http://www.horiba-mira.com/our-services/full-scale-wind-tunnel-(fswt))]



Fig. 1.2: Full scale symmetrical test, Monash Motorsports [27]

overall aerodynamic load, while changing set-up of aerodynamic package. Also tests with yaw angle up to 20 degrees were conducted. [11] – [14], [15]

Other teams that are known to have been testing in a full-scale wind tunnel are Rennteam Stuttgart (University of Stuttgart) and AMZ Zurich (ETH Zurich university).

More often, FSAE teams have access to smaller wind tunnels and also rapid prototyping technologies. Then, scaled wind tunnel tests are not as problematic to conduct. Still, information and data regarding these tests are usually limited to promotional photos and posts on social media. (For illustration, in fig. 1.3 there is a picture of scaled model in a test section – team LUMotosport (Loughborough University).)

1.3 Aerodynamics of Dragon cars

To introduce this section on aerodynamics of Dragon cars, firstly, information about the Dragon family needs to be recapped. Dragon is a name of every car designed and built by TU Brno Racing team, every evolution having its respective number. Dragon 1 was built and raced with in 2011. As of 2016, there are six cars built by TU Brno Racing, Dragon 6 being the last addition into the family.

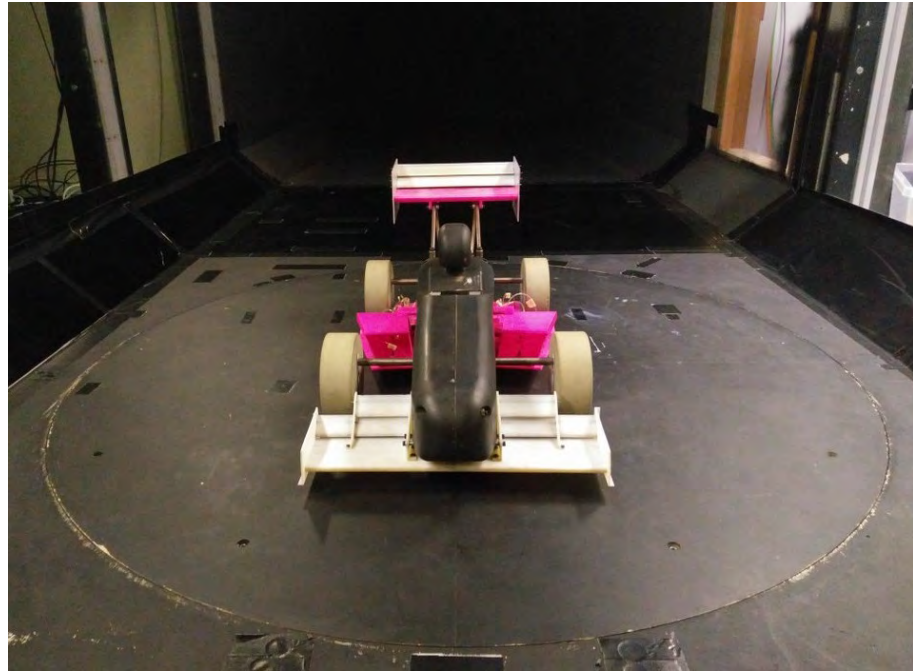


Fig. 1.3: LUMotorsport scaled wind tunnel test [twitter.com/LUMotorsport]

1.3.1 Dragon 4

Dragon 4 was the first car designed with downforce inducing parts. There were two main reasons that led to the decision to include this new area to the car's concept.

Firstly, Dragon 1 and Dragon 2 had substantial reliability problems. That was because the team was new and had little experience with designing, building and maintaining a car. Then with Dragon 3 a reasonable amount of testing mileage was covered and reliability was no longer a decisive issue. On track, this car was able to get very close to its designed mechanical grip, i.e. very close to the boundaries of its G-G diagram (schematically shown in fig. 1.4, for further reference see [3], [6]). Thus it made sense to include aerodynamic parts into the Dragon 4 concept.

Once including aerodynamic parts into the Dragon 4 concept was decided, basic design goals were set. First of the goals, as mentioned above, was to enlarge boundaries of the G-G diagram. In other words, generate downforce⁵, which would result in lower lap time.

Aerodynamics can have strong effect on dynamic behaviour of the car. So it was desired that aerodynamic parts have the least possible effect on car handling.

Final aerodynamic package, for this first year, should be relatively simple, because of limited time for both design and manufacturing.

⁵ Downforce = negative lift force

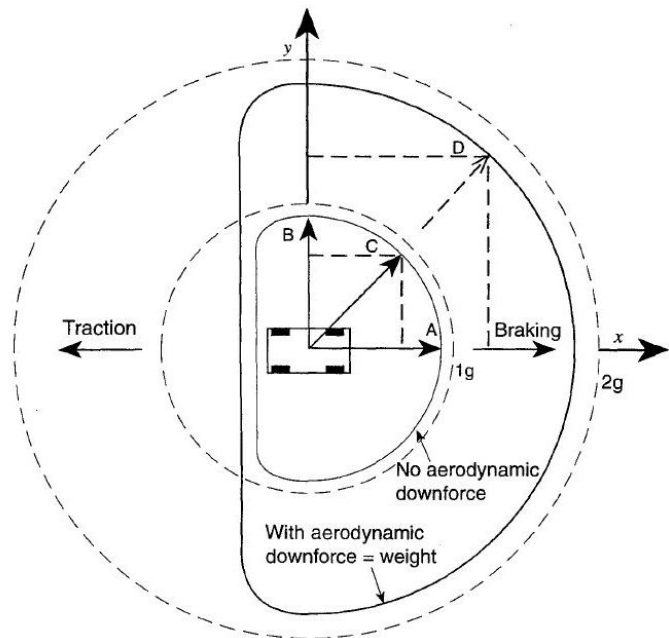


Fig. 1.4: Schematic sketch of G-G diagram [6]

According to the design goals listed above, aerodynamic package was designed – pictured in fig. 1.5. It consists of two-element front and rear wing and undertray with diffusers. When designing bodywork, cooling was not really considered.

In design phase, several CFD simulations were done. However, there were no experience in the team with this numerical tool. Consequently, they were done quite late into the design phase, and the results were not really used as an input for changes or improvements. Rather, the results were used as an estimate of the overall performance of the package.

Table 1.1 shows overall aerodynamic characteristics of Dragon 4 acquired from CFD simulations and compares it to Dragon 5. More information on the design of Dragon 4 aerodynamic package can be found in [3]. Aerodynamic package of Dragon 5 will be described in the following section 1.3.2.

As was mentioned before, it was important to experimentally quantify performance of the aerodynamic package and confirm into what extent were CFD predictions correct. For this purpose a specifically aerodynamic track testing was done. This track test was supposed to determine downforce values at different speed. The method of choice was constant speed testing. When using this method, downforce is calculated based on damper position at each speed level. Whole test procedure and methodology is closely described in [21]. In fig. 1.6 downforce is plotted against speed. Blue dotted line represents measured 'High lift' configuration, which means rear wing is in its default position. Black solid line represents CFD results of the



Fig. 1.5: Dragon 4 aerodynamic package [23]

Tab. 1.1: Overall aerodynamic characteristics of Dragon 4 and Dragon 5, data from CFD simulations

(a) Table 1.1 – first part

Car	Note	Ref. area	Lift coeff. – front	Lift coeff. – rear
		A_{ref} m^2	C_{LF} [1]	C_{LR} [1]
Dragon 4	no radiator	1.278	-1.09	-1.55
Dragon5	with radiator	1.103	-1.59	-1.11
Comparison		-13.7%	45.8%	-28.6%

(b) Table 1.1 – continued

Car	Rear bias	Lift coeff.	Drag coeff.	Lift to drag ratio
	C_{LR}/C_L [1]	C_L [1]	C_D [1]	C_L/C_D [1]
Dragon 4	0.59	-2.64	1.24	2.13
Dragon5	0.41	-2.69	1.14	2.37
Comparison	-30.1%	2.0%	-8.4%	11.5%

same configuration. Measured downforce is approximately 25% lower than predicted values. That can be mostly accounted to geometry that was used for numerical simulation. It was substantially simplified.

To conclude this section, it was deemed – based on the CFD and measured data as well as driver's feedback – that aerodynamic development would be continued. The main areas of focus for the following year were floor performance, downforce distribution and cooling.

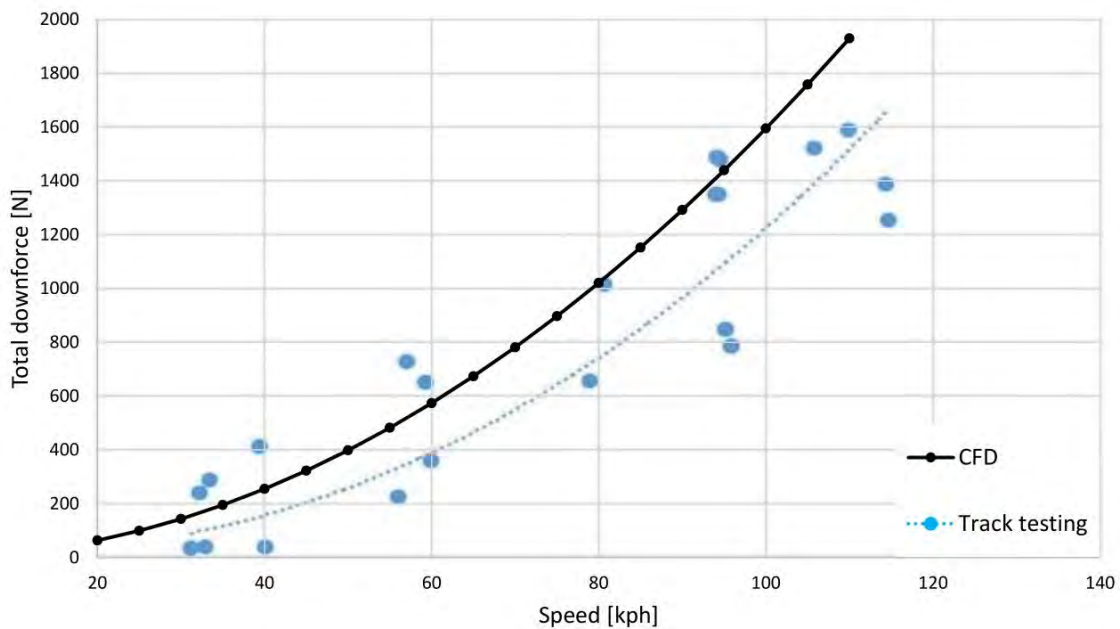


Fig. 1.6: Comparison of CFD results and measured data [21] (modified)

1.3.2 Dragon 5

Design of aerodynamic package for Dragon 5 was mostly affected by extensive changes in the Formula SAE rules. In 2015, regulations describing aerodynamic devices started a two year cycle. Every other year, the regulations would substantially change, enforcing new approaches to FSAE car aerodynamics.

Although the change of rules itself resulted in a necessity to make changes to the design, it was also desired to make changes based on experience gained previous year.

Initially, the following design goals were set: removing errors from Dragon 4 (in terms of both aerodynamics and structural design), retention of downforce despite rules changes, cooling enhancement, achievement of aerodynamic balance (i.e.

achievement of neutral behaviour in terms of car handling) and last, but not least, revision/optimization of airfoil sections and floor.

All of the mentioned design goals were taken into consideration. The final design, as shown in fig. 1.7, was a result of several iterations. Base for every design change was a full car 3D CFD analysis. Overall aerodynamic characteristics of Dragon 5 can be found in table 1.1. These characteristics are also compared to Dragon 4.



Fig. 1.7: Dragon 5 aerodynamic package [24]

1.3.3 Dragon 6

As was explained above, for 2016 aerodynamic rules remained stable. Therefore it was decided to carry over main features of the aerodynamic design from the previous car. For example, decision to use the same wing airfoils enabled to use already manufactured moulds. However, certain changes were made.

Firstly, structural changes, that would remove problems that were encountered on Dragon 5, had to be made. Newly designed rear suspension and engine packaging also required significant changes to the floor. It was also required that the setup of the rear wing was changeable. That was aimed on the ability to change downforce distribution with changes to the rear wing's angle of attack.

The final design of aerodynamic devices for Dragon 6 reflects all of the aforementioned changes/new design goals.

2 CURRENT STATE-OF-THE-ART

This chapter's purpose is to provide a brief insight into road vehicle aerodynamics and into current state-of-the-art aerodynamic development tools.

2.1 Aerodynamics in automotive industry

From the very beginning of road vehicle development, there were attempts to make the vehicles "aerodynamic". These attempts were based on borrowing shapes from naval architecture and aeronautics. In the beginning of those respective fields, naval and aeronautical engineers had somewhat of an advantage, since they could find an inspiration for their designs in nature: fish and birds. From these natural shapes, essential features could have been taken. Automobiles, however, have no such "equivalent" in nature. These first aerodynamic vehicles did not meet with much appreciation, as they were done far too early. Automobiles were slow then. Streamlined bodies on the bad roads of those days would have looked ridiculous. [4]

When speed started to get higher, it became clear that aerodynamic drag really plays an important role in vehicle design. Either for economical reasons, or to achieve higher maximum speed.

It was in the late 1930's, that importance of other components of aerodynamic load emerged, mainly lift force. Between years 1936-39, Daimler-Benz was doing speed record-breaking trials with a special all-enclosed streamlined car. In speed in excess of 400 kph, the driver reported complete loss of steering and roadside observers had an impression that front wheels were off the ground. Such was the effect of lift force acting on the front axle. [16]

These days, aerodynamics plays much more important role in automobile development than that of the public interest, which is aerodynamic drag. Vehicle aerodynamics has to take into account a lot more aspects, as shown in fig. 2.1. Straight line stability, dynamic passive steering and crosswind sensitivity are all result of external flow around a car. Moreover, external flow should also prevent droplets of rain water from accumulating on windows and outside mirrors, keep headlights free of dirt, prevent wind shield wipers from lifting off and cool the engine's oil pan, muffler and brakes. Reducing wind noise is also connected to flow around a vehicle. On the other hand, there is internal flow, which must ensure (with the aid of radiator) that engine is cooled enough in all driving conditions. Other part of the internal flow system has to provide comfortable climate in the passenger compartment. [4]

Although aerodynamics does contribute to several important characteristics of a car, overall shape is not primarily influenced by it. Other functions that play



Fig. 2.1: Aspects of vehicle aerodynamics [4]

a role in vehicle design are safety, regulations, economy and, last but not least, aesthetics. [4]

Hucho [4] presents two approaches for aerodynamic optimization of a car. When using detail optimization, an aerodynamicist has to take the stylistic concept of a car as it is. Only then, by carefully altering design features one at a time, can aerodynamic characteristics be improved. On the other hand, shape optimization uses a basic body. Then, iteratively, small changes to the body's shape are done, which are similar to detail optimization. These steps bring the shape closer to that of a real car. That shape is then used as a starting point for further design.

Both of the aforementioned approaches were used. Nevertheless, they reached a limit, when it was no longer possible to lower the drag coefficient.

New possibilities of aerodynamic optimization emerged with numerical simulation. CFD provides several more approaches to shape optimization, that can reveal areas for aerodynamic improvement that would not be exposed by neither intuition nor experience. [10]

What was mentioned so far in this chapter is mostly related to road cars history and development. But in the latter half of 1960's a new branch of road vehicle aerodynamic development started to surface.

After the second World War, aerodynamic lift on race cars was noted, as was described in the beginning of this chapter. This led to development of aerodynamic surfaces that should counteract the negative effects of lift.

It was not until 1966 that the benefit of adding substantial downforce on the tyres, while negligibly increasing total vehicle weight, was recognised. Frank Winchell and his Chevrolet / Chaparral associates mounted a large inverted wind over the



Fig. 2.2: 1996 Chaparral 2E Chevrolet (picture taken in 2005, Retrieved from: <http://www.ultimatecarpage.com/img/1553/Chaparral-2E-Chevrolet.html>)

rear wheels to increase the vertical load on the rear axle. This first appeared on the Chaparral Can-Am Model 2E (fig. 2.2). [16]

By 1968 wings appeared in other racing categories, notably Grand Prix racing. High mounted rear wings were combined with smaller wings attached to the nose cone. Those high mounted rear wings were prone to structural failures. Thus, FIA issued first restrictions on aerodynamic devices for safety reasons. Nevertheless, downforce generation on race cars started to be a subject of very progressive development. [16]

These days, aerodynamics is of the utmost importance in most of the racing categories, most notably F1. Teams are spending considerable resources on aerodynamic development. However, regulations still impose extensive restrictions regarding aerodynamic design.

2.2 Various aspects of on-road driving

A vehicle, moving in its real environment is schematically depicted in fig. 2.3. It provides a simple overview of all aspects of on-road driving, that affect flow around a vehicle and also its thermal loading. They are vehicle speed, gusty crosswinds, rain, sun load, road dirt, and the grade of the road. [4]

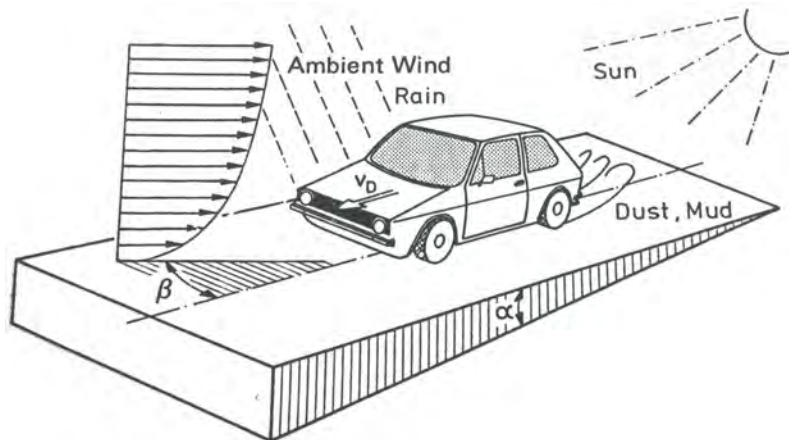


Fig. 2.3: Real environment in which a vehicle operates [4]

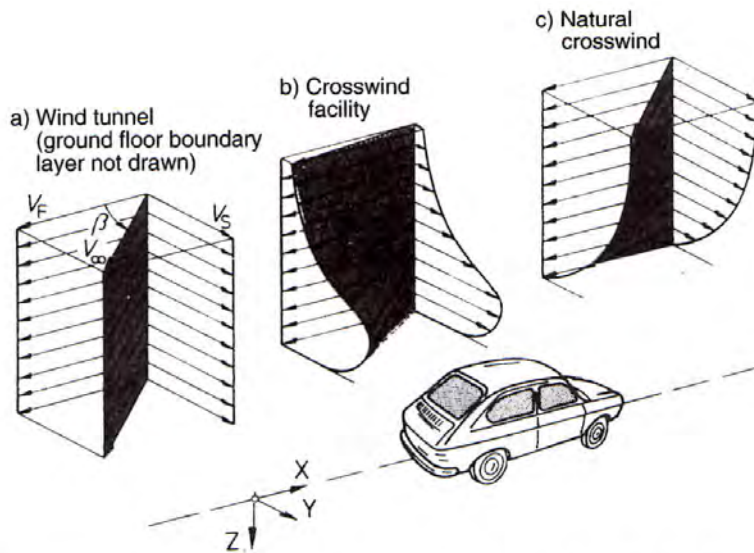


Fig. 2.4: Comparison of various crosswind profiles [4]

The resulting oncoming flow can be broken into two components: first is the airflow resulting from a vehicle's forward motion; the other has its origin in natural winds. The latter forms a turbulent boundary layer above the ground. As a result, the flow coming onto a vehicle is far from uniform. Natural crosswind velocity profile can be seen in fig. 2.4 (along with two simulated crosswind velocity profiles).

Moreover, the magnitude and direction of natural winds vary randomly with time. The flowfield, that a vehicle moves in, is further disturbed by its surrounding, such as trees or bridges, or a passing vehicle. [4]

That said, it is clear that some aspect of on-road driving are very difficult, or even impossible to simulate. Thus, the manner in which the flow is represented in vehicle aerodynamic development is extreme simplification.

2.3 Tools of the trade

There are three main tools, that are used for vehicle aerodynamic development. They are: wind tunnel testing, numerical simulations and on-track testing. Each of these methods has its advantages and disadvantages. Often, main reasons in deciding what method in which design phase to use are also budget constraints and availability of certain testing facilities.

According to Katz [6], aerodynamic information typically expected from the aforementioned methods are: total aerodynamic coefficients, surface pressure distribution and flow visualisation data (such as streamlines). Nevertheless, these remarks are in respect to racecar development. For road vehicles, further data may be collected, e.g. wind noise, etc.

2.3.1 Road testing

For investigation of vehicle's aerodynamic characteristics, road testing comes as first obvious choice. Its biggest advantage is that an actual vehicle is run on actual track. Thus, the vehicle can move in its full speed and it deforms in a real way under aerodynamic load. This makes it the closest simulation of the real operating conditions.

On the other hand, there are also several disadvantages to this method. Firstly, the test conditions are changing all the time – the weather, track temperature, the state of the tyres, the consistent behaviour of the driver, etc. Another downside of track testing is cost. In some racing categories, Formula 1 for example, the cost of operating a car is really high. [22]

Furthermore, in development phase, there is no real car to test. Therefore, this method cannot be applied in early design stages. [6].

To sum up, road testing is the most realistic way of testing, but the least repeatable.

2.3.2 Wind tunnel testing

Wind tunnel is a test facility, that creates controlled and repeatable test conditions, while all measuring instrumentations and test model stay stationary (as opposed to track testing).

The basic idea behind a wind tunnel is rather simple. However, there are many possible ways to constructing a wind tunnel and even more problems associated with each approach. Some of the technical issues of wind tunnel testing are discussed in chapter 3.

2.3.3 Computational methods

Computational fluid dynamics (CFD) is sometimes also called a virtual wind tunnel. It enables to predict aerodynamic characteristics of a vehicle via a computer simulation – before a single part is manufactured. A strong emphasis is placed on development of this tool, due to the ever growing requirements on reducing development cycle times. Relative to road and wind tunnel testing, this method is considerably cheaper and quicker.

In the past 20 years, computational methods were evolving so rapidly, that it was thought it would replace experiments altogether. This did not turn out to be the case, though. But still, numerical simulations play an equally big part in aerodynamic development as experiments in these days. They complement one another.

CFD is based on detailed solution of the entire flow field around an object. This opens possibilities in analyzing and evaluating aerodynamic performance of a car, that would not be possible in neither wind tunnel, nor road testing.

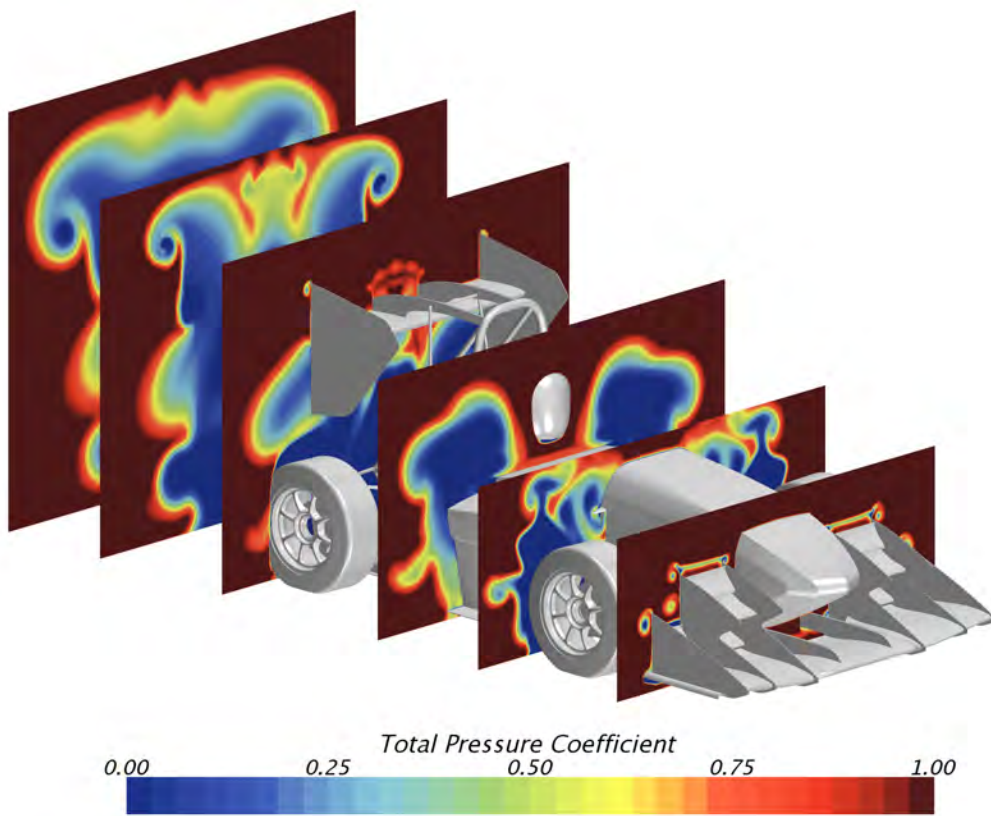


Fig. 2.5: Illustrative picture – CFD. Total pressure coefficient displayed in several planes along the car's x axis to trace vortices that are shed from front and rear wing's end plates.

3 WIND TUNNEL TESTING

As was mentioned in section 2.3.2, wind tunnel is a test facility, that creates controlled and repeatable test conditions. Nevertheless, it only simulates the conditions on a road. It does not reproduce them exactly.

There are many possible approaches to wind tunnel testing. For example, either full scale or scaled tests can be conducted. With each different test layout, several aspects have to be considered. An overview of these is described in the following sections.

3.1 Wind tunnel nomenclature

A conventional, single-return wind tunnel is schematically depicted in fig. 3.2. Its component parts are marked with their common names.

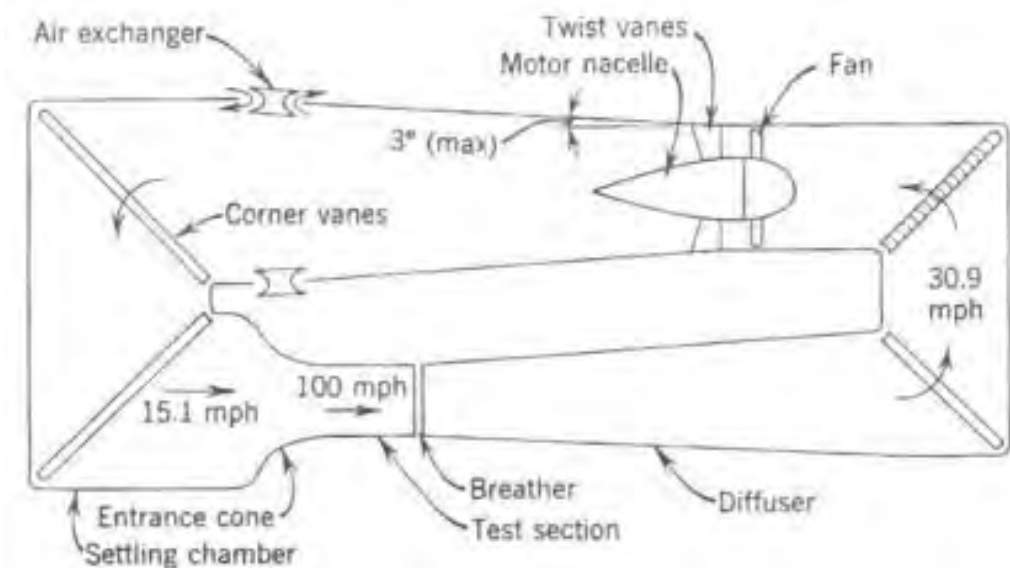


Fig. 3.1: Wind tunnel nomenclature [18]

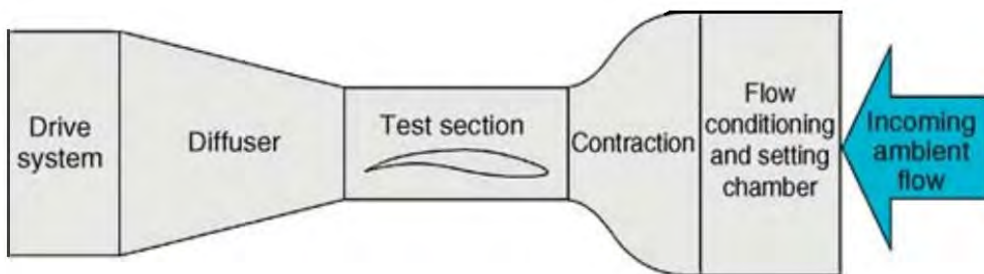
3.2 Types of wind tunnels

In terms of basic wind tunnel layout, two types can be distinguished.

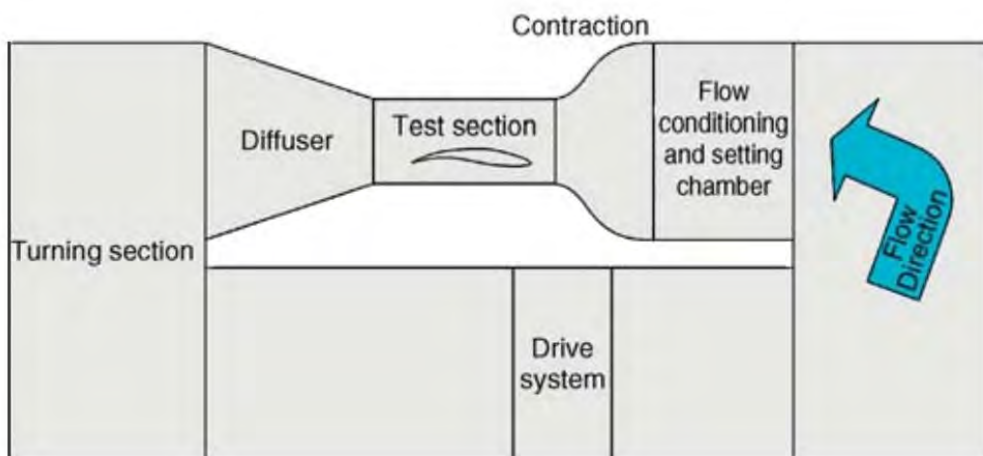
In fig. 3.2a, an open return wind tunnel is described, sometimes also called Eiffel type wind tunnel. Its advantage is, that it is relatively cheap to build. On the other hand, the operating costs are high. If the air is being sucked from outside of a building, another setback is that the operating conditions are dependent on the

weather. Also, keeping the flow quality can be difficult. There are some further disadvantages to these types of open return wind tunnels, therefore new large outdoor tunnels are no longer built. [4]

Closed return wind tunnel's (Göttingen type, fig. 3.2b) main advantage over the Eiffel type is that it requires less power to run. There are three reasons for that. Firstly, the cost of the drive unit is comparatively low; secondly, the operating costs are low and finally, the electric power connection costs are low. On the other hand, its longer ducting and larger settling chamber result in higher building costs. It is also desirable to control temperature of the air inside the wind tunnel, therefore a heat exchanger needs to be installed. The resulting pressure loss then means, that the original savings of cost in terms of lower power consumption are lessened. [4]



(a) Open return wind tunnel (Eiffel type)



(b) Closed return wind tunnel (Göttingen type)

Fig. 3.2: Types of wind tunnels [1]

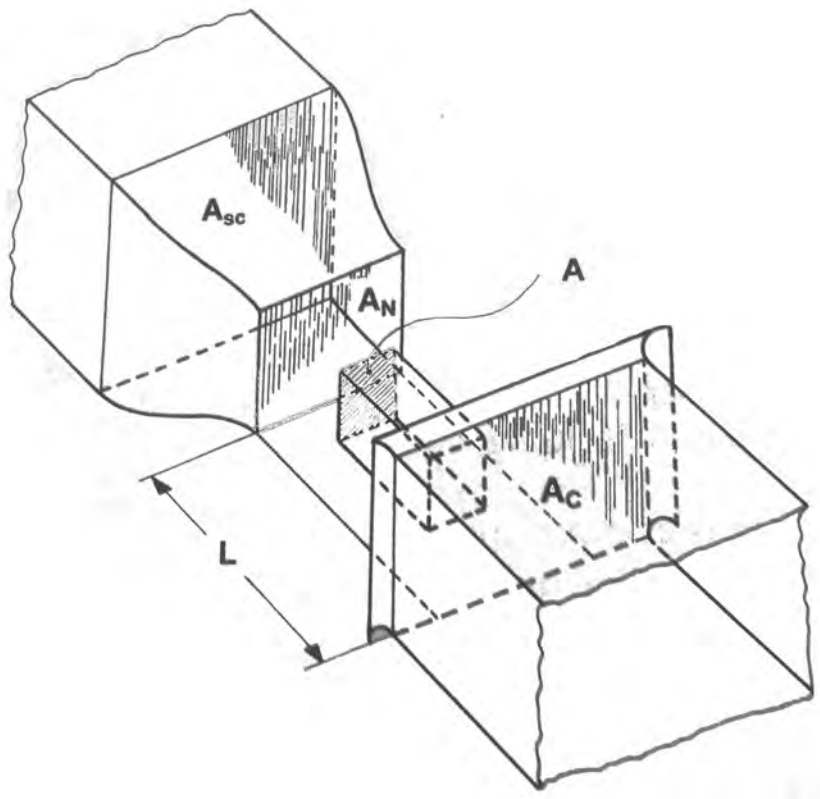


Fig. 3.3: Main geometric characteristics of a wind tunnel test section [4]

3.3 Types of test sections

When wind tunnel test is conducted, a model is mounted in a test section. These can differ in both size and type.

There are two properties that characterize every test section: size and the kind of airstream lateral boundary. The size of the test section is determined by cross-section area A_N of the nozzle and the length L between the nozzle's exit and the entrance to the collector (see fig. 3.3).

These geometrical characteristics can be defined in a non-dimensional form. The blockage ratio of a test section is defined as:

$$\varphi = \frac{A}{A_N} \quad (3.1)$$

where A is vehicle frontal area. The relative length is then:

$$\lambda = \frac{L}{D_N} \quad (3.2)$$

where D_N is the equivalent hydraulic diameter of the nozzle.

In order to obtain kinematic similarity of the flow in a wind tunnel to that on road, it is desirable that the test section is as large as possible. In other words –

the blockage should be as low as possible. On the other hand, cost considerations for both construction and operation demand that the test section is as large as "feasible." What does feasible mean in this sense is then a topic for discussion. [4]

The design of the test section should allow easy access and installation of tested model and wind tunnel instrumentation. [1]

Historically, many different test section shapes have been adopted: round, elliptical, square, rectangular, duplex, octagonal, rectangular with chamfered corners, round with flats on the sides and floor, elliptical with a floor flat, and several other shapes. [18]

In automotive wind tunnel testing, the following three types of jet boundary are standardly used: open, closed and slotted walls. The closed test section has been further developed to specific configurations such as streamlined (contoured) walls and adaptive walls. All of these test section types are sketched in fig. 3.4. Typical for automotive testing is that the ground floor is not part of the test section, although it is physically bound to it. It requires special treatment, which is further discussed in section 3.5. [4]

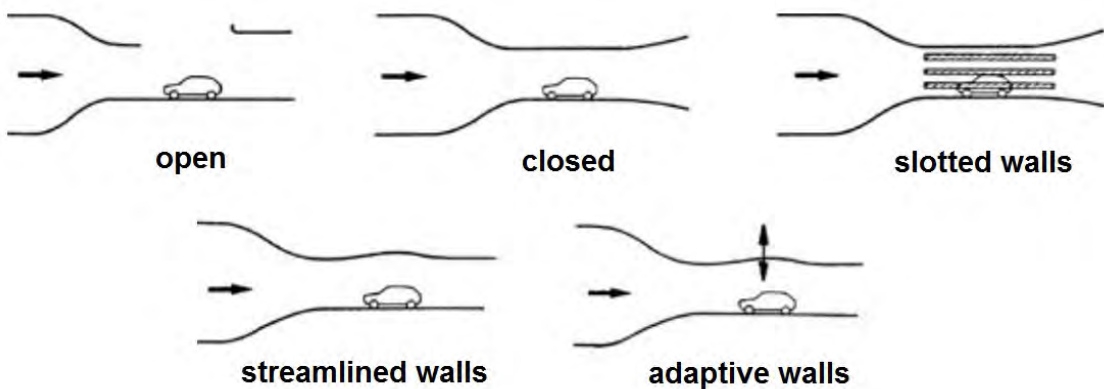


Fig. 3.4: The different types of wind tunnel test sections [5]

3.4 Facility characterization

Once a wind tunnel is built, its characteristics must be evaluated, and improved – should some of them turn out to be unsatisfactory.

3.4.1 Flow uniformity

Clearly, uniform velocity in the test section is desired. The inviscid core of the test section flow should have as little deviations from the mean velocity as possible.

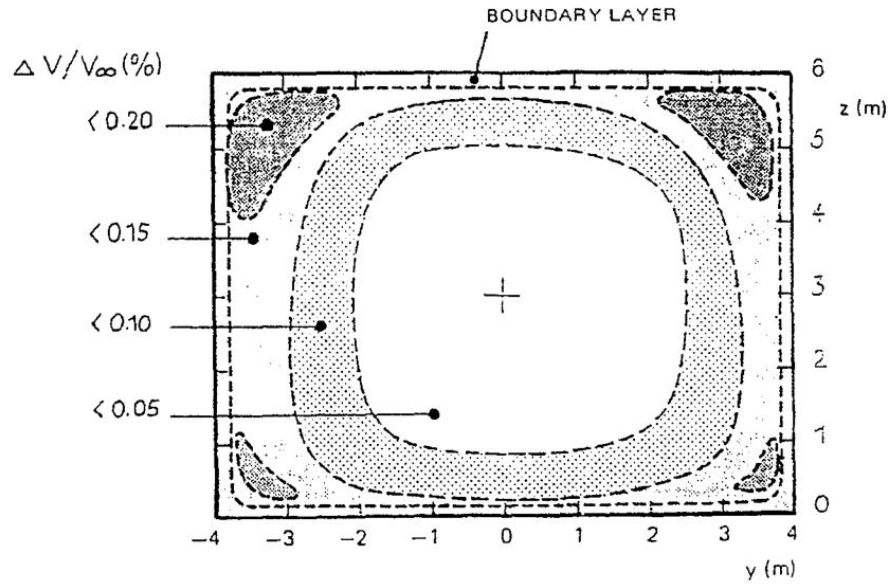


Fig. 3.5: Variation in the test section freestream velocity [6]

However, it is not correct to think of the tunnel as having uniform flow.

A velocity distribution can be measured, for example, by traversing a Prandtl probe across a test section. Results of such a survey are plotted in fig. 3.5. The variation in dynamic pressure q should be less than 0.5% from the mean, which is a 0.25% variation in velocity. [18]

If satisfactory velocity distribution is not obtained, there are several methods how to adjust and improve the situation. These methods are: adjusting the guide vanes, change propeller blade's angle of attack or propeller hub fairing, and adding screens to the wind tunnel largest section. [18]

3.4.2 Longitudinal static pressure gradient

The static pressure gradient along the test section must be known in order to make the necessary buoyancy corrections.

3.4.3 Angular flow variation in a jet

In a wind tunnel there is a certain level of angular flow variation in a jet. Accurate testing cannot be done with a variation greater than $\pm 0.5\%$. [18]

Angular variation may change with wind speed. If such a change is noted, a testing speed must be selected and the guide and anti-twist vanes adjusted to give a smooth flow at that speed. [18]

3.4.4 Turbulence

While in real conditions turbulence is significant, in wind tunnel testing, it is desirable to have low turbulence levels.

Turbulence intensity (TI) is typically computed from equation 3.3 and expressed as a percent of the local mean velocity. [1]

$$TI = \frac{u'}{U_\infty} \quad (3.3)$$

Usually, turbulence intensity varies from 1.0 to 3.0. A value of 1.1 is not difficult to obtain, and values above 1.4 probably indicate, that the tunnel has too much turbulence for reliable testing. [18]

3.4.5 Surging

Pope [18] calls surging "the most vexatious problem a tunnel engineer may have to face." It is a random low-frequency variation in velocity that may run as high as 5% of dynamic pressure q . It makes trouble for all measurements, as it effects force balances, and pressure measurements. Doubts also arise, when assigning Reynolds number to the test.

Surging is associated with separation and reattachment in the diffuser. There are methods how to cure this problem, but they have to be assessed individually. [18]

3.4.6 Acoustics

If the facility is used for acoustic measurements, background noise should be assessed. Ideally, an aeroacoustic flow facility could have background noise levels at least 10 dB below the acoustic source of interest in a test. [1]

3.5 Representation of the road

Simulation of the road brings considerable difficulties when it comes to wind tunnel testing of road vehicles. Difference between boundary layer shapes on the road and in wind tunnel is sketched in fig. 3.6.

In a wind tunnel, floor is stationary. And even without a vehicle in the test section, naturally, a boundary layer forms. A certain treatment of this boundary layer has to be applied in order to simulate on-road driving as closely as possible. This problem is further complicated by the fact, that wheel of the vehicle driving on a road are rotating. That has to be accounted for as well.

Various possibilities of road representation are depicted in fig. 3.7. The most simple methods rely on disturbing the wind tunnel boundary layer with either a

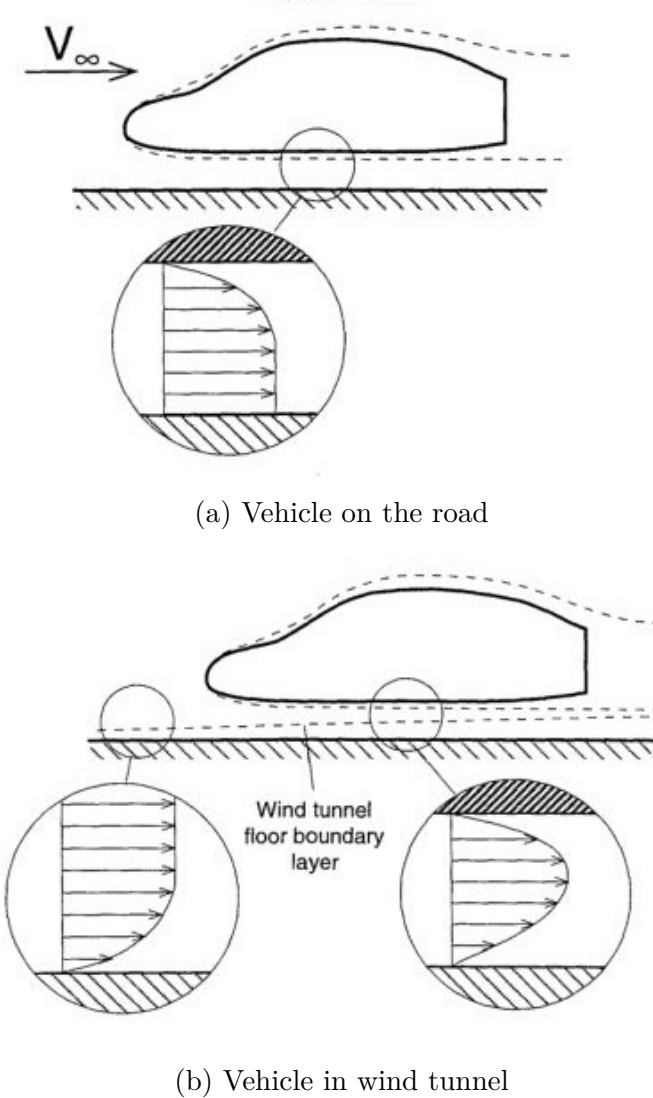


Fig. 3.6: Generic shape of the boundary layer [6]

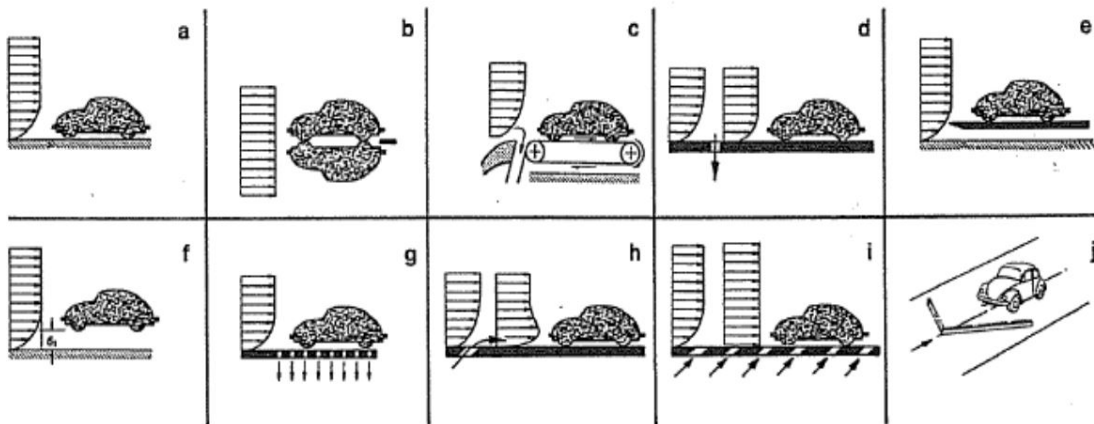


Fig. 3.7: Various possibilities of road simulation [4]

fence – 3.7(j), or elevated ground plane – 3.7(e). Other methods use sucking or blowing air from or to the boundary layer – 3.7(d, g, h, i). Most sophisticated road representation brings a moving belt solution – 3.7(c).

Every solution has its advantages and disadvantages, nevertheless it comes hand in hand with not only technical difficulties but also financial constraints.

3.5.1 Wheel-road contact, wheel rotation

As was mentioned in previous text, wheels are rotating on a real car driving on road. This motion, along with the contact patch itself, has to be considered in wind tunnel testing, because it can have significant effect on the results.

Firstly, the contact between wheel and wind tunnel ground plane is assessed. Unless it is possible to directly measure the forces in wheel contact patches, the wheels cannot touch the wind tunnel floor. That is desired so that only loads due to airflow are recorded. However, lifting the wheels off the ground poses a problem. If the gap is not sealed, the measured forces are not correct and are dependent on the gap, as can be seen in fig. 3.8. Measured lift is lower, while the effect on drag is not so pronounced.

Fig. 3.8 also shows the effect of wheel rotation on recorded forces. Again, introducing wheel rotation to the tested model brings some technical difficulties.

As seen in fig. 3.9, the pressure distribution under a wheel is altered the more the gap to the ground is reduced. When reducing the gap, the flow beneath the wheel is accelerated, resulting in increased suction. However, when the wheel touches the ground and air can no longer pass under the wheel a stagnation point forms in front of the contact patch, causing a formation of a horseshoe vortex further downstream as schematically sketched in fig. 3.10. In fig. 3.11 the horseshoe vortex is clearly

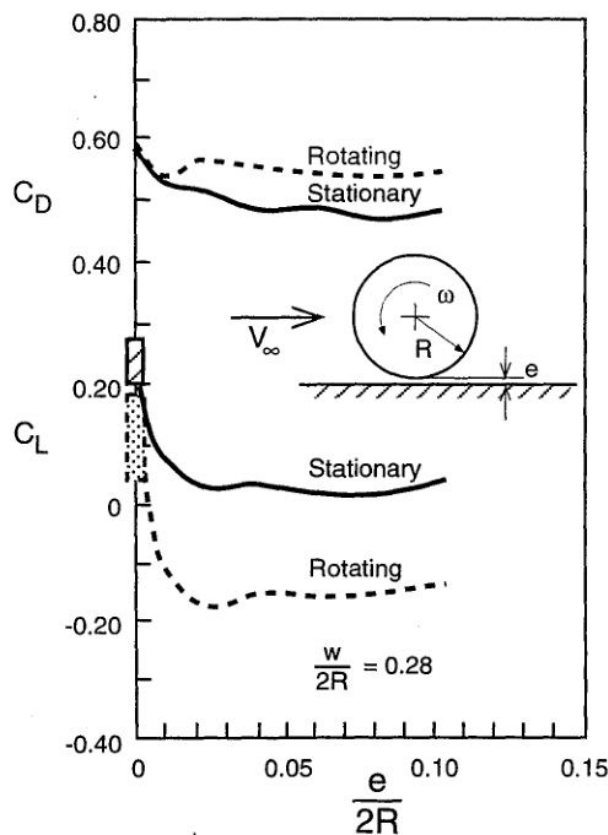


Fig. 3.8: Drag and lift coefficients of isolated stationary and rotating wheel versus ground clearance. The range of C_L shown for zero ground clearance indicates the range of results obtained with a variety of ground-to-wheel seals. [6]

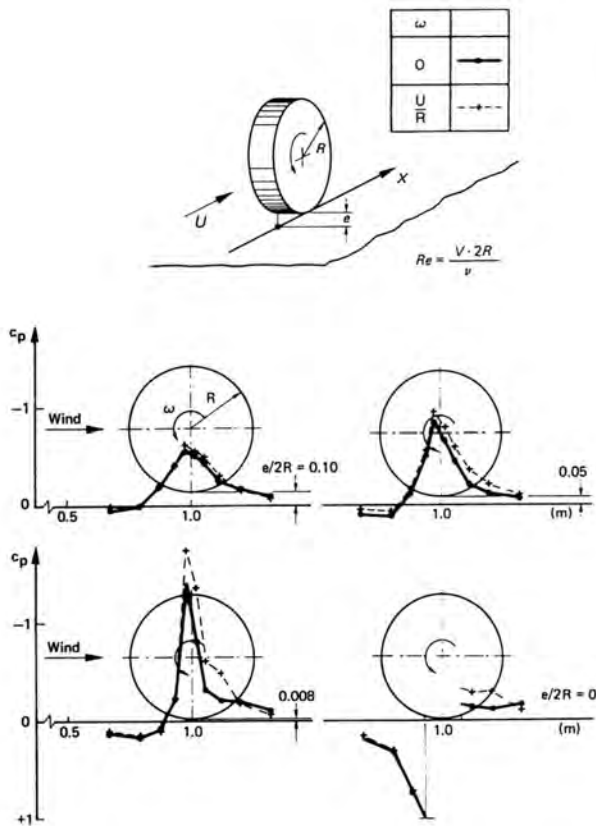


Fig. 3.9: Pressure distribution on the floor beneath a wheel for different ground clearances [4]

visible, due to the flow visualisation paint.

When the whole wheel is exposed to the oncoming flow – as is the case for open-wheel race cars – the flow separates in the upper part. The separation point for a stationary wheel is sketched in fig. 3.12a. When wheel rotation is introduced, the separation point moves forward, as is depicted in fig. 3.12b. This forward movement of the separation point can be simulated by attaching a trip mold onto the wheel’s surface – fig. 3.12c. This mold forces the flow to separate and is a simple simulation of wheel rotation. [4]

3.6 Wind tunnel corrections

As was previously pointed out, in reality a vehicle moves in free air – road being the only limiting surface. In a wind tunnel, however, test section has finite dimensions. Its cross-section area and usable length are limited. Compared to unlimited space, proximity of the stream boundary to the test object ultimately causes modification of the flow field. Angularity of the flow field, and distribution of velocity and pressure

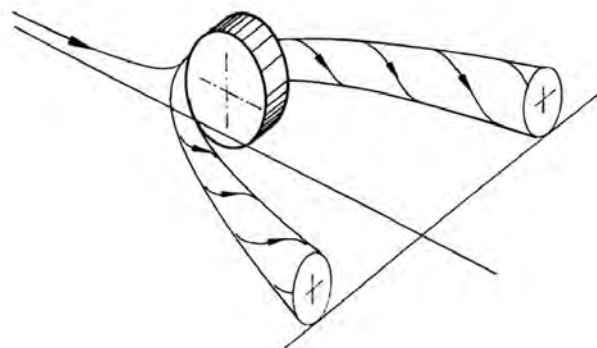


Fig. 3.10: Schematic sketch of flow separation and horseshoe vortex forming under a stationary wheel [4]



Fig. 3.11: Wind tunnel testing of a passenger car, using flow visualisation paint. This test was conducted with stationary wheels. The horseshoe vortex is clearly visible. [17]

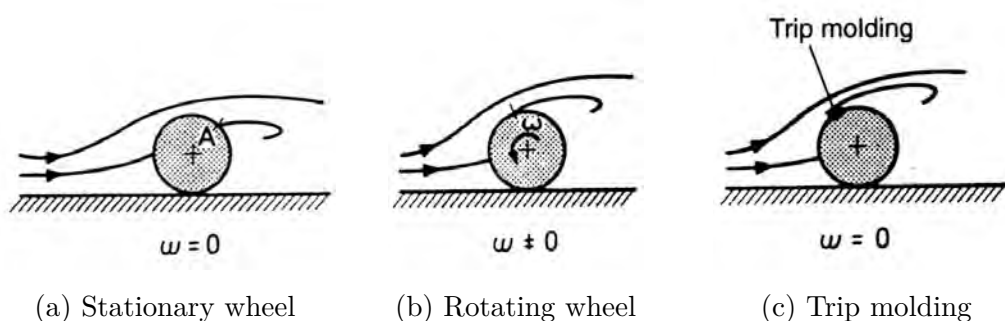


Fig. 3.12: Simulation of wheel rotation by attachment of trip molding[4]

over a model is altered to a certain extent. Consequently, the measured forces and moments are somewhat different than they would be in unlimited space. The smaller the wind tunnel relative to the model, the higher are these discrepancies. [4]

When only relative results are sought, such as effect of shape modification on drag force, these discrepancies might be tolerable – provided the wind tunnel's size is reasonable. Nevertheless, it is absolute results that are usually desired. Then the results are comparable to competing manufacturers, tests in different wind tunnels, or comparison of results with numerical computations. [4]

Corrections make allowances for the flow deviations in a wind tunnel. Originally, for automotive testing, these corrections were taken over from aeronautics. Over time, though, doubts arose as to whether the aerospace corrections can be applied to road vehicles, since there is substantial difference in their respective flow fields. Cars are bluff bodies and their flow field has large areas of separation, while on aircraft, the flow is mostly attached. [4]

Eventually, methods for determining wind tunnel corrections for automotive testing were developed under the roof of the SAE. These methods are different for open test section and closed test section. Only the methods for closed test section are discussed furhter (section 3.6.1) as they are relevant to this work.

The basic premise of all wind tunnel corrections is that the flow pattern does not change. That means that streamlines, pressure distribution and separation points all stay the same as in free air. Although, CFD methods enable this premise to be relaxed. [4]

Perturbations of the various stream boundaries result in two effects:

- Velocity of the oncoming flow is altered.
- An axial pressure gradient is superimposed on the flow field.

Then, linear approach can be applied. Effects of these perturbations are superimposed by addition. [4]

This linear approach is only meaningful when each of the perturbations are small and the resulting correction is small. This applies only if the wind tunnel's test section size is "reasonable" relative to the test object. However, it is not possible to exactly determine the range in which this approach is valid. [4]

3.6.1 Closed test section

In a closed test section, three types of boundary perturbations can be distinguished:

- Solid blockage
- Wake blockage
- Horizontal buoyancy

In principle, each of these perturbations has the two aforementioned effects. Firstly, the oncoming flow is altered and secondly, pressure gradients along test section's axis are introduced. [4]

Solid blockage (SB): As can be seen in fig. 3.13, the solid walls of closed test section prevent streamlines around a body from diverging as much as they would in free air. Therefore, velocity in vicinity of the model is greater – relative to the velocity of the oncoming air – than it would be in free air. That leads to a higher measured drag force. [4]

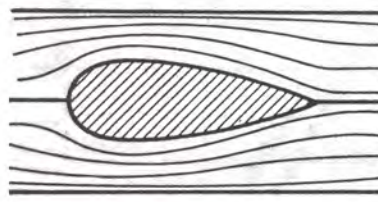


Fig. 3.13: Streamlines around a body in a closed test section [4]

In fig. 3.14a the variation of the velocity u along the axis of a duplex tunnel is shown schematically, together with interference pressure c_{pSB} on the ceiling of the tunnel (both in non-dimensional form). The velocity change is not constant along the tunnel axis. The interference pressure is also variable along the tunnel axis, but it is symmetrical with respect to the largest cross-section of the model. [4]

Wake blockage (WB): The wake of the model creates a velocity defect in the core of the airstream behind the body. This in effect reduces the effective cross-section remaining for the flow, inducing an interference velocity. The velocity along the tunnel axis is plotted in fig. 3.14b, together with the corresponding change in pressure, again at the ceiling. [4]

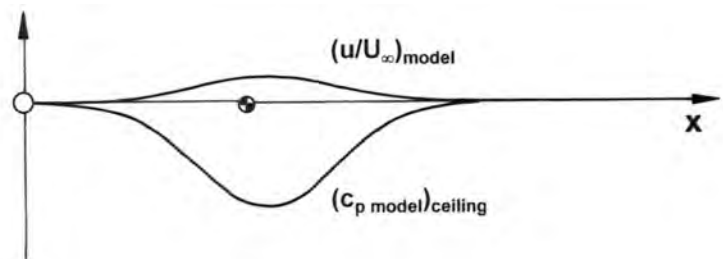
Solid blockage and wake blockage are superimposed in fig. 3.14c.

Horizontal buoyancy (HB): The thickness of the boundary layer on solid walls of the test section, is growing from the inlet to outlet. That causes increase of velocity on the inviscid core, thus producing a decrease in static pressure. The pressure drop from the first point of the model to the last causes a drag-type pressure force, that is not present in free air. [4]

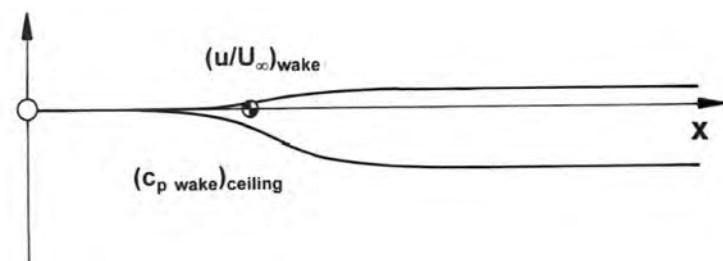
3.6.2 Further comments on blockage

All of the effects in the section above are directly proportional to the relative size of the model and the test section. This ratio, in its non-dimensional form, was defined in section 3.3 as

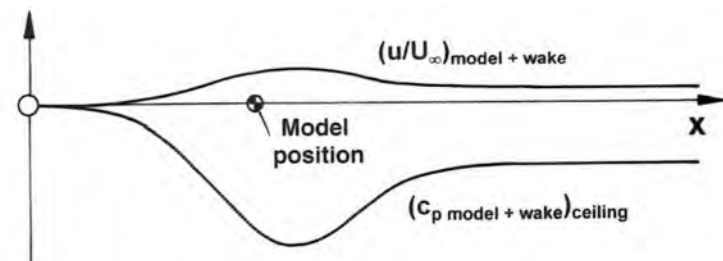
$$\varphi = \frac{A}{A_N} \quad (3.4)$$



(a) Solid blockage



(b) Wake blockage



(c) Solid + wake blockage

Fig. 3.14: Wall effects in closed test section [4]

3 Wind tunnel testing

and was called blockage.

For a long time $\varphi = 0.05$, the typical value in aeronautics, was used in automotive wind tunnel testing. Today, automotive wind tunnels operate with blockage $\varphi \approx 0.10$. However, there are wind tunnel that operate with blockage ratio as high as $\varphi \approx 0.20$.

Hucho states, that contoured wall test section and blockage ratio $\varphi \approx 0.20$ can yield the same results as tests with $\varphi \approx 0.05$. [4]. On the other hand, streamlined test section also has its considerable disadvantages – it substantially limits the variety of shapes, that can be tested and it also prevents yawing the model. [4][22]

Katz also presents experimental data from wind tunnel tests with rather high blockage. In [8] an investigation of wind tunnel wall effects in high blockage testing was done. Four differently sized bluff bodies with blockage ranging from 5% to 20% were measured in a wind tunnel. The same cases were also numerically computed. It is concluded that "As the blockage ratio increases, some effects may become quite large and simple corrections can not account for all the changes. Up to blockage values of 7% or even 10%, some of the traditional corrections can be applied since the effects are not very large. However at blockage values of near 20% the result may differ considerably. But valuable work is still possible in certain disciplines, when a single geometry is constantly being modified and the correlation between wind-tunnel and free-air data is constantly being verified. This is because the shape of the pressure distribution is not changing in nature – but rather being magnified by the proximity of the walls.". By "traditional corrections", those presented by Pope and Harper in [18] are meant.

In another paper co-written by Katz [7] a 25% scaled model of generic Indy Car¹ formula is tested in a wind tunnel. The tests are conducted with both wheels and ground plane stationary (elevated ground plane is used). The blockage in these experiments was "quite large" – 15% – and use of numerical corrections is suggested. With this experimental set up – high blockage, stationary ground plane and wheels – certain differences are stressed out, but it is deemed that such tests can be used for basic studies and can yield useful aerodynamic data.

3.6.3 Boundary layer effects

When measurements are made using a stationary floor, the drag force should be corrected for a boundary layer effect. Wheels of the tested vehicle are partly immersed in boundary layer. Therefore, the measured drag is too low. For cars, as an average, such a correction would be on the order of $C_D \approx 0.01$ on average. According to Hucho [4], this correction is often being neglected.

¹ Indy Car is a North American open-wheel racing series.

3.7 Tests with reduced-scale models

Historically, the attitude towards small scale tests changed a few times – from positive to absolutely negative and back to positive. In the beginning of vehicle aerodynamics, only small aeronautical wind tunnels were available, so a scale of 1:10 was common. [4]

With small scale tests, considerable problems were realised. Transfer of results from small models to full-scale was burdened with substantial risk, for two reasons:

- Lack of *geometric similarity*. Model dimensions were small, so it was difficult to reproduce all the details. Also, cooling flow was often neglected.
- Lack of *kinematic similarity*. Reynolds numbers were far too small, and road representation was inadequate.

On the whole, scaled tests have considerable advantages over full scale tests. Scaled models are faster to build and also faster to modify. If a model is scaled to 50%, only 12.5% of material volume is needed for its construction. Logically, manipulation of the model and installation into the test section is also easier. [4]

On the other hand, the risks regarding the transfer of results to full scale are present to this day. These risks are the smaller the greater scale is used. For example, a scale of 40% (1:2.5) is a typical value in Europe [4], while current Formula 1 uses 60% scale models.

3.7.1 Details of model construction

Generally, models are fabricated with a high degree of fidelity. [4] Especially in recent years, the availability of rapid prototyping technologies makes manufacturing of detailed models quite easy. For illustration, an example of a 25% scaled model of passenger car is shown in fig. 3.15

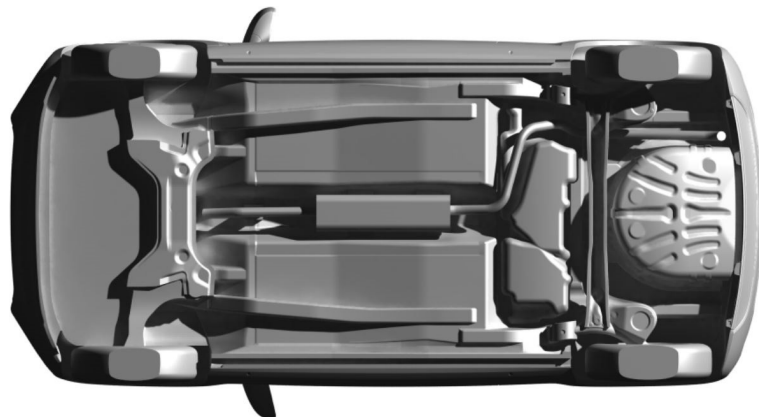
For an accurate assessment of the drag, cooling airflow must be considered. The volume flow of cooling air must be well simulated. There are methods that enable to achieve an accurate simulation. Another aspect of scaled wind tunnel testing that must be considered is the accuracy of road simulation and wheel rotation. [4] The latter was discussed in 3.5.1.

3.7.2 Reynolds number effects

As was mentioned in section 3.7, kinematic similarity between full scale and scaled tests has to be maintained. In order to maintain this kinematic similarity, all forces determining a flow field must be the same for both cases. For incompressible flow, only the forces from inertia and friction need to be considered. Ratio of inertia



(a) Side view



(b) Bottom view

Fig. 3.15: Example of a detailed scaled model (1:4) of a passenger car [17]

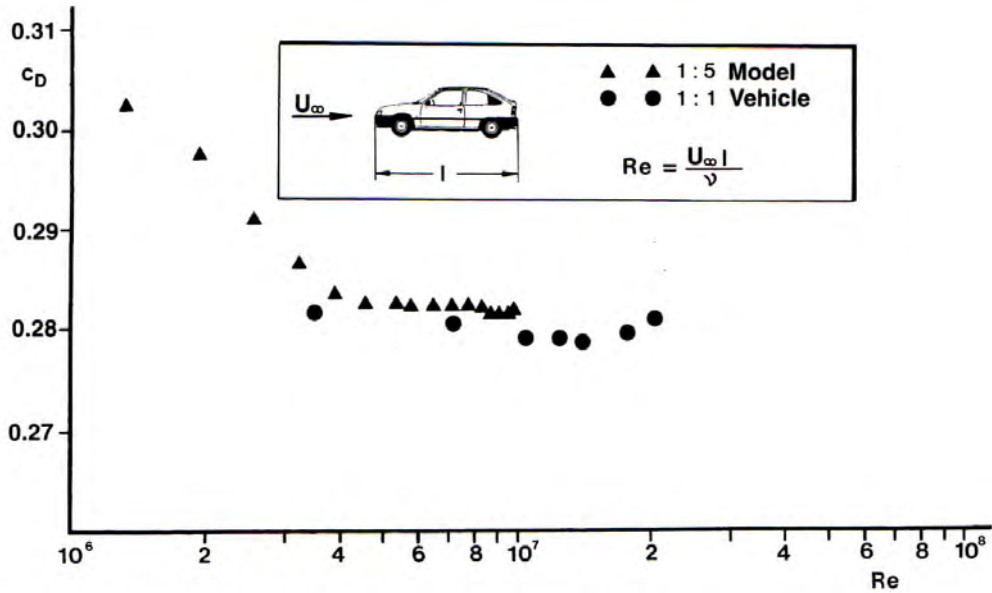


Fig. 3.16: Drag coefficient versus Reynolds number for a 1:5 model and a real car [4]

forces to friction forces – the Reynolds number – is defined as [4]:

$$Re = \frac{U_\infty l}{\nu} \quad (3.5)$$

where U_∞ is the velocity of the undisturbed oncoming flow, l is reference length of a vehicle and ν is kinematic viscosity.

Two flow fields are kinematically similar if the following condition is met [4]:

$$\frac{U_{\infty 1} l_1}{\nu_1} = \frac{U_{\infty 2} l_2}{\nu_2} \quad (3.6)$$

To recognize Reynolds number effects a dependency test should be done. Results from such a dependency study are presented in fig. 3.16. At high Reynolds numbers, the drag coefficient is almost constant, and the values for the full scale vehicle are slightly lower than those for the scaled model. Below a certain Reynolds number, however, the drag coefficient from the scaled test noticeably deviates from the full scale results. That is due to the fact, that in this range, individual components of the car go through their critical Reynolds number. [4]

Violating Reynolds' law of similarity can cause considerable error. On the other hand, for small scales, sometimes it is hard to maintain the same Reynolds number. That is for two main reasons. Wind tunnels have limited top speed. At the same time, increasing speed in model testing also has its limits in another perspective. With bluff bodies, Mach number effects become noticeable at relatively low wind speed. Automobiles are blunt bodies, with high curvatures. Therefore high local

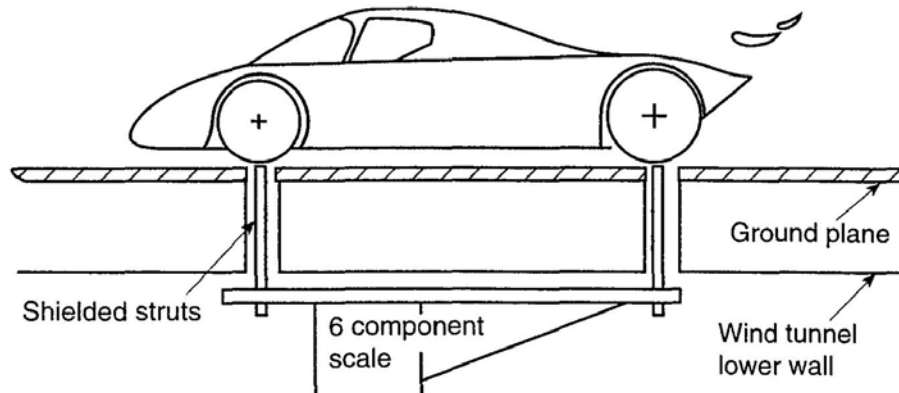


Fig. 3.17: Mounting a model through the tyre patches, while using elevated ground plane [6]

values of u/U_∞ occur. The rule of thumb according to which compressibility effects can be neglected up to $Ma = 0.3$ does not apply to bodies as bluff as cars. $Ma = 0.2$ seems to be a more reasonable limit. Consequently, wind speed is limited to $U_\infty = 70 \text{ m/s}$. [4]

To conclude, the advantages of working with reduced scale models are realized only if the results achieved with them can reliably be transferred to full-scale. [4]

3.8 Model mounting

Generally, model mounting methods can be distinguished into two main approaches. They are: (a) mounting a model via the wheel-road contact, and (b) using a post – a sting – to mount the model.

Mounting a model in the tyre contact patches, as sketched in fig. 3.17, appears to be the simplest method, especially for full scale vehicles. Wheels rest on small panels, that are separated from the rest of the floor (or the elevated ground plane) and must be kept as small as possible. These panels are then connected to a force balance with struts. The separated panels for wheels and shielding of the struts, provided elevated ground plane is used, must be included in order to measure forces due only to air flow. [6] With this solution, complications arise when a moving belt system is to be used to simulate the road. Then, only a narrow belt between the wheels can be used and the wheel supporting panels have to be equipped with motors that rotate the wheels.

The other method, that is attractive for light small-scale models, relies on mounting a model on a single sting. There are more options as to how exactly to do that. In fig. 3.18, model mounted on a sting from behind is shown. According to Katz [6] this creates less aerodynamic interference than mounting from above, as can be seen

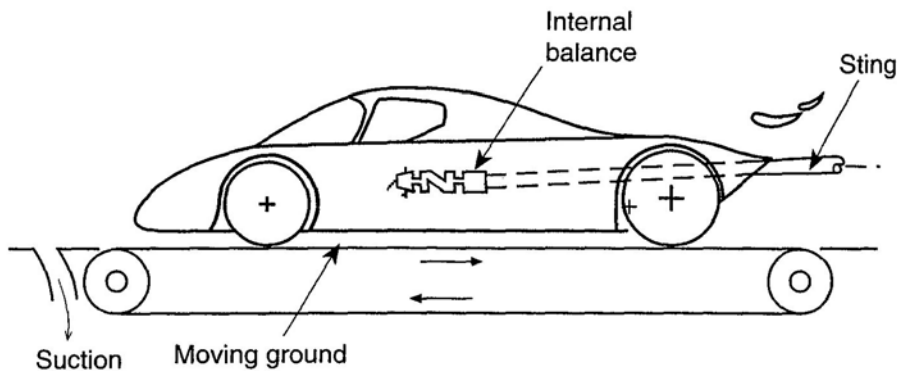


Fig. 3.18: Model mounted on a sting from behind [6]

in fig. 3.19. However, according to Toet [22], mounting the model from above (approximately in the middle of the car) "appears to give the least overall aerodynamic interference to the flow around a car." The reason for this is probably the fact, that Toet's statement is regarding F1 (or open wheel race car) testing. With these car, the wake behind a vehicle is required undisturbed because the exit of a diffuser is an area of great interest and its effect on the rear wing performance is investigated.

A sting can also be mounted to a vehicles underbody (fig. 3.20) and the set-up is similar to that using the external scales, but the balance can be more compact. [6] On the other hand, a race car's underbody is also an area of great interest, since at its surface, majority of downforce is generated. Although, when moving belt is not used, the pressure on the underbody is not going to be accurate. Therefore an evaluation as to what causes greater error in measured data should be done.

3.9 Wind tunnel balances

To measure aerodynamic forces and moments in a wind tunnel, a device that enables that has to be installed – a balance. Again, there are two main technical solutions that can be distinguished: (a) external balance, and (b) internal balance. As was apparent from figures in the previous section, the technical solution of a force balance that is chosen for an experiment is directly connected to the model mounting method and vice versa.

In [4], Hucho presents a list of basic requirements, that wind tunnel balances must fulfil in order to accurately measure aerodynamic forces and moments. The list is as follows:

- The structure of a balance must not alter the flow around a test vehicle. If an auxiliary construction is used – e.g., when attaching a vehicle model to a sting – its effects on the test results must be previously determined in order



Fig. 3.19: Sauber F1 Team – wind tunnel testing of 60% scale model mounted from above [22]

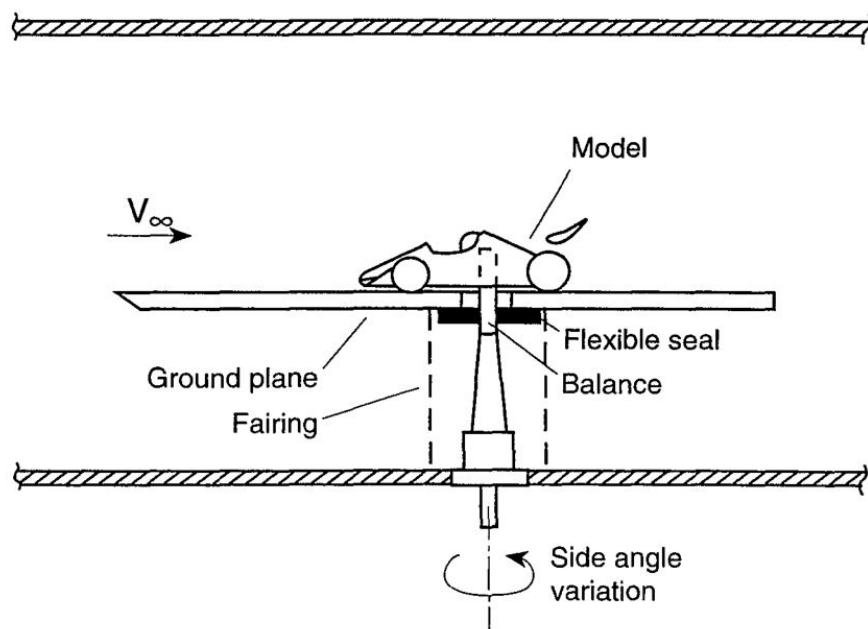


Fig. 3.20: Model mounted on a sting from below

to be able to correct the test values accordingly.

- The vehicle position must not change uncontrolled during the measurement.
- Since the aerodynamic lift forces to be measured are only fractions of the total vehicle weight, the preloads of the z axis must be compensated by corresponding tare weights for better accuracy.
- If measurements are to be performed under yaw, the balance must be rotatable around the z axis accordingly.
- The transmission of the forces between test object and force pick-up points must occur free of friction and hysteresis. For this reason, the use of special accurate elements is essential, such as knife-edge and groove combinations, elastic hinges, or hydrostatic and pneumatic bearings, etc.

An overview of six-component balances developed for vehicle testing is shown in fig. 3.21. Part of the figure is a brief description of every solution, with main advantages and disadvantages.

Internal balance is shown schematically in fig. 3.22. It is a very sophisticated measuring element. By cutting holes and various shapes into the metal core of this balance, its structure becomes sensitive in particular spots to loads such as drag. At these spots, strain gauges are installed and the balance is calibrated for a certain range. [6] These balances can be purchased off-the-shelf, an example being a balance by Aerolab in fig. 3.23.

3.9.1 Deflections

One of the most troublesome problems of wind tunnel balances is their rigidity. Deflections of the balance may result in undesired movement of the test object. It can even lead to distortion of individual components of the aerodynamic loads (e.g., part of lift appears as drag or side force). [18]

Solution to this problem seems obvious enough. Either keep the deflections so low, they can be rendered negligible, or they must be evaluated and accounted for in the work-up. Keeping the deflections low is, of course, preferable.

The effects of deflections are evaluated during the calibration process, and corrections, if necessary, are included.

3.9.2 Measurement of the aerodynamic coefficients

As was described in the previous section (3.9), aerodynamic forces and moments are measured with a balance. To achieve more reliable data a few simple test details must be observed to secure good test results, as presented by Hucho [4]:

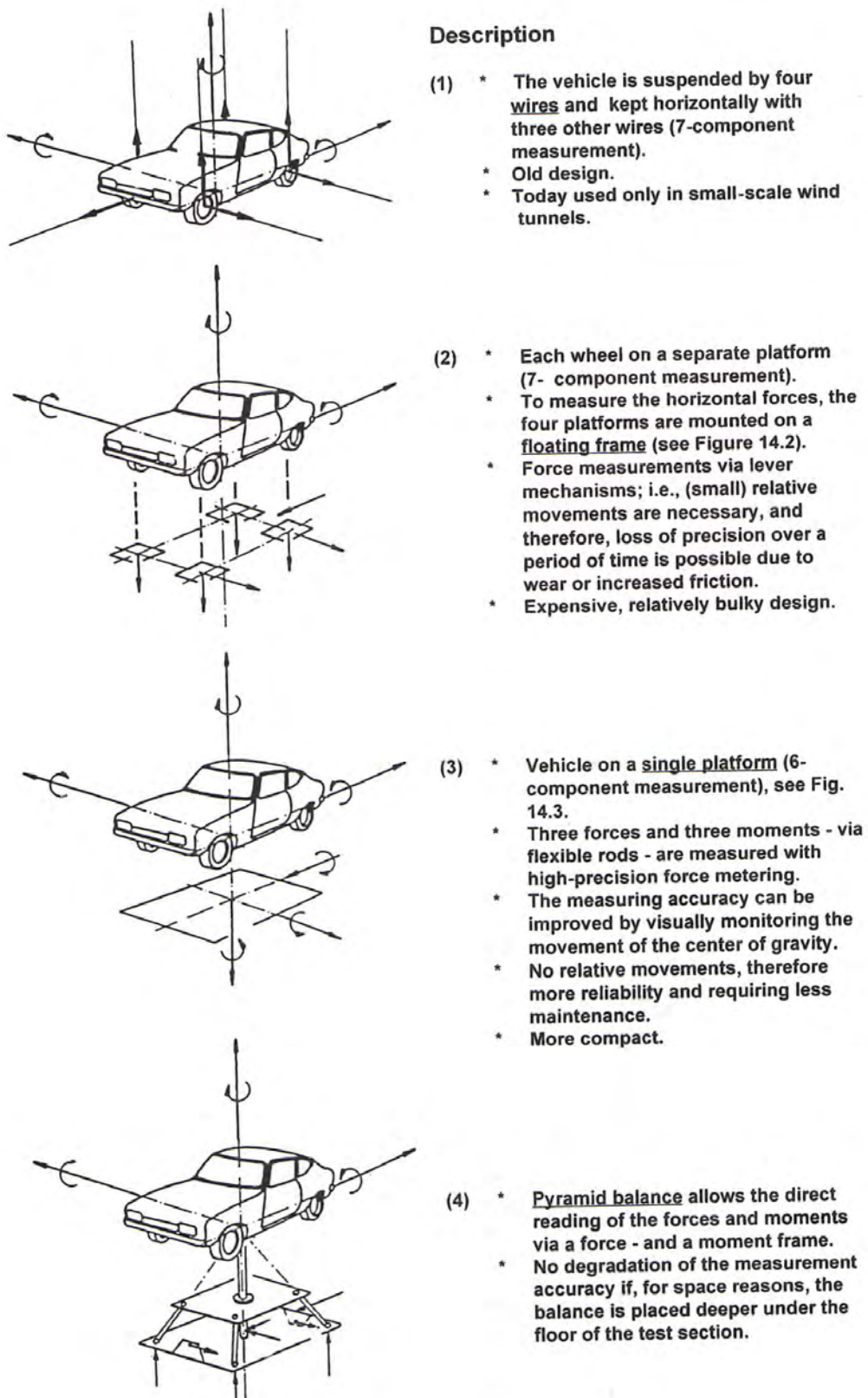


Fig. 3.21: Overview of wind tunnel balance types after Hucho [4]

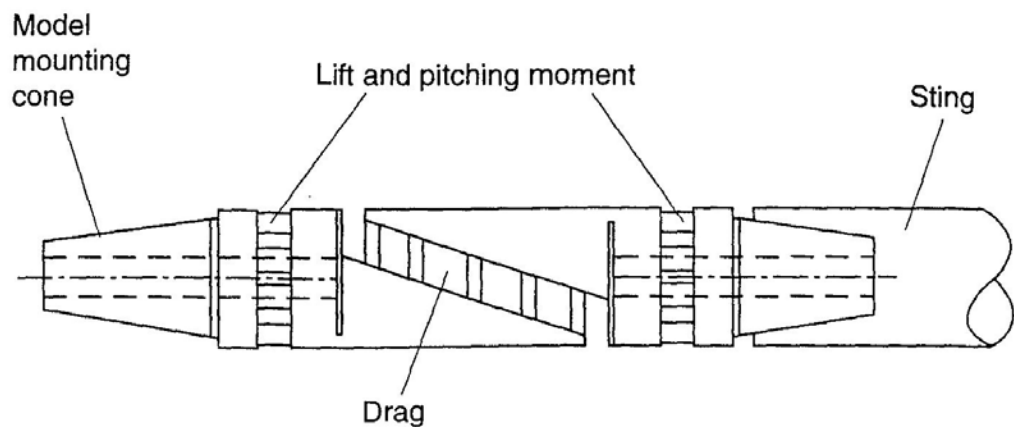


Fig. 3.22: Internal balance schema [6]

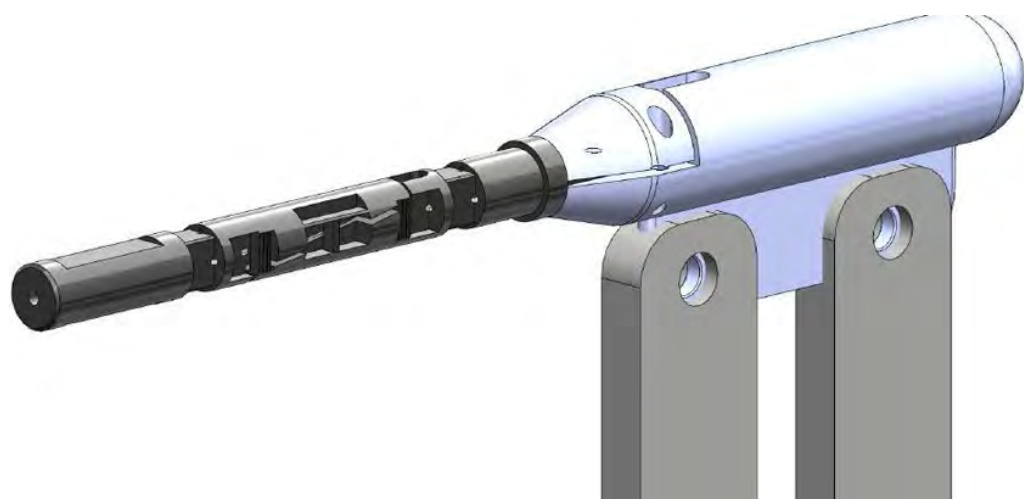


Fig. 3.23: Off-the-shelf internal balance, as sold by Aerolab [aerolab.com]

3 Wind tunnel testing

- Correct loading of the vehicle should be checked – not only total weight but also weight distribution between axles. Incorrect weight distribution might have an effect on ride height, thus also on the test results.
- Flow around a vehicle is unsteady – separations occur, vortices are shed. Therefore the model is exposed to vibrations and obtained test signals are not steady. For this reason, data readings should be long enough to gain representative mean value. The minimum time period required for the measurement must be experimentally determined.

Part II

Experimental testing

4 INTRODUCTION TO PART II

The second part of this work is focused on aerodynamic analysis of an FSAE car. There are two main goals that are to be accomplished. Firstly, it is determination of basic aerodynamic characteristics of current configuration. The second part should focus on determination of areas for improvements in aerodynamic characteristics. These areas for optimisation should be identified with respect to increasing downforce, distribution of downforce and/or reducing drag.

There are two different methods that are accessible and would enable accomplishing both of the aforementioned goals. First of them is numerical model, while the other is experimental model. Naturally, both bring their respective advantages and disadvantages.

Should numerical model be employed, it would enable to determine overall aerodynamic characteristics as well as detailed analysis of the entire flow field around the car. Areas for improvement could be very well found due to the ability to review flow structures and interaction of specific parts on the car. This analysis was previously done in the team and results are available for all the cars mentioned in chapter 1.3. However, the CFD results themselves are not sufficient to really understand the real on-track performance of the aerodynamic design. These results include a high degree of uncertainty.

Employing experimental testing in this work would mean having relatively unrestricted access to low-speed wind tunnel at the Institute of Aerospace Engineering (IAE). This would present an opportunity to obtain a different set of data that would complement the numerical results that are already available. It would not be done with the aim to replace the numerical results altogether. Numerical model could be correlated with the experimental results. Consequently, this would considerably reduce the uncertainty in the numerical model and enable detailed optimization in CFD.

Eventually, being able to use both CFD and wind tunnel results during design could make the process more efficient and enable extraction of the best performance possible.

All of the above being said, the method of choice for the aerodynamic analysis and optimisation in this work is experimental model – wind tunnel testing.

5 EXPERIMENTAL SETUP

5.1 Facility

In this section, the facility where the experiments are conducted is described.

5.1.1 Wind tunnel

The wind tunnel used for experiments in this work is the closed return type (Göttingen type) and its schematic picture can be seen in fig. 5.1. Its basic parameters can be found in tab. 5.1. It was designed and built primarily to measure characteristics of aircraft and automotive heat exchangers.

Tab. 5.1: Wind tunnel parameters

Length	11 500 mm
Height	3 700 mm
Width	1 500 mm
Maximum TI	0.25 %
Engine power	55 kW

5.1.2 Test section and its equipment

Part of the wind tunnel is a closed rectangular test section. Its dimensions are listed in tab. 5.2. Maximum freestream velocity in this *empty* test section is 60 m/s. Schematic picture of the test section can be seen in fig. 5.2.

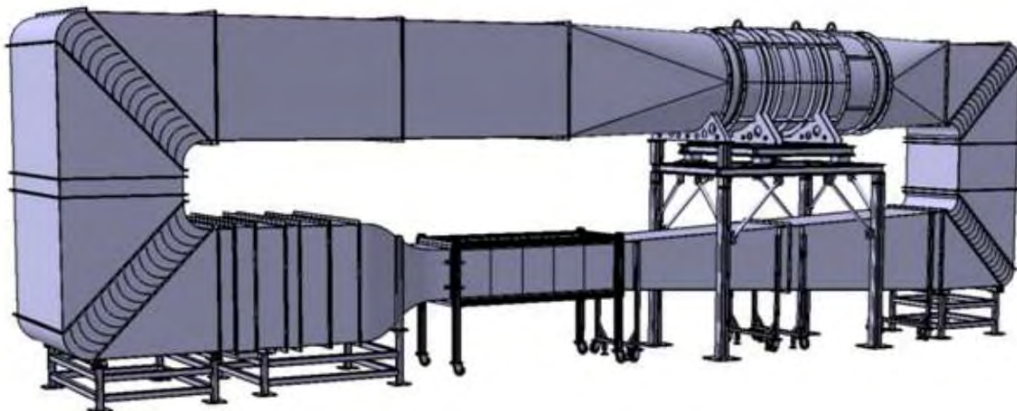


Fig. 5.1: Wind tunnel at the IAE [9]

Tab. 5.2: Test section parameters

Length	2 000 mm
Height	500 mm
Width	700 mm
Maximum freestream velocity	60 m/s



Fig. 5.2: Test section used for wind tunnel testing [9]

With the test section mentioned above, it is possible use different methods for measuring.

First item of this equipment is a pressure transducer. It enables to measure the difference between ambient static pressure and pressure connected to the transducer's sensors. It is possible to log eight of these pressure differences at a time.

The second device that is used for data acquisition is a traverser. It is a device that enables to traverse through a plane perpendicular to the longitudinal axis of the test section. There can be different probes mounted on the traverser. Here prandtl probe and hot wire probe are used. Output from the prandtl probe is dynamic pressure, which enables to calculate local velocity of the flow. The hot wire probe gives two output values. It measures mean velocity over a certain time period. With that value it also provides the root-mean-square of the turbulent velocity fluctuations. Thus, it enables to calculate local turbulence intensity.

5.2 Description of the experimental setup

Purpose of this section is to describe the experimental setup and the reasoning behind it. The main aspects that are considered here are model scale, model mounting and what is actually measured.

5.2.1 Model scale

Theoretically, the only parameter that influences the choice of the model's scale is Reynolds number. However, the scale based on Reynolds number similarity is often limited by the wind tunnel's maximum speed. Furthermore, test section blockage should remain reasonably small. Usually a value of 5 – 10 % is said to be suitable for automotive testing, [4] [6] On top of that, the scale should also take into account the fact, that if it was too small, it would not be possible to manufacture the model with appropriate geometric accuracy.

The scale that best fits the requirements mentioned above was chosen based on fig. 5.3. The diagram is based on the following condition.

$$Re_M = Re_R \quad (5.1)$$

In the equation above, Re_M stands for model Reynolds number and Re_R stands for Reynolds number in real conditions. In real conditions, freestream velocity of 50 km/h is used. That is the speed of interest when designing aerodynamic package for an FSAE car, because that is the average speed in corners.

In section 5.1.2 it is stated that maximum free stream velocity in an *empty* test section is 60 m/s. However, when a model is placed in the test section, the subsequent pressure losses mean, that the maximum wind tunnel velocity is somewhat lower. It is expected, that the maximum velocity with model in the test section is 55 m/s – dashed line in fig. 5.3.

The blue and red solid lines represent how needed wind tunnel velocity and test section blockage, respectively, depend on used model scale.

For 25 % scaled model the desired wind tunnel velocity is just the 55 m/s – expected maximum achievable velocity. With this scale the blockage is 20 %. Such blockage is quite substantial and it is certain that results would be influenced quite considerably by this fact. But as was mentioned in section 3.6.2, testing with blockage up to 20 % can still yield useful aerodynamic data. [8]

Nevertheless, making the model smaller is not an option, because (a) it would compromise the Reynolds number similarity, and (b) at 25 % scale some parts of the model are already really small and it would not be feasible to make them any smaller.

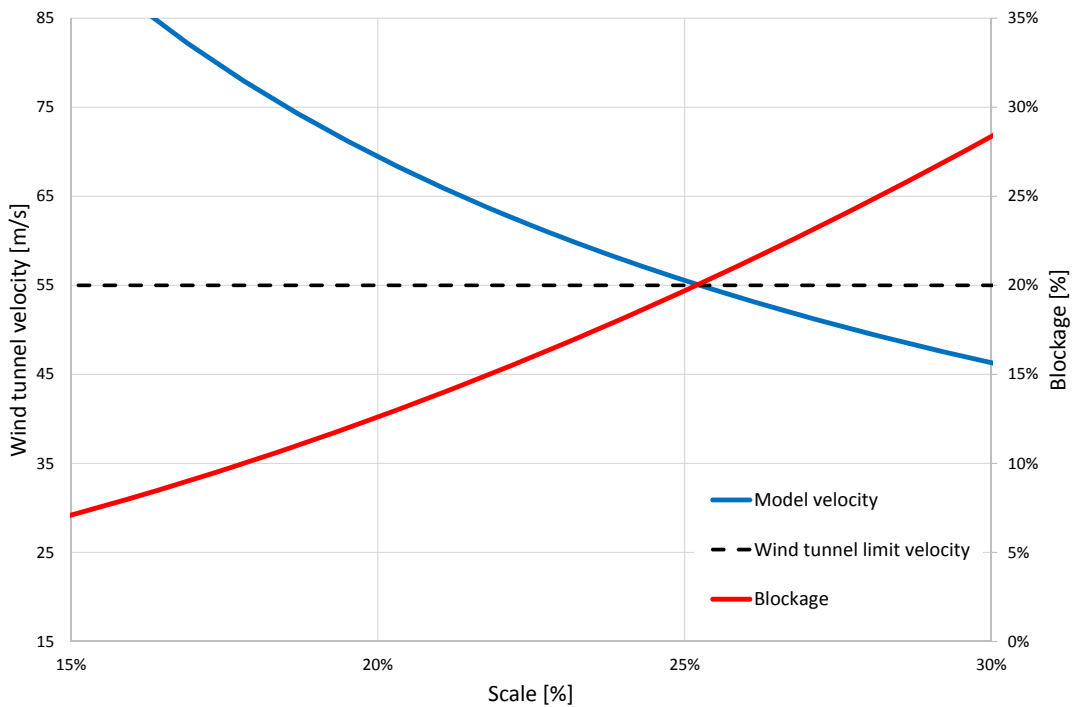


Fig. 5.3: Wind tunnel freestream velocity and test section blockage versus model scale. Based on Reynolds number calculation.

Therefore, the scale chosen for experimental testing in this work is 25 %. The calculations behind fig. 5.3 are shown in appendix A.

5.2.2 Measured quantities

Before considering the way that the model would be eventually mounted in the test section, measured quantities are listed. Consequently, determining what and where on the model is measured places restrictions on the model mounting.

Both of the measuring techniques that were mentioned in section 5.1.2 are used. Firstly, it is desired to obtain pressure coefficient distribution on the model's body-work and floor. Therefore, there are pressure taps installed in the symmetry plane. Secondly, wake traversing is also used.

To determine overall aerodynamic load on the model, it is essential to measure forces acting on the model. Nevertheless, force balance is not available as part of the off-the-shelf equipment. Force balance is further discussed in chapter 7.

5.2.3 Model mounting

Different possible ways of mounting a model to a test section were described in section 3.8. There, four options were presented.

In a more general way, the options could be divided into two categories. Firstly, it is mounting the model through struts directly connected to the wheels (see fig. 3.17). And a second option is using a sting mounting (see fig. 3.18, 3.19, and 3.20).

Connecting a model by its wheels directly to struts going through the ground plane offers the least flow disturbance of the surrounding flow field. However, there are two reasons that render it inconvenient. The actual connection of the struts to the wheels is rather complicated. There must be a gap between the struts and wind tunnel floor, so that there is no contact. This gap has to be sealed to prevent any flow alteration around the wheel contact patch. When this mounting solution is used, usually the entire force balance beneath the test section is hermetically closed.

If the model was placed on its wheels, it would mean that the wishbones would have to support the entire model. With the 25 % scale, the wishbone diameter is 4 mm. It is not believed that such a solution would be structurally sufficient.

Ruling out the first option leaves the choice to mounting the model on a sting. It can be mounted from behind, from below or from above. Sting introduced from every mentioned direction results in flow disturbance. But considering that introducing the sting from below would alter the flow field in the vicinity of pressure taps and introducing the sting from behind would bring disturbances to the wake – both areas being of interest – it would consequently introduce an error in measured data. Therefore, mounting the model on a sting from above appears to be the best option.

5.2.4 Final experimental setup

Final experimental set up used for wind tunnel tests in this work can be seen in fig. 5.4. In the picture the 25% scale model mounted on a sting balance from above is placed in a test section at the IAE wind tunnel facility.

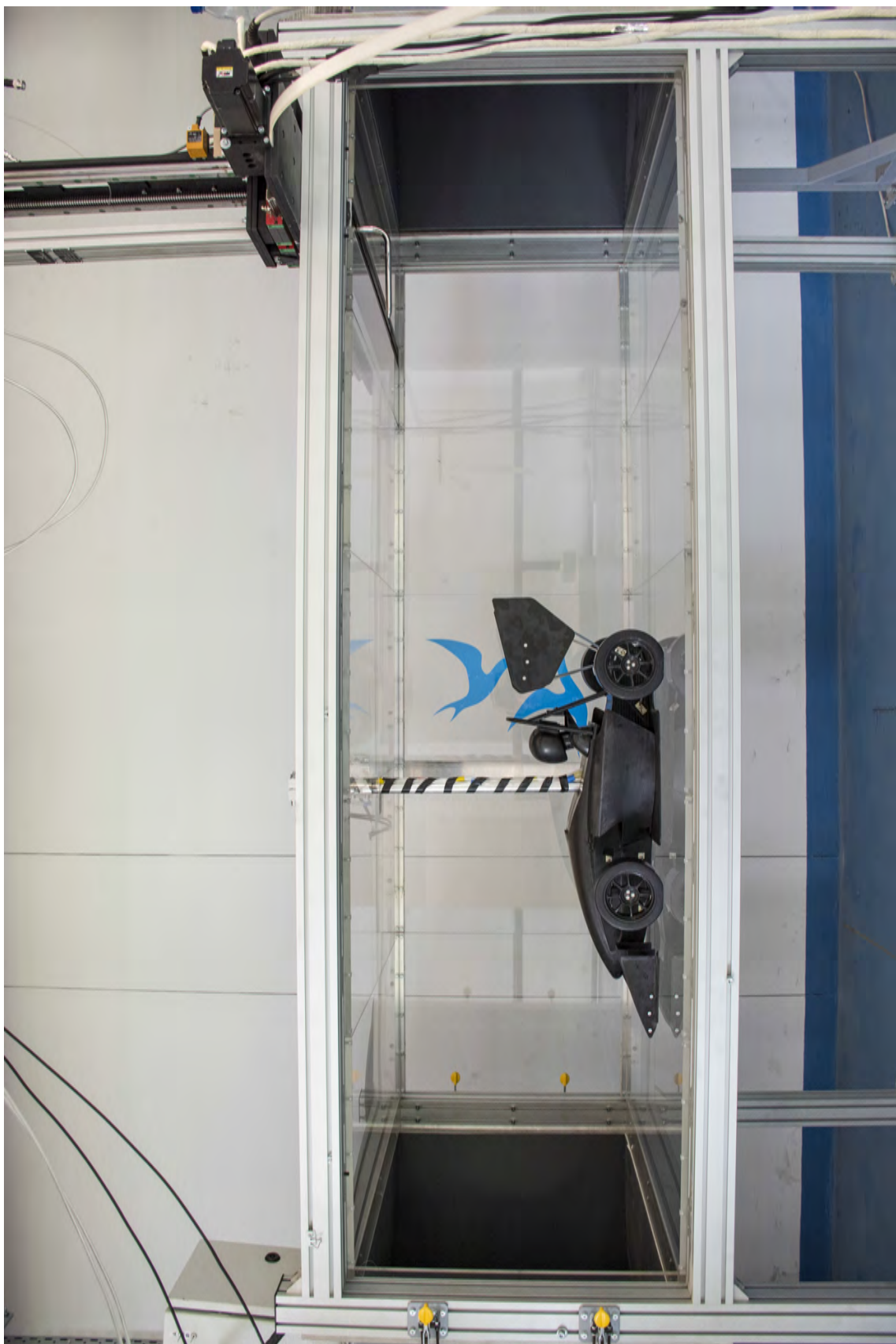


Fig. 5.4: Final experimental set up used for wind tunnel tests in this work

6 MODEL

According to the decision taken in section 5.2.1, the model that is used for the experiments in this work is 25% scale of the real car.

From the beginning, the model was designed based on the fact that it would be manufactured by rapid prototyping technologies. The model is 3D printed from plastic material.

First aspect that was addressed when designing the model was geometric accuracy. Even though, the assembled model is quite large (for overall dimensions see fig. 6.1), some parts are rather small. All airfoils used on flaps had to be modified, so that their minimum thickness does not go below 0.5 mm. Then, the model geometry was considerably simplified, compared to a real car. The reason for the simplification is that it was obvious, that the wind tunnel blockage would have dominant influence on the results. Therefore, for this first investigation of the experiment set up used in this work, the geometry was simplified where possible (e.g. the engine compartment (fig. 6.2), wheel assembly, suspension (fig. 6.3)). More simple geometry consequently means shorter computation time, should the numerical simulation be done with the same geometry and the same set up.

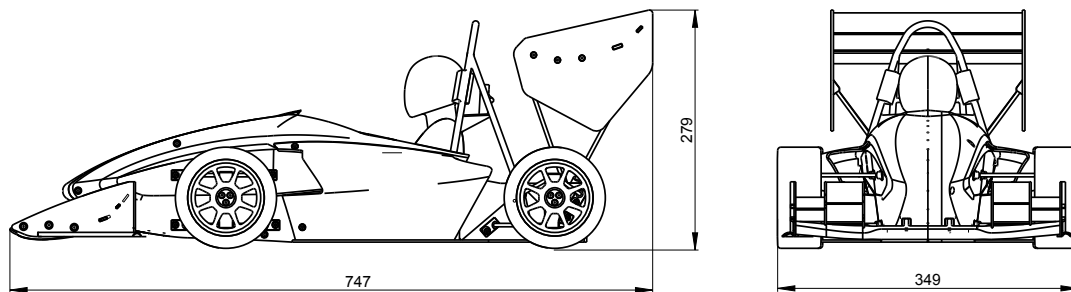


Fig. 6.1: Overall model dimensions

Apart from the aforementioned changes in geometry, compared to the real car, other changes also had to be made. These were done based on structural considerations. One of these is the addition of a 'fin' to the rear wing's airfoil section (visible in fig. 6.2). Based on a manufactured test flap, it was obvious that it would not be rigid enough and that it would be subjected to significant deflections.

As was mentioned, all parts of the model are 3D printed. The only exception are suspension arms and rods for rear wing attachment – for this aluminium tube is used. As is apparent from the overall model dimensions in fig. 6.1, it is too large to be manufactured in one piece. Furthermore, manufacturing the model in one piece would also be inconvenient with respect to final surface treatment. Therefore, the

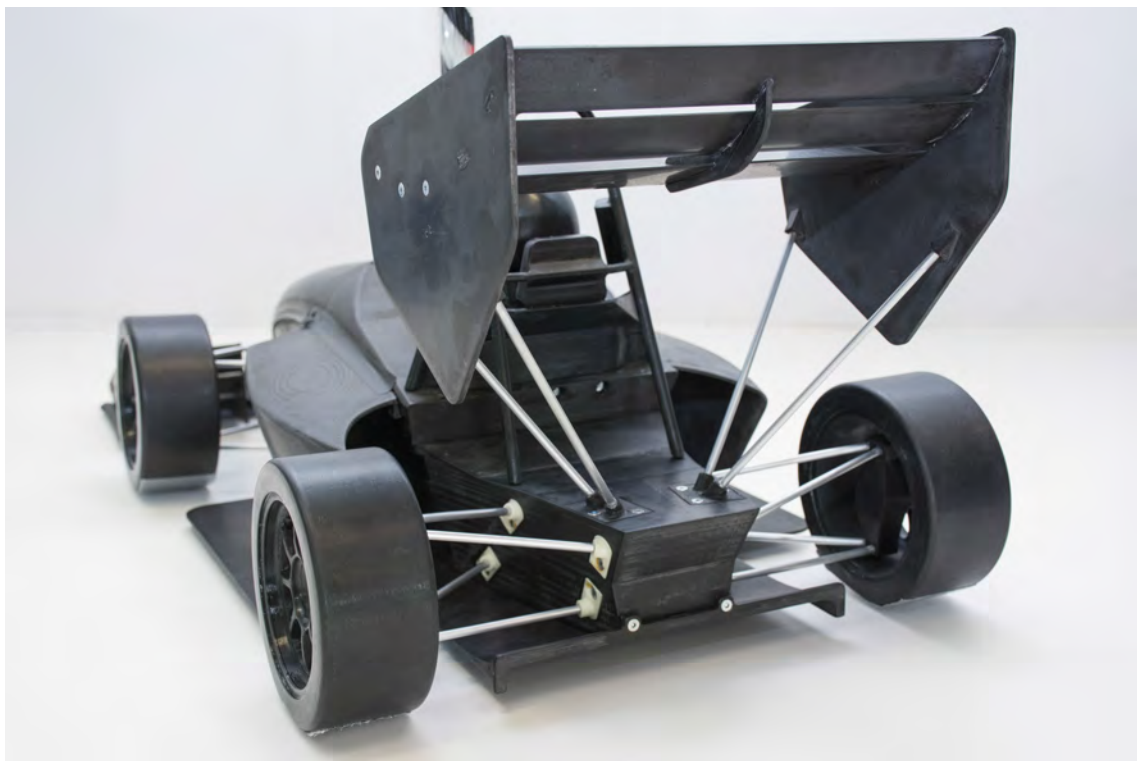


Fig. 6.2: Geometry simplification – engine compartment; rear wing with the additional fin in the symmetry plane



Fig. 6.3: Geometry simplification – upright assembly, suspension

model is divided into separate parts. In most cases, the parts are divided as they would be on a real car – wing flaps, wheels, uprights, floor, sidepods, etc.

The main bodywork is divided into two parts and is hollow inside to accommodate pressure taps. The pressure taps are brass tubes with 1.2 mm inner diameter that are aligned with the model's outer surface and glued into the plastic parts (fig. 6.4). The final arrangement of pressure taps and rubber hoses inside the model can be seen in fig. 6.5.



(a) View from outside of the model

(b) View from inside of the model

Fig. 6.4: Detailed view of the pressure taps

To be able to compare the contribution of the diffuser to downforce, two versions of the floor were manufactured. The floor with diffuser, in fig. 6.6, is the 'default' one and resembles the design actually used on the real car. For comparison, simplified floor was designed (fig. 6.7). It does not have a diffuser and is cut just around the sidepods. Detailed view of both floor's rear part is captured in fig. 6.8.

Finally, the assembled model can be seen in fig. 6.9.



Fig. 6.5: Pressure taps connected to rubber hoses inside of the model



Fig. 6.6: Floor with diffuser



Fig. 6.7: 'Simple' floor – cut around sidepods, without a diffuser



(a) Diffuser

(b) Planar floor

Fig. 6.8: Detailed view of the floor versions



Fig. 6.9: Model used for the experiment

7 BALANCE DESIGN AND CALIBRATION

7.1 Basic definitions

Before it is proceeded to the following sections, aerodynamic loads and reference coordinate system for their description are defined.

7.1.1 Coordinate system

A reference coordinate system for description and evaluation of aerodynamic loads acting on a vehicle is schematically shown in fig. 7.1. The coordinate system is positioned on the ground plane just in the middle of wheelbase and track. The x axis is then going forward, in the direction of driving, the y axis is going to right from drivers perspective and the z axis is directed to the ground.

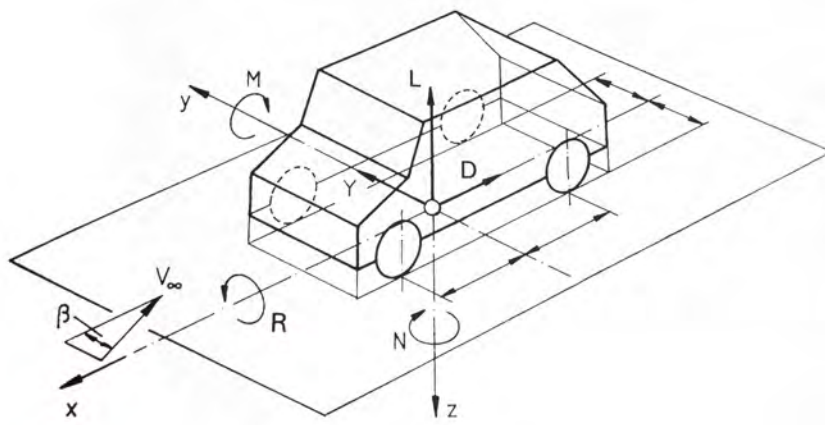


Fig. 7.1: Aerodynamic loads on a vehicle acting in the reference coordinate system [4]

Unless stated otherwise, all aerodynamic loads in this work are referred to this coordinate system.

7.1.2 Aerodynamic loads

Aerodynamic loads acting on a vehicle can also be seen in Fig. 7.1. These loads act in the origin of the coordinate system described above (section 7.1.1). The aerodynamic loads are described by three forces and three moments. The forces are:

- Drag force (D, C_D)
 - Drag force acts parallel to the x axis
 - Positive drag force has opposite direction to the x axis

- Side force (Y, C_Y)
 - Side force acts parallel to the y axis
 - Positive side force has the same direction as the y axis
- Lift force (L, C_L)
 - Lift force acts parallel to the x axis
 - Positive lift force has opposite direction to the y axis

The moment vectors – when positive – always have the same direction as their respective axes.

- Rolling moment (R, C_R)
 - The rolling moment vector acts parallel to the x axis
- Pitching moment (M, C_M)
 - The pitching moment vector acts parallel to the y axis
- Yawing moment (N, C_N)
 - The yawing moment vector acts parallel to the z axis

Aerodynamic loads can be calculated with equations 7.1 and 7.2. In these equations F_i stands for a general aerodynamic force, while M_i stand for a general aerodynamic moment. ρ , V_∞ , A and l represent air density, freestream velocity, vehicle reference area and vehicle reference length, respectively. C_{F_i} and C_{M_i} are dimensionless coefficients of aerodynamic force and moment.

$$F_i = \frac{1}{2} \rho V_\infty^2 A C_{F_i} \quad (7.1)$$

$$M_i = \frac{1}{2} \rho V_\infty^2 A C_{M_i} l \quad (7.2)$$

Based on these equations, both aerodynamic forces and moments are dependent on the square of velocity. Usually, it is desirable to quantify aerodynamic loads in a way that it is independent of velocity. Also, aerodynamic forces and moments are generally taken from wind tunnel testing. Then, dimensionless aerodynamic coefficients are defined as follows. [4]

$$C_{F_i} = \frac{F_i}{\frac{1}{2} \rho V_\infty^2 A} \quad (7.3)$$

$$C_{M_i} = \frac{M_i}{\frac{1}{2} \rho V_\infty^2 A l} \quad (7.4)$$

7.2 Balance design

Available measuring equipment at the IAE's wind tunnel facility was described in section 5.1.2. Force balance is not mentioned, because it is not part of the equipment. Nevertheless, to determine aerodynamic characteristics of a vehicle model, it is necessary to measure aerodynamic load.

Since off-the-shelf force balances are considerably expensive, it was decided to design and build a simple force balance, that would use strain gauges to measure load on the model. The resulting balance design should implement two key design points – it should be low cost and easy to manufacture.

First intention was to design a balance that would measure only two components of the resulting aerodynamic load – lift and pitching moment. The reasoning behind this was an effort to make the balance as simple as possible. However, this approach was rendered inconvenient, because drag force ultimately has a significant effect on the pitching moment. Therefore, it would not be possible to determine the point, where the lift resultant is positioned, i.e. downforce distribution could not be properly determined.

The iteration that followed was a balance, that would measure three components – drag, lift, and pitching moment. With symmetrical model in a wind tunnel and no side wind ($\beta = 0$), the rest of the components should be zero. Although, in reality there is no guarantee that this would indeed be the case. Parasitic forces and moments can be present during the experiment.

At last, it was decided to design a balance, that would measure all six components of the aerodynamic load.

Maximum load on the balance was estimated based on CFD computations of Dragon 5. The computations are shown in equations 7.5, 7.6, and 7.7. The calculated values are then multiplied by a safety factor of 1.5.

$$L_M = \frac{1}{2} \cdot \rho \cdot V_\infty^2 \cdot A_M \cdot C_L = \frac{1}{2} \cdot 1.225 \cdot 55^2 \cdot 0.069 \cdot 2.69 = 344 \text{ N} \quad (7.5)$$

$$D_M = \frac{1}{2} \cdot \rho \cdot V_\infty^2 \cdot A_M \cdot C_D = \frac{1}{2} \cdot 1.225 \cdot 55^2 \cdot 0.069 \cdot 1.14 = 146 \text{ N} \quad (7.6)$$

$$M_M = \frac{1}{2} \cdot \rho \cdot V_\infty^2 \cdot A_M \cdot l_m \cdot C_M = \frac{1}{2} \cdot 1.225 \cdot 55^2 \cdot 0.069 \cdot 382 \cdot 1.14 = 11\,702 \text{ N.mm} \quad (7.7)$$

The remaining components of the aerodynamic load were estimated as follows:

- Side force – 40% of lift force
- Rolling moment and yawing moment – 40% of pitching moment

Tab. 7.1: Maximum estimated load on the force balance

D	220 N
Y	200 N
L	500 N
R	7 200 N.mm
M	18 000 N.mm
N	7 200 N.mm

The final values, that are later used for balance design, are shown in tab. 7.1.

In section 5.2.3 it was decided that the model would be mounted on a sting from above. That means that one beam of the balance is the sting and it goes all the way outside of the test section above the model. This can be seen in fig. 7.2.

As far as the overall configuration goes, it was found that the most convenient is to position the balance's horizontal beam to the side of the test section, as is sketched in fig. 7.3.

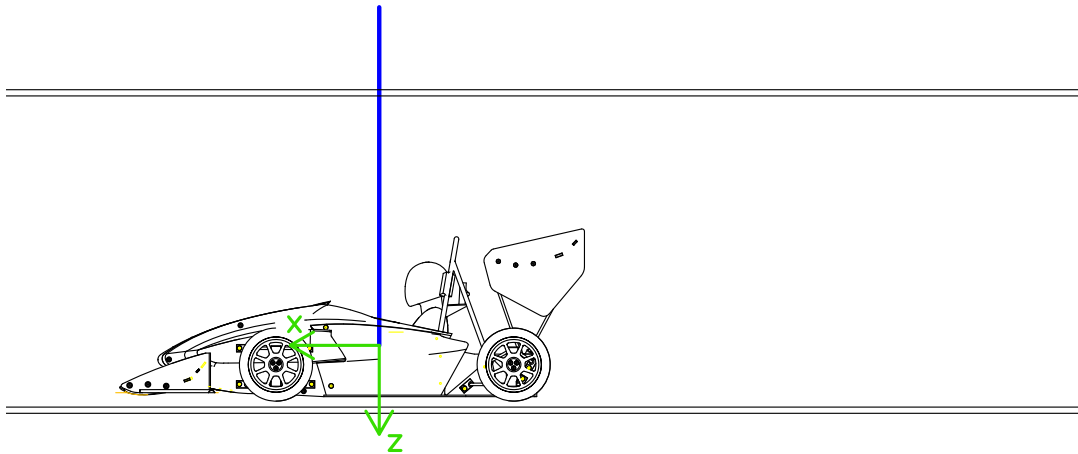


Fig. 7.2: Sketch of the force balance in the test section with model – left view

Firstly, the idea was to create two 'load-cell-like' parts, that would measure bending moment around two perpendicular axis and torque around the beam's longitudinal axis. These two parts would be placed at points *A*, and *B*, according to fig. 7.3. However, this is not possible for two reasons: (a) the resulting dimensions of the cross-section where torque would be measured would be too small, and (b) in this configuration, it would not be possible to calculate the load at the model's attachment point.

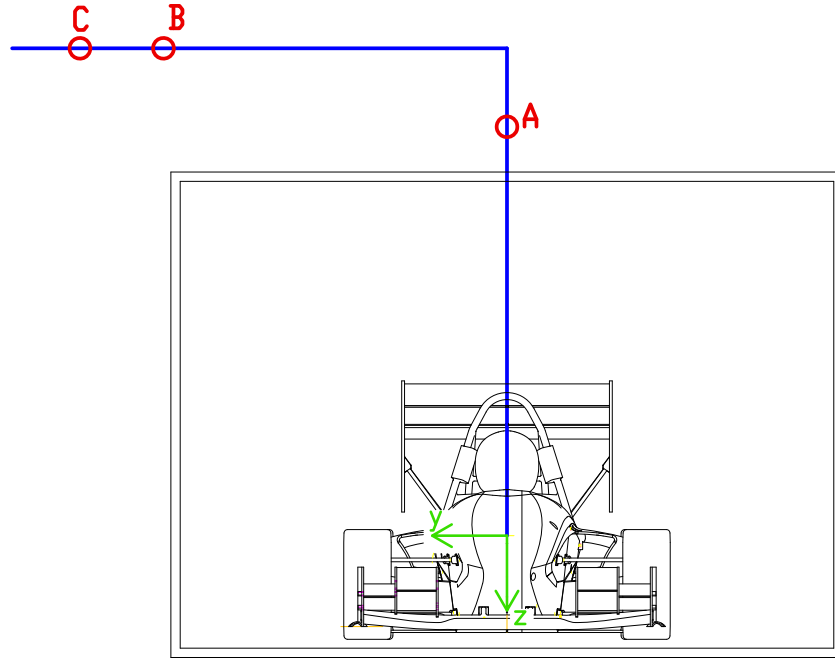


Fig. 7.3: Sketch of the force balance in the test section with model – front view

The solution to this problem that was found convenient is following. Instead of measuring torque at points A and B , a new point C is introduced. Then, at all three points A , B , and C two bending moments around perpendicular axes are measured.

In fig. 7.4 the final version of the force balance is schematically depicted. Six strain gauge bridges $B1$ – $B6$ are showed there – two bridges at each point A , B , and C . Six components of load are introduced in the model attachment point. Then the strain gauge bridges measure moments $M1$ – $M6$, respectively. These moments can be calculated based on equations 7.8 to 7.13.

$$M_1 = M_x - F_y r_1 \quad (7.8)$$

$$M_2 = M_y + F_x r_1 \quad (7.9)$$

$$M_3 = M_x - F_y r_0 - F_z r_2 \quad (7.10)$$

$$M_4 = M_z + F_x r_2 \quad (7.11)$$

$$M_5 = M_x - F_y r_0 - F_z r_3 \quad (7.12)$$

$$M_6 = M_z + F_x r_3 \quad (7.13)$$

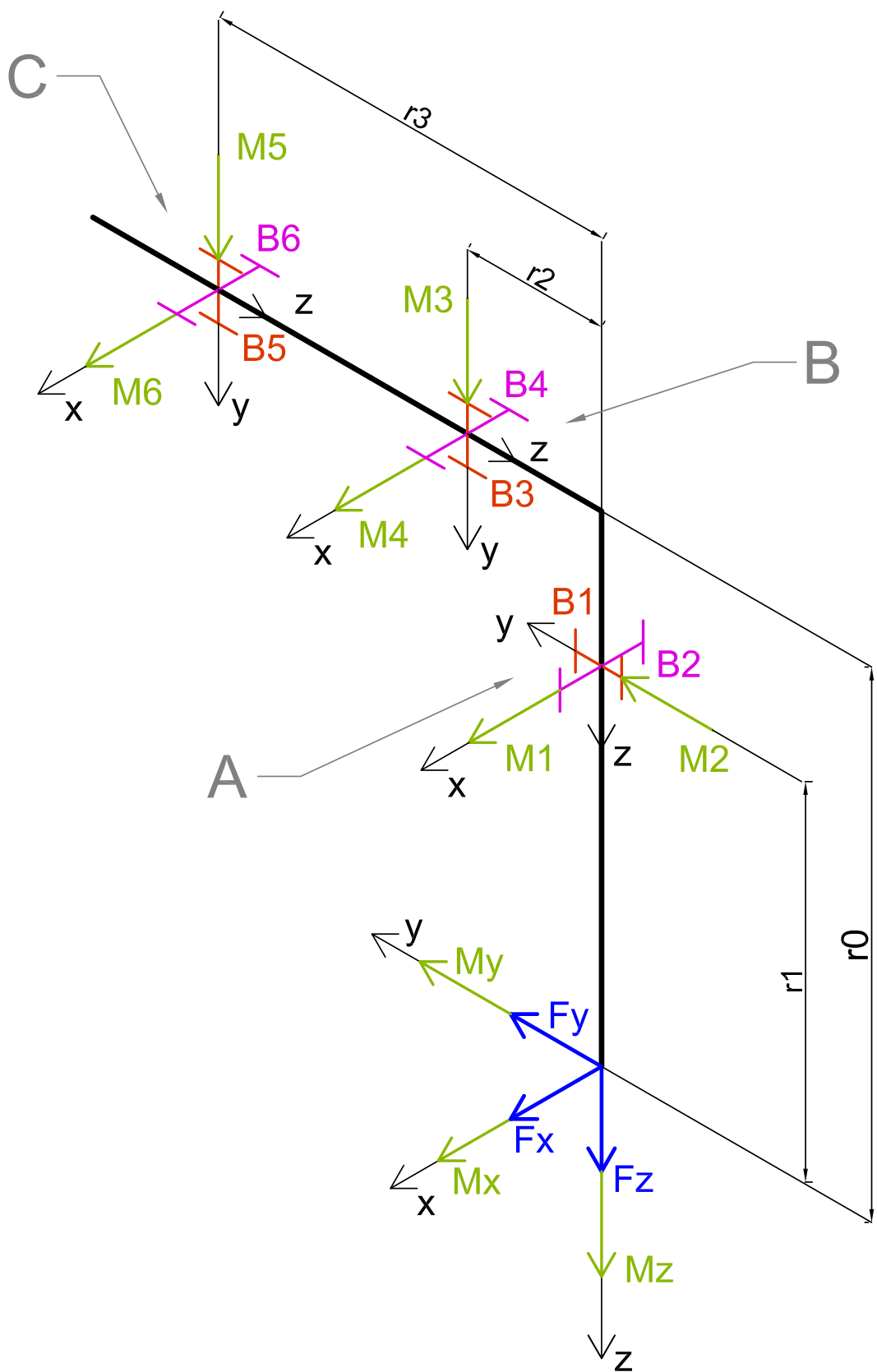


Fig. 7.4: Schematic picture of force balance

The equations 7.8 to 7.13 can be expressed in matrix form as follows.

$$\begin{bmatrix} 0 & -r_1 & 0 & 1 & 0 & 0 \\ r_1 & 0 & 0 & 0 & 1 & 0 \\ 0 & -r_0 & -r_2 & 1 & 0 & 0 \\ r_2 & 0 & 0 & 0 & 0 & 1 \\ 0 & -r_0 & -r_3 & -1 & 0 & 0 \\ r_3 & 0 & 0 & 0 & 0 & 1 \end{bmatrix} \cdot \begin{bmatrix} F_x \\ F_y \\ F_z \\ M_x \\ M_y \\ M_z \end{bmatrix} = \begin{bmatrix} M_1 \\ M_2 \\ M_3 \\ M_4 \\ M_5 \\ M_6 \end{bmatrix} \quad (7.14)$$

Equation 7.14 can also be written as eq. 7.15.

$$\mathbb{K} \cdot \mathbb{X} = \mathbb{M} \quad (7.15)$$

According to eq. 7.15, based on known load in the model attachment point, moments at points A , B , and C can be computed. However, when measuring in wind tunnel, moments $M_1 - M_6$ are measured. Then, the aerodynamic load in the model attachment point is computed from equation 7.16.

$$\mathbb{K}^{-1} \cdot \mathbb{M} = \mathbb{X} \quad (7.16)$$

Values representing balance geometry are shown in tab. 7.2 (apart from design values, the table also includes values that were eventually measured on assembled balance that was used during experiment).

Arm	Design [mm]	Measured [mm]
r_0	550	539
r_1	500	479
r_2	430	426
r_3	480	475.5
a	180	180

Tab. 7.2: Balance geometry values

At this point, the cross-sections of the balance at the points of strain gauge bridges can be computed. Input information for this step is the maximum anticipated load shown in tab. 7.1. This load is transformed into moments at points A , B , and C according to eq. 7.15.

To ensure sufficient accuracy of the balanced, deformation of $\varepsilon = 2000 \mu\text{m}/\text{m}$ is taken into account for computation of cross-section dimensions at all points. At all points, rectangular cross-section area – as sketched in fig. 7.5 – is desired.

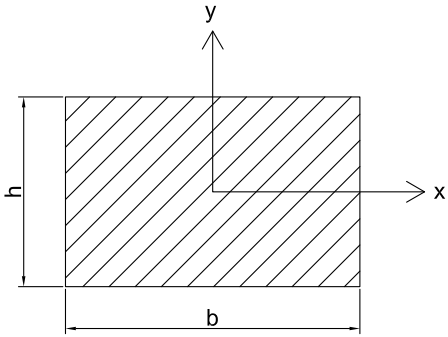


Fig. 7.5: Sketch of balance's rectangular cross-section

For such a cross-section second moment of inertia around its x and y axes is defined as follows.

$$J_x = \frac{b \cdot h^3}{12} \quad (7.17)$$

$$J_y = \frac{b^3 \cdot h}{12} \quad (7.18)$$

Second moment of inertia can be transformed to bending stiffness by following equations.

$$W_x = \frac{\frac{b \cdot h^3}{12}}{\frac{h}{2}} = \frac{b \cdot h^2}{6} \quad (7.19)$$

$$W_y = \frac{\frac{b^3 \cdot h}{12}}{\frac{b}{2}} = \frac{b^2 \cdot h}{6} \quad (7.20)$$

Then, bending stress σ_b in both x and y directions is defined by eq. 7.21 and 7.22.

$$\sigma_{b,x} = \frac{M_{b,x}}{W_x} \quad (7.21)$$

$$\sigma_{b,y} = \frac{M_{b,y}}{W_y} \quad (7.22)$$

From equations 7.21 and 7.22, bending stiffness W can be expressed. At the same time Hook's law is used to substitute stress σ_b .

$$W_x = \frac{M_{b,x}}{E \varepsilon_x} \quad (7.23)$$

$$W_y = \frac{M_{b,y}}{E \varepsilon_y} \quad (7.24)$$

In eq. 7.23 and 7.24, bending stiffness W is substituted from eq. 7.19 and 7.20, respectively.

$$\frac{b \cdot h^2}{6} = \frac{M_{b,x}}{E\varepsilon_x} \quad (7.25)$$

$$\frac{b^2 \cdot h}{6} = \frac{M_{b,y}}{E\varepsilon_y} \quad (7.26)$$

Then, dimension b is expressed from eq. 7.25.

$$b = \frac{6M_{b,x}}{E\varepsilon_x h^2} \quad (7.27)$$

Dimension b in eq. 7.26 is then substituted by eq. 7.27.

$$\left(\frac{6M_{b,x}}{E\varepsilon_x h^2} \right)^2 \cdot \frac{h}{6} = \frac{M_{b,y}}{E\varepsilon_y} \quad (7.28)$$

Finally, from eq. 7.28, dimension h can be expressed – eq. 7.29. In this equation, all variables are part of input information. Aluminum is used for balance manufacturing, therefore young's modulus is $E = 72\,000\text{ MPa}$. As was mentioned before, deformation for all cross-sections is $\varepsilon = 2000\text{ }\mu\text{m/m}$. Bending moments are calculated according to eq. 7.14. So, for example, for cross-section at point A , bending moment around x axis $M_{b,x}$ is moment M_1 and bending moment around y axis $M_{b,y}$ is moment M_2 .

$$h = \sqrt[3]{\left(\frac{6M_{b,x}}{E\varepsilon_x} \right)^2 \cdot \frac{E\varepsilon_y}{6M_{b,y}}} \quad (7.29)$$

Equation 7.29 is retrospectively substituted into eq. 7.27 to enable calculation of dimension b .

$$b = \frac{6M_{b,x}}{E\varepsilon_x \left(\sqrt[3]{\left(\frac{6M_{b,x}}{E\varepsilon_x} \right)^2 \cdot \frac{E\varepsilon_y}{6M_{b,y}}} \right)^2} \quad (7.30)$$

Finally, computed dimensions of cross-section at all points A , B , and C are shown in tab. 7.3.

Final mechanical design of the balance can be seen from drawings that are shown in appendix B.1. The balance assembly – captured during calibration – can be seen in fig. 7.10.

Tab. 7.3: Dimensions of balance's cross-section at points of strain gauge bridges

Point on balance	b [mm]	h [mm]
A	19.5	14
B	12	35
C	11	35

7.3 Balance calibration

During balance calibration, known load is applied on the balance and strain gauge responses are then evaluated based on the applied load. This is done so that later, the balance can be used inversely – determine load from strain gauge responses.

Here, respective components of load were applied on the balance separately, in order to obtain strain gauge responses for these separate load components. Aerodynamic load and its components were sketched in fig. 7.4. They are three forces F_x , F_y and F_z and three moments M_x , M_y and M_z .

For calibration, the balance was set up as it would eventually be in the wind tunnel. Strain gauges were connected to a data logger (see fig. 7.6). Load was applied through a load cell (see fig. 7.7). The load cell's output is force in [N], and it was also connected to the data logger. This enables to match strain gauge responses to accurate force for the whole range of load that was applied.

Firstly, forces were applied on the balance. This was carried out simply by pressing the load cell against the balance in the model attachment point by hand. Forces were applied up to the maximum values that were used for the balance design (see tab. 7.1).

Moments were applied according to schematic sketch in fig. 7.8. Then, the final set up that was used to apply moments is in fig. 7.9, and 7.10. Again, the respective moments were applied up to their maximum design values.

The data logging process when applying the calibration loads was following:

- balance strain gauges, so that they start logging at $0 \mu m/m$
- log zero values
- log data when applying load

Generally, the data output from the data logger is in the format as shown in equation 7.31. In the first column of the matrix, there are responses for strain gauge



Fig. 7.6: Data logger used to log strain gauge responses (during both calibration and wind tunnel testing)

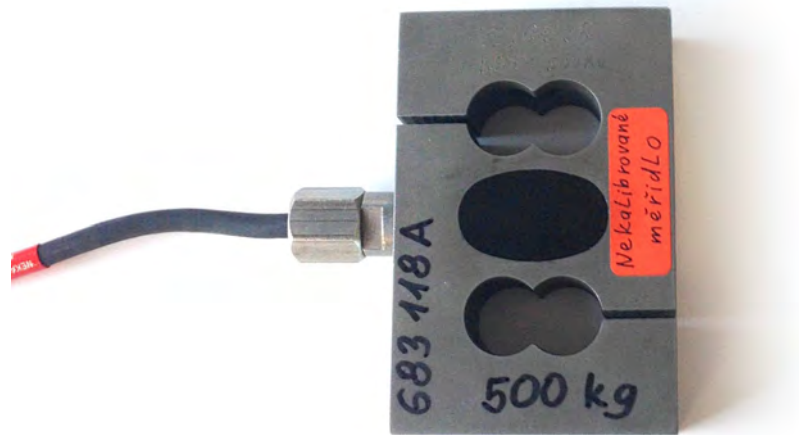


Fig. 7.7: Load cell used for applying load during calibration

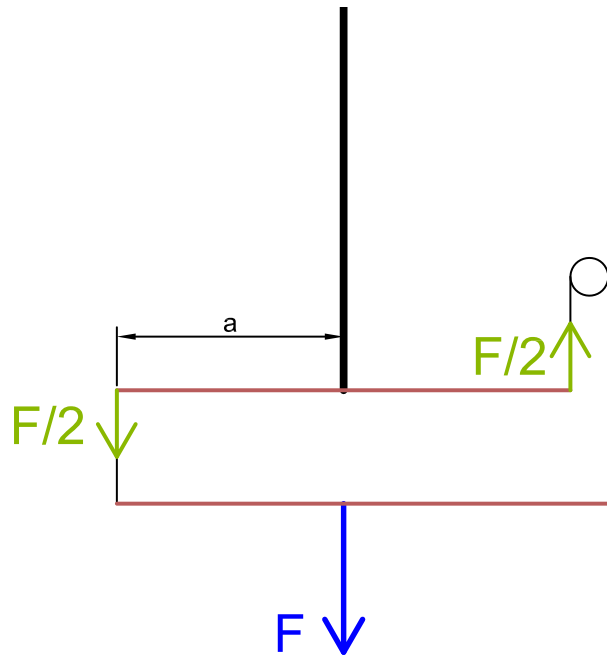


Fig. 7.8: Schematic sketch of moment application on the balance

bridge $B1$. Values for the bridge $B2$ are in the second column and so on.

$$Z = \begin{bmatrix} r_{1,B1} & r_{1,B2} & \dots & r_{1,B6} \\ r_{2,B1} & r_{2,B2} & \dots & r_{2,B6} \\ \vdots & \vdots & \ddots & \vdots \\ r_{n,B1} & r_{n,B2} & \dots & r_{n,B6} \end{bmatrix} \frac{\mu m}{m} \quad (7.31)$$

However, since the output from the load cell is also logged, the matrix in eq. 7.31 changes into the one shown in eq. 7.32. The force in $[N]$ is in the seventh column.

$$Z = \begin{bmatrix} r_{1,B1} & r_{1,B2} & \dots & r_{1,B6} & F_1 \\ r_{2,B1} & r_{2,B2} & \dots & r_{2,B6} & F_2 \\ \vdots & \vdots & \ddots & \vdots & \vdots \\ r_{n,B1} & r_{n,B2} & \dots & r_{n,B6} & F_n \end{bmatrix} \left[\frac{\mu m}{m}; N \right] \quad (7.32)$$

The same calibration process is done for all strain gauge bridges and for all of them the process is the same. Response of a strain gauge bridge is matched and calibrated with a moment acting at the point of the bridge.

Here, the calibration is shown only for bridge $B2$.

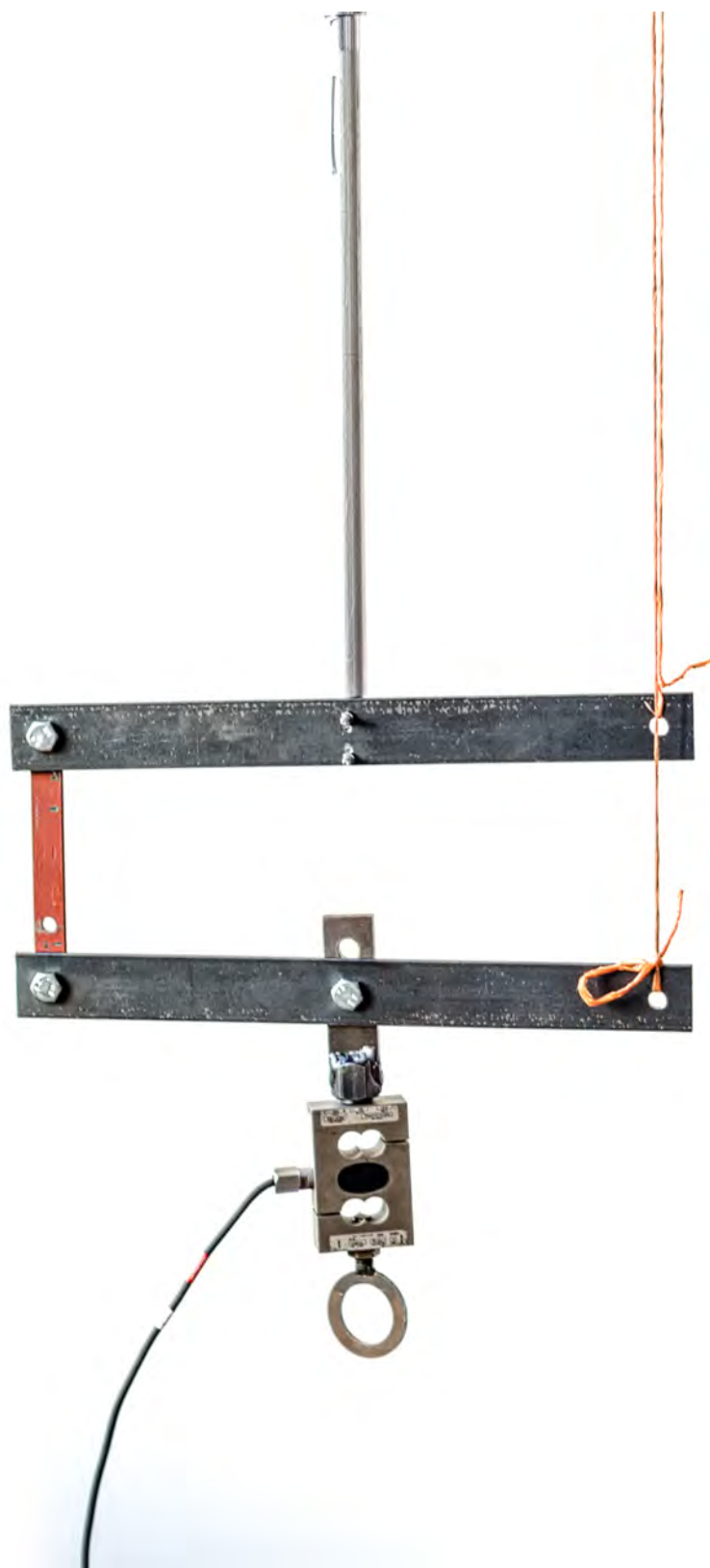


Fig. 7.9: Moment application on balance (1)



Fig. 7.10: Moment application on balance (2)

The first step of the calibration is to subtract zero values from the values measured when load was applied. Zero values are first averaged and then subtracted. It can be expressed by the following equations.

$$R_{zero}^{B2} = \text{average}(Z_{zero}^{B2}) \quad (7.33)$$

$$R^{B2} = Z^{B2} - R_{zero}^{B2} \quad (7.34)$$

Bridge B2 responds to components of load F_x and M_y . Therefore, only data for bridge B2 logged when only F_x and M_y were applied are taken into account for calibration. These are:

- $R_{F_x}^{B2}$ – vector of responses of bridge B2 under loading by force F_x
- $R_{M_y}^{B2}$ – vector of responses of bridge B2 under loading by moment M_y
- F_{F_x} – vector of force that was applied on balance as F_x
- F_{M_y} – vector of force that was applied on balance when M_y was introduced

The logged forces have to be recalculated into moments acting in the point of bridge B2. Geometrical characteristics of the balance are introduced in this step. The balance geometry is shown in tab. 7.2.

$$M_{F_x}^{B2} = F_{F_x} \cdot r_1 \quad (7.35)$$

$$M_{M_y}^{B2} = F_{M_y} \cdot a \quad (7.36)$$

Now, moment recorded at the point of bridge B2 – M^{B2} – can be plotted against the bridge's response R^{B2} . This is done in fig. 7.11. It can be seen, that the relation between the two quantities is linear.

Finally, the data in the fig. 7.11 is fitted with a linear curve. Such curve is described by the following equation.

$$M^{Bi} = p_1^{B2} \cdot R^{Bi} + p_2^{B2} \quad (7.37)$$

In the equation 7.37 p_1^{B2} is the desired calibration coefficient for strain gauge bridge B2. Coefficient p_2^{B2} is not used in the calibration matrix, because only slope of the approximated line is of interest.

The calibration process, that was described above, is done for all of the strain gauge bridges. The only exception from the example above is bridge B1. For this bridge, the relation between moment and response does not appear to be satisfactorily

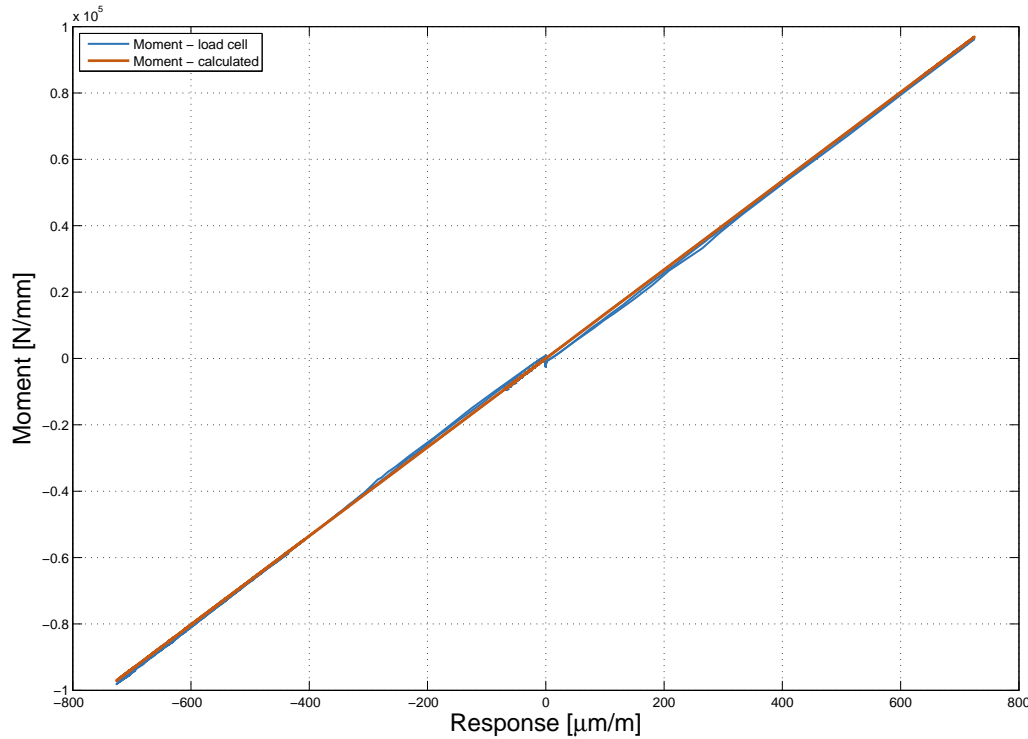


Fig. 7.11: Data used for calibration of bridge B2, plotted with approximated moment

linear. Therefore the data is fitted with a quadratic curve, which is described by equation 7.38.

$$M^{B1} = p_1^{B1} \cdot R^{B1} + p_2^{B1} \cdot R^{B1} + p_3^{B1} \quad (7.38)$$

From all calibration coefficients a calibration matrix is assembled. The final calibration matrix \mathbb{C} is shown in equation 7.39.

$$\mathbb{C} = \begin{bmatrix} p_1^{B1} & p_2^{B1} & p_3^{B1} \\ p_1^{B2} & 0 & 0 \\ p_1^{B3} & 0 & 0 \\ p_1^{B4} & 0 & 0 \\ p_1^{B5} & 0 & 0 \\ p_1^{B6} & 0 & 0 \end{bmatrix} = \begin{bmatrix} 0.0311 & 99.90 & 342.76 \\ 133.70 & 0 & 0 \\ 333.84 & 0 & 0 \\ 113.98 & 0 & 0 \\ 378.09 & 0 & 0 \\ 138.00 & 0 & 0 \end{bmatrix} \quad (7.39)$$

Figures and data for calibration of all strain gauge bridges are shown in appendix B.2.

7.3.1 Test case

Apart from the six respective components of the resulting aerodynamic load, a case when two components of load were applied simultaneously was also measured for calibration purposes. Such case was measured with the aim to verify whether the

balance calibration is correct and does what it is supposed to when applied load is 'general'.

This test case consists of loading by force F_z . This force is introduced eccentrically with respect to the balance axis. Therefore, moment M_x is also present, according to fig. 7.12.

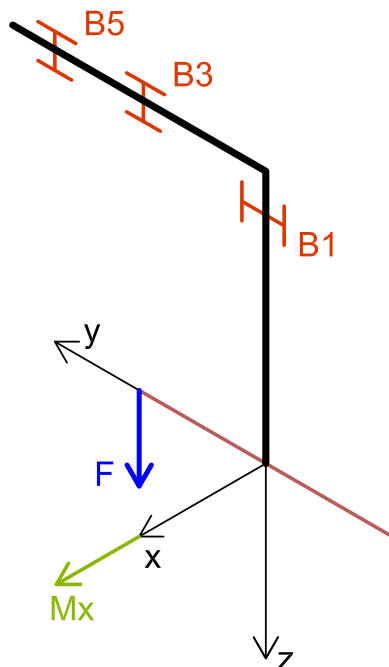


Fig. 7.12: Balance calibration; test case – sketch

From the measured data, load at the model attachment point is evaluated. The process is the same as described in appendix C.2. At the same time, load at the model attachment point can be determined based on the data acquired by the load cell.

In fig. 7.13, there is comparison of moments at points of bridges B1, B3, and B5. These are the strain gauge bridges that respond to loading by both force F_z and moment M_x . Blue line represents moment based on the load cell. Red line represents moment calculated from strain gauges responses and calibration matrix \mathbb{C} . It can be seen that the values calculated based on the calibration are a good approximation of exact data from the load cell.

Then, moments at points of the respective strain gauge bridges is transformed to load acting at the model attachment point (for information about this transformation see appendix C.2). In fig. 7.14 the load at the model attachment point is compared. In the left side of the picture, force F_z is compared. Both curves match quite well. On the other hand, the curves comparing moments M_x in the right side of the picture do not match at all.

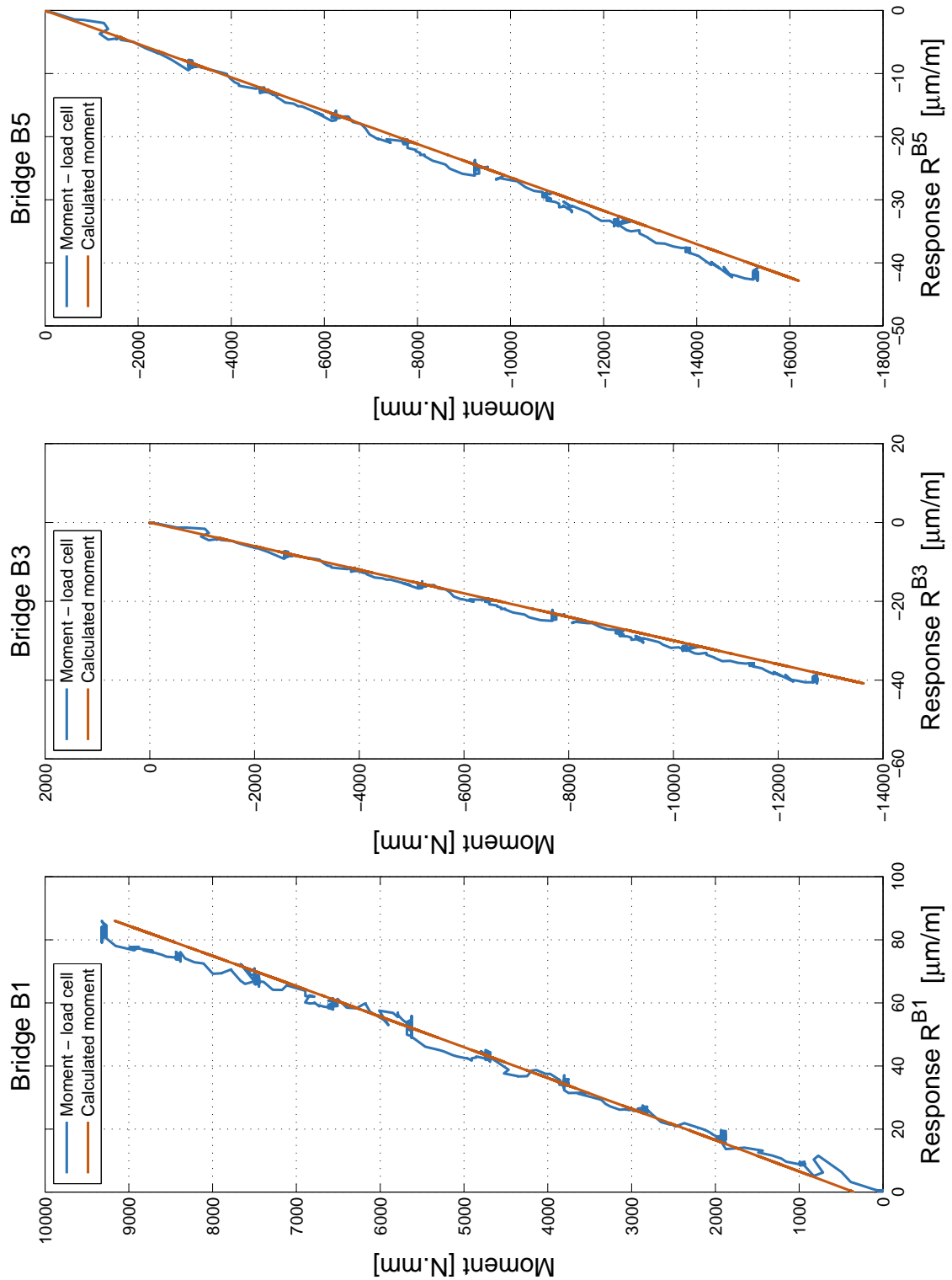


Fig. 7.13: Balance calibration; test case. Comparison of values calculated based on balance calibration and values based on load cell log – moments at points of respective strain gauge bridges.

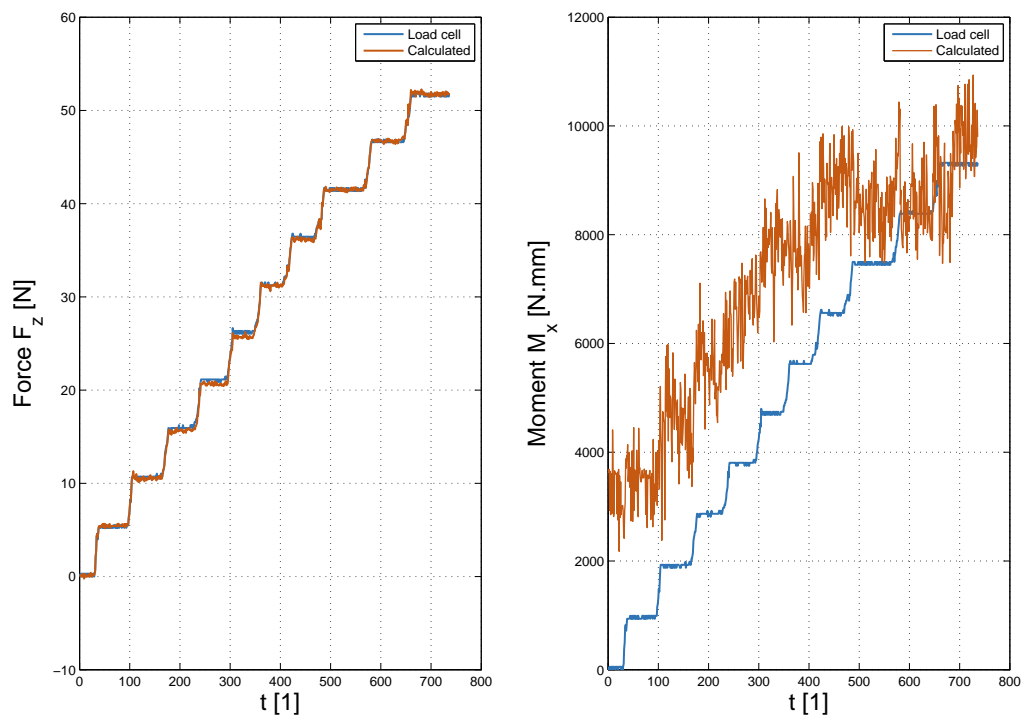


Fig. 7.14: Balance calibration, test case. Comparison of values calculated based on balance calibration and values based on load cell log – resulting load at the model attachment point

The reason for the difference in the M_x was not discovered. Moreover, when the same process as in this test case was applied to all calibration logs, all values that take into account responses from bridge B1 showed inaccurate results.

The components of aerodynamic load that use responses from bridge B1 are – side force F_y and moment M_x . Moreover, when transforming load between the two coordinate systems, moment M_z also includes the inaccuracy from bridge B1 (see app. C.2).

For the reason mentioned above, in the following evaluation of aerodynamic load, components F_y , M_x , and M_z are not taken into account. Furthermore, these components should all be zero when testing a symmetrical model with symmetrical flow ($\beta = 0$). Only components F_x , F_z , and M_y are evaluated.

8 EXPERIMENT RESULTS

This chapter presents the experiment and its results.

8.1 Measurement procedure

As part of the experimental testing, four different cases were measured. This was done to be able to compare different configurations and determine influence of different parts.

Two different undertrays were manufactured, as mentioned in chapter 6. One with diffuser (cases 1 and 3) and one without diffuser (cases 2 and 4). Then, cases without wings (cases 1 and 2) and with wings (cases 3 and 4) were measured. All cases are summed up in tab. 8.1. Numbers of the respective cases reflect the order in which they were measured.

Tab. 8.1: Description of measured cases

	Floor	Wings
Case 1	Floor with diffuser	No wings
Case 2	Simple floor	No wings
Case 3	Floor with diffuser	Both wings
Case 4	Simple floor	Both wings

Measurement was done in two basic steps. Firstly, each case was measured while logging data from force balance and pressure taps. Then, separately, the two winged cases were measured with the traverser, with both Prandtl probe and hot wire probe.

As was previously mentioned, in an empty test section, the maximum velocity is 60 m/s . When choosing model scale and calculating Reynolds number, it was expected that with the model in the test section, the maximum velocity would be 55 m/s (see section 5.2.1). Nevertheless, that did not turn out to be the case. In the end, the maximum achievable velocity in the wind tunnel was much lower, different for all the cases. Unwinged cases – 1 and 2 – generate smaller pressure losses, therefore the maximum speeds are higher, compared to winged cases.

However, for the winged cases, wind tunnel speed was no longer the limiting factor. That turned out to be the model mounting. The model is mounted on a strain gauge balance, that is inherently not rigid. On top of that, the model itself is relatively heavy. At speeds in excess of 30 m/s whole model started to considerably oscillate. A car is a bluff body, which means that the surrounding flow field is dominated by large areas of separated flow. It could be that the vibrations were

triggered by a movement of a separation line somewhere on the model. Or a change in the way vortices are shed from the model, e.g. wing tip vortices.

Consequently, the maximum speed for winged cases 3 and 4 – when logging forces and pressure distribution – was set for 30 m/s .

The model vibrations were even more pronounced when prandtl probe was traversed in the wake behind the model. Firstly, traversing was done at 30 m/s . But when the prandtl probe moved into the area dominated by two counter rotating vortices shed from tips of the rear wing, the vibrations were triggered again. Therefore, for measuring winged cases 3 and 4 with the traverser, the maximum velocity was set to 25 m/s .

Maximum velocities, that can be achieved in the wind tunnel are summed up in tab. 8.2.

Tab. 8.2: Maximum wind tunnel velocity achieved for all cases

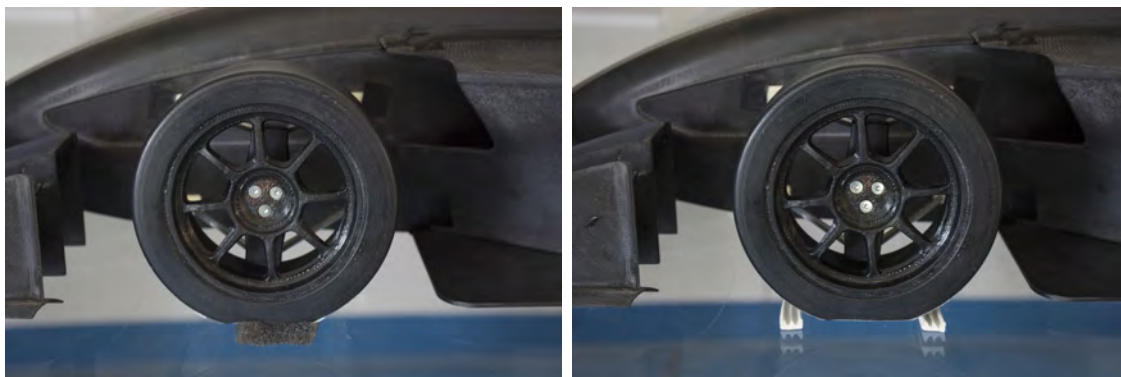
	Maximum wind tunnel velocity [m/s]
Case 1	43
Case 2	40
Case 3	30
Case 4	30

As was discussed in section 3.5.1, conducting the experiments with sting mounted model, stationary ground plane and stationary wheels requires certain treatment. To prevent air from flowing under the wheels and thus introducing an error into the measured forces, the gap has to be sealed. In the aforementioned chapter, using a piece of foam is suggested to be used to seal the gap. This was used for the first measurement. However, it did not have the desired effect. Although the gap was sealed, the foam had an effect on the balance. Therefore the foam had to be removed and was replaced with a strip of rubber seal. Both solutions can be seen in fig. 8.1.

Eventually, for time reasons, an effect of trip mould on the upper wheel surface on the flow around the wheel could not be investigated. Therefore, it was decided not to place it there.

To sum up this section on measurement procedure tables 8.3, 8.4, and 8.5 are presented. All test cases from which data is acquired are listed¹.

¹ In tab. 8.4 case 1a stands for data acquired with foam seal glued to wheels, while case 1b stands for rubber seal used to prevent air from going beneath wheels.



(a) Foam used to seal tyre contact patch (b) Rubber seal at tyre contact patch

Fig. 8.1: Tyre contact patch treatment

Tab. 8.3: Test cases measured – force balance

	Measured velocity [m/s]
Case 1	10, 20, 30, 36, 43
Case 2	30, 36, 40
Case 3	25, 30
Case 4	25, 30

8.2 Aerodynamic load

8.2.1 Evaluation of acquired data

Strain gauge responses were logged with the same equipment as they were during calibration.

The measurement process for all the cases was following:

- With wind tunnel turned off – balance strain gauge responses so that they start logging at $0 \mu\text{m}/\text{m}$
- With wind tunnel turned off – log zero values for 10 to 15 seconds

Tab. 8.4: Test cases measured – pressure reading

	Measured velocity [m/s]
Case 1a	30, 36, 40
Case 1b	36, 40
Case 2	30, 36, 40
Case 3	25, 30
Case 4	25, 30

Tab. 8.5: Test cases measured – traverser

	Measured velocity [m/s]
Case 3 – Prandtl probe	25
Case 3 – Hot wire probe	25
Case 4 – Prandtl probe	25

- For a given speed – log strain gauge responses. Logging was done for about two minutes on average. After logging is finished, increase wind tunnel speed and repeat logging.
- After wind tunnel speed dropped to 0 m/s, log zero values for 10 to 15 seconds. Logging frequency was 100 Hz.

As was described in the previous section four cases were measured. For every case, at least two different velocities were measured (see tab. 8.3).

Loads acting on the balance were measured separately, so that it can be later subtracted from the loads measured with the model.

Load on balance was measured for five different speeds – 10, 20, 30, 35, and 40 m/s. After calculation of all components of the load on balance, measured values were fitted with a quadratic curve. This enables to calculate load on balance at a given speed and subtract it from load on the model. The evaluation and curve fitting is described in appendix C.1.

When it comes to the final data evaluation of aerodynamic loads, for all the cases the approach is the same. The only difference is in the number of measured points – different velocities measured.

As was mentioned above, the measuring process consists of: (a) zero values before wind tunnel is turned on, (b) measured data for a given speed, and (c) zero values after wind tunnel was turned off.

Here, only the general process is shown. More detailed information can be found in appendix C.2.

First step of the evaluation is averaging measured values over the entire measuring period.

Next step is to subtract the average zero values from values at different velocities. After that, these values are multiplied by the balance's calibration matrix. This step yields moment values at points of strain gauge bridges. These moments are multiplied again by a transformation matrix, that transforms moments at strain gauge bridges into loads acting at the model attachment point.

At this point, loads acting on a balance separately are subtracted. Then, the calculated values are components of aerodynamic load acting at the model attachment point. This has to be transformed into loads acting at the origin of the coordinate system defined in section 7.1.

Last but not least, dimensionless coefficients as defined in section 7.1.2 can be calculated.

Again, for detailed description of the evaluation see appendix C.2.

8.2.2 Results – Cases 1-4

In this section, measured aerodynamic load acting on the model in respective cases is presented.

Case 1

(Floor with diffuser, no wings)

Case 1 – as the first case measured – was measured for the largest range of velocities. The lowest measured velocity is 10 m/s and it goes to 43 m/s, which is the maximum wind tunnel speed, that can be achieved with this configuration.

In fig. 8.2 aerodynamic forces and moments are plotted as a function of speed. Unlike in appendix C.2, the forces are expressed in a more customary way – as drag force D and lift force L (positive lift force acts upwards, while negative lift force means that downforce is generated). All components appear to follow the expected quadratic relation between the respective components of aerodynamic load and velocity. In this case, lift is positive, which can be expected for an open wheel race car without wings.

Aerodynamic coefficients are plotted against velocity in fig. 8.3. Theoretically, these values should be constant when plotted against speed. However, in the low speeds, the flow field around the car is not yet fully developed. Therefore, the values for 10 m/s are considerably different compared to the higher velocities. Drag coefficient and pitching moment coefficient are then relatively constant in the range of speeds from 20 to 43 m/s. Lift coefficient is increasing in the whole range, although the increment appears to be getting smaller between 36 and 43 m/s.

A possible explanation for the increasing lift coefficient could be behaviour of the flow around the wheels. With increasing velocity, the separation line on the upper surface of the wheels may be moving aft, the result of which would be generation of greater lift force on the wheels.

Final aerodynamic characteristic for case 1 are taken following: for drag and pitching moment, values for 30, 36, and 43 m/s are averaged. For lift coefficient,

only the last two values are averaged – 36, and 43 m/s . These values can be found in tab. 8.6.

Case 2

(Simple floor, no wings)

Case 2 was measured at 30, 36, and 43 m/s , the latter being the achievable maximum again.

While the values of drag force and pitching moment – fig. 8.4 – appear to be following the same trend as those measured for case 1, the lift force – at 43 m/s – is somewhat lower than expected. The same can be seen in fig. 8.5, where aerodynamic coefficients are plotted against speed. Drag coefficient and pitching moment coefficient are relatively constant in the whole range of velocities. Lift coefficient does not change substantially between 30, and 36 m/s , but then, at 40 m/s , the value drops.

The reason for this might be of the same nature as was suggested before, i.e. Reynolds number effects. Nevertheless, with only three points measured it is difficult to draw any conclusions.

Final values of drag coefficient and pitching moment coefficient are averaged from all values – 30, 36, and 40 m/s . For lift coefficient, only values for 30, and 36 m/s are averaged (see tab. 8.7).

Case 3

(Floor with diffuser, both front and rear wings)

Case 3 was measured only at two velocities – 25, and 30 m/s . For that reason, the trend in which the forces and moments are increasing with velocity (fig. 8.6) cannot be judged. Naturally, after front and rear wings were mounted, generated lift force is negative.

For all coefficients (fig. 8.7), both values for 25, and 30 m/s are averaged (see tab. 8.8).

Case 4

(Simple floor, both front and rear wings)

For case 4, the same applies as in the previous case. Resulting forces and moments are shown in fig. 8.8, while aerodynamic coefficients are shown in fig. 8.9.

For all coefficients, both values for 25, and 30 m/s are averaged (see tab. 8.9).

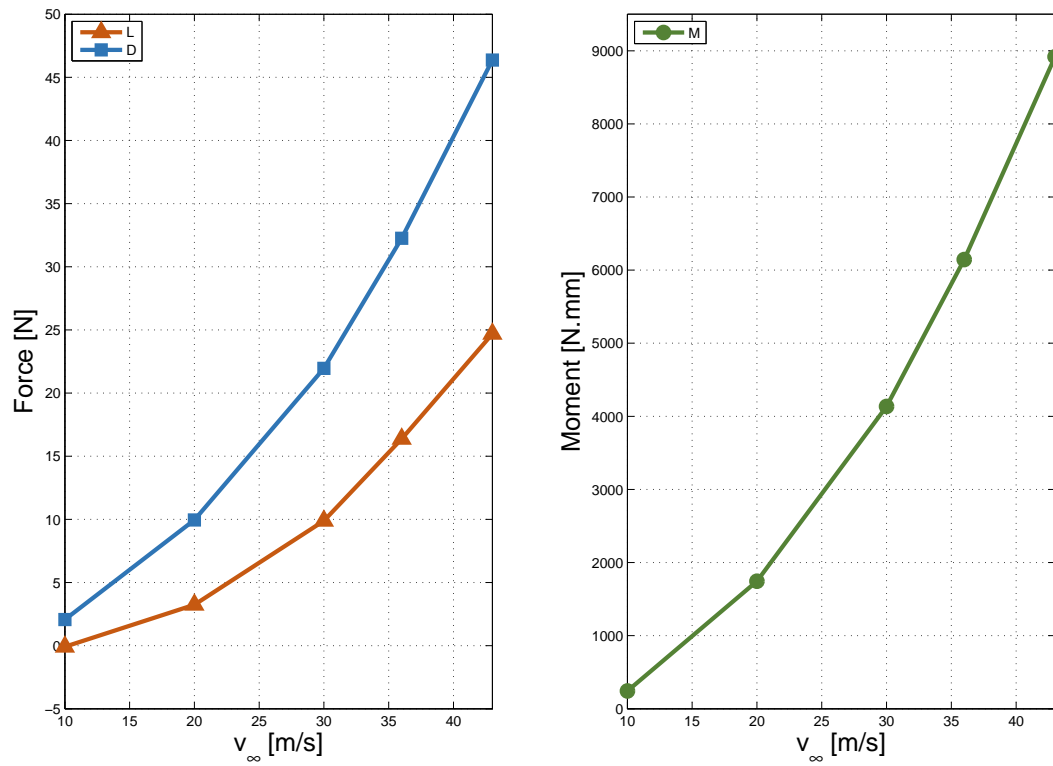


Fig. 8.2: Case 1 – aerodynamic forces (left) and moments (right) versus velocity

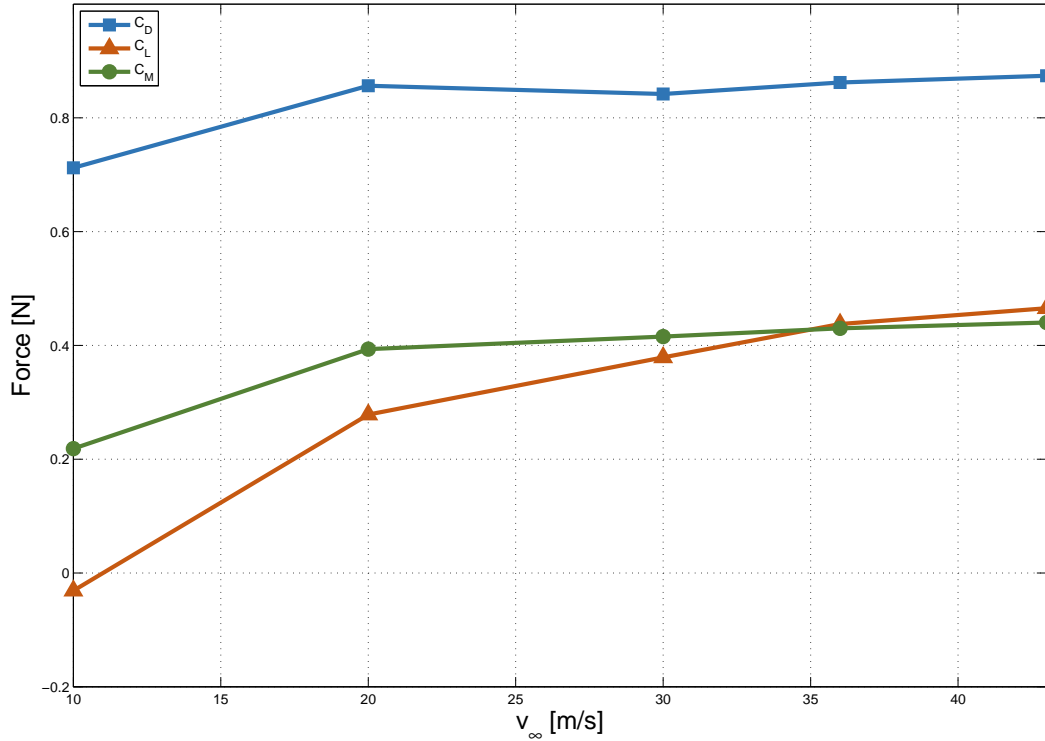


Fig. 8.3: Case 1 – aerodynamic coefficients versus velocity

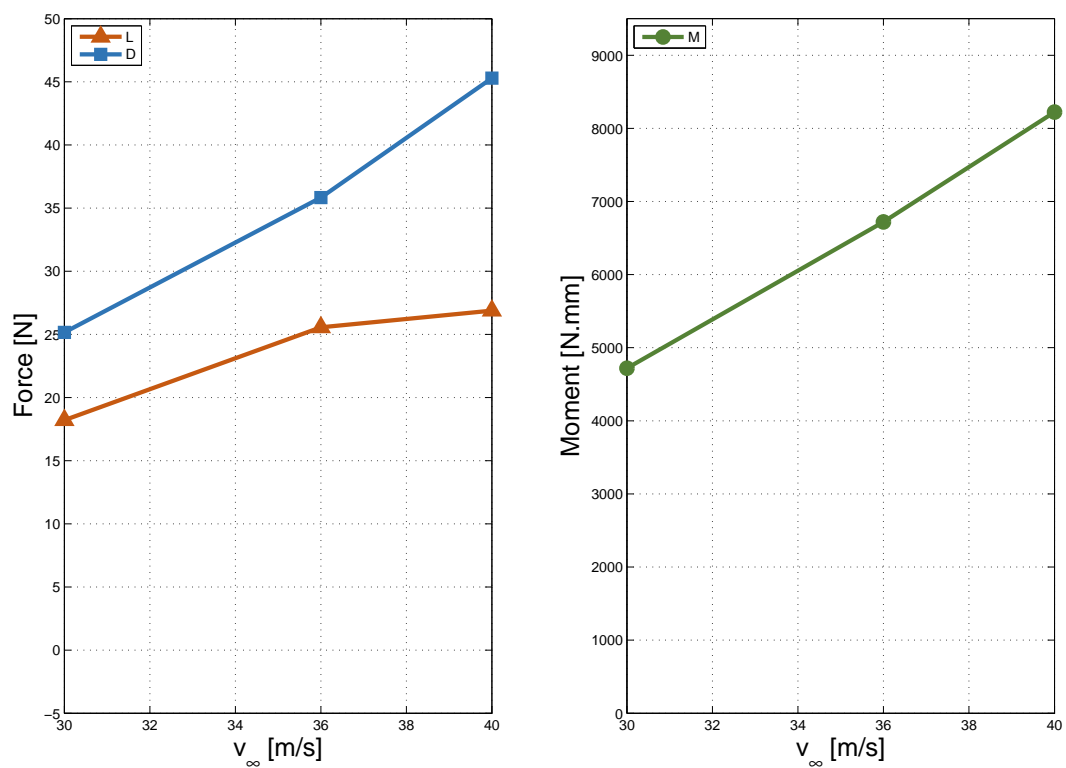


Fig. 8.4: Case 2 – aerodynamic forces (left) and moments (right) versus velocity

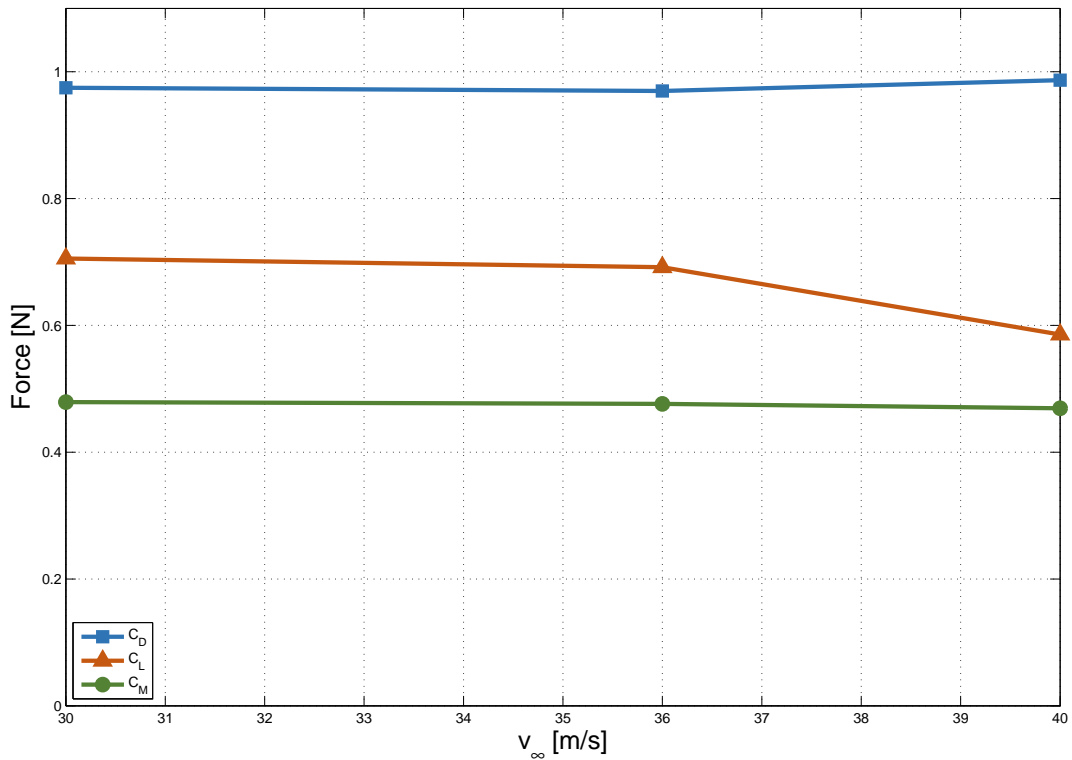


Fig. 8.5: Case 2 – aerodynamic coefficients versus velocity

8 Experiment results

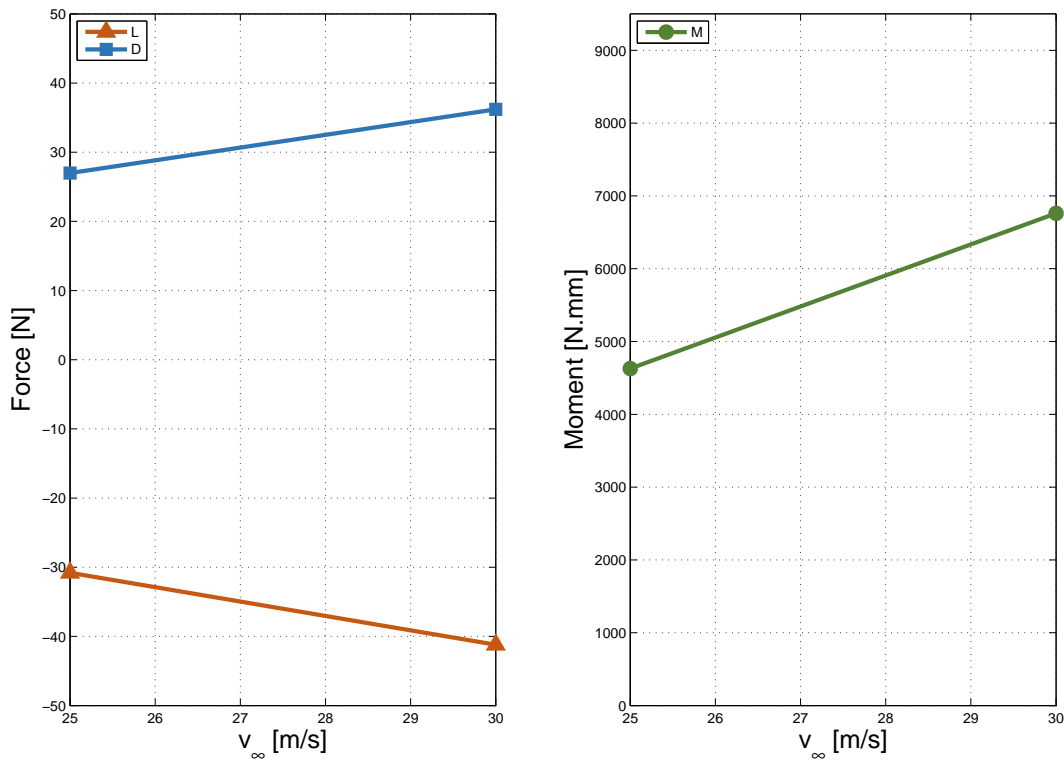


Fig. 8.6: Case 3 – aerodynamic forces (left) and moments (right) versus velocity

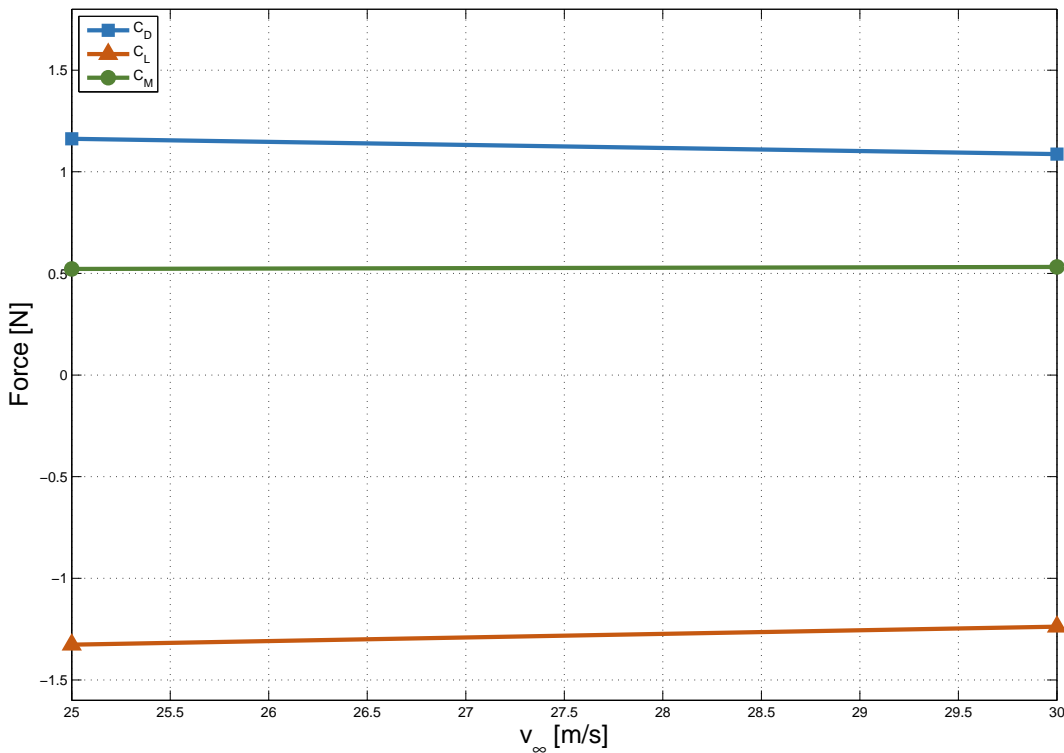


Fig. 8.7: Case 3 – aerodynamic coefficients versus velocity

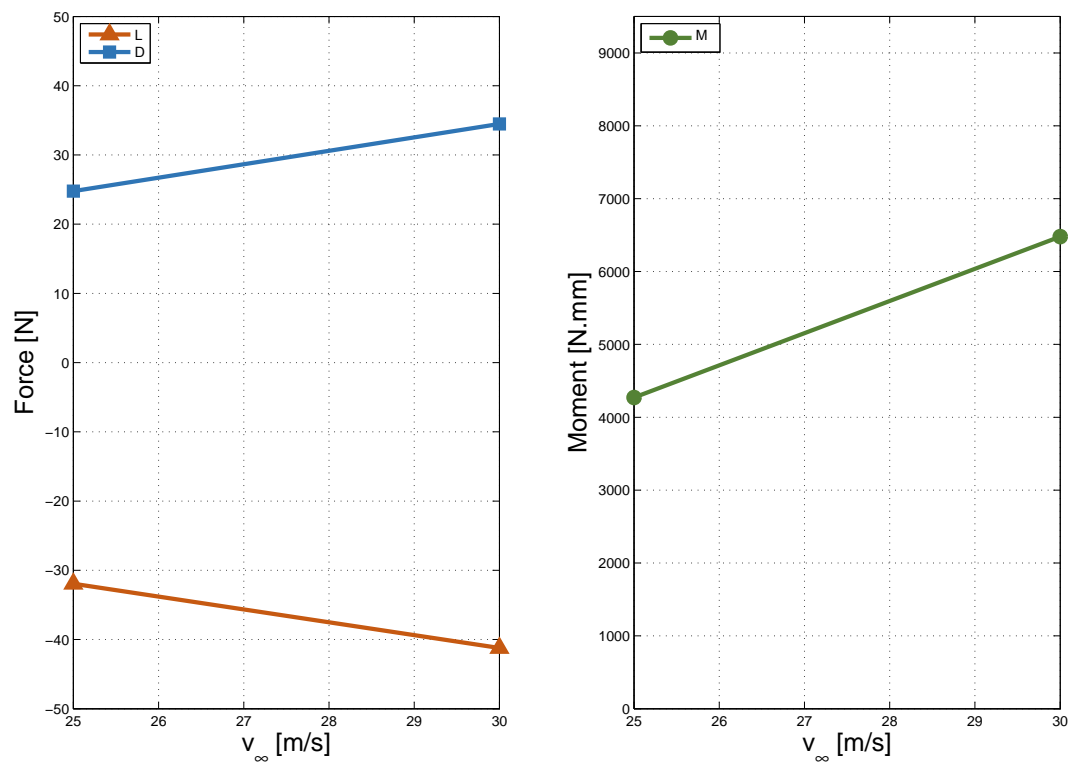


Fig. 8.8: Case 4 – aerodynamic forces (left) and moments (right) versus velocity

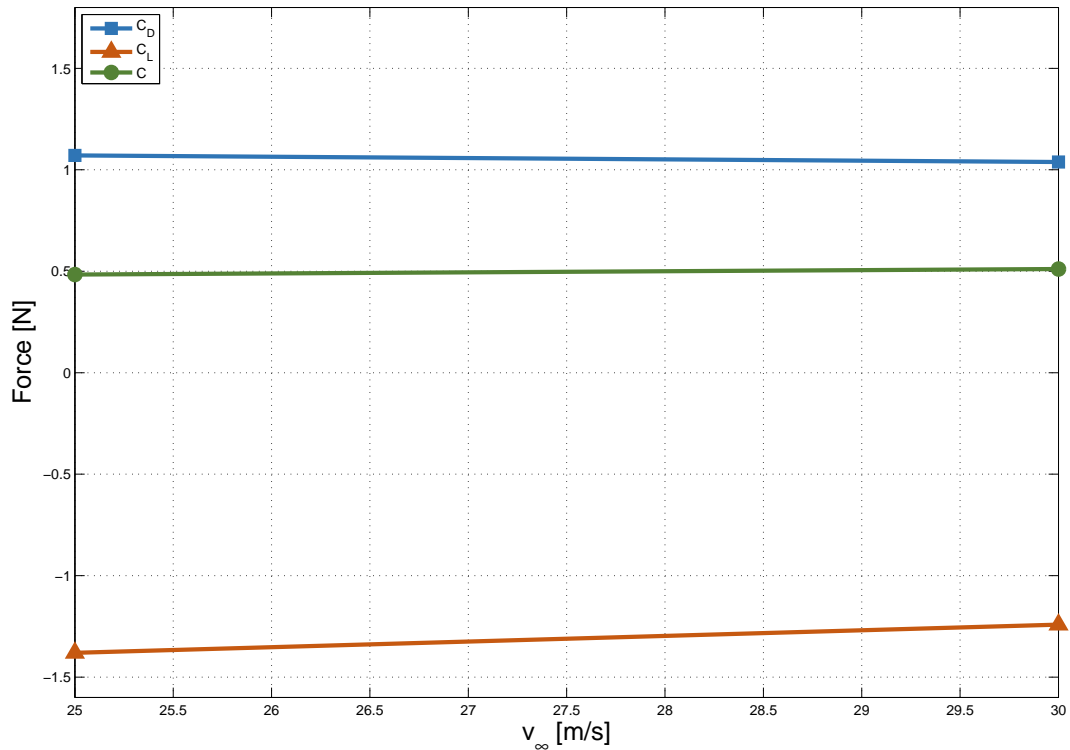


Fig. 8.9: Case 4 – aerodynamic coefficients versus velocity

8 Experiment results

Tab. 8.6: Case 1 – drag and lift forces, pitching moment and aerodynamic coefficients

Velocity [m/s]	D [N]	C_D [-]	L [N]	C_L [-]	M [N · mm]	C_M [-]
10	2.1	0.712	-0.1	-0.031	242.6	0.219
20	10.0	0.857	3.2	0.278	1744.7	0.393
30	22.0	0.842	9.9	0.379	4135.2	0.415
36	32.3	0.862	16.4	0.438	6144.0	0.430
43	46.4	0.874	24.7	0.465	8918.6	0.440

Tab. 8.7: Case 2 – drag and lift forces, pitching moment and aerodynamic coefficients

Velocity [m/s]	D [N]	C_D [-]	L [N]	C_L [-]	M [N · mm]	C_M [-]
30	25.2	0.975	18.2	0.705	4719.5	0.479
36	35.8	0.970	25.6	0.692	6719.6	0.476
40	45.3	0.987	26.9	0.586	8223.0	0.469

Tab. 8.8: Case 3 – drag and lift forces, pitching moment and aerodynamic coefficients

Velocity [m/s]	D [N]	C_D [-]	L [N]	C_L [-]	M [N · mm]	C_M [-]
25	27.0	1.163	-30.8	-1.327	4628.4	0.522
30	36.2	1.087	-41.2	-1.238	6760.2	0.532

Tab. 8.9: Case 4 – drag and lift forces, pitching moment and aerodynamic coefficients

Velocity [m/s]	D [N]	C_D [-]	L [N]	C_L [-]	M [N · mm]	C_M [-]
25	24.8	1.071	-31.9	-1.380	4272.0	0.484
30	34.5	1.038	-41.2	-1.241	6478.6	0.511

8.2.3 Results – comparison of all cases

Fig. 8.11 compares final aerodynamic coefficients for all cases.

Firstly, cases 1 and 2 are compared. Case 2 configuration has higher drag coefficient. That was expected based on the fact that maximum wind tunnel speed was lower – 40 m/s , compared to 43 m/s . After mounting the floor with diffuser, the drag coefficient reduced by 12%, while the overall lift of the car reduced by 35%. Such reduction in lift means, significantly greater downforce is generated by floor with diffuser. The pitching moment for case 1 is slightly lower, compared to case 2. That is because in these configurations, drag force is dominant over the lift force, i.e. greater drag results in greater pitching moment.

When comparing cases 3 and 4, the trend is reversed. Configuration with both wings and diffuser yields higher drag and lower downforce, compared to configuration with both wings and 'simple' floor. After mounting the floor with diffuser, downforce dropped by 2.2%. Such difference is marginal. Nevertheless, it would be expected that the difference would be exactly opposite – that the downforce would increase.

A possible explanation for this could be the fact that the balance deflects quite considerably. This deflection results in change of the model's pitch – it increases and results in a positive rake angle of the floor (see illustration in fig. 8.10). Such angle of the floor is normally used in motor sport to increase downforce. Another fact is, that the diffuser's design on the model is not very aggressive. It could be, that the configuration resulting from the balance deflection has higher downforce due to the induced rake angle.

Pitching moment is then slightly higher for case 3. On a floor with diffuser, the greatest suction is generated right at the start of the diffuser. Therefore, the resultant of the downforce is further back, compared to planar floor. This aft position of the resultant force acting on the floor results in the increase of pitching moment. Such statement is further supported by pressure coefficient distribution in section 8.3 (see fig. 8.19).



Fig. 8.10: Positive rake angle [30]

Although, fig. 8.11 enables to compare difference in aerodynamic coefficients between the respective cases, it does not provide true differences in the resulting aerodynamic load. That is because coefficients in fig. 8.11 are referenced to the

Tab. 8.10: Resulting aerodynamic coefficient for all cases

	C_D	C_L	C_M
Case 1	0.859	0.451	0.429
Case 2	0.977	0.699	0.475
Case 3	1.125	-1.282	0.527
Case 4	1.054	-1.311	0.497

Tab. 8.11: Resulting aerodynamic coefficients for all cases, multiplied by models reference area A

	$C_D \cdot A$	$C_L \cdot A$	$C_M \cdot A$
Case 1	0.043	0.022	0.021
Case 2	0.049	0.035	0.024
Case 3	0.072	-0.064	0.026
Case 4	0.067	-0.065	0.025

model's frontal cross-section area, which is different for cases 1 and 2, and cases 3 and 4. The true difference in aerodynamic load for all the cases can be seen in fig. 8.12, where aerodynamic coefficient are multiplied by reference area A .

Resulting coefficient values can be seen in tab. 8.10, while the coefficients multiplied by model's reference area are in tab. 8.11

8.3 Pressure coefficient distribution

This section presents results from static pressure reading on the bodywork and floor of the model in the symmetry plane. Firstly, all cases are discussed separately. That is followed by comparison of data for all cases.

8.3.1 Results – Cases 1-4

Case 1

(Floor with diffuser, no wings)

As was already mentioned in section 8.1, pressure – for case 1 – was measured for two different configurations. First set of data (fig. 8.13) was logged with foam, sealing the gap between wheel and wind tunnel floor. The foam was later removed and replaced with a strip of rubber seal (fig. 8.14). From both there figures, it can be seen, that the pressure coefficient distribution does not change much with varying speed.

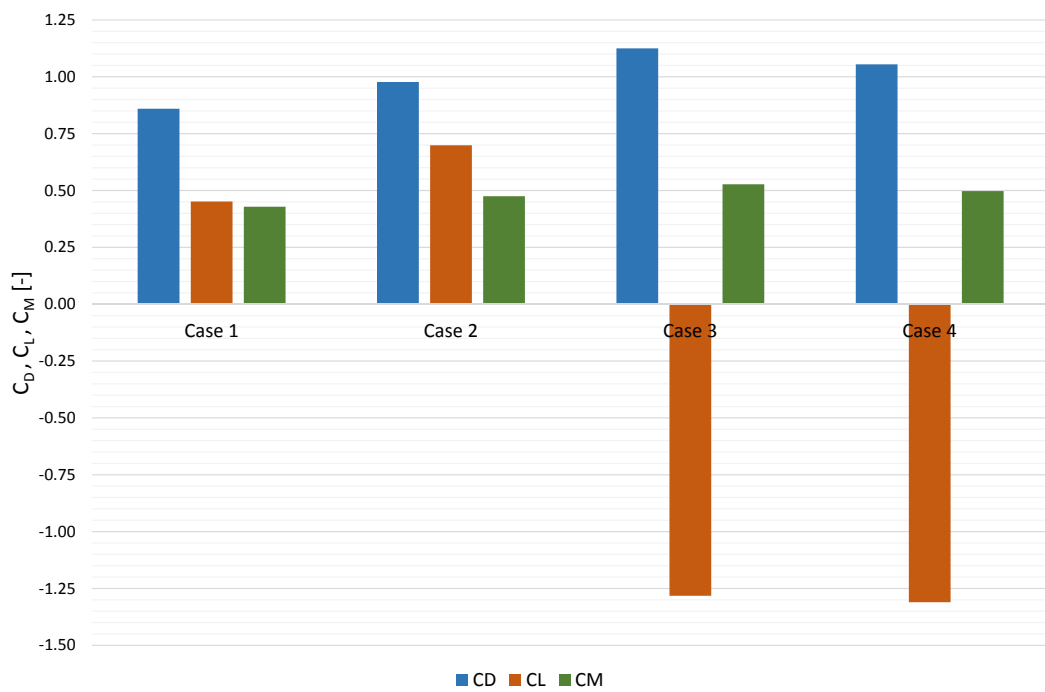


Fig. 8.11: Resulting aerodynamic coefficients for all cases

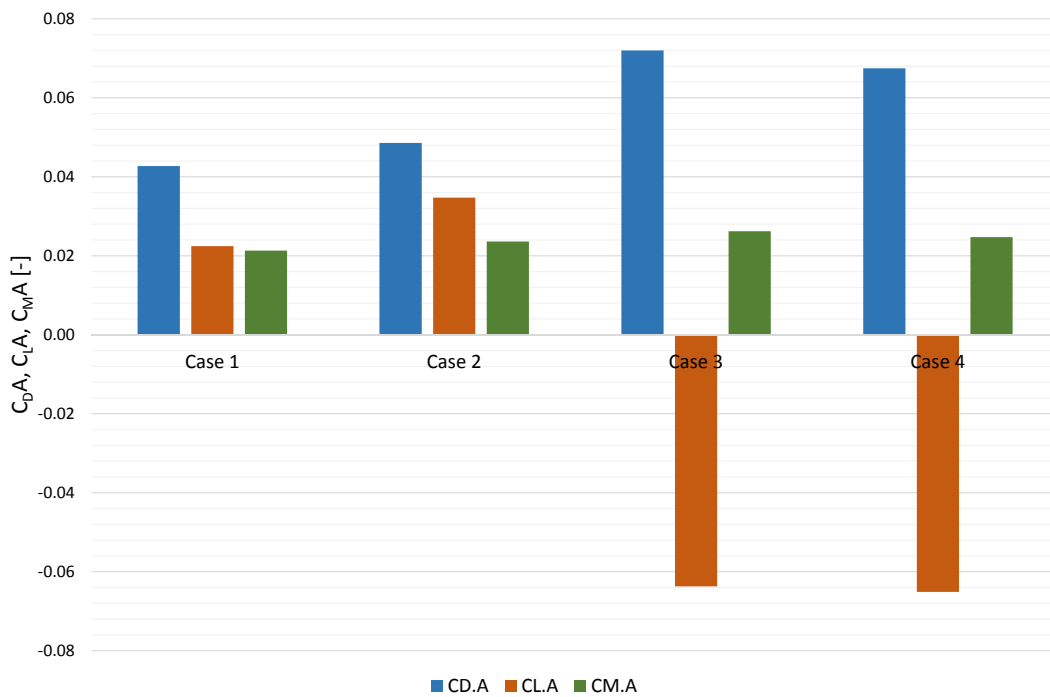


Fig. 8.12: Resulting aerodynamic coefficients for all cases, multiplied by models reference area A

Both of the two configurations are plotted together in fig. 8.15. The pressure coefficient distribution matches in both cases, although there is one pressure tap, where there is noticeable difference.

On the upper surface of the bodywork, the pressure coefficient keeps getting lower towards the cockpit. On the bodywork's lower surface and floor, the pressure coefficient decreases in a similar manner as on the upper surface. It keeps dropping until the airflow reaches area, where the ride height is constant, around $x = -120\text{ mm}$. There, the pressure coefficient stays quite constant until it starts lowering again in front of the diffuser. At the start of the diffuser, the pressure reaches its minimum and in the diffuser, the air flow decelerates, resulting in increasing pressure.

Case 2

(Simple floor, no wings)

For case 2, the pressure coefficient distribution is plotted in fig. 8.16. Compared to case 1, there is no visible change in the pressure distribution on the upper surface. On the other hand, on the bodywork's lower surface and floor, the difference is quite substantial. From the stagnation point, the pressure keeps decreasing until around $x = -50\text{ mm}$. There, the pressure reaches its minimum value, i.e. it is the place of greatest suction. From there, the pressure gradient is adverse until $x = 140\text{ mm}$, where the gradient changes and pressure coefficient starts decreasing again.

Case 3

(Floor with diffuser, both front and rear wings)

For case 3 (fig. 8.17), the pressure coefficient distribution changes substantially in the area directly behind the front wing, compared to case 1. In the first part of the nose's lower surface – between the nose cone and the front wing, the pressure coefficient decreases at quite a steep gradient. Then in the area of the airfoil's wake, the pressure gradient changes. Pressure appears to be increasing for a short distance before it decreases again, but not at such a steep gradient. Then the pressure coefficient distribution towards the diffuser is similar to that in case 1.

Case 4

(Simple floor, both front and rear wings)

Pressure coefficient distribution for case 4 is shown in fig. 8.18. The difference caused by the front wing, compared to case 2 appears to be the same as was described for case 3.

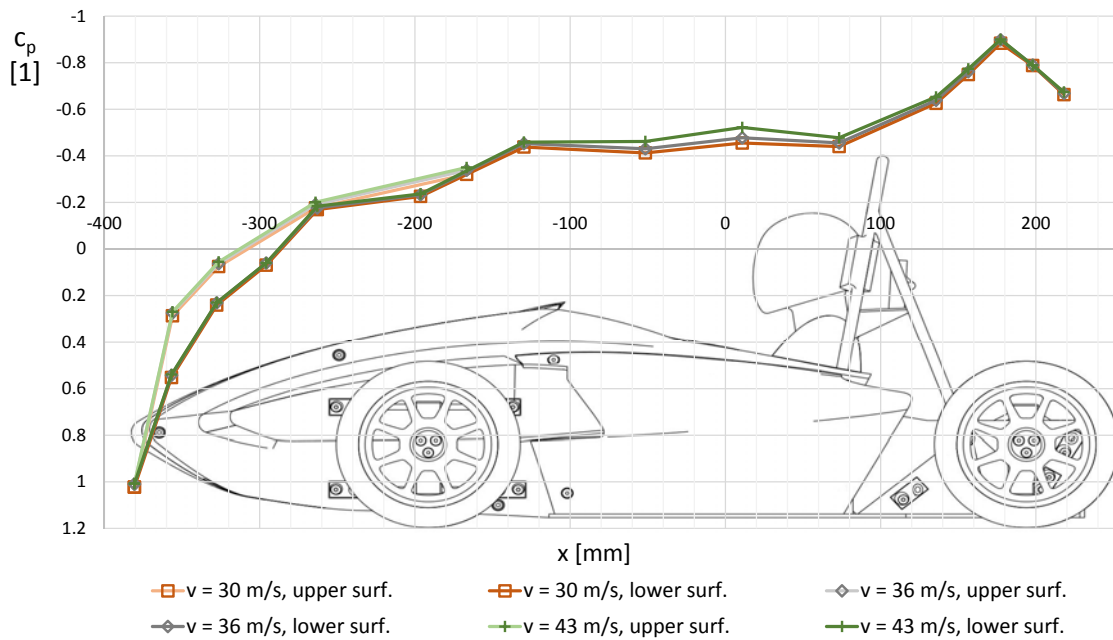


Fig. 8.13: Pressure coefficient distribution, Case 1 – foam used to seal tyre contact patch

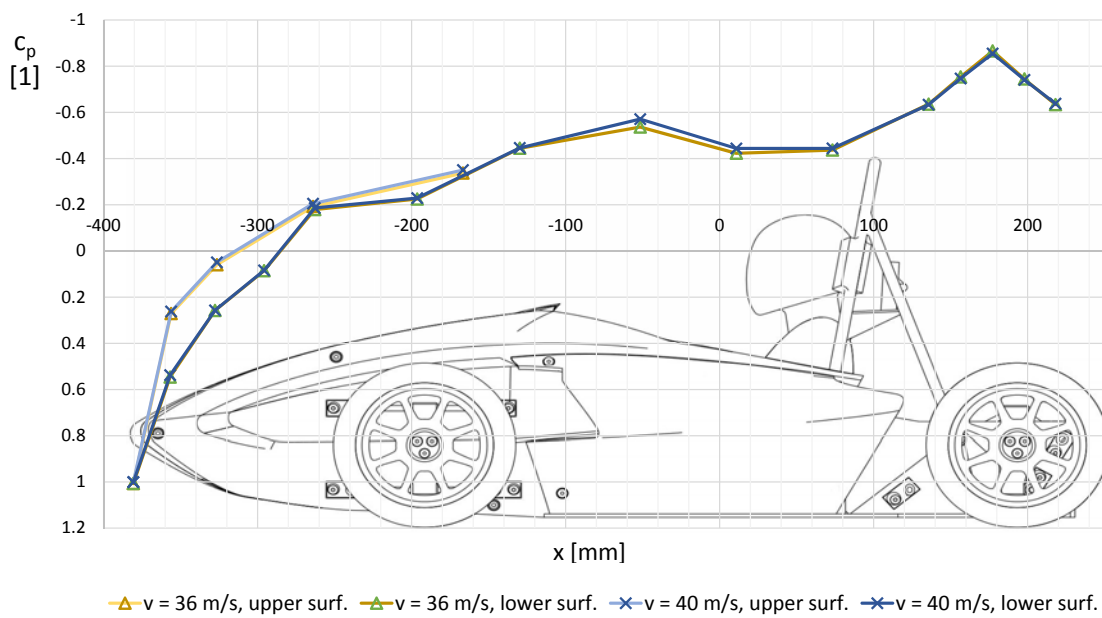


Fig. 8.14: Pressure coefficient distribution, Case 1 – rubber strip used to seal tyre contact patch

8 Experiment results

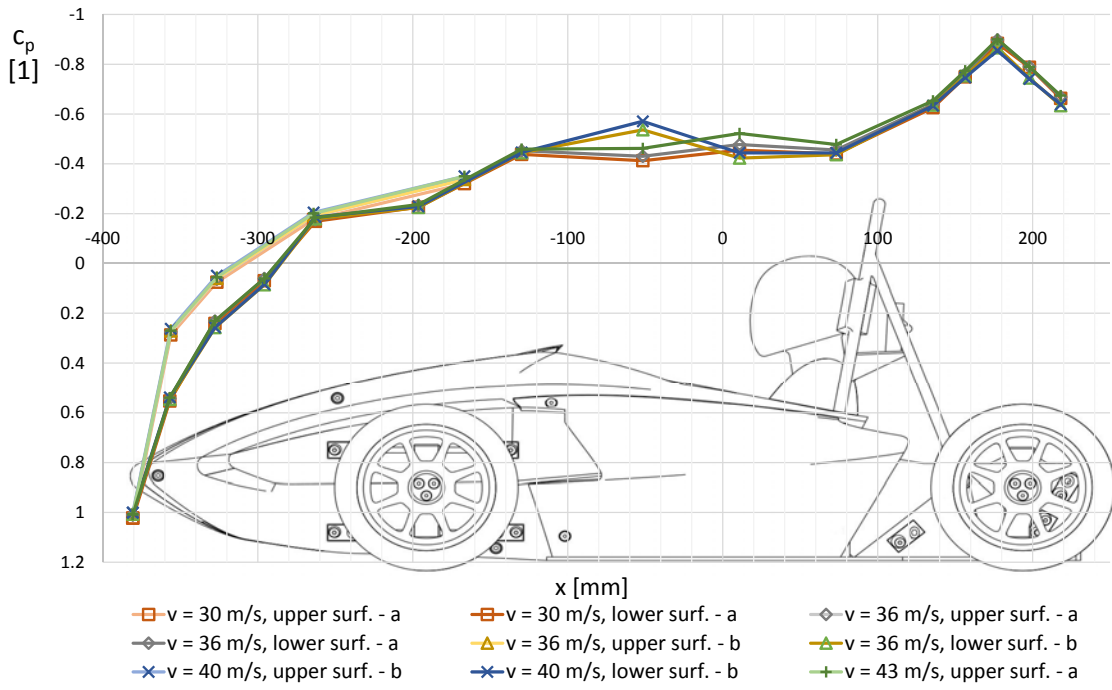


Fig. 8.15: Pressure coefficient distribution, Case 1. (a) stands for foam used to seal tyre contact patch; (b) stands for rubber strip used to seal tyre contact patch

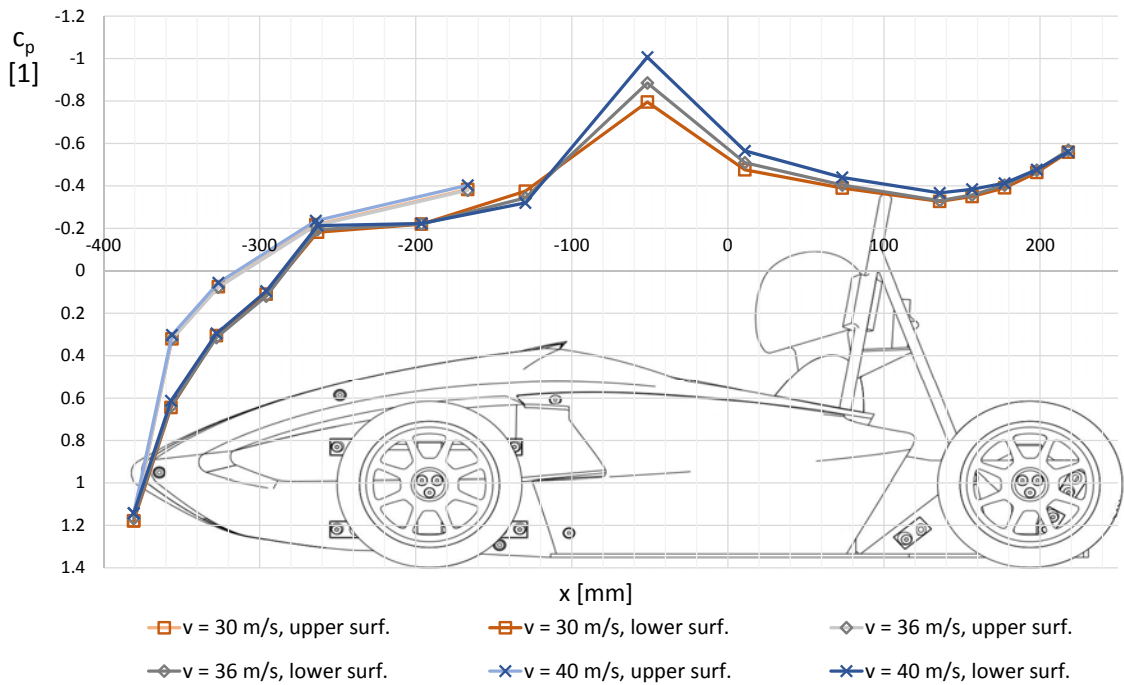


Fig. 8.16: Pressure coefficient distribution, Case 2

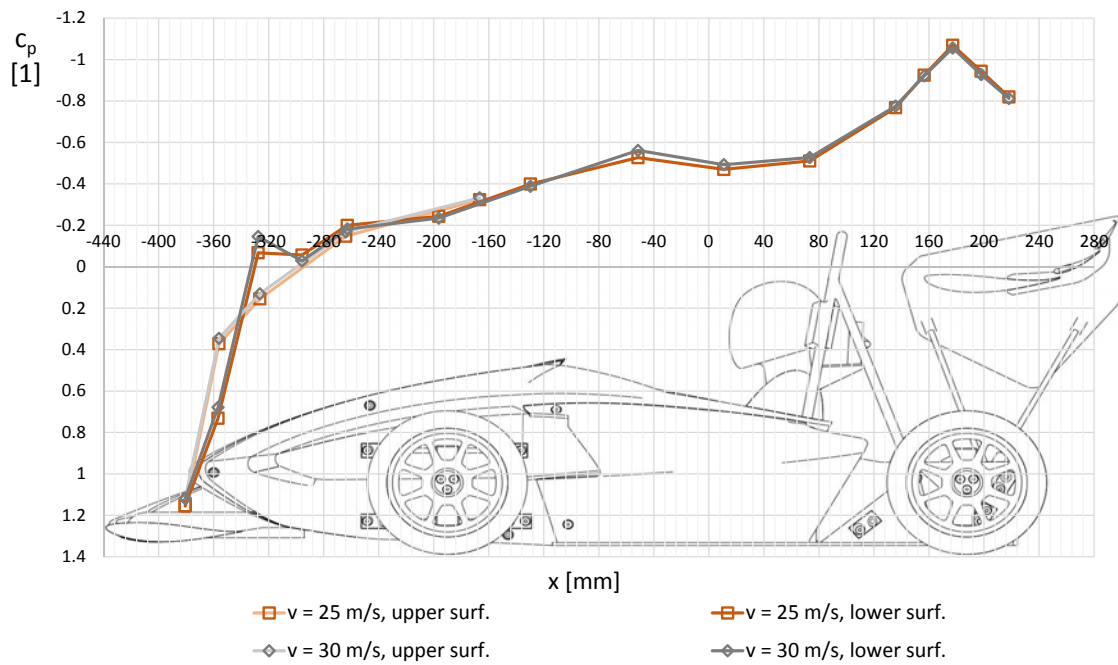


Fig. 8.17: Pressure coefficient distribution, Case 3

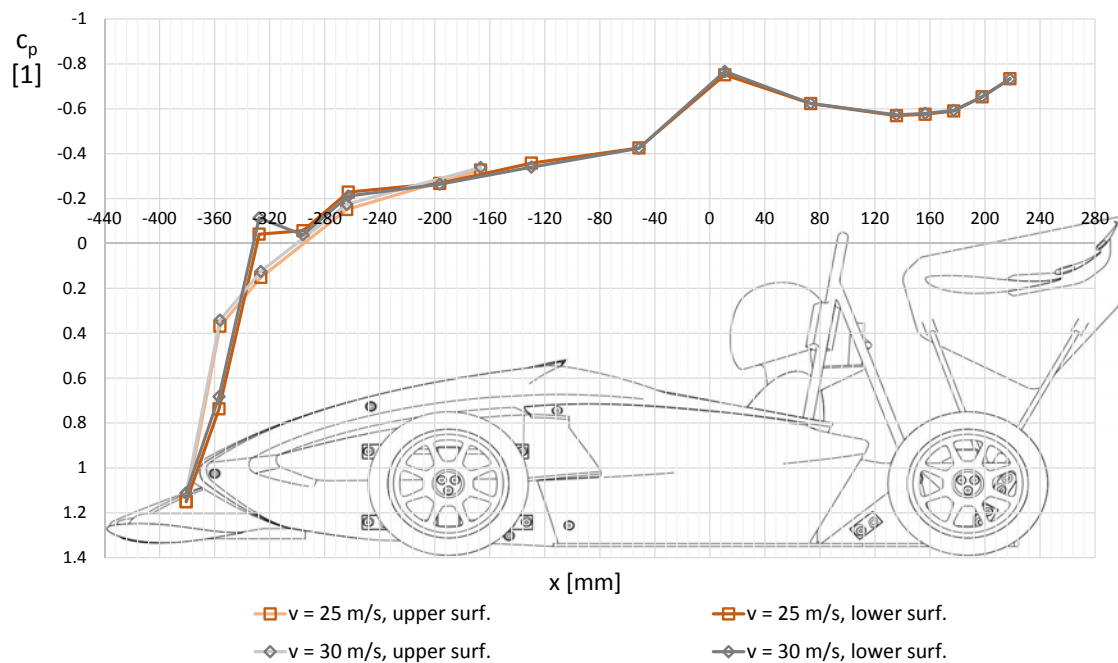


Fig. 8.18: Pressure coefficient distribution, Case 4

8.3.2 Results – comparison of all cases

Pressure coefficient distribution for all cases is plotted in fig. 8.19. All curves are for 30 m/s velocity.

There is no significant change in the pressure distribution on the upper surface.

In the front part of the lower surface, naturally, the effect of the front wing is visible. However, downstream from the front wing – approximately from $x = -250\text{ mm}$ to $x = -130\text{ mm}$, the pressure coefficient appears to be quite similar for all the cases.

When comparing case 1 and case 3, the curves follow similar trend, with the curve for case 3 shifted a bit into lower values.

For case 4, the minimum pressure shifted aft, compared to case 2, with the absolute values being the same. Again, from the point of minimum pressure, the trend is similar. However, configuration in case 4 is not subjected to such an adverse pressure gradient as case 2, resulting in lower pressure coefficient values at the last part of the floor.

Conclusion from what was said above is that the rear wing contributes to generate greater suction on the floor, resulting in greater downforce on the floor itself, compared to car without wings.

As was suggested in section 8.2.3, from the pressure coefficient distribution in fig. 8.19, it can be estimated that the resultant of the force acting on the floor is mainly influenced by the position of the suction peak. Then the floor with diffuser would have higher pitching moment compared to planar floor.

8.4 Wake traversing

8.4.1 Prandtl probe

Traverser with prandtl probe was used to measure velocity in a plane 410 mm behind the model (see fig. 8.20). The resulting velocity contour plots are shown in fig. 8.21 and 8.22 for cases 3 and 4, respectively. Both cases were measured at 25 m/s . The range of the axes in both plots determine the test section's dimensions. The white area close to the borders of the graph is area, where measurement was not done. That is because the prandtl probe error is outside guaranteed range when proximity of a wall is less than five times the probe's diameter.

In both pictures, it can be seen that the wake behind the model is dominated by two large counter rotating vortices, that originate at the tips of the rear wing. Although it is obvious that the measurement is influenced by the large blockage, the fact that

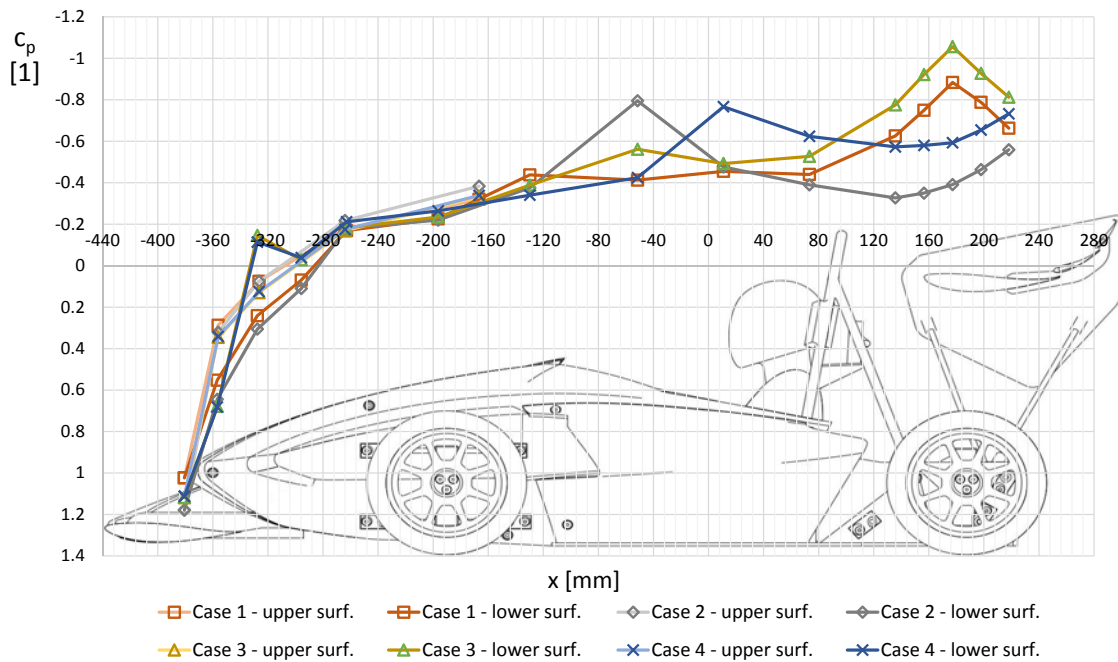


Fig. 8.19: Pressure coefficient distribution, All cases, 30 m/s

the vortices are comfortably distanced from the wind tunnel walls means, that the results are not rendered useless because of the blockage. The asymmetry is probably caused by turbulence and pulsing of the wind tunnel flow.

In the upper part of both figures, close to the symmetry plane, it can be seen that the flow is affected by the balance.

From comparison of fig. 8.21 and 8.22, no conclusions can be drawn, since there is no clearly visible difference in the wakes.

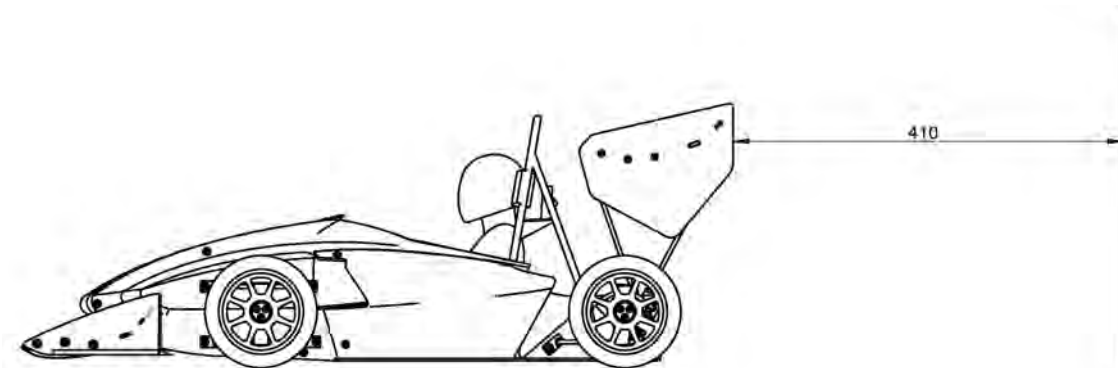


Fig. 8.20: Distance from the rearmost point of the model to the traversing plane

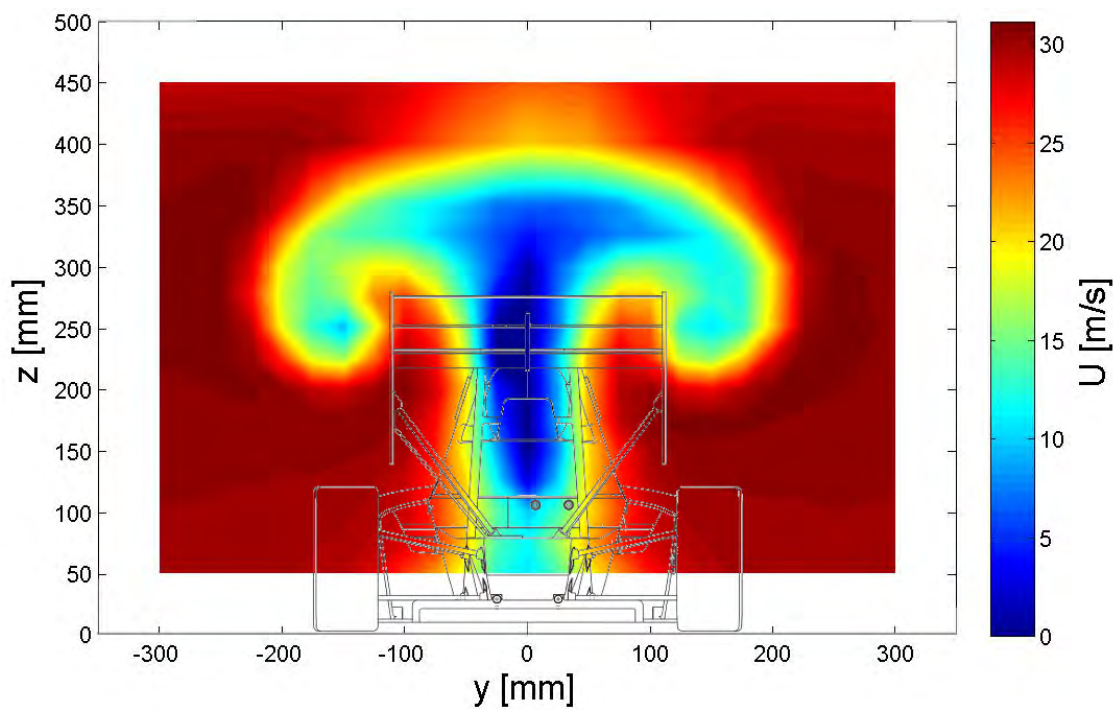


Fig. 8.21: Case 3, $U_\infty = 25 \text{ m/s}$. Velocity distribution behind a car – prandtl probe traversing.

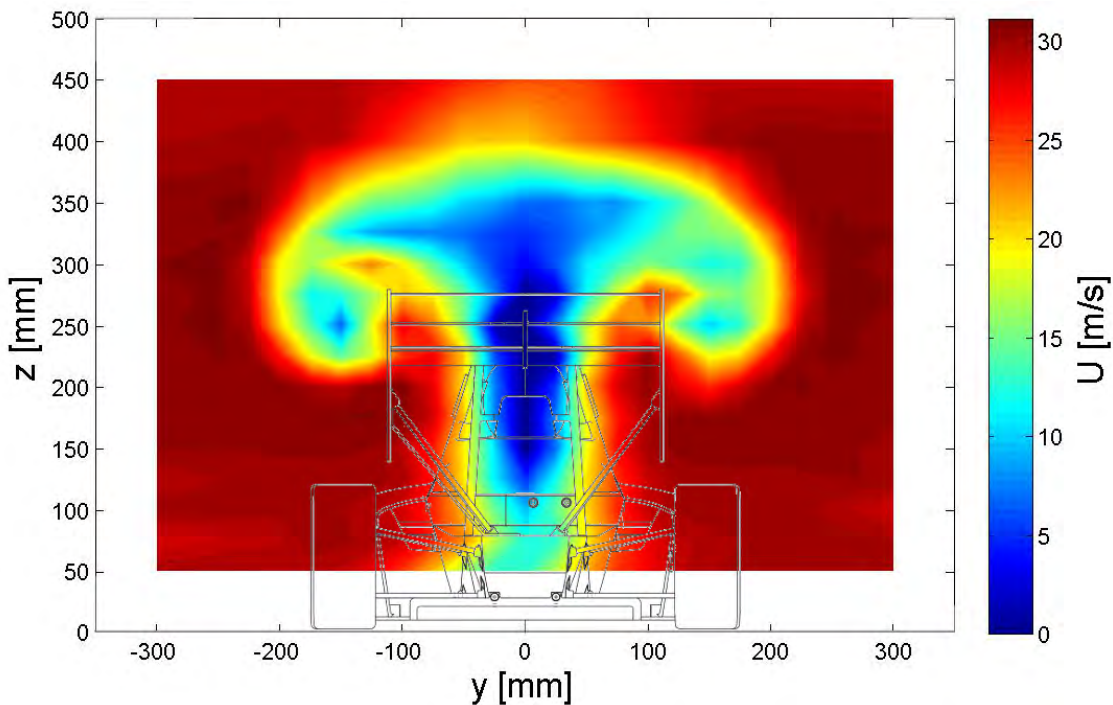


Fig. 8.22: Case 4, $U_\infty = 25 \text{ m/s}$. Velocity distribution behind a car – prandtl probe traversing.

8.4.2 Hot wire probe

Traversing with hot wire probe was done only for case 3. The resulting turbulence intensity (TI) contour plot is shown in fig. 8.23.

Again, it is clearly visible from the picture, how the area is dominated by the wing tip vortices. The turbulence intensity drops to low values towards both side walls and outer parts of the ground plane. The higher values of turbulence intensity in the upper part of the figure, close to the symmetry plane can be attributed to the effect of the balance, rather than blockage.

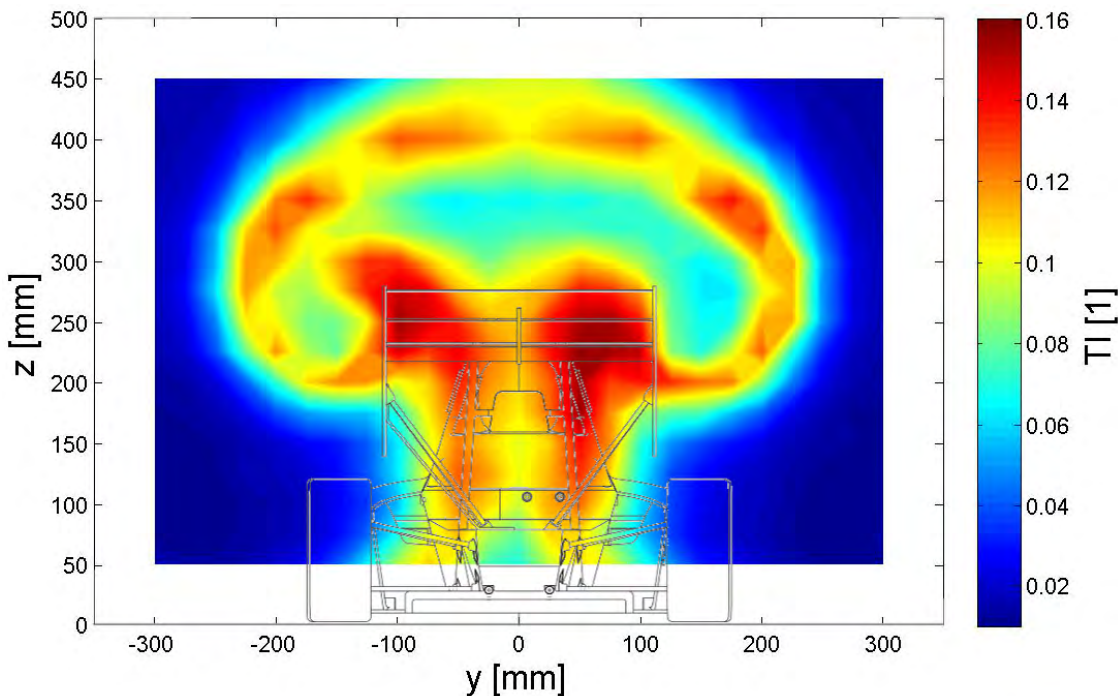


Fig. 8.23: Case 3, $U_\infty = 25 \text{ m/s}$. Turbulence intensity distribution behind a car – hot wire probe traversing.

8.5 Review of Reynolds number during the experiment

Targeted Reynolds number similarity during design of the experiment in section 5.2.1 was the following: to obtain the same Reynolds number during experiment with 25% scale model as in reality for 50 km/h – the wind tunnel speed would have to be 55 m/s .

However, for measurements with traverser, the wind tunnel speed was as low as 25 m/s . This equals to 22.5 km/h in reality. Maximum wind tunnel speed at which

a test was conducted was 43 m/s . This equals to 39 km/h in reality. Therefore, it is obvious that the tests were conducted at much lower Reynolds numbers and that this fact does have an adverse effect on the results that are presented here.

8.6 Comparison with numerical simulations

In this section, experimental data are compared to available results from CFD simulations, which are taken from [25].

Numerical results presented here were obtained by simulating a full scale geometry at 16.7 m/s , which equals to 60 km/h . The geometry used for CFD computation was a little bit different – somewhat more complicated (most noticeably in the engine compartment area). The simulation was done in a computational domain large enough that it is safe to say that there are no blockage effects. Both moving floor and rotating wheels are included in the simulation. The CFD results are compared to case 3, which is the same configuration.

The comparison is done to verify, that both results are generally similar and that the experimental results are not too different from the numerical results and vice versa.

8.6.1 Aerodynamic coefficients

Lift and drag coefficients from experiment and CFD simulation are shown and compared in tab. 8.12.

From experiment, the drag coefficient is 6% higher, compared to CFD, which is a very good similarity.

In terms of lift coefficient, the difference is substantially bigger. The C_L value from experiment is 46% lower compared to the one from CFD. This difference can be most probably attributed to the considerably lower Reynolds number during experiment and wind tunnel blockage.

Tab. 8.12: Comparison of experimental and numerical results – aerodynamic coefficients

	Experiment	CFD	Δ
C_D	1.125	1.06	6.13%
C_L	-1.282	-2.39	-46.36%

8.6.2 Wake

Velocity distribution – from CFD – in the wake behind a car can be seen in fig. 8.24. In this picture, the whole computational domain is captured. The axes in the figure are inserted to provide reference of the test section boundaries. It can be seen, that the velocity profile is still changing outside the test section walls, therefore the wind tunnel blockage does have an influence on the experimental results.

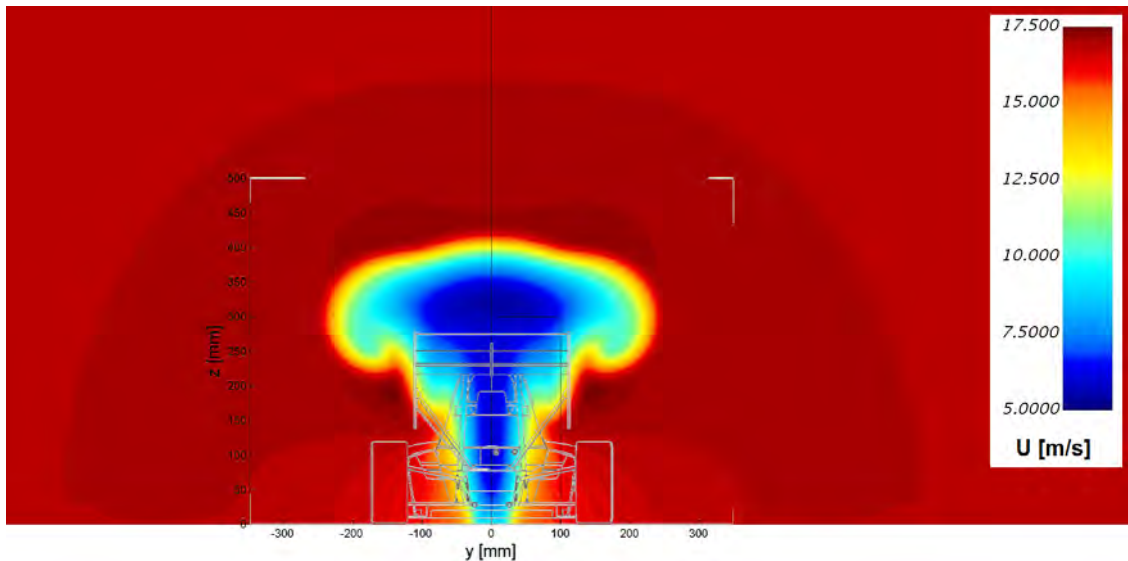


Fig. 8.24: CFD – full scale, $U_{\infty} = 16.7 \text{ m/s}$, velocity distribution behind a car [25]

From comparison of fig. 8.25 and fig 8.26, it can be seen that the wake directly behind the car is not too much different. In the figure from experiment (8.26) the wing tip vortices appear to have shifted slightly lower and towards the symmetry plane. This can be result of blockage effects – the vortices cannot move upward and to the sides due to proximity of the wind tunnel walls.

8.7 Load distribution

Distribution of the resulting aerodynamic load on the vehicle's front and rear axle is an important characteristic. This topic – with respect to aerodynamic on track testing – was covered by Stipak in [21].

Tab. 8.13 shows load distribution for case 3 and case 4 calculated based on the experiment results. The calculation was done as is described by equation 8.1. In this equation C_{RR} is a coefficient of reaction force acting at the rear axle's contact patch. In other words, fraction C_{RR}/C_L expresses ratio of resulting load on the rear

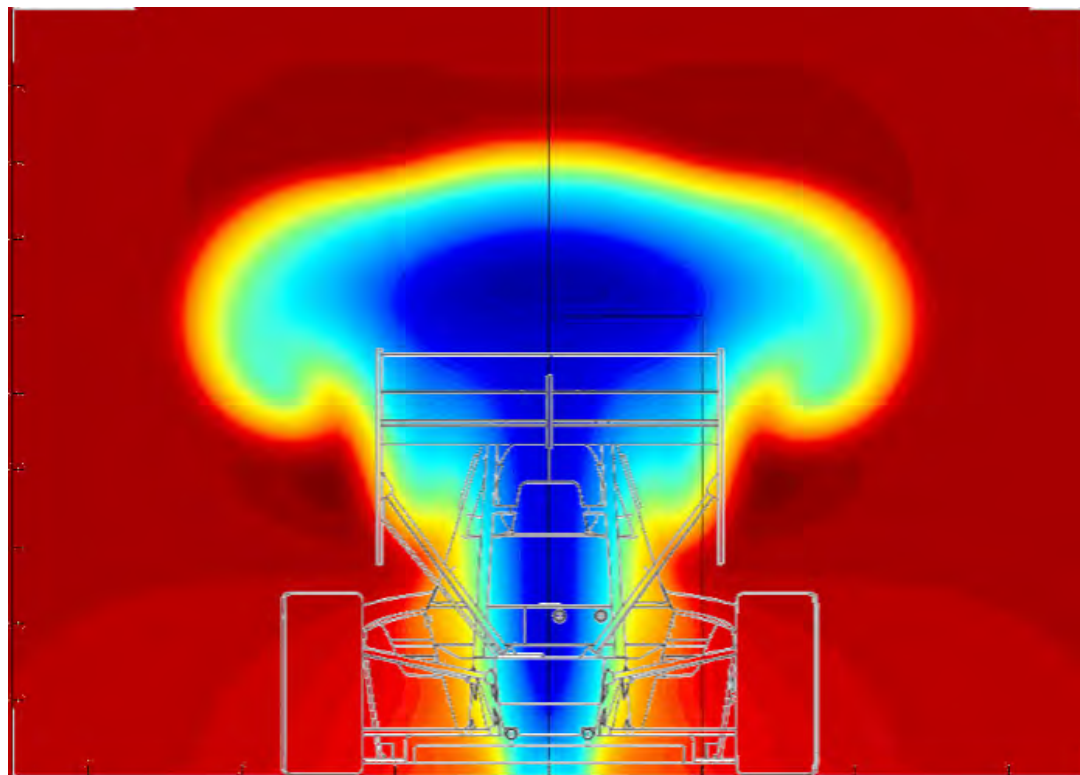


Fig. 8.25: Velocity contour plot – CFD

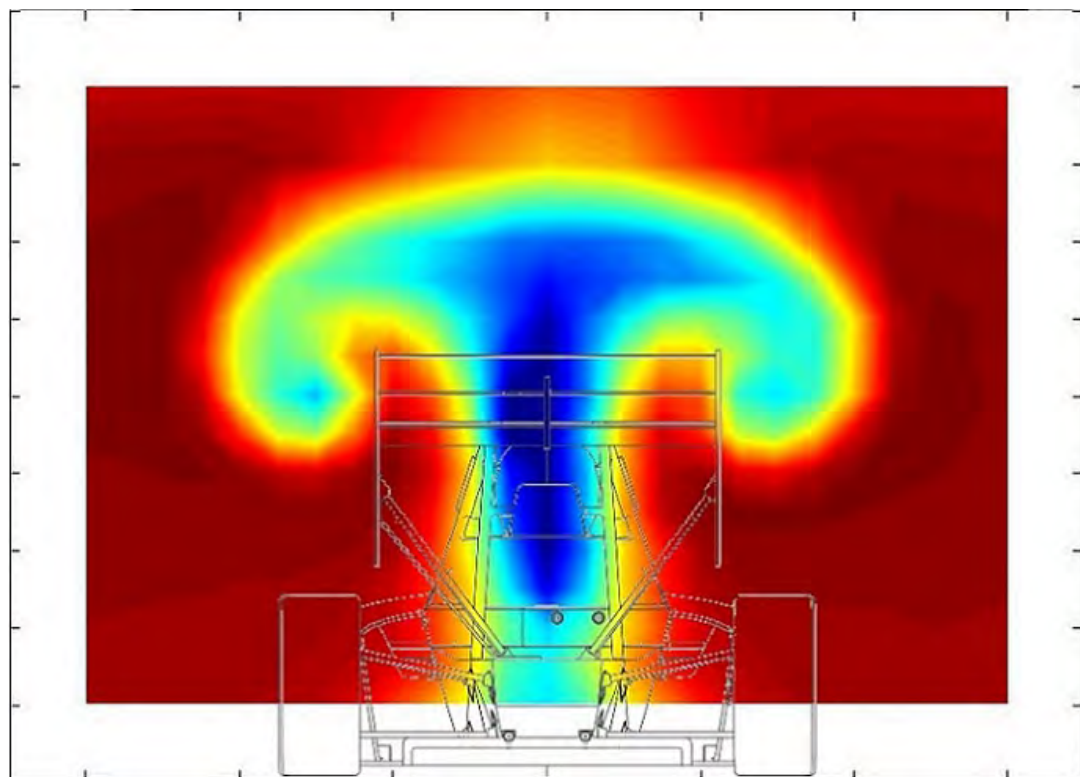


Fig. 8.26: Velocity contour plot – experiment (case 3)

axle to downforce of the car.

$$\frac{C_{RR}}{C_L} = \frac{1}{2} + \frac{C_M}{C_L} \quad (8.1)$$

Tab. 8.13: Load transfer based on measured aerodynamic load

	Case 3	Case 4
C_{RR}/C_L	91%	88%

The values for both case 3 and case 4 in tab. 8.13 – around 90% – appear to be quite high. However, as can be seen in fig. 8.27, from aerodynamic on track testing of Dragon 4, as high values as 90% were also obtained, although the load distribution was found to be dependent on velocity and such high values were measured for speeds close to maximum speed [21].

The reason for such high values can be found in comparison of aerodynamic coefficients from experiment and CFD. Total downforce of the car appears to be underestimated, while drag seems to be reasonably accurate. Consequently, this relation between downforce and drag results in higher pitching moment. And higher pitching moment directly translates into higher ratio C_{RR}/C_L .

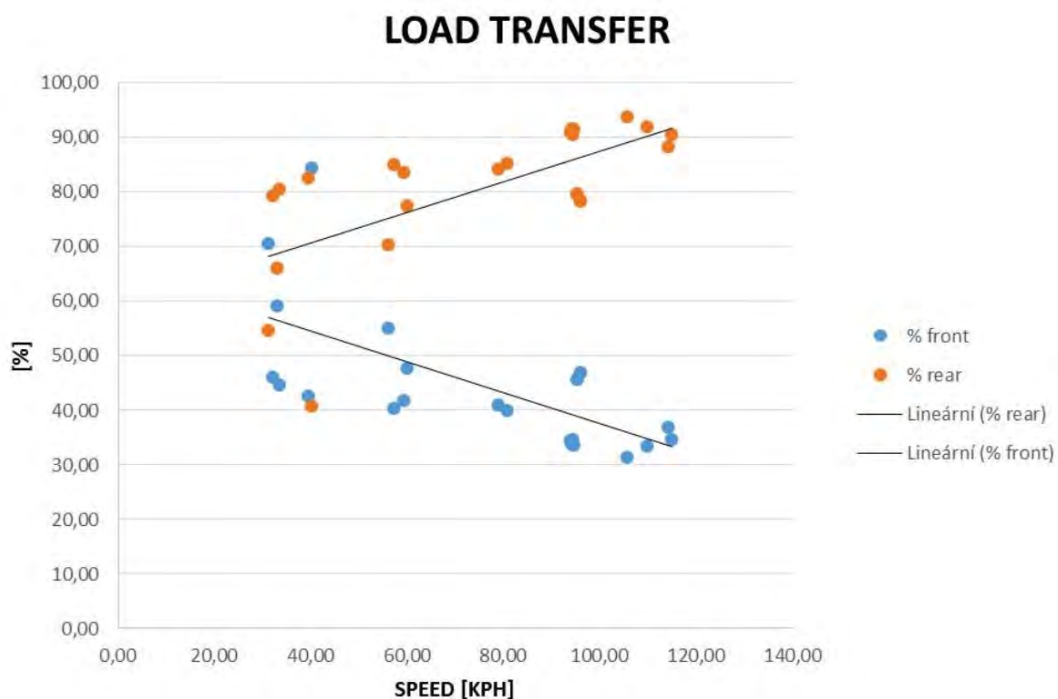


Fig. 8.27: Load transfer vs. speed from Dragon 4 on track testing [21]

9 CONCLUSION

Over the recent years, aerodynamics became an integral part of car development in Formula SAE. In this work a study of a Formula SAE car's aerodynamic characteristics was conducted, the method for aerodynamic analysis being subscale experimental testing. The goal was to determine aerodynamic characteristics of the model and find areas from which improvement of these characteristics could be extracted.

The testing was done with a 25% scaled model of a Formula SAE race car derived from TU Brno Racing's 2016 car – Dragon 6. Four different configurations were measured, differing in usage of a floor with diffuser and inverted wings. The model was mounted on a sting balance and measurements were done with stationary both wheels and floor. The wind tunnel blockage in this configuration was quite high – approximately 20%.

The aforementioned force balance was initially not available as part of the wind tunnel's equipment. Therefore, part of this work focuses on design and calibration of a six component balance, that uses strain gauges to measure the aerodynamic load.

From load measurement – for configurations without wings – it was found that the model produces lift. When using a floor with diffuser, the overall lift can be reduced. Here, the resulting difference is 35% reduction in the overall lift, while reduction in drag is 12%. Configurations with wings produce downforce, but also considerably higher drag. However, the trend is different compared to configurations without wings. Although the difference is marginal – only 2% – with wings, the configuration with diffuser produces lower downforce, than the configuration with planar floor. Probable cause for such unexpected behaviour is thought to be resulting from balance deflection. Such deflection consequently induces a rake angle of the model, thus generating greater downforce.

Dominant source of downforce are the wings. However, pressure coefficient distribution on the floor showed, that the rear wing also contributes to higher downforce generation on the floor.

It is obvious that as high blockage as 20% must have a strong influence on the experiment results. However, the fact that the two counter rotating vortices shed from tips of the rear wing were found to be comfortably distanced from the wind tunnel walls means, that the results are not rendered useless because of the blockage.

It was desired to obtain Reynold number equivalent to full scale car's velocity of 50 km/h. However, due to high blockage of the test section and the consequent pressure losses, the maximum speed that was achieved in the wind tunnel was equal

to full scale velocity as low as 22.5 km/h . This fact also has an adverse effect on the measured results.

Should the current car configuration be improved, either increasing downforce or decreasing drag would be possible. However, it is more important to achieve a reasonable aerodynamic balance. Therefore it is required to move the resulting centre of pressure forward. That could be done in different ways. One of them being – as suggested above – using a rake angle instead of a diffuser to generate downforce on the vehicle's underbody

Even though conclusions can be drawn from the presented experimental data, further effort is required to make this experimental set up truly useful when designing aerodynamic parts for a Formula SAE car.

Effect of wind tunnel blockage on the results should be determined via numerical simulations. Then, all three available design tools should also be correlated - CFD, wind tunnel testing, and track testing.

BIBLIOGRAPHY

- [1] CATTAFESTA, Louis, BAHR, Chris and MATHEW, Jose, 2010, Fundamentals of Wind-Tunnel Design. *Encyclopedia of Aerospace Engineering* [online]. 15 December 2010. DOI 10.1002/9780470686652.eae532. Retrieved from: <http://doi.wiley.com/10.1002/9780470686652.eae532>
- [2] CURTIS, Michael, 2016, *Private communication*. Loughborough University.
- [3] FRYŠTÁK, Lukáš, 2013, *Design of aerodynamic wings of Formula Student / SAE* [online]. Bachelor's Thesis. Brno. Retrieved from: https://www.vutbr.cz/www_base/zav_prace_soubor_verejne.php?file_id=84183
- [4] HUCHO, Wolf-Heinrich, 1998, *Aerodynamics of road vehicles: from fluid mechanics to vehicle engineering*. 4th ed. Warrendale, PA : Society of Automotive Engineers. ISBN 07-680-0029-7.
- [5] HUCHO, Wolf-Heinrich, 2013, *Aerodynamik des Automobils: Strömungsmechanik, Wärmetechnik, Fahrdynamik, Komfort ; mit 49 Tabellen*. 6. Aufl. Wiesbaden : Vieweg. ISBN 978-383-4819-192.
- [6] KATZ, Joseph, 1995, *Race Car Aerodynamics: Designing for Speed*. Cambridge, MA, USA : Bentley Publishers. ISBN 0-8376-0142-8.
- [7] KATZ, Joseph and GARCIA, Darwin, 2002, Aerodynamic Effects of Indy Car Components. *Proceedings of the 2002 SAE Motorsports Engineering Conference and Exhibition* [online]. 2002. No. 2002-01-3311p. 11. DOI 10.4271/2002-01-3311. Retrieved from: <http://papers.sae.org/2002-01-3311/>
- [8] KATZ, Joseph and WALTERS, Robert, 1995, Investigation of wind-tunnel wall effects in high blockage testing. In : *33rd Aerospace Sciences Meeting and Exhibit* [online]. Reston, Virginia : American Institute of Aeronautics and Astronautics. 09 January 1995. p. -. Retrieved from: <http://arc.aiaa.org/doi/abs/10.2514/6.1995-438>
- [9] LAJZA, Ondřej, 2014, Aircraft engine cooling system testing. 2014.
- [10] LYU, Zhoujie and MARTINS, Joaquim R. R. A., 2014, Aerodynamic Design Optimization Studies of a Blended-Wing-Body Aircraft. In : *Journal of Aircraft* [online]. Grapevine, TX : AIAA. 2014. p. 1604-1617. Retrieved from: <http://arc.aiaa.org/doi/10.2514/1.C032491>
- [11] MCBEATH, Simon, 2013, Aerobytes: Students unleashed. *Racecar Engineering*. 01 December 2013. Vol. 2013, no. 12p. 57-59.

- [12] MCBEATH, Simon, 2014, Aerobytes: Further education. *Racecar Engineering*. 01 January 2014. Vol. 2014, no. 1p. 53-54.
- [13] MCBEATH, Simon, 2014, Aerobytes: Continuing studies. *Racecar Engineering*. 01 February 2014. Vol. 2014, no. 2p. 45-46.
- [14] MCBEATH, Simon, 2014, Aerobytes: Final examinations. *Racecar Engineering*. 01 March 2014. Vol. 2014, no. 3p. 39-40.
- [15] MCBEATH, Simon, 2014, Aerobytes: The flying limpet. *Racecar Engineering: Formula Student*. 2014. No. 1p. 14-24.
- [16] MILLIKEN, William F. and MILLIKEN, Douglas L., 1995, *Race Car Vehicle Dynamics*. Warrendale, PA, USA : SAE International. ISBN 1-56091-526-9.
- [17] PLACZEK, Robin, SCHOLZ, Peter and OTHMER, Carsten, 2014, An Analysis of Drag Force Components and Structures in the Wake of a Detailed Road Vehicle Model by Means of SPIV. *17 th International Symposium on Applications of Laser Techniques to Fluid Mechanics* [online]. 2014. Retrieved from: http://ltces.dem.ist.utl.pt/lxlaser/lxlaser2014/finalworks2014/papers/01.7_3_136paper.pdf
- [18] POPE, Alan and HARPER, John J., 1966, *Low-Speed Wind Tunnel Testing*. New York : John Wiley & Sons, Inc. ISBN 978-0-471-55774-6.
- [19] ROYCE, Michael and ROYCE, Suzanne, 2012, *Learn and Compete: A primer for Formula SAE, Formula Student and Formula Hybrid teams*. ISBN 978-0953352470.
- [20] ŠPIČÁK, Milan, 2015, *Performance optimisation of turbocharged engine for Formula Student* [online]. Master's Thesis. Brno. Retrieved from: https://www.vutbr.cz/www_base/zav_prace_soubor_verejne.php?file_id=104750
- [21] ŠTIPÁK, Patrik, 2015, *Suspension Development of Formula Student Vehicle* [online]. Master's Thesis. Brno. Retrieved from: https://www.vutbr.cz/www_base/zav_prace_soubor_verejne.php?file_id=103919
- [22] TOET, Willem, 2014, *How WIND TUNNELS Work - F1 explained - Sauber F1 Team* [online]. Hinwil, Switzerland. [Accessed 25 March 2016]. Retrieved from: <https://www.youtube.com/watch?v=KC0E0wU6inU>. Sauber F1 Team; Sauber Motorsport AG
- [23] TU BRNO RACING, 2014, *Dragon 4 - Design Book: Presentation materials*. Brno : TU Brno Racing.

- [24] TU BRNO RACING, 2015, *Dragon 5 - Design Book: Presentation materials.* Brno : TU Brno Racing.
- [25] TU BRNO RACING, 2016, *Dragon 6 - Design Book: Presentation materials.* Brno : TU Brno Racing.
- [26] WORDLEY, Scott and SAUNDERS, Jeff, 2006, Aerodynamics for Formula SAE: Initial Design and Performance Prediction. *SAE Paper* [online]. 2006. No. 2006-01-0806. DOI 10.4271/2006-01-0806. Retrieved from: <http://papers.sae.org/2006-01-0806/>
- [27] WORDLEY, Scott and SAUNDERS, Jeff, 2006, Aerodynamics for Formula SAE: A Numerical, Wind Tunnel and On-Track Study. *SAE Paper* [online]. 2006. No. 2006-01-0806. DOI 10.4271/2006-01-0808. Retrieved from: <http://papers.sae.org/2006-01-0808/>
- [28] SAE International, 2015. [online], 2015. [Accessed 30 December 2015]. Retrieved from: sae.org
- [29] *SAE J 1594: Vehicle Aerodynamics Terminology*, 1987. , Warrendale : SAE International. SAE J 1594
- [30] Rake Angle, In : *Formula1-dictionary.net* [online], [Accessed 22 May 2016]. Retrieved from: http://www.formula1-dictionary.net/rake_angle.html
- [31] Formula SAE: Competition History 1981-2004, In : *SAE.org* [online], [Accessed 03 January 2016]. Retrieved from: <http://www.sae.org/students/fsaehistory.pdf>

LIST OF SYMBOLS AND ABBREVIATIONS

ε	Deformation
φ	Wind tunnel blockage
λ	Test section relative length
ν	Kinematic viscosity
ν_M	Kinematic viscosity for model
ν_R	Kinematic viscosity for real conditions
ρ	Air density
σ_b	Bending stress
A	Vehicle reference area
A_N	Cross-section area of wind tunnel nozzle
A_M	Model reference area
A_R	Real car reference area
\mathbb{C}	Calibration matrix
C_D	Drag coefficient
C_L	Lift coefficient
C_M	Pitching moment coefficient
C_N	Yawing moment coefficient
c_p	Pressure coefficient
C_R	Rolling moment coefficient
C_Y	Side force coefficient
C_{RR}	Coefficient of reaction force acting at vehicle's rear axle
CFD	Computational fluid dynamics
D	Drag force acting on a vehicle
D_N	Equivalent (hydraulic) diameter of wind tunnel nozzle

dB	Decibel
E	Young's modulus
$F1$	Formula 1
FIA	Fédération Internationale de l'Automobile (In english: International Automobile Federation)
FSAE	Formula SAE
HB	Horizontal buoyancy
IAE	Institute of Aerospace Engineering
L	Lift force acting on a vehicle
l	Vehicle reference length
l_m	Model reference length
M	Pitching moment acting on a vehicle
Ma	Mach number
\mathbb{M}_{bc}	Balance correction matrix
M_b	Bending moment
N	Yawing moment acting on a vehicle
q	Dynamic pressure
R	Rolling moment acting on a vehicle
R	Strain gauge response $\mu\text{m}/\text{m}$
Re	Reynolds number
Re_M	Model Reynolds number
Re_R	Real car Reynolds number
s_c	Model scale
SAE	Society of Automotive Engineers
SB	Solid blockage

TI	Turbulence intensity
u	Local velocity, x axis direction
u'	Root-mean-square of the turbulent velocity fluctuations
U_∞	Velocity of the oncoming flow
U_∞^M	Freestream velocity for model
U_∞^R	Freestream velocity for real car
V_∞	Freestream velocity
WB	Wake blockage
Y	Side force acting on a vehicle

LIST OF APPENDICES

A	Reynolds number and blockage calculation	139
B	Balance – further information	141
B.1	Balance drawings	141
B.2	Balance – calibration graphs	150
C	Aerodynamic load evaluation	157
C.1	Loads on balance	157
C.2	Load on model	161

A REYNOLDS NUMBER AND BLOCKAGE CALCULATION

This appendix shows equations that are used in the diagram in fig.. 5.3.

Model velocity

As is mentioned in section 5.2.1 the diagram is based on the similarity of Reynolds numbers of the model and the real car.

$$Re_M = Re_R \quad (\text{A.1})$$

Reynolds number was defined in section 3.7.2.

$$\frac{U_\infty^M l_M}{\nu_M} = \frac{U_\infty^R l_R}{\nu_R} \quad (\text{A.2})$$

The difference in kinematic viscosity for the model and real conditions is neglected.

$$\nu_M = \nu_R \quad (\text{A.3})$$

Then the equation A.2 can be rearranged and model velocity U_∞^M can be expressed.

$$U_\infty^M = U_\infty^R \frac{l_R}{l_M} \quad (\text{A.4})$$

The scale of the model is defined as follows.

$$s_c = \frac{l_M}{l_R} \quad (\text{A.5})$$

Then, the model velocity U_∞^M can be expressed as a function of model scale s_c .

$$U_\infty^M = U_\infty^R \frac{1}{s_c} \quad (\text{A.6})$$

Blockage

Blockage was defined in section 3.3.

$$\varphi = \frac{A_M}{A_N} \quad (\text{A.7})$$

Model scale is defined as follows.

$$s_c = \frac{l_M}{l_R} \quad (\text{A.8})$$

If the model scale s_c is multiplied by l_M/l_R , it can be written as:

$$s_c^2 = \frac{l_M^2}{l_R^2} \approx \frac{A_M}{A_R} \quad (\text{A.9})$$

$$s_c^2 = \frac{A_M}{A_R} \quad (\text{A.10})$$

Model reference area can be then expressed as follows.

$$A_M = A_R s_c^2 \quad (\text{A.11})$$

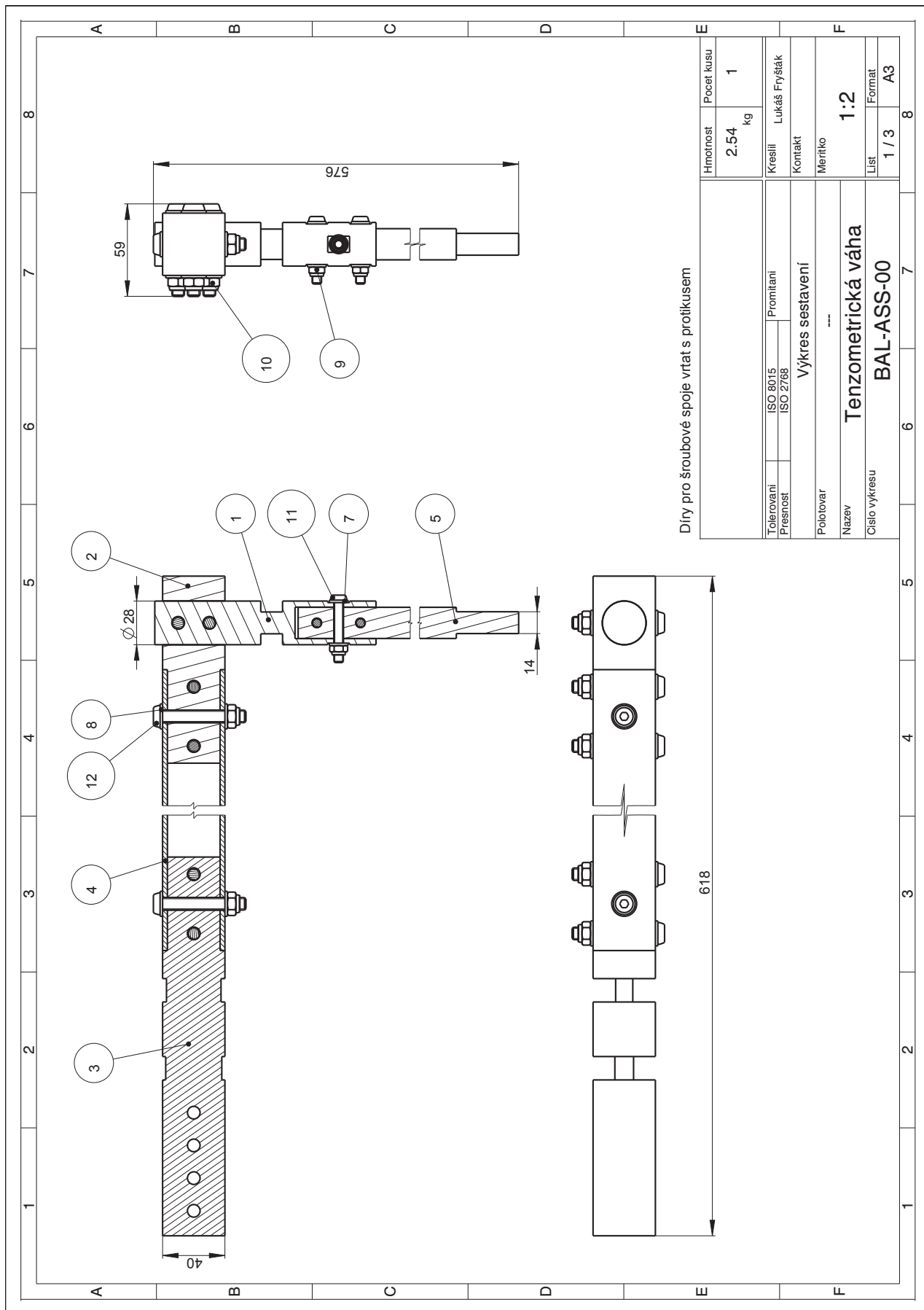
The model reference area is the substituted in the equation A.7, which gives blockage φ as a function of model scale s_c .

$$\varphi = \frac{A_R}{A_N} s_c^2 \quad (\text{A.12})$$

B BALANCE – FURTHER INFORMATION

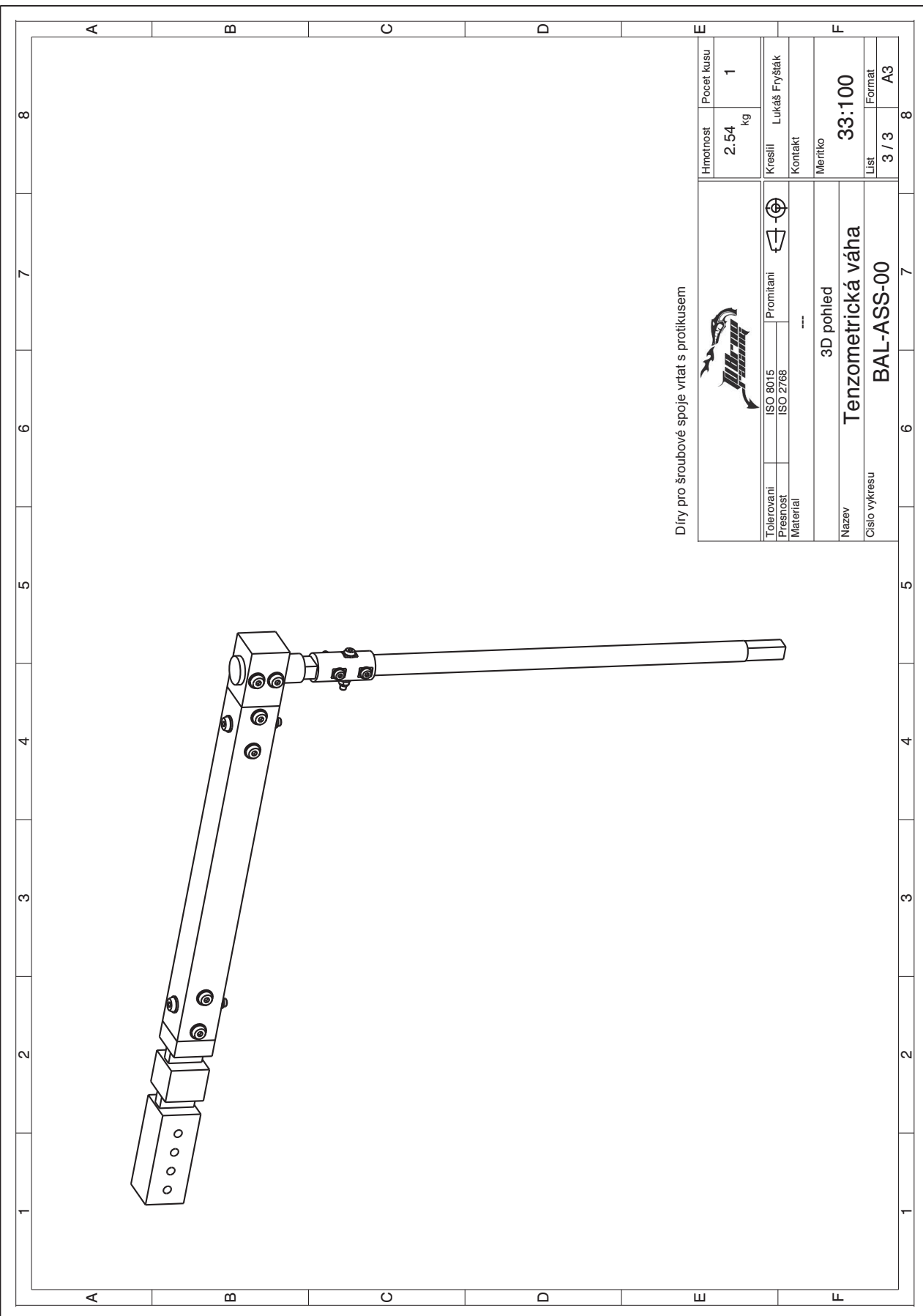
B.1 Balance drawings

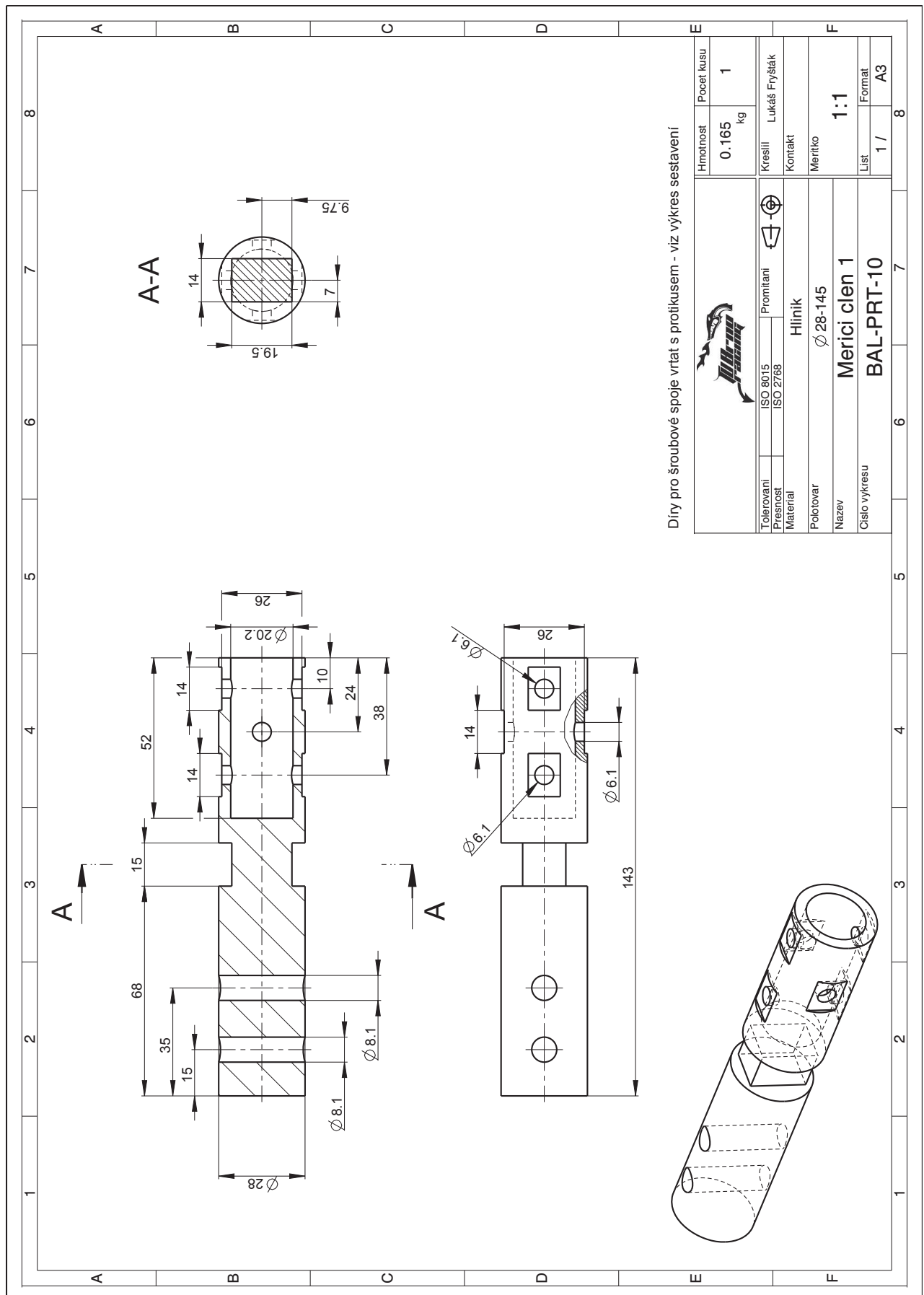
On the following pages, balance drawings are shown. First, there are drawings of the whole assembly and then, there are drawings of the respective parts.

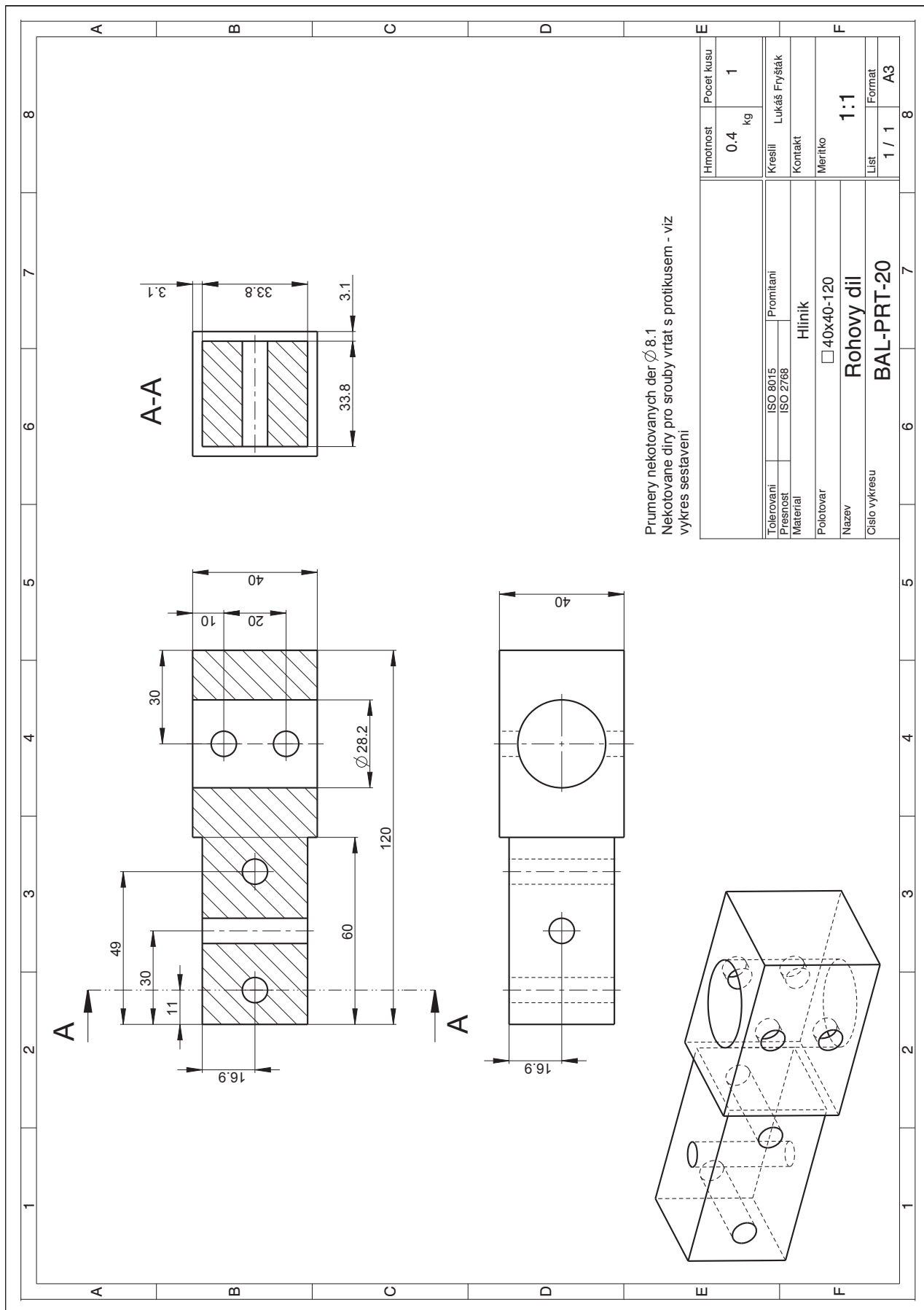


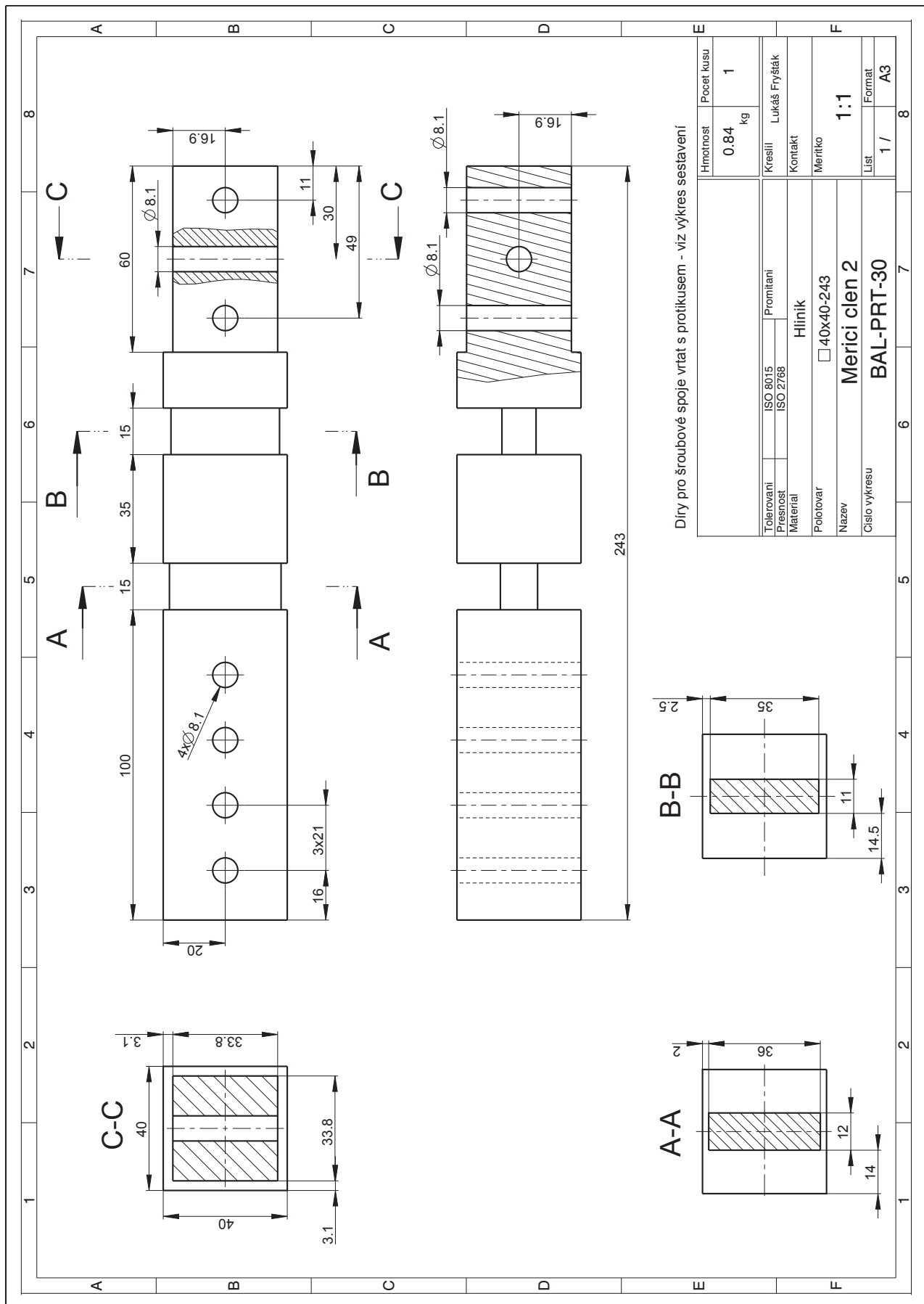
ITEM NO	PART NUMBER	QTY	DESCRIPTION	NOTES
1	BAL-PRT-10	1	bal-prt-10.prt	8tenzometru
A	BAL-PRT-20	1	bal-prt-20.prt	
3	BAL-PRT-30	1	bal-prt-30.prt	16 tenzometru
4	BAL-PRT-40	1	bal-prt-40.prt	
5	BAL-PRT-50	1	bal-prt-50.prt	
6	BAL-SIMPLIFIED	1	prt0002.prt	Model pro zakladni geometri, neni soucast sestavy
7	DIN_125_6	6		Podlozka M6
B	DIN_125_8	16		Podlozka M8
9	DIN_985_M6	3		Matici M6
10	DIN_985_M8	8		Matici M8
11	ISO_7380_M6_X_40	3		Sroub M6x40
12	ISO_7380_M8_X_55	8		Sroub M8x55

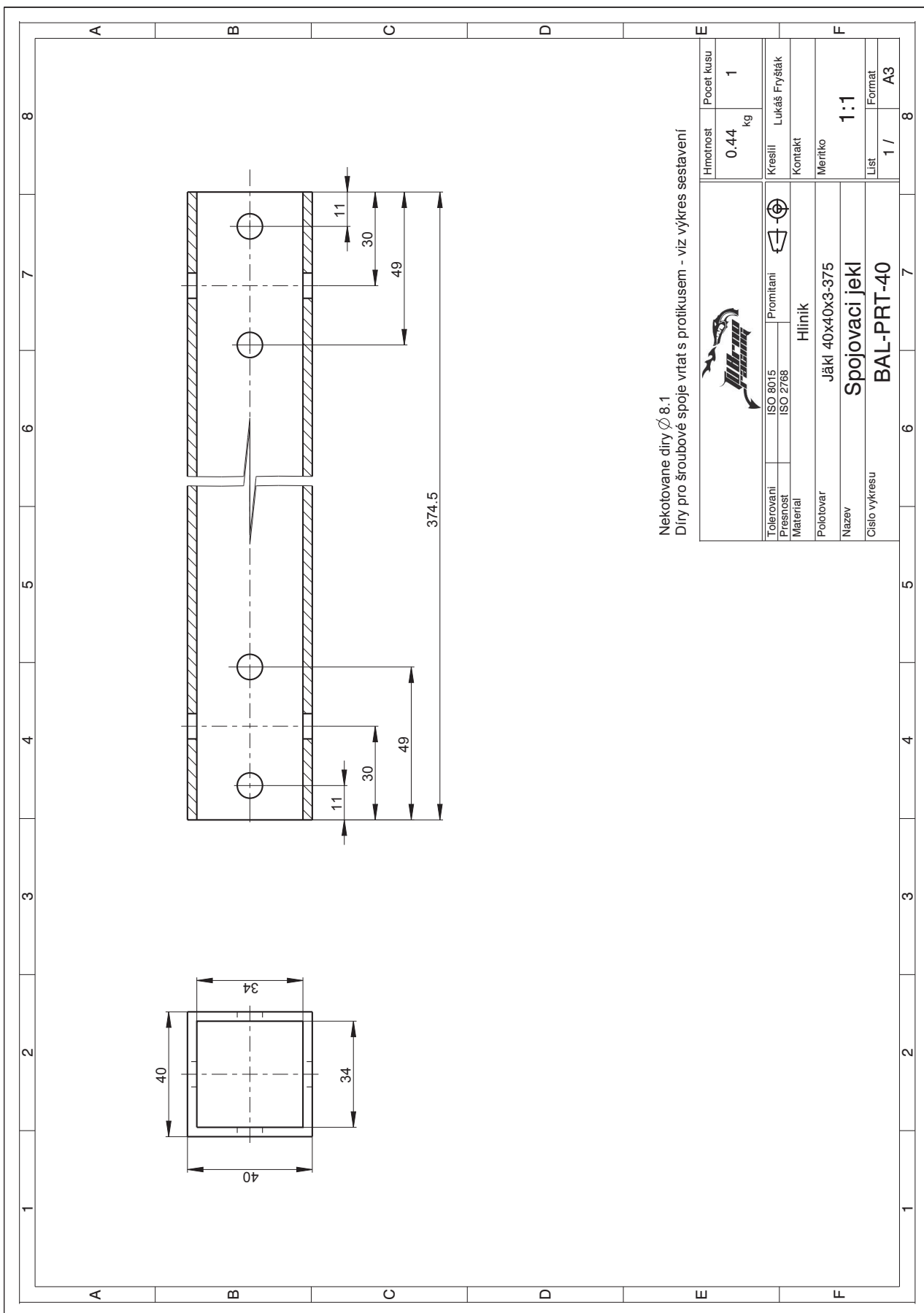
A		B		C		D		E		F	
								Hmotnost	Pocet kusu		
								---	---		
								kg	---		
								Kresilí	Lukáš Fryšták		
									Kontakt		
										Meritko	
										Nazev	1 : 1
										Cislo výkresu	Tenzometrická váha
											BAL - ASS-00
								list	2 / 3	Format	A3
											8
1		2		3		4		5	6		7

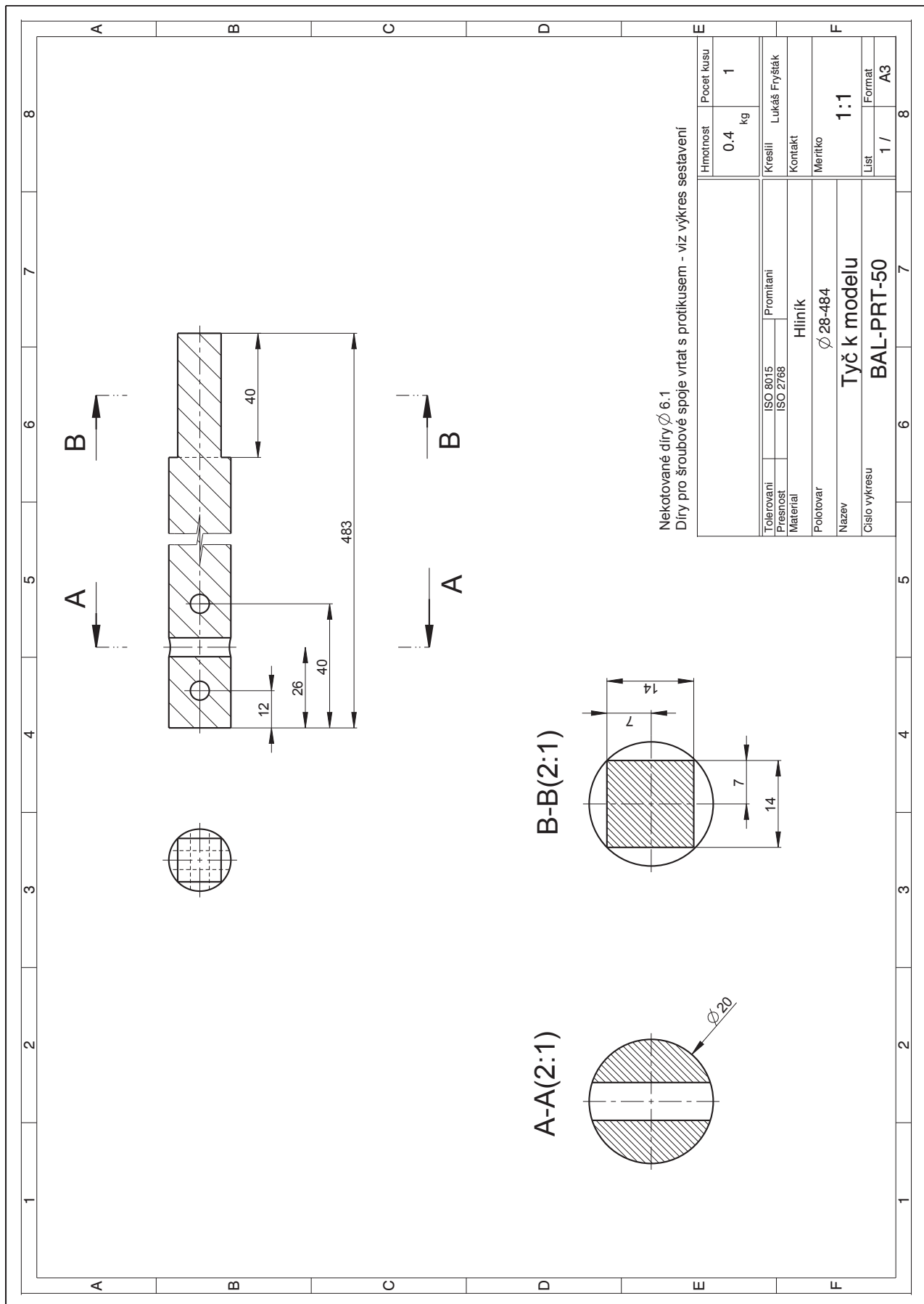












B.2 Balance – calibration graphs

In this section, graphs regarding balance calibration are shown.

Firstly, raw data logged when applying respective components of load are shown in fig. B.1 – B.6.

In fig. B.7 – B.12, data used for calibration are shown. These are plotted with the respective approximated lines.

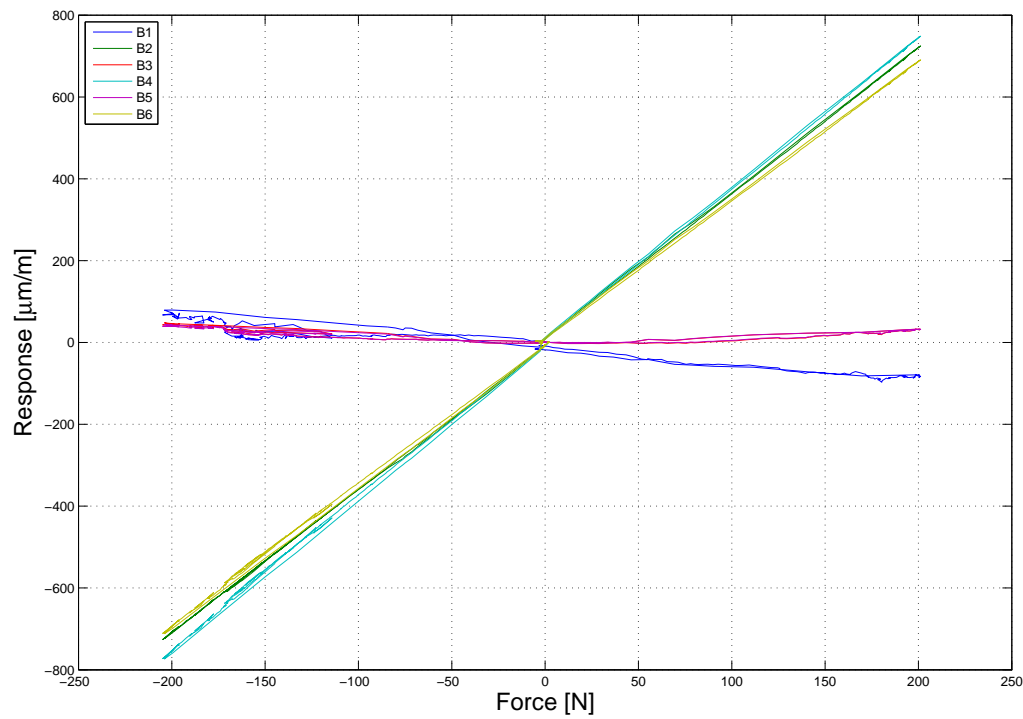


Fig. B.1: Raw data recorded when a single component of load was applied – F_x

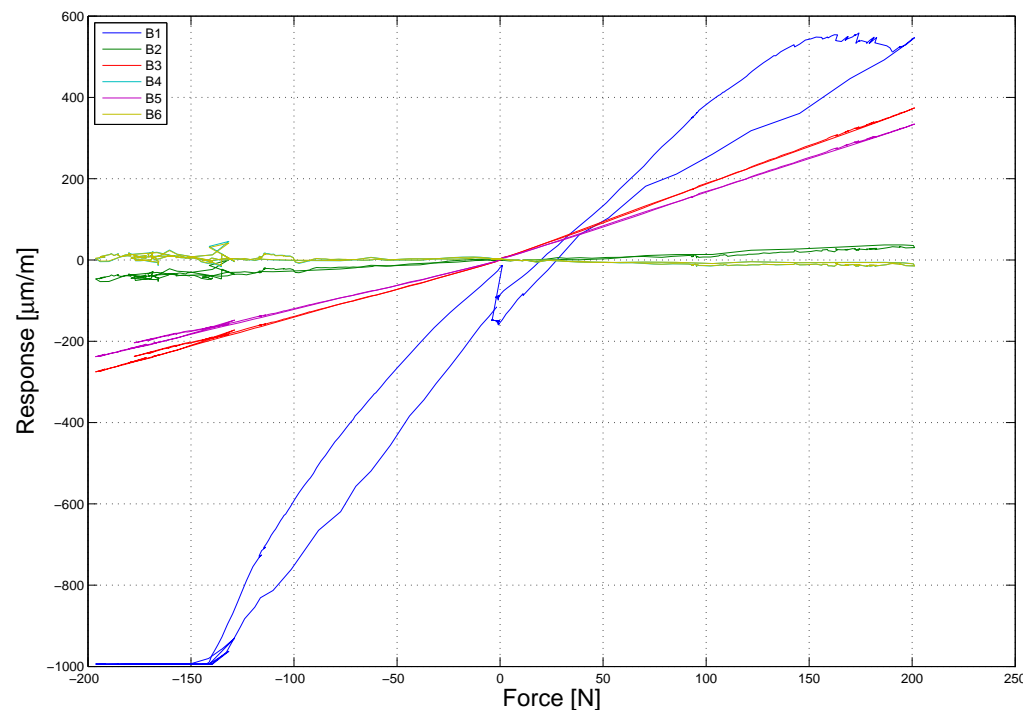


Fig. B.2: Raw data recorded when a single component of load was applied – F_y

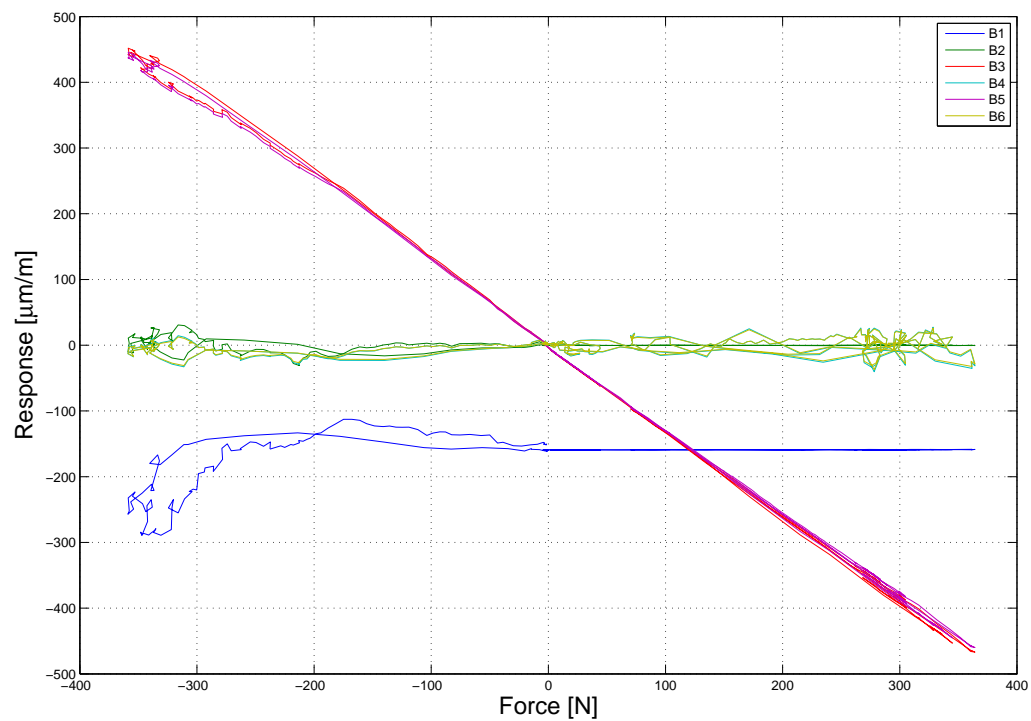


Fig. B.3: Raw data recorded when a single component of load was applied – F_z

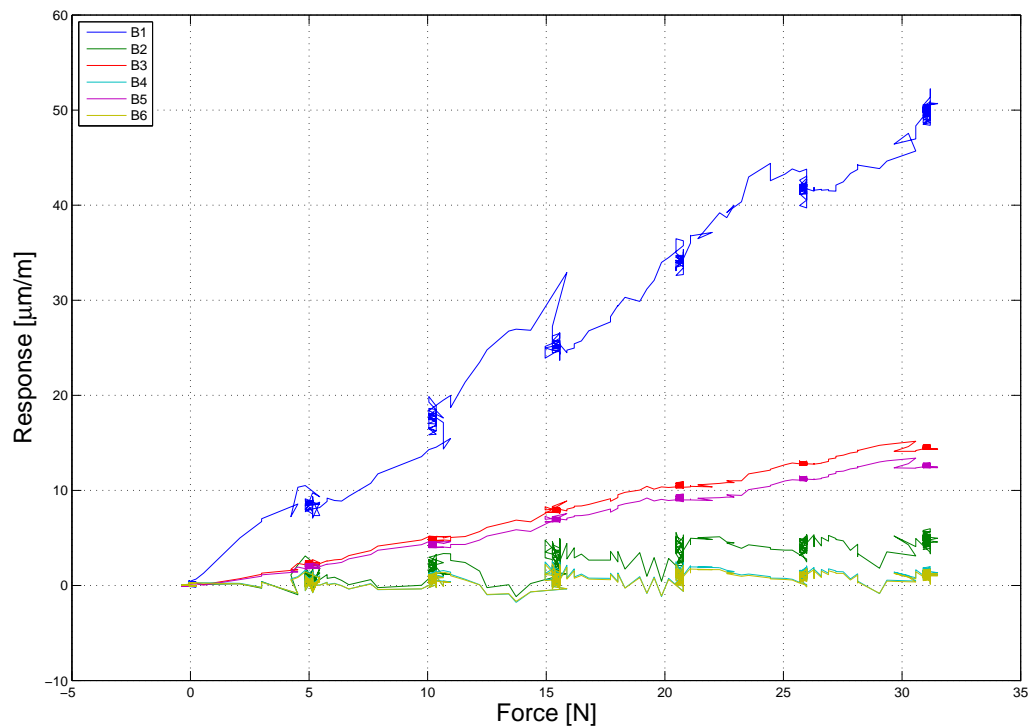


Fig. B.4: Raw data recorded when a single component of load was applied – M_x
(after subtraction of zero values)

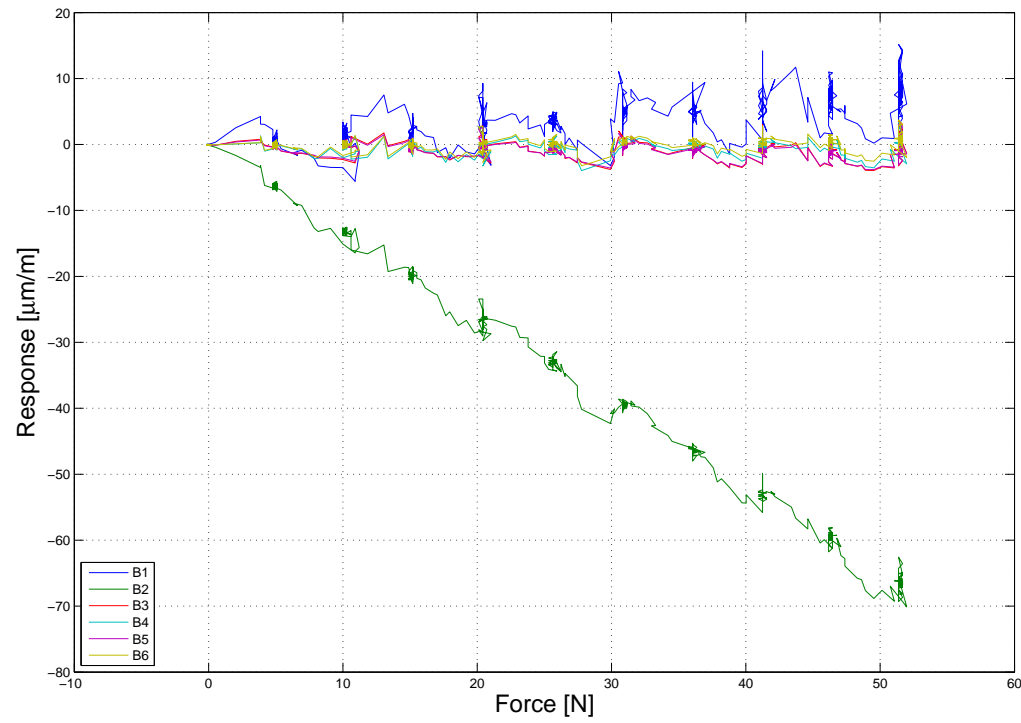


Fig. B.5: Raw data recorded when a single component of load was applied – M_y (after subtraction of zero values)

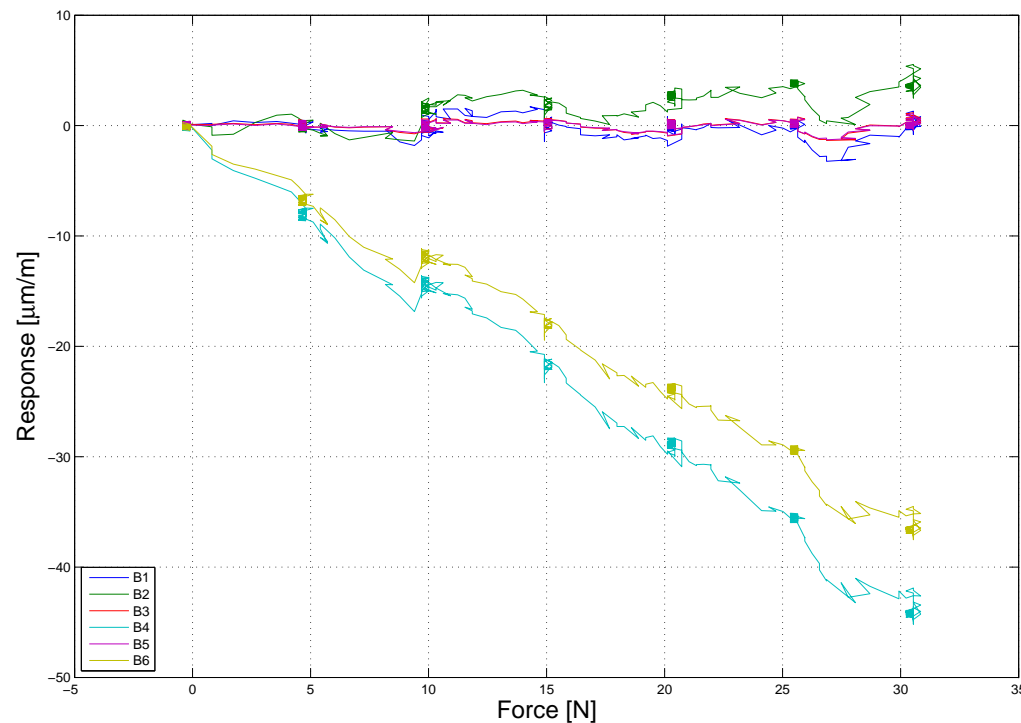


Fig. B.6: Raw data recorded when a single component of load was applied – M_z (after subtraction of zero values)

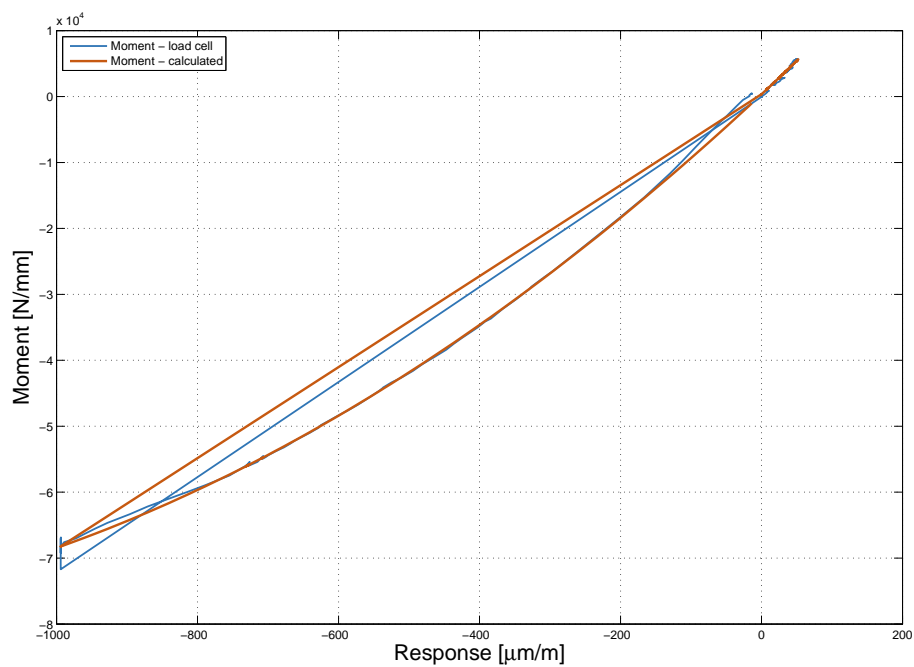


Fig. B.7: Data used for calibration of bridge B1, plotted with approximated moment

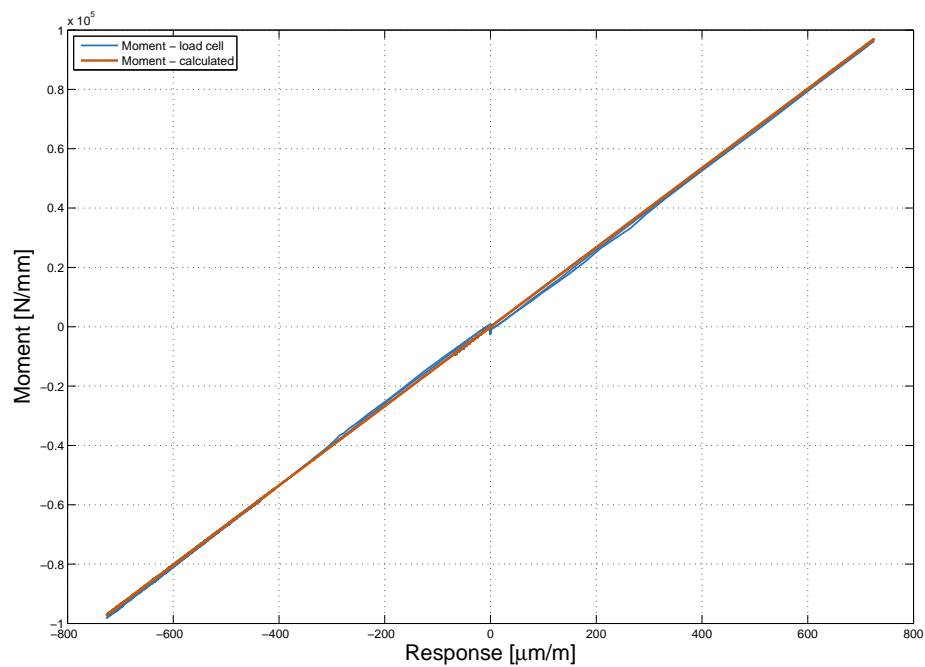


Fig. B.8: Data used for calibration of bridge B2, plotted with approximated moment

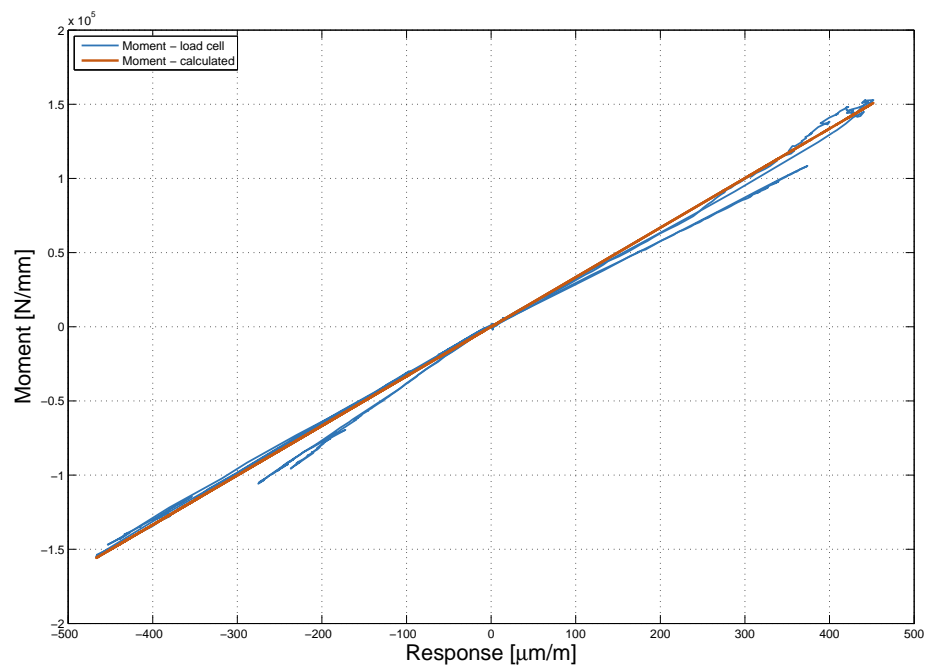


Fig. B.9: Data used for calibration of bridge B3, plotted with approximated moment

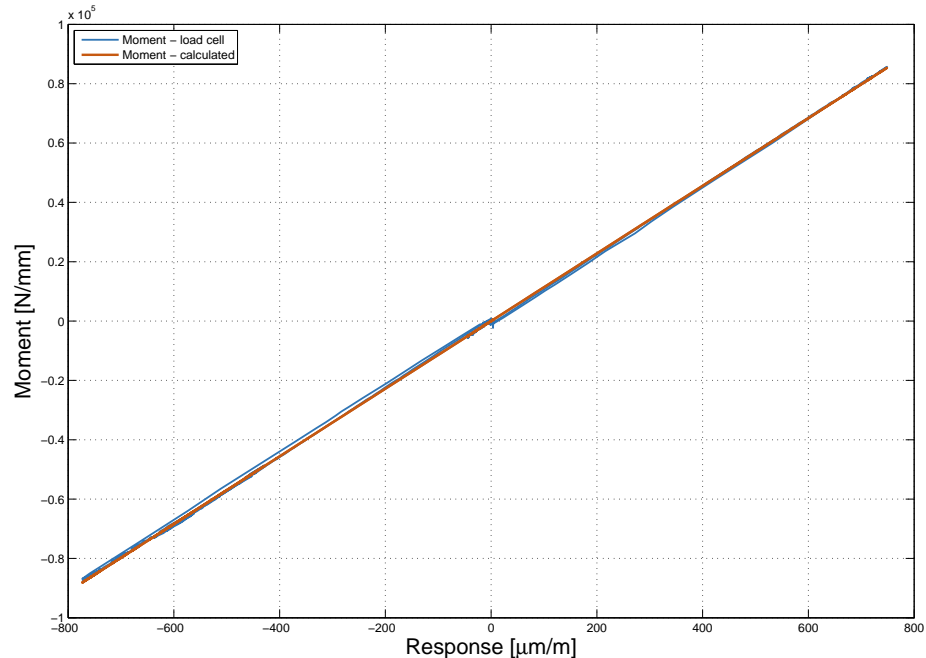


Fig. B.10: Data used for calibration of bridge B4, plotted with approximated moment

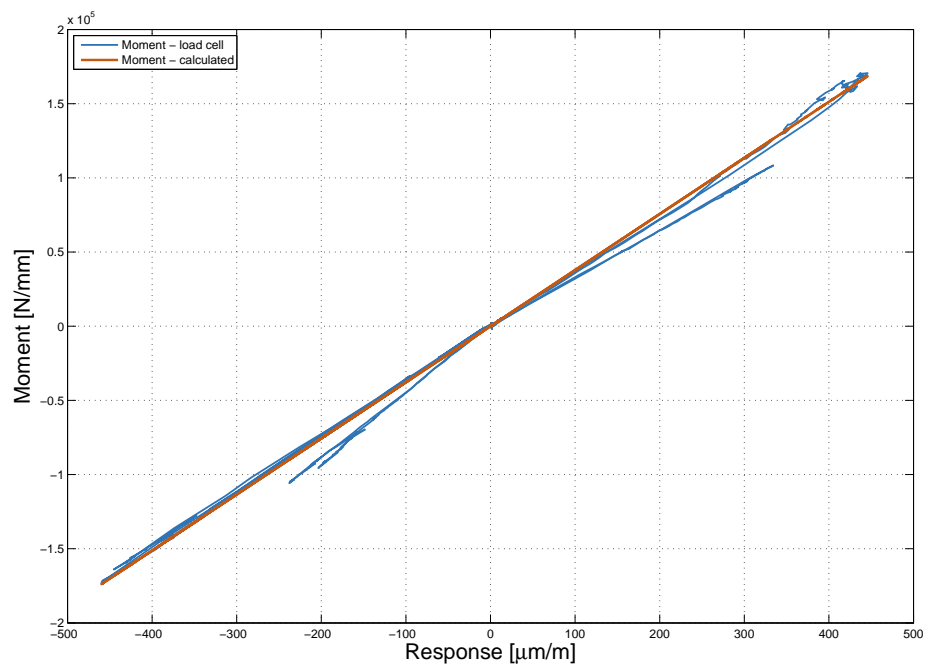


Fig. B.11: Data used for calibration of bridge B5, plotted with approximated moment

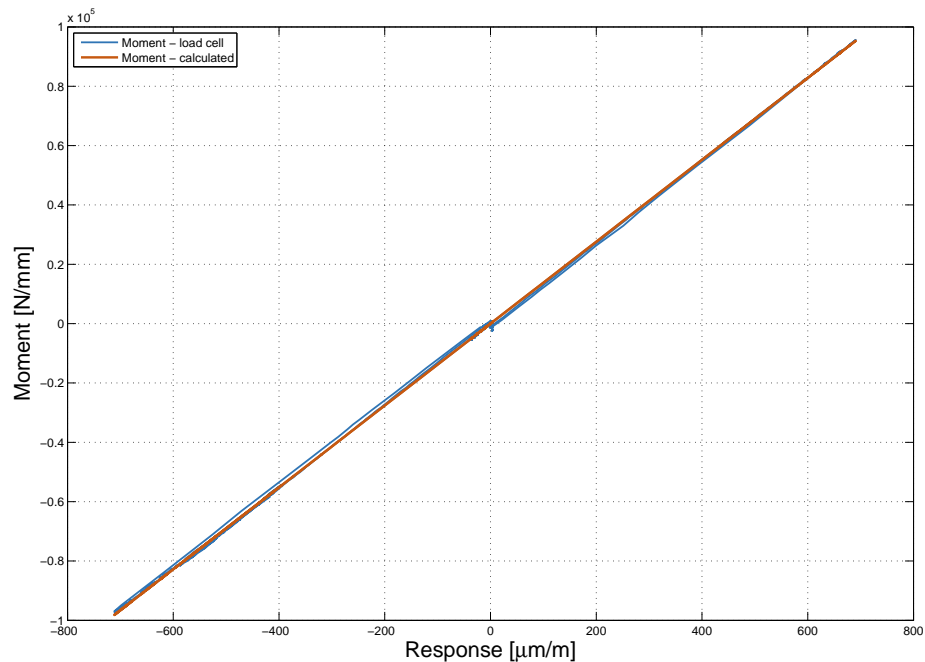


Fig. B.12: Data used for calibration of bridge B6, plotted with approximated moment

C AERODYNAMIC LOAD EVALUATION

C.1 Loads on balance

This section shows, how loads on the balance itself were measured and evaluated. As was described in section 8.2.1, loads on balance were logged for 5 different velocities – 10, 20, 30, 35, and 40 m/s. As part of the general process that was applied when logging all cases, zero values before and after measuring were logged.

Measured zero values are shown in fig. C.1, while strain gauge responses to balance loading are shown in fig. C.2.

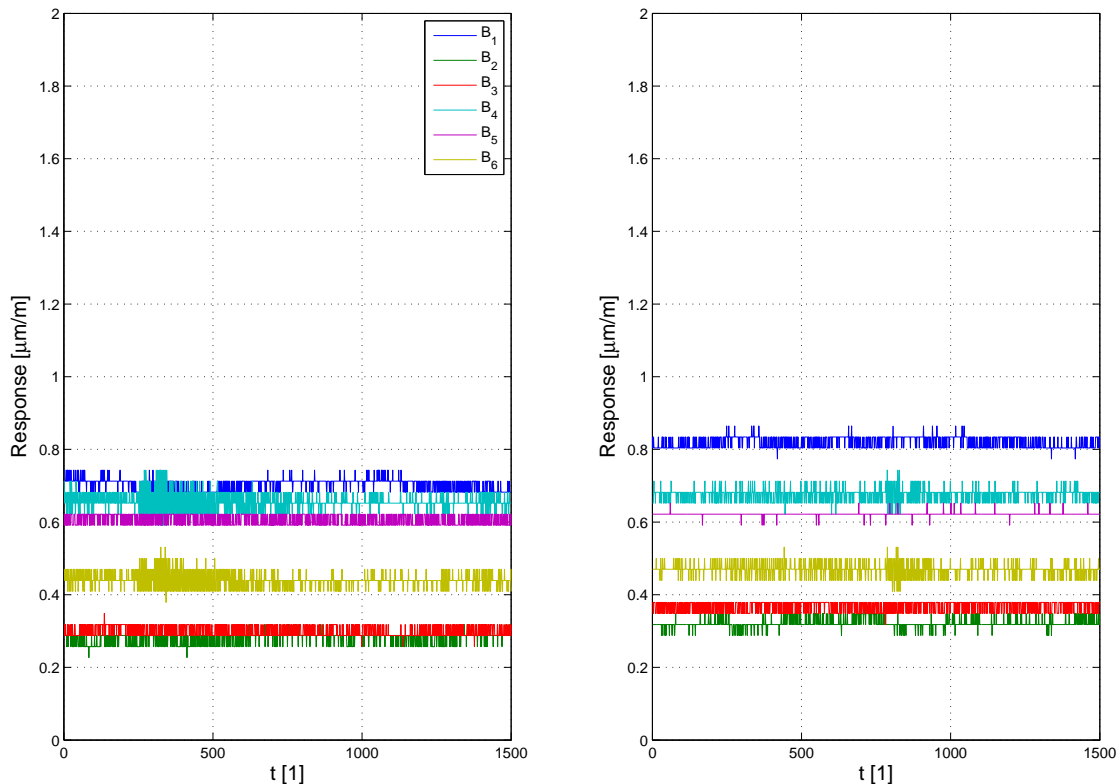


Fig. C.1: Measurement of forces acting on balance, zero values

The output from the balance – strain gauge responses in $\mu\text{m}/\text{m}$ – are obtained in a matrix that is generally described in equation C.1. In the first column of the matrix, there are responses for strain gauge bridge B_1 . Values for the bridge B_2 are in the second column and so on.

$$Z = \begin{bmatrix} r_{1,B1} & r_{1,B2} & \dots & r_{1,B6} \\ r_{2,B1} & r_{2,B2} & \dots & r_{2,B6} \\ \vdots & \vdots & \ddots & \vdots \\ r_{n,B1} & r_{n,B2} & \dots & r_{n,B6} \end{bmatrix} \frac{\mu\text{m}}{\text{m}} \quad (\text{C.1})$$

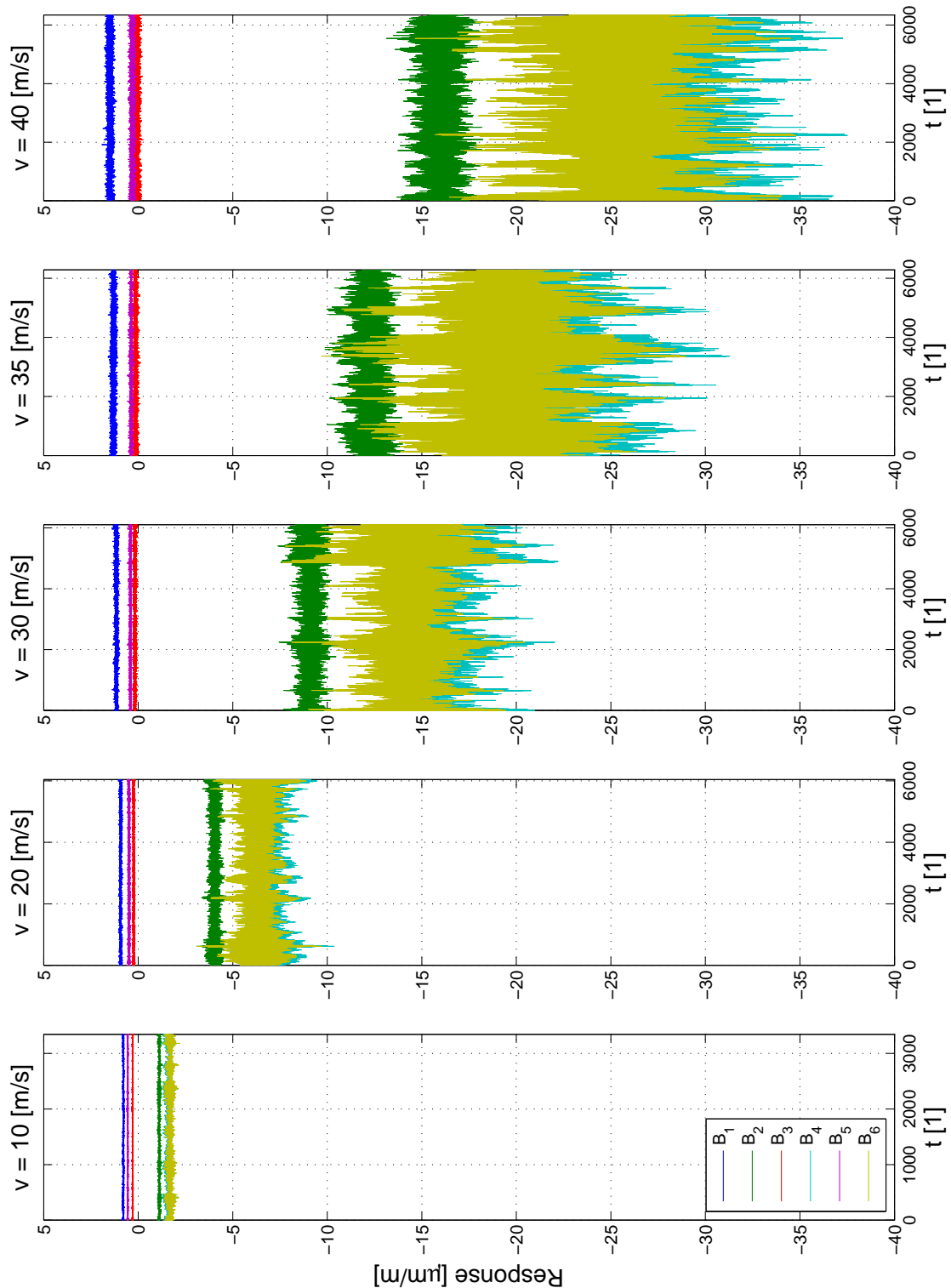


Fig. C.2: Measurement of forces acting on balance, strain gauge response to loads

The first step of the load evaluation is averaging responses from strain gauges over the entire measurement period. Both zero values files are firstly averaged, and the resulting zero values are obtained by averaging zero values from before and after measuring. Responses to loads are also averaged.

$$R_{zero,1} = \text{average}(Z_{zero,before}) \quad (\text{C.2})$$

$$R_{zero,2} = \text{average}(Z_{zero,after}) \quad (\text{C.3})$$

$$R_{zero} = \text{average}(Z_{zero,1}, Z_{zero,2}) \quad (\text{C.4})$$

$$R'_{10} = \text{average}(Z_{10\ m/s}) \quad (\text{C.5})$$

$$R'_i = \text{average}(Z_{i\ m/s}) \quad (\text{C.6})$$

Then, zero values are subtracted from strain gauge responses for all the velocities.

$$R_i = R'_i - R_{zero} \quad (\text{C.7})$$

Calculated strain gauge responses R_i can be multiplied by calibration matrix \mathbb{C} , which was defined in chapter 7. Multiplication of responses results in obtaining a vector of moments in the points of strain gauge bridges.

$$R \cdot \mathbb{C} = \begin{bmatrix} M_1 \\ M_2 \\ M_3 \\ M_4 \\ M_5 \\ M_6 \end{bmatrix} = \mathbb{M} \quad (\text{C.8})$$

Based on the balance's geometry, moments at points of strain gauge bridges can be transformed into separate components of aerodynamic load acting at the point of model mounting (see chapter 7). This transformation is done by multiplying the vector of moments \mathbb{M} by a transformation matrix as follows.

$$\mathbb{K}^{-1} \cdot \mathbb{M} = \mathbb{L}' \quad (\text{C.9})$$

In the previous equation, \mathbb{K}^{-1} is an inverse matrix to matrix \mathbb{K} , which is defined as (see chapter 7):

$$\mathbb{K} = \begin{bmatrix} 0 & -r_1 & 0 & 1 & 0 & 0 \\ r_1 & 0 & 0 & 0 & 1 & 0 \\ 0 & -r_0 & -r_2 & 1 & 0 & 0 \\ r_2 & 0 & 0 & 0 & 0 & 1 \\ 0 & -r_0 & -r_3 & -1 & 0 & 0 \\ r_3 & 0 & 0 & 0 & 0 & 1 \end{bmatrix} \quad (\text{C.10})$$

And \mathbb{L}' is defined as:

$$\mathbb{L}' = \begin{bmatrix} F'_x \\ F'_y \\ F'_z \\ M'_x \\ M'_y \\ M'_z \end{bmatrix} \quad (\text{C.11})$$

All components of aerodynamic load are calculated for all the velocities that were measured. Therefore, the load \mathbb{L}' can be plotted as a function of velocity U_∞ . Resulting forces acting on the balance are plotted in fig. C.3 and resulting moments are plotted in fig. C.4.

To be able to calculate load on balance at any velocity, all components of the resulting load are fitted with a quadratic curve. The curve is described by the following equation.

$$L'_i = p_1 \cdot U_\infty^2 + p_2 \cdot U_\infty + p_3 \quad (\text{C.12})$$

Coefficients of all fitted quadratic curves were assembled in a matrix \mathbb{M}_{bc} .

$$\mathbb{M}_{bc} = \begin{bmatrix} p_1^{F_x} & p_2^{F_x} & p_3^{F_x} \\ p_1^{F_y} & p_2^{F_y} & p_3^{F_y} \\ p_1^{F_z} & p_2^{F_z} & p_3^{F_z} \\ p_1^{M_x} & p_2^{M_x} & p_3^{M_x} \\ p_1^{M_y} & p_2^{M_y} & p_3^{M_y} \\ p_1^{M_z} & p_2^{M_z} & p_3^{M_z} \end{bmatrix} = \begin{bmatrix} -0.0047 & -0.0002 & -0.1800 \\ 0.0021 & -0.1028 & 5.2762 \\ -0.0001 & 0.0166 & 0.0582 \\ 1.0734 & -49.535 & 2870.7 \\ 0.9689 & -1.2542 & 43.625 \\ 0.1297 & -1.8637 & 25.430 \end{bmatrix} \quad (\text{C.13})$$

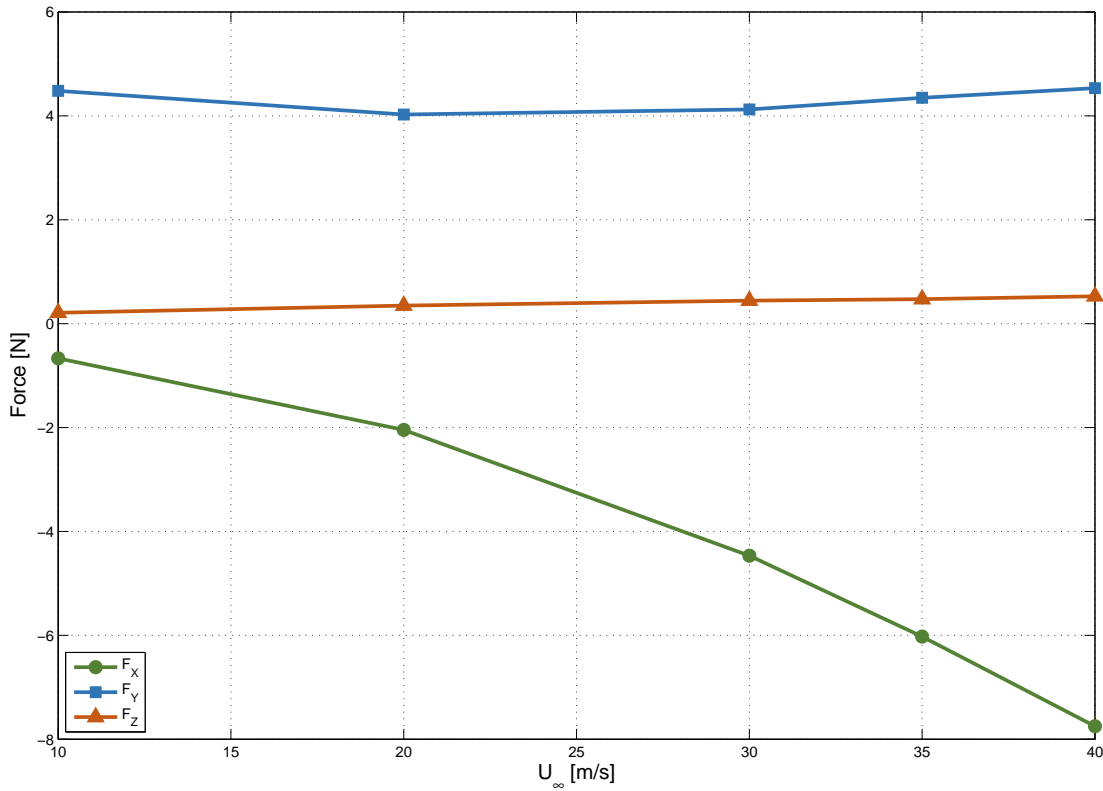


Fig. C.3: Measurement of load acting on balance. Resulting forces on balance

C.2 Load on model

When evaluating actual aerodynamic loads acting on the model, the first part is exactly the same as was described in the previous section – from averaging logged data to components of aerodynamic load acting at the model attachment point.

However, after load at the model attachment point \mathbb{L}' for a given speed is calculated, further calculations have to follow. That is because \mathbb{L}' is load acting on both the model and the balance. It is desired to subtract the load acting on the balance and reference the final aerodynamic forces and moments to the coordinate system defined in section 7.1.

Based on section C.1, load acting on the balance is computed from equation C.14.

$$L'_{bal,i} = p_1^i \cdot U_{\infty}^2 + p_2^i \cdot U_{\infty} + p_3^i \quad (\text{C.14})$$

Then, subtracting load acting on balance from previously calculated load \mathbb{L}' is expressed by the following equation.

$$\mathbb{L}^* = \mathbb{L}' - \mathbb{L}_{bal} \quad (\text{C.15})$$

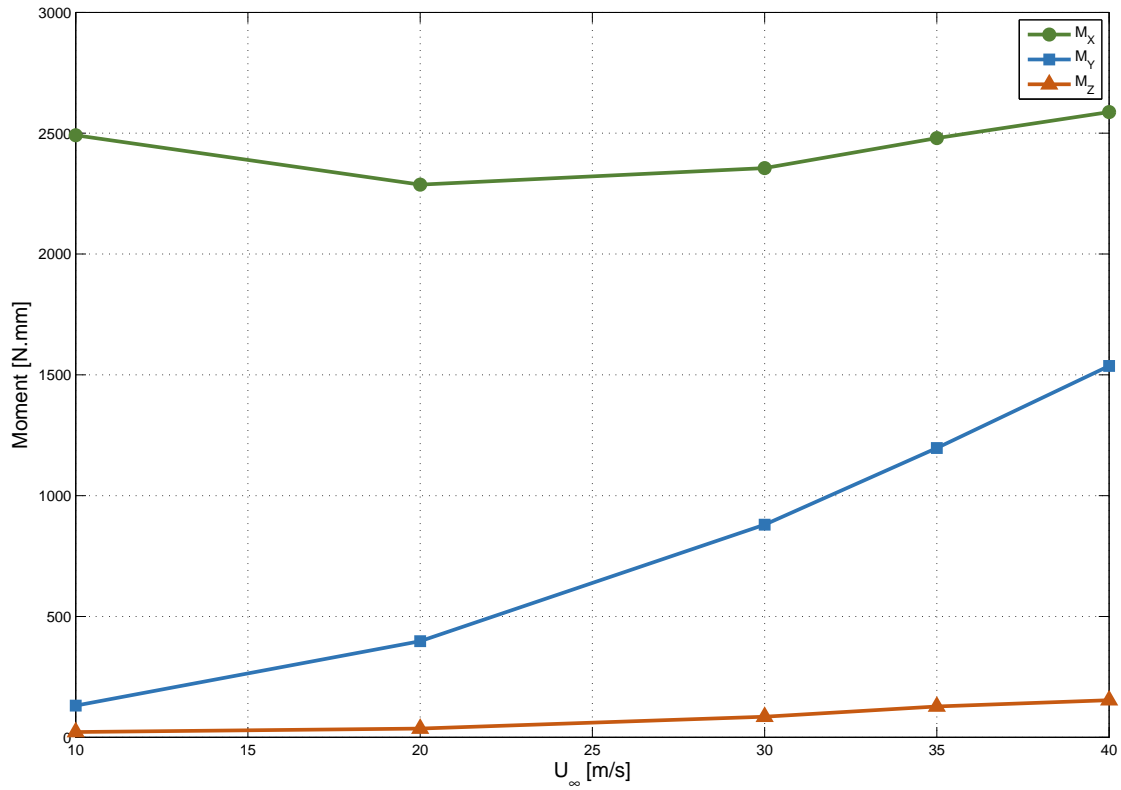


Fig. C.4: Measurement of load acting on balance. Resulting moments on balance

Now, \mathbb{L}^* is vector of load components acting on the model (equation C.16), referenced to the coordinate system, which has origin point located on the balance at the point of model attachment. As was described before, it is customary to reference the aerodynamic load to coordinate system defined in the section 7.1

$$\mathbb{L}^* = \begin{bmatrix} F_x^* \\ F_y^* \\ F_z^* \\ M_x^* \\ M_y^* \\ M_z^* \end{bmatrix} \quad (\text{C.16})$$

The transformation between the two coordinate system is schematically depicted in fig. C.5. Mathematically, it can be expressed by equation C.17.

$$\mathbb{L} = \mathbb{T} \cdot \mathbb{L}^* \quad (\text{C.17})$$

In the equation above, \mathbb{T} is transformation matrix derived from the geometrical

difference of the coordinate systems (see fig. C.5).

$$\mathbb{T} = \begin{bmatrix} 1 & 0 & 0 & 0 & 0 & 0 \\ 0 & 1 & 0 & 0 & 0 & 0 \\ 0 & 0 & 1 & 0 & 0 & 0 \\ 0 & dz & 0 & 1 & 0 & 0 \\ -dz & 0 & -dx & 0 & 1 & 0 \\ 0 & dx & 0 & 0 & 0 & 1 \end{bmatrix} \quad (\text{C.18})$$

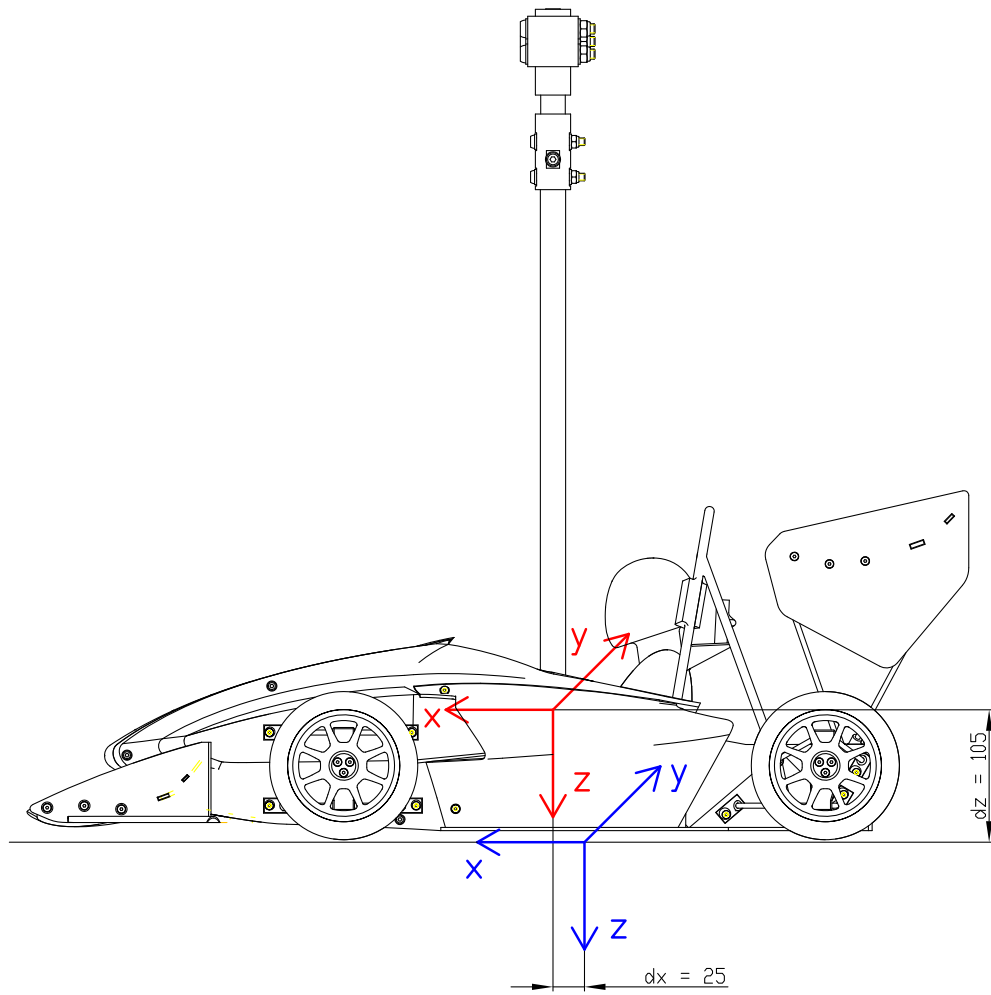


Fig. C.5: Transformation of aerodynamic load to default coordinate system

Finally, \mathbb{L} is vector of components of aerodynamic load, acting on the model. The

respective components are:

$$\mathbb{L} = \begin{bmatrix} F_x \\ F_y \\ F_z \\ M_x \\ M_y \\ M_z \end{bmatrix} \quad (\text{C.19})$$

From these components, dimensionless coefficient can be computed. They were defined in section 7.1.2.

$$C_{F_i} = \frac{F_i}{\frac{1}{2}\rho V_\infty^2 A_M} \quad (\text{C.20})$$

$$C_{M_i} = \frac{M_i}{\frac{1}{2}\rho V_\infty^2 A_M l_m} \quad (\text{C.21})$$

Density, that figures in both equations C.20, and C.21, is one of the output parameters from wind tunnel measurement. All values for the respective cases are listed in tables C.1, C.2, C.3, and C.4. These are average values over the measuring period.

Reference dimensions also figuring in the above equations are shown in table C.5. Reference area A_M is model's frontal cross-section area, while reference length l_m is model's wheel base. Frontal cross-section area is different for unwinged cases (1 and 2) and winged cases (3 and 4).

To sum up the following pages:

- tables C.1 – C.4 show densities used for aerodynamic coefficient computation
- table C.5 shows reference values used for aerodynamic coefficient computation
- tables C.6 – C.9 show final forces acting on the model and the respective aerodynamic coefficients
- figures C.6 – C.33 show seven following graphs for cases 1 – 4
 - Strain gauge responses – zero values
 - Strain gauge responses – values under load
 - Measured forces – loads on balance subtracted
 - Transformation of loads to default reference coordinate system
 - Final forces acting on the model
 - Final moments acting on the model
 - Final aerodynamic coefficients

Tab. C.1: Density used for calculation of aerodynamic coefficients – case 1

Velocity [m/s]	Density [kg/m ³]
10	1.170
20	1.169
30	1.166
36	1.162
43	1.155

Tab. C.2: Density used for calculation of aerodynamic coefficients – case 2

Velocity [m/s]	Density [kg/m ³]
30	1.154
36	1.148
40	1.155

Tab. C.3: Density used for calculation of aerodynamic coefficients – case 3

Velocity [m/s]	Density [kg/m ³]
25	1.161
30	1.156

Tab. C.4: Density used for calculation of aerodynamic coefficients – case 4

Velocity [m/s]	Density [kg/m ³]
25	1.157
30	1.153

Tab. C.5: Model reference dimensions for dimensionless coefficient computation

Reference area – Case 1 and 2	$A = 0.049693 \text{ m}^2$
Reference area – Case 3 and 4	$A = 0.063985 \text{ m}^2$
Reference length	$l = 381.75 \text{ mm}$

Tab. C.6: Forces and moment acting on the model – case 1

Velocity [m/s]	F_x [N]	C_{F_x} [-]	F_z [N]	C_{Fz} [-]	M_y [N · mm]	C_{My} [-]
10	-2.1	-0.712	0.1	0.031	242.6	0.219
20	-10.0	-0.857	-3.2	-0.278	1744.7	0.393
30	-22.0	-0.842	-9.9	-0.379	4135.2	0.415
36	-32.3	-0.862	-16.4	-0.438	6144.0	0.430
43	-46.4	-0.874	-24.7	-0.465	8918.6	0.440

Tab. C.7: Forces and moment acting on the model – case 2

Velocity [m/s]	F_x [N]	C_{F_x} [-]	F_z [N]	C_{Fz} [-]	M_y [N · mm]	C_{My} [-]
30	-25.2	-0.975	-18.2	-0.705	4719.5	0.479
36	-35.8	-0.970	-25.6	-0.692	6719.6	0.476
40	-45.3	-0.987	-26.9	-0.586	8223.0	0.469

Tab. C.8: Forces and moment acting on the model – case 3

Velocity [m/s]	F_x [N]	C_{F_x} [-]	F_z [N]	C_{Fz} [-]	M_y [N · mm]	C_{My} [-]
25	-27.0	-1.163	30.8	1.327	4628.4	0.522
30	-36.2	-1.087	41.2	1.238	6760.2	0.532

Tab. C.9: Forces and moment acting on the model – case 4

Velocity [m/s]	F_x [N]	C_{F_x} [-]	F_z [N]	C_{Fz} [-]	M_y [N · mm]	C_{My} [-]
25	-24.8	-1.071	31.9	1.380	4272.0	0.484
30	-34.5	-1.038	41.2	1.241	6478.6	0.511

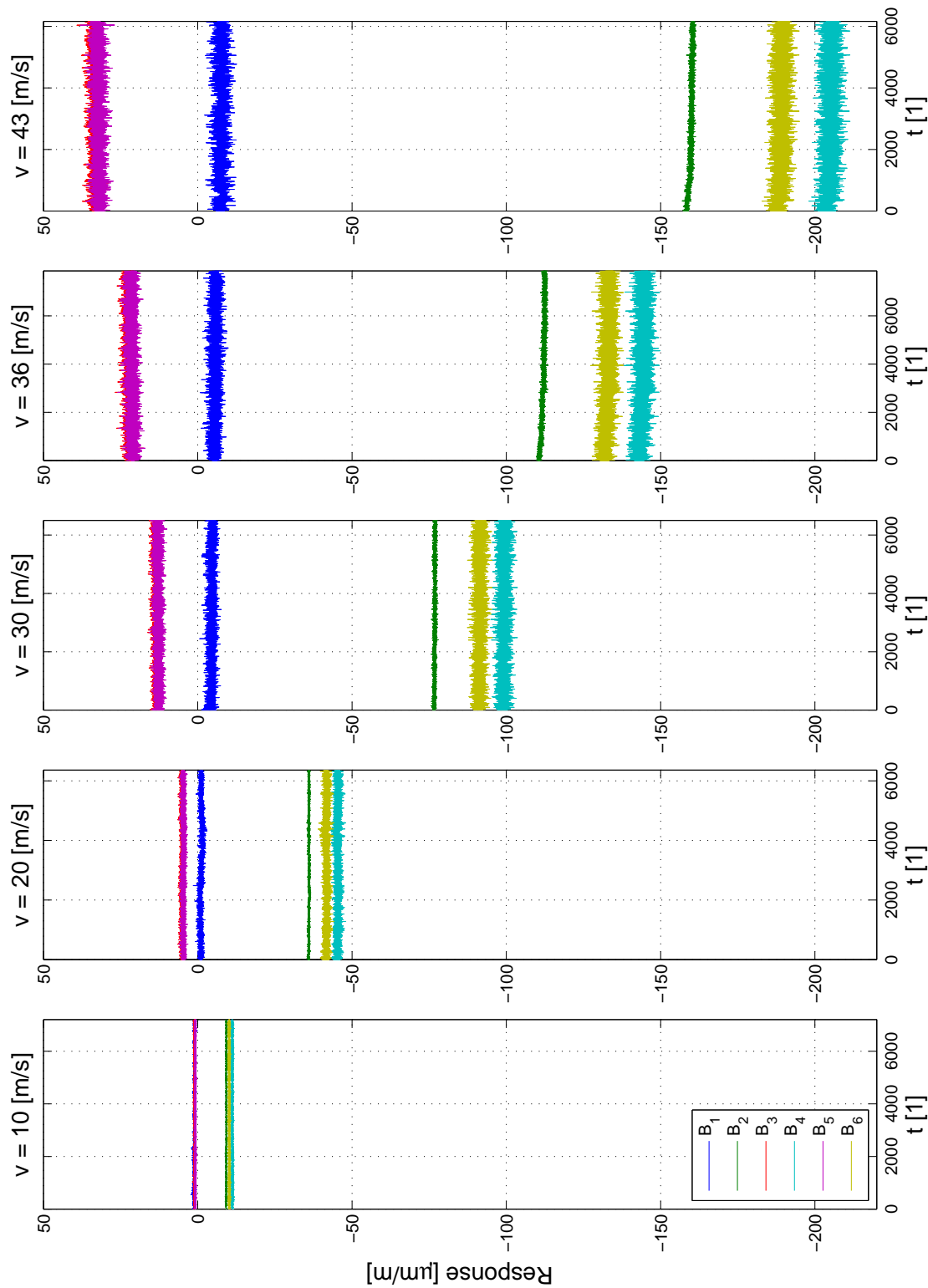


Fig. C.6: Case 1 – measured strain gauge responses for all measured velocities

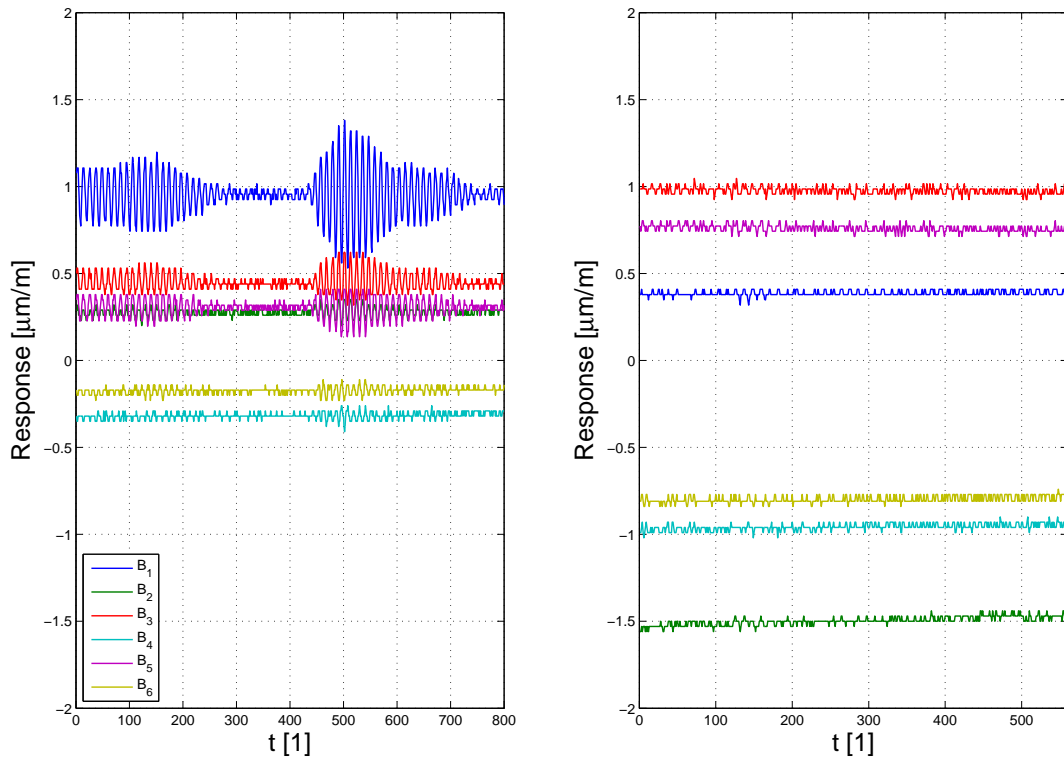


Fig. C.7: Case 1 – measured strain gauge responses – zero values

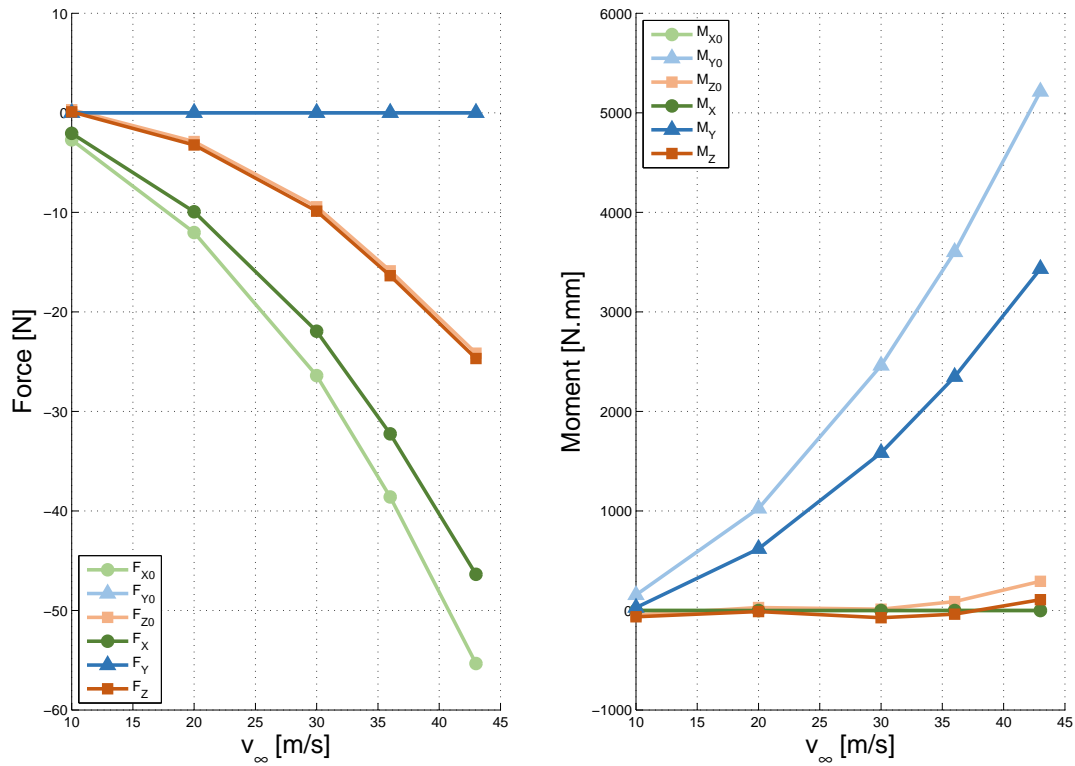


Fig. C.8: Case 1 – measured forces corrected – loads acting on the balance subtracted

C Aerodynamic load evaluation

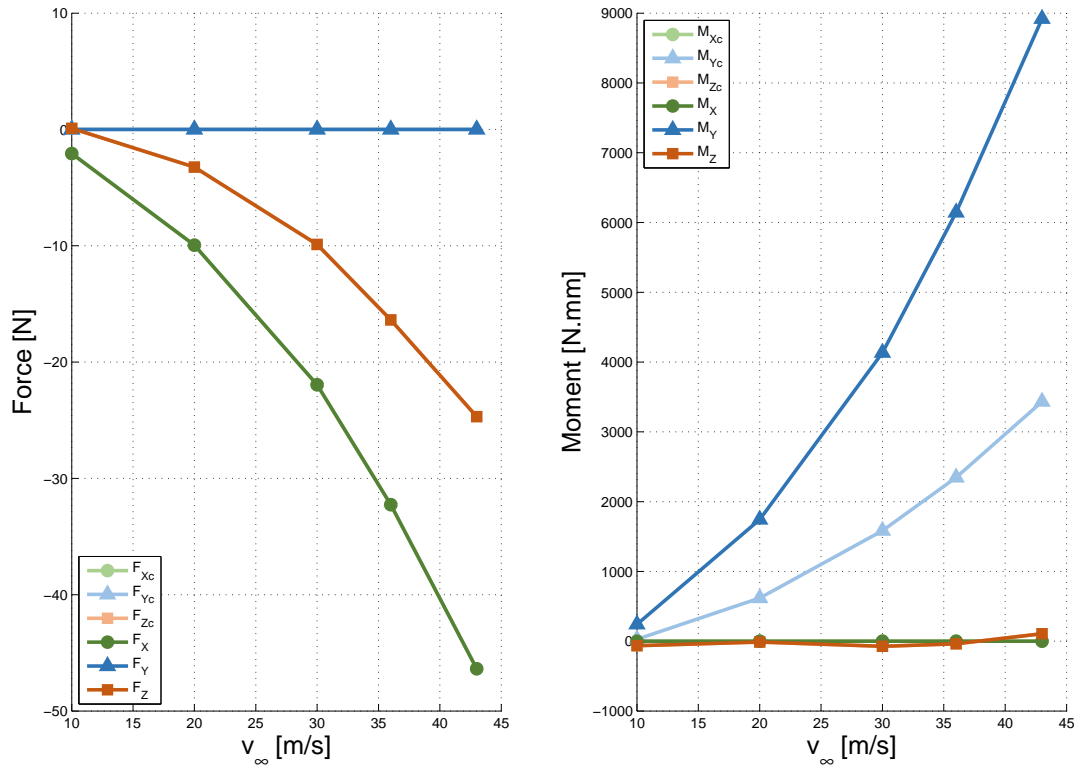


Fig. C.9: Case 1 – transformation of the reference coordinate system

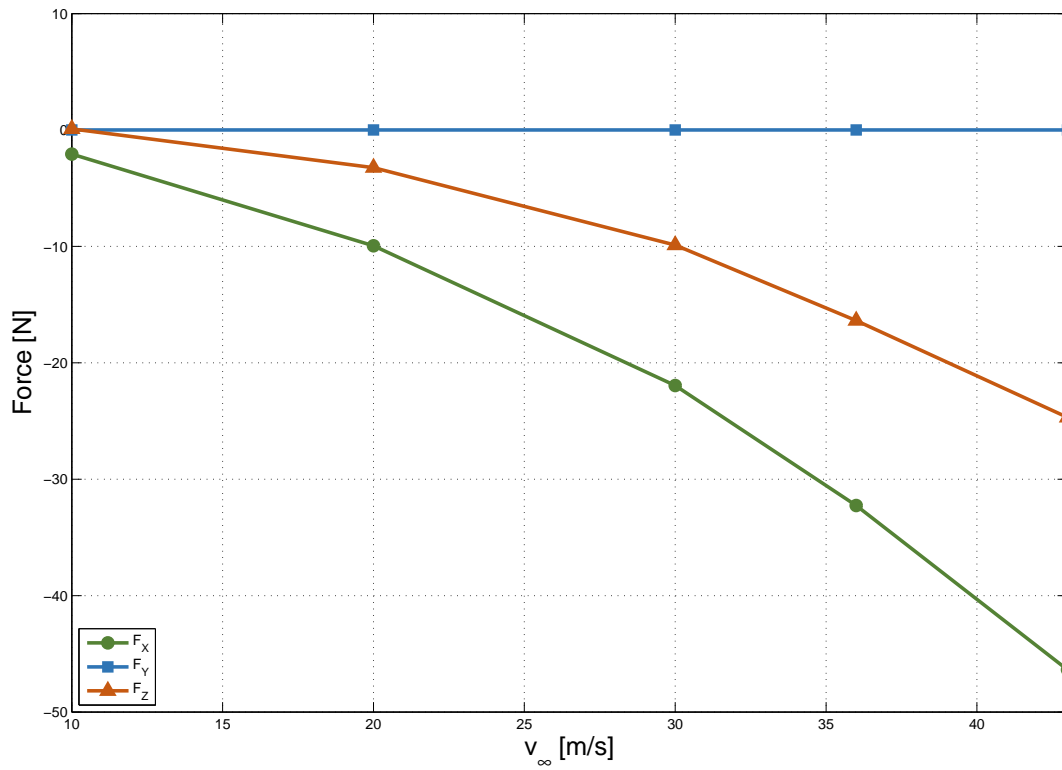


Fig. C.10: Case 1 – resulting forces acting on the model

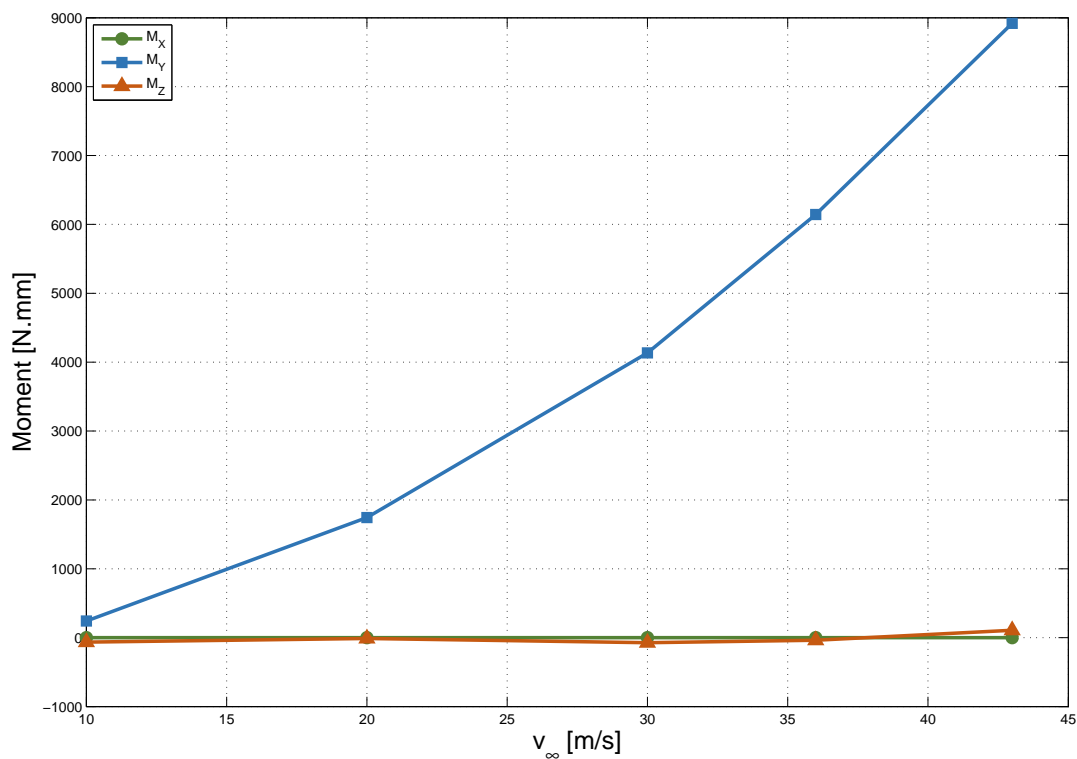


Fig. C.11: Case 1 – resulting moments acting on the model

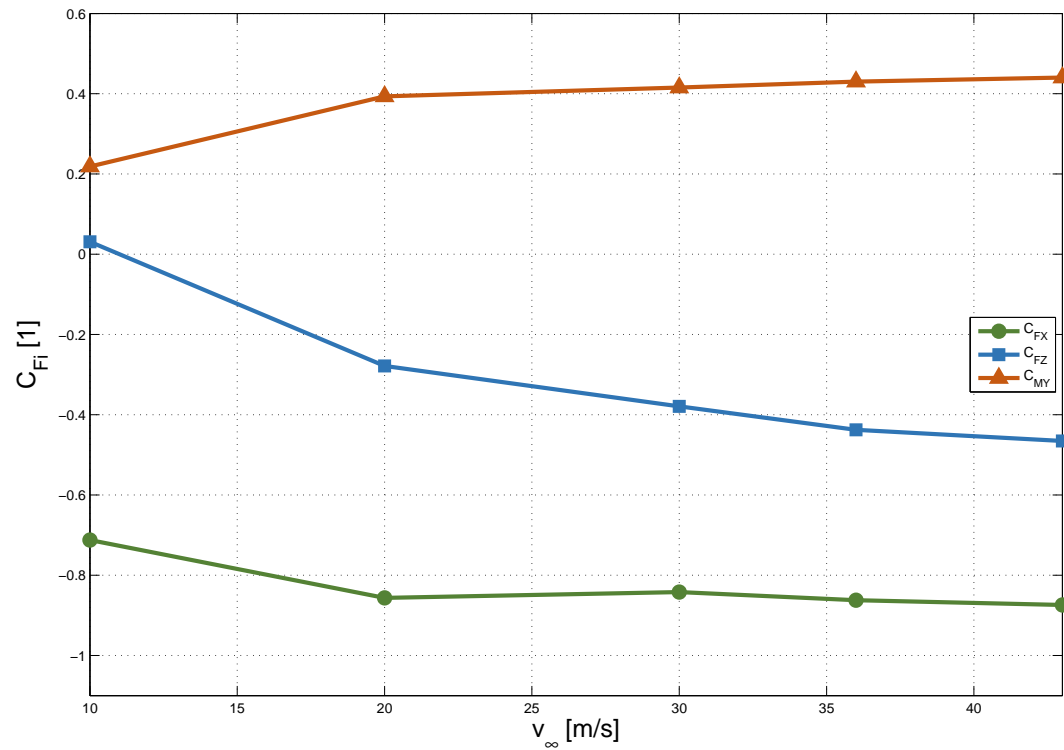


Fig. C.12: Case 1 – resulting aerodynamic coefficients of the model

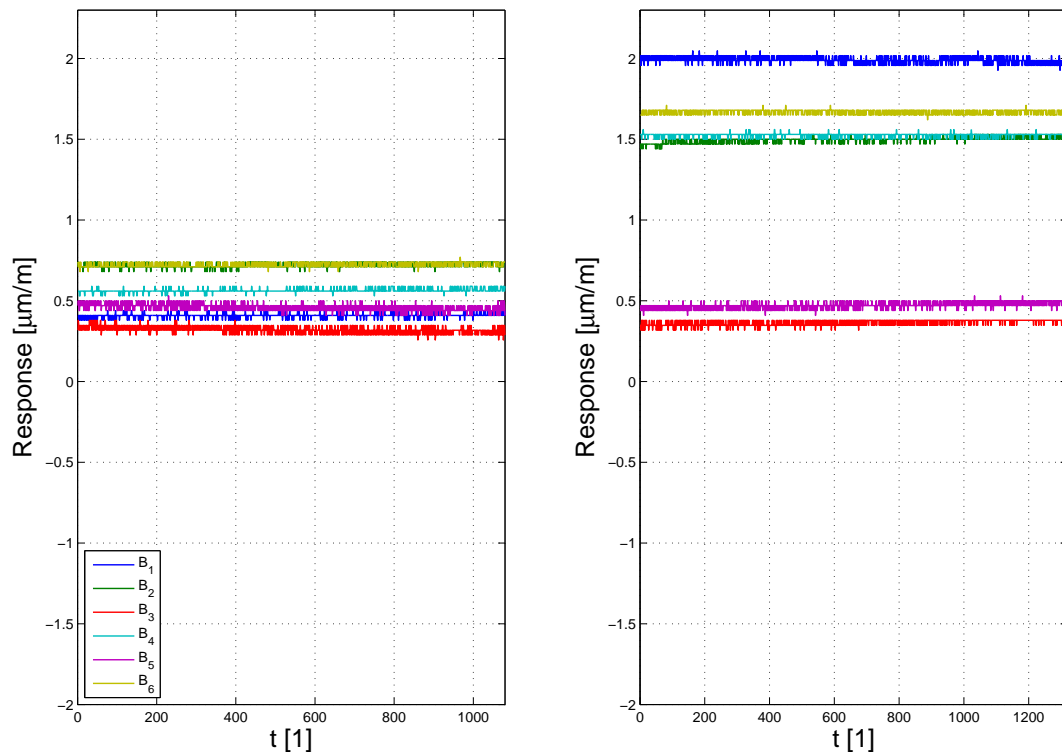


Fig. C.13: Case 2 – measured strain gauge responses – zero values

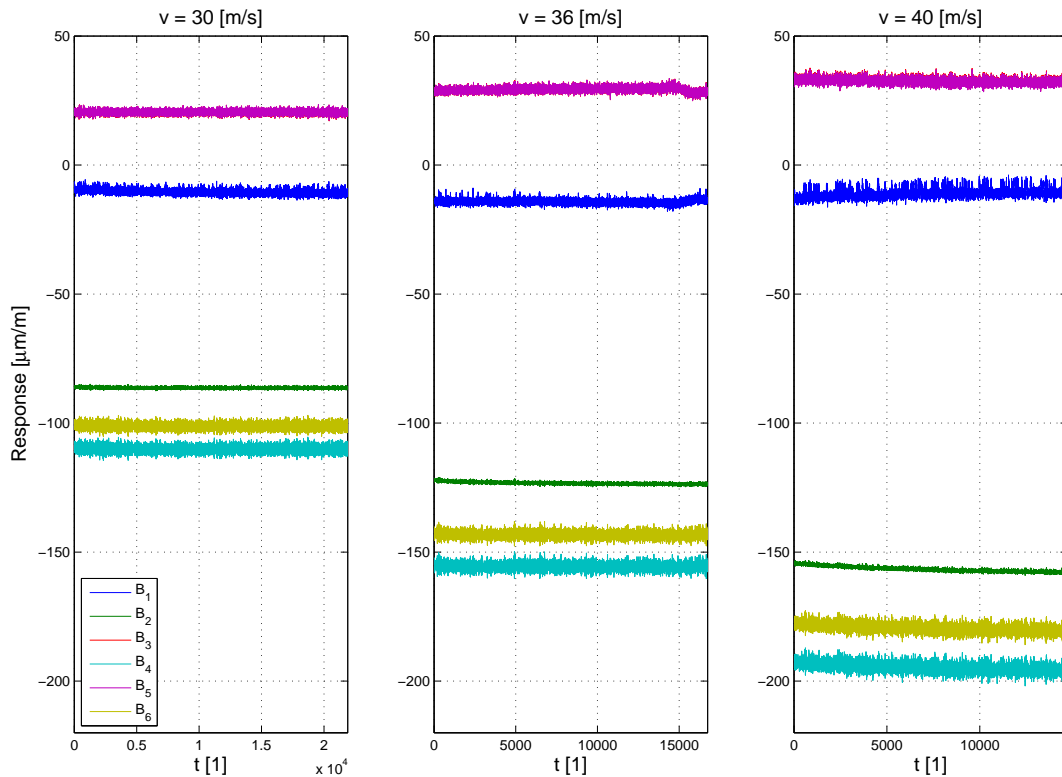


Fig. C.14: Case 2 – measured strain gauge responses for all measured velocities

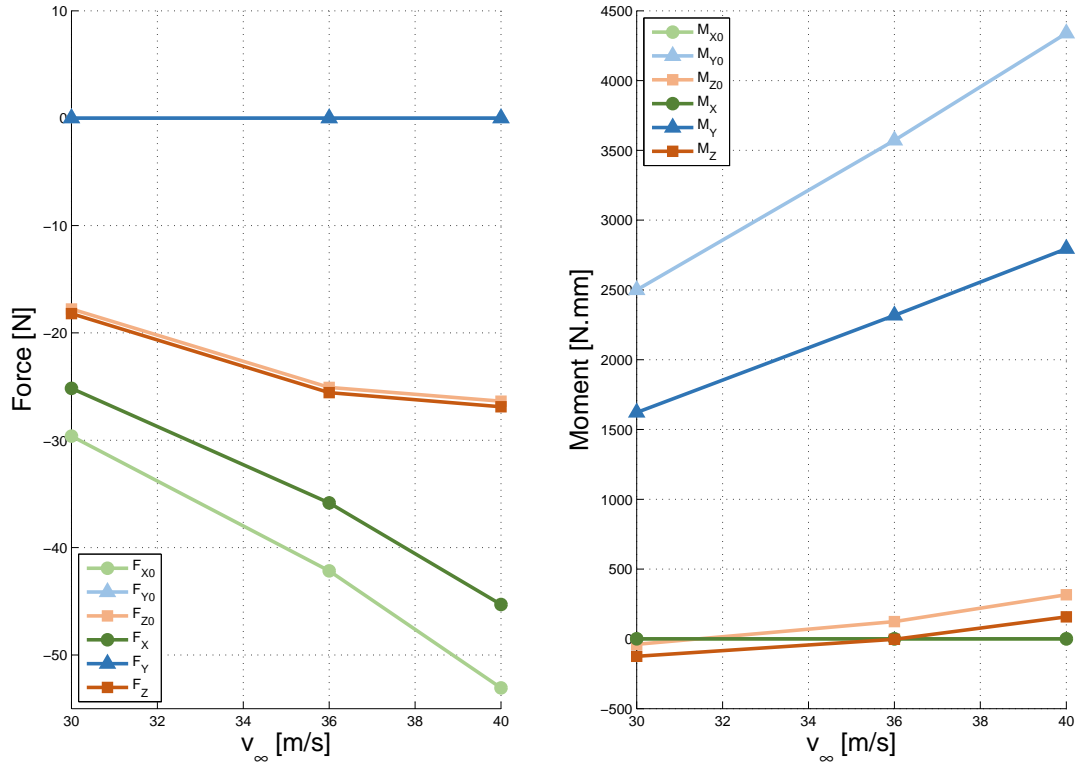


Fig. C.15: Case 2 – measured forces corrected – loads acting on the balance subtracted

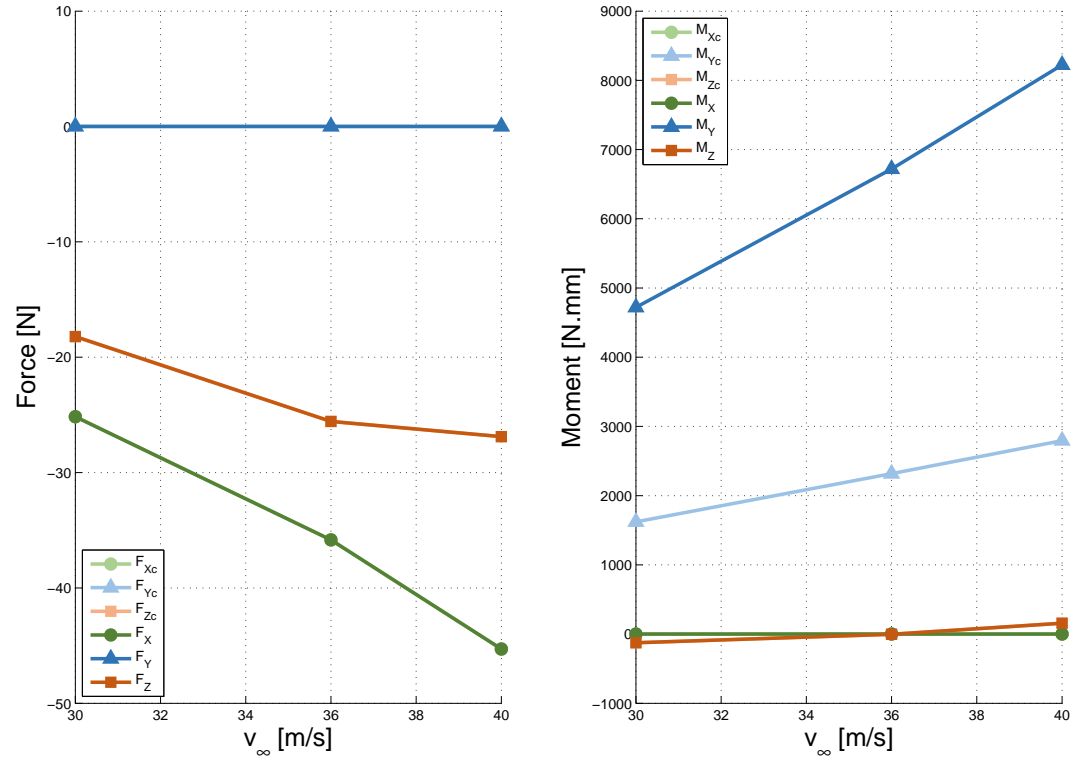


Fig. C.16: Case 2 – transformation of the reference coordinate system

C Aerodynamic load evaluation

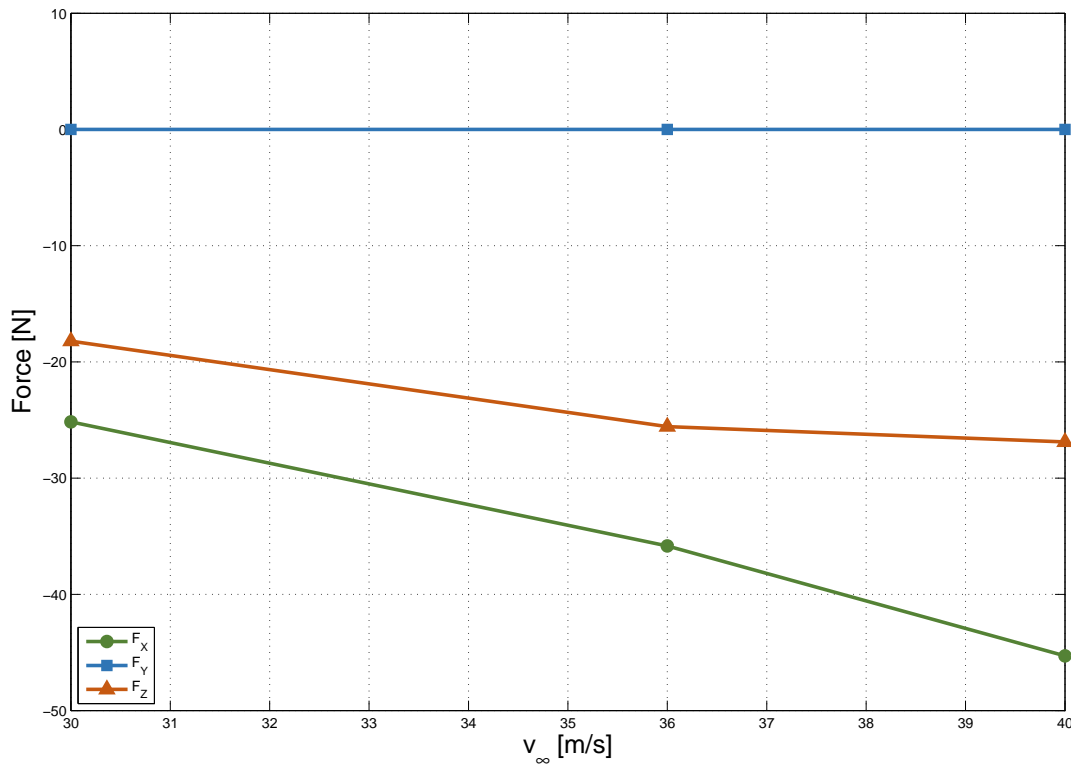


Fig. C.17: Case 2 – resulting forces acting on the model

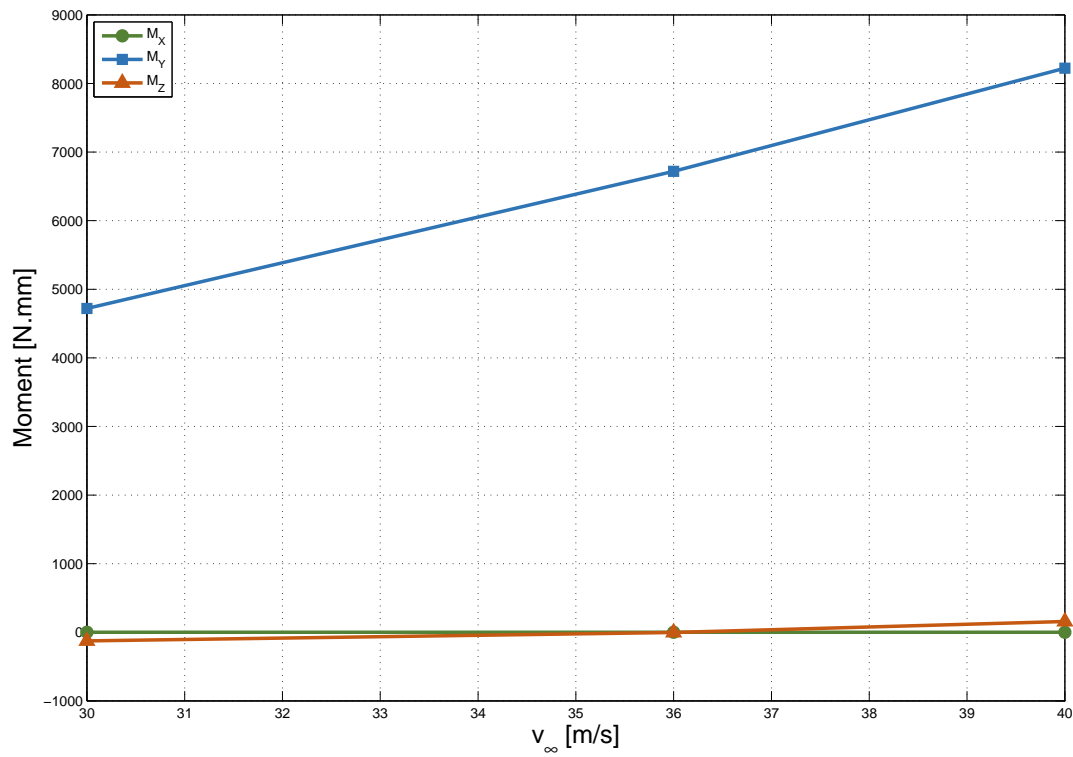


Fig. C.18: Case 2 – resulting moments acting on the model

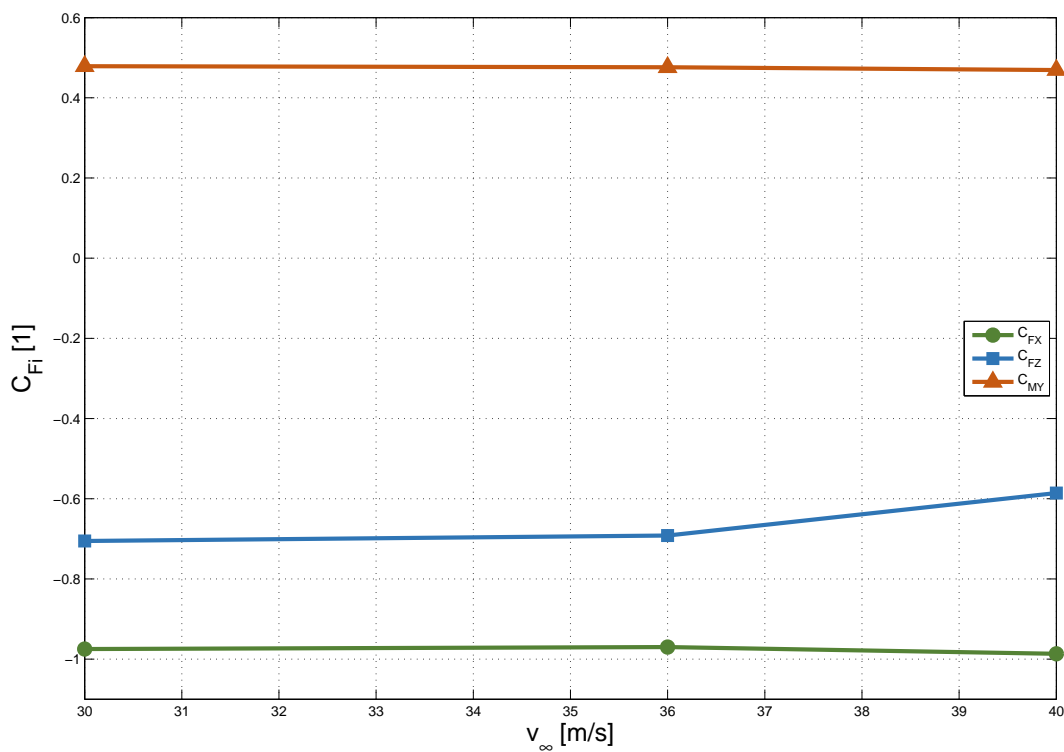


Fig. C.19: Case 2 – resulting aerodynamic coefficients of the model

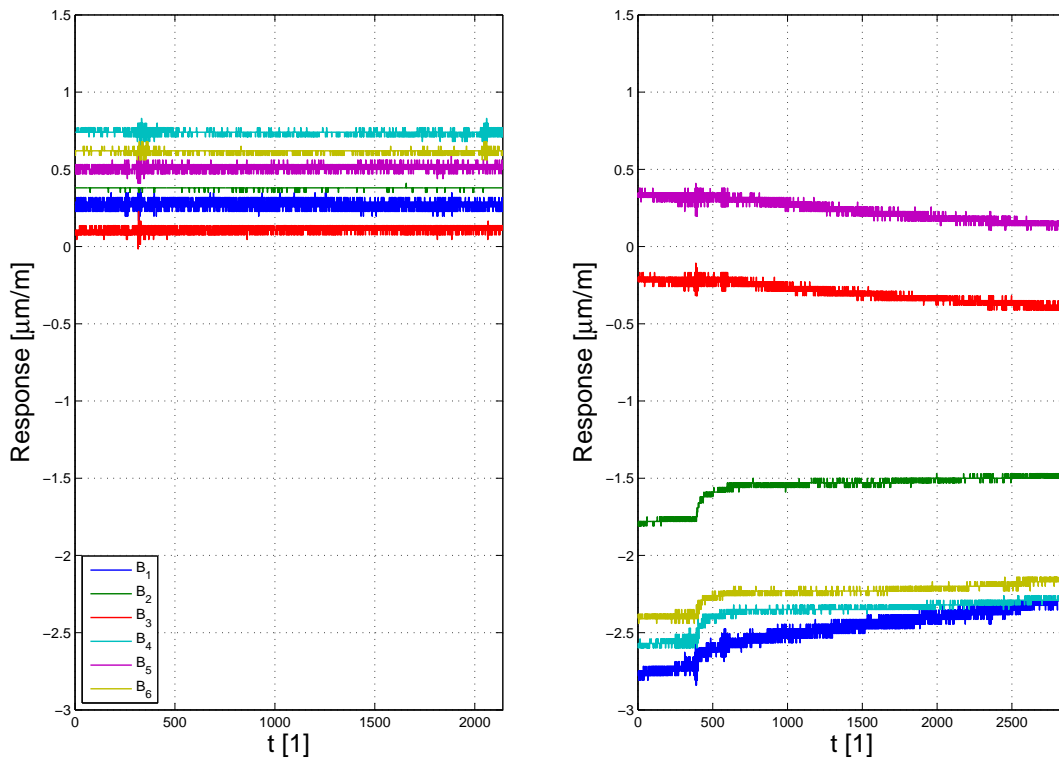


Fig. C.20: Case 3 – measured strain gauge responses – zero values

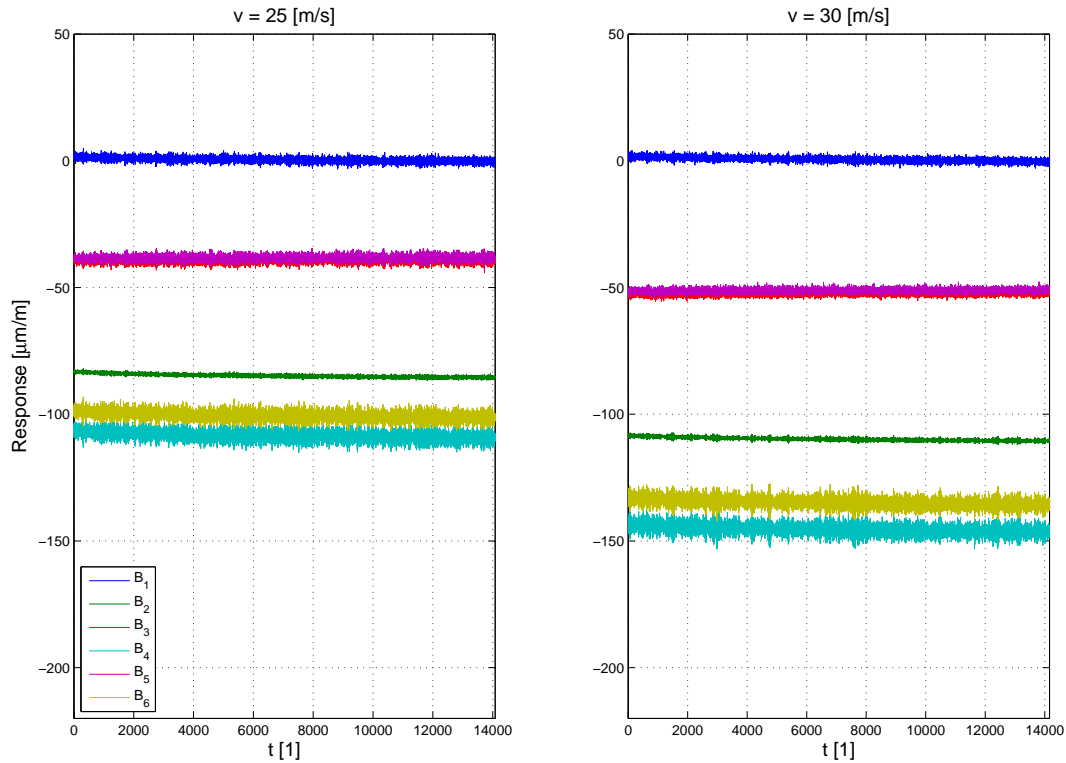


Fig. C.21: Case 3 – measured strain gauge responses for all measured velocities

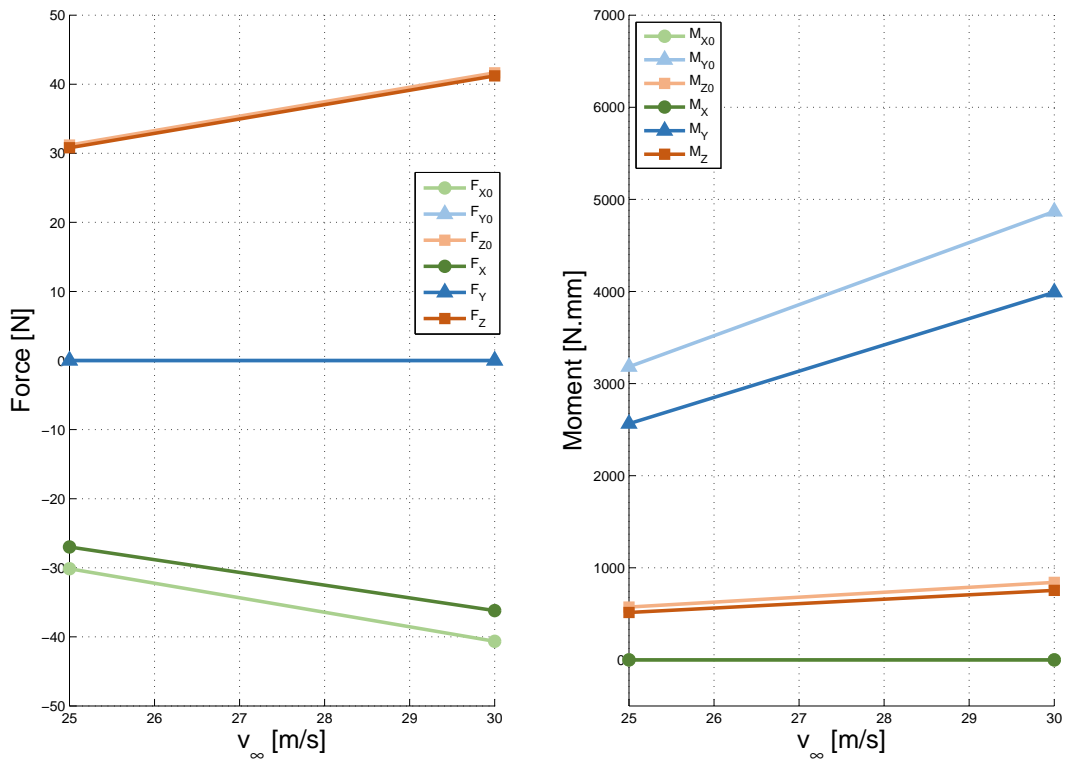


Fig. C.22: Case 3 – measured forces corrected – loads acting on the balance subtracted

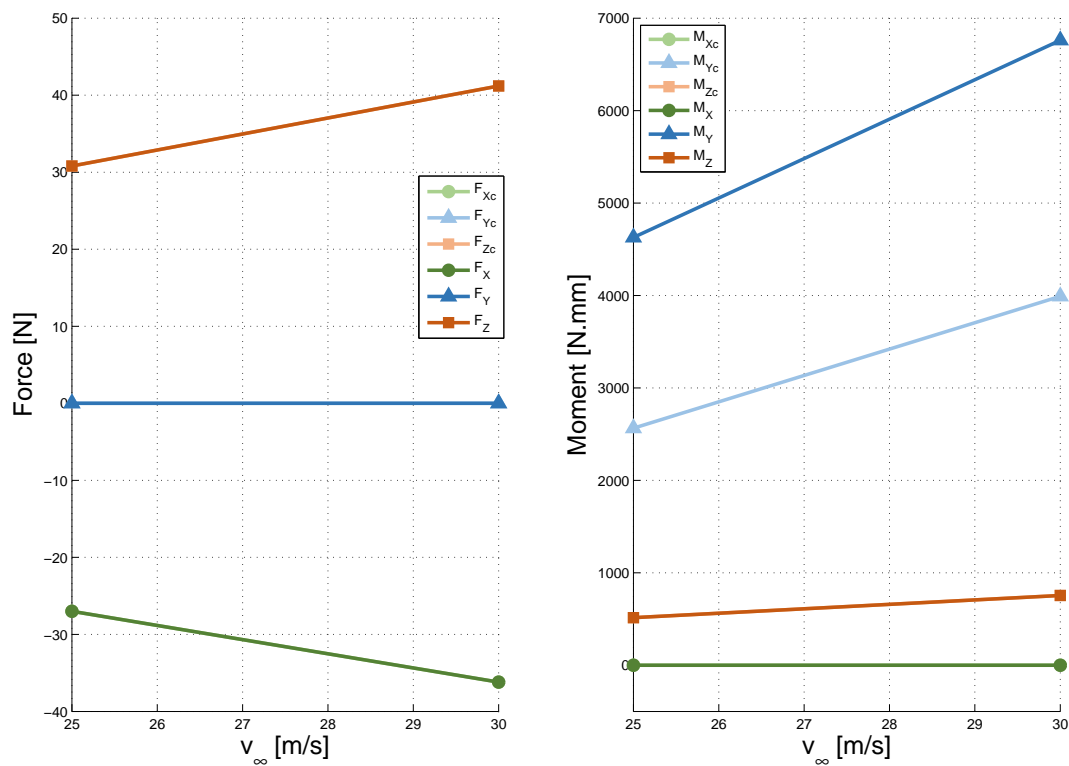


Fig. C.23: Case 3 – transformation of the reference coordinate system

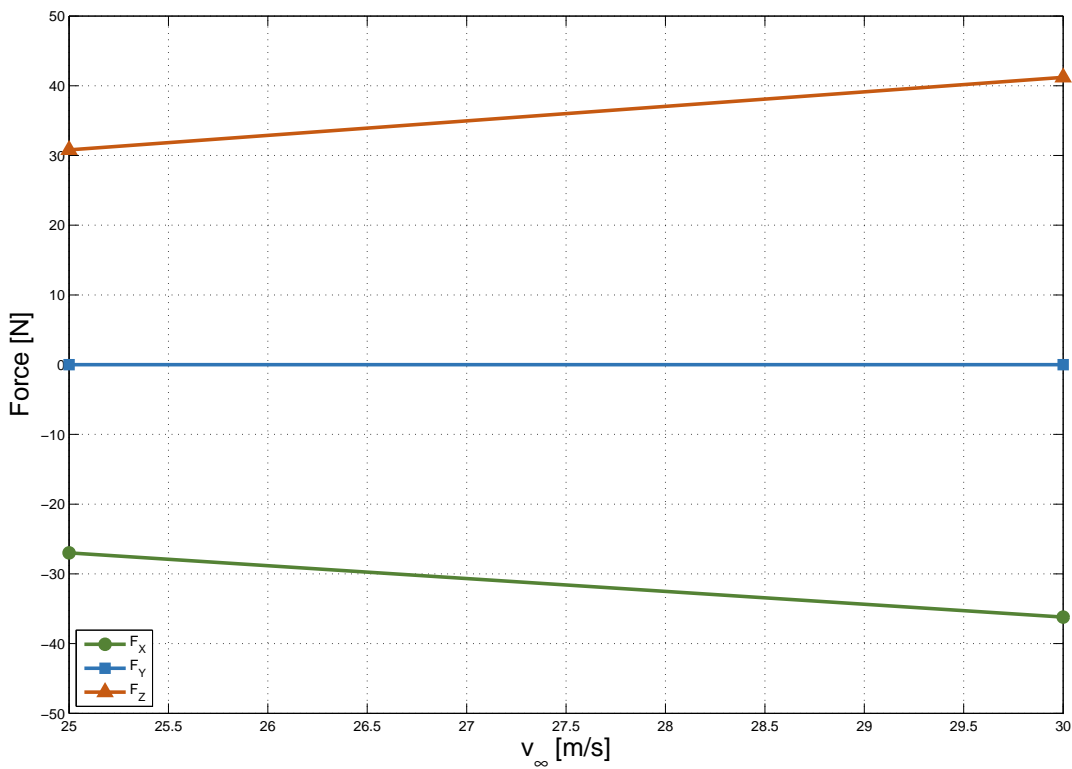


Fig. C.24: Case 3 – resulting forces acting on the model

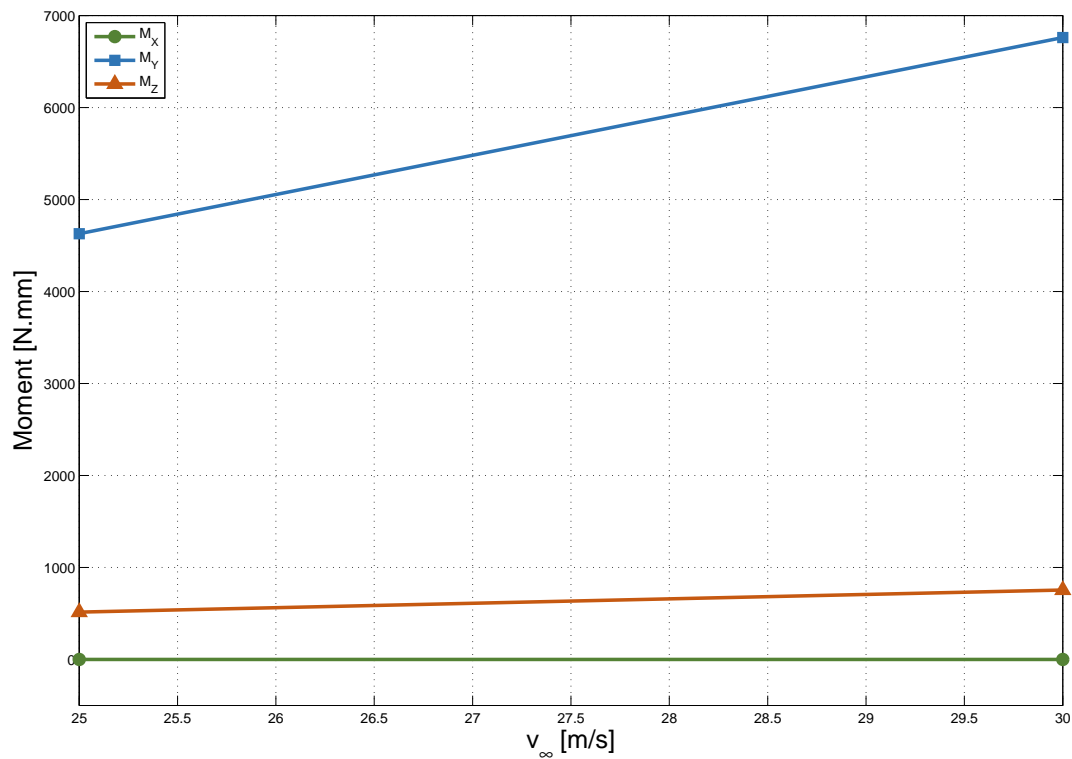


Fig. C.25: Case 3 – resulting moments acting on the model

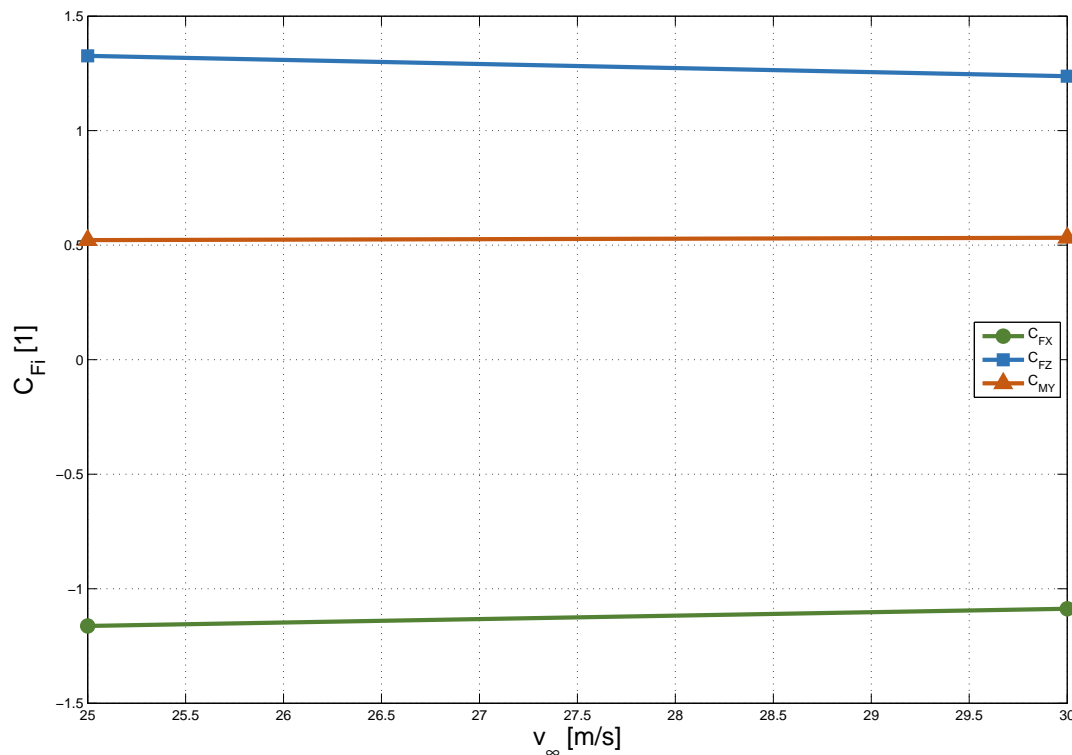


Fig. C.26: Case 3 – resulting aerodynamic coefficients of the model

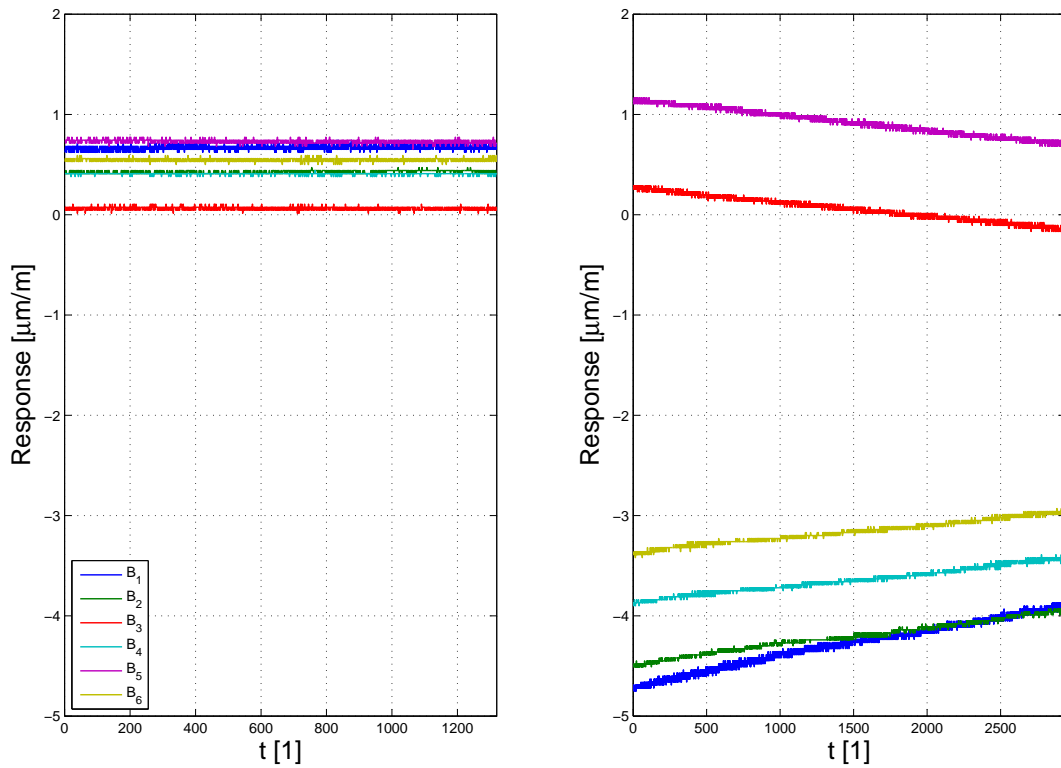


Fig. C.27: Case 4 – measured strain gauge responses – zero values

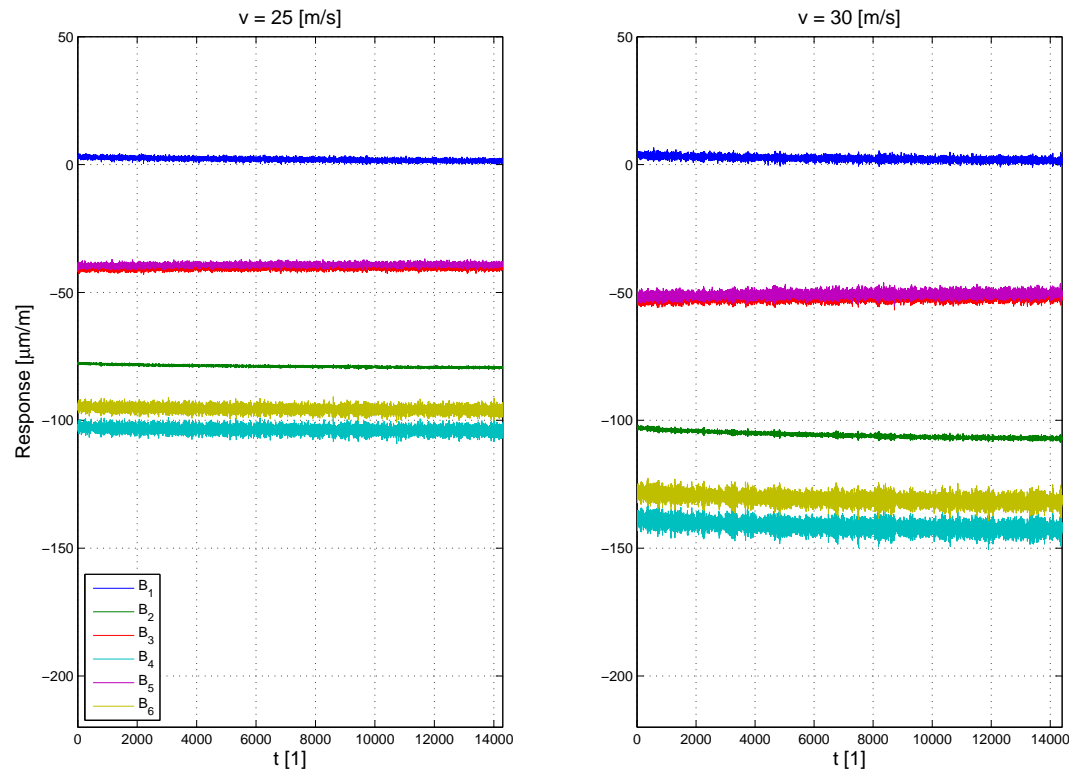


Fig. C.28: Case 4 – measured strain gauge responses for all measured velocities

C Aerodynamic load evaluation

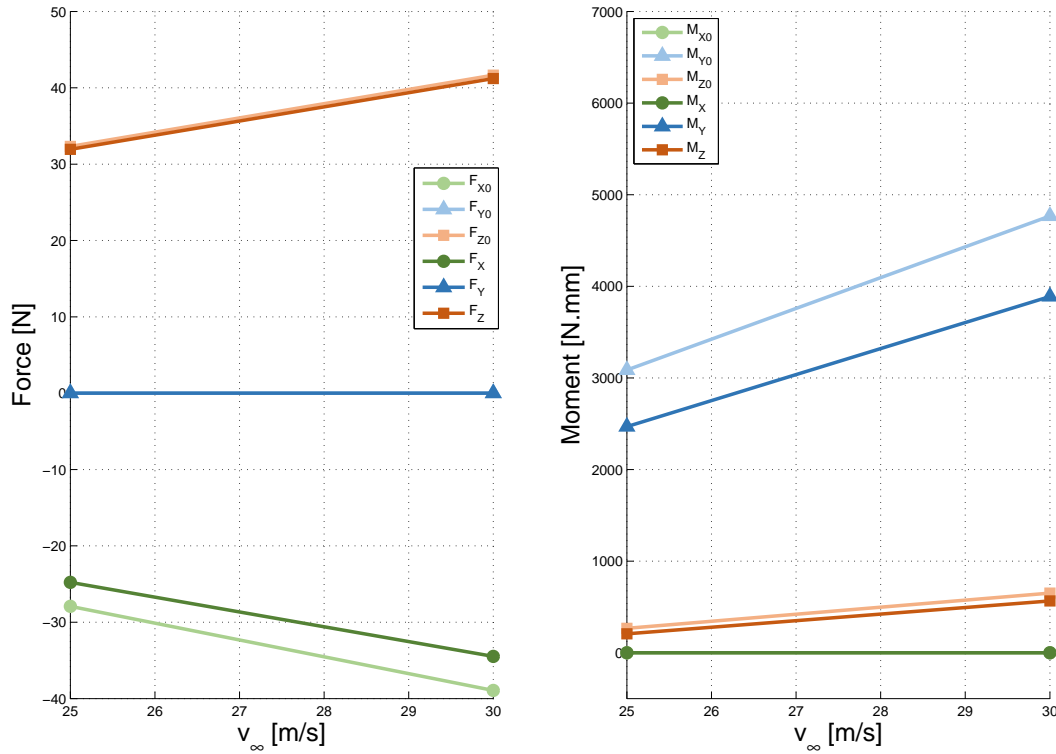


Fig. C.29: Case 4 – measured forces corrected – loads acting on the balance subtracted

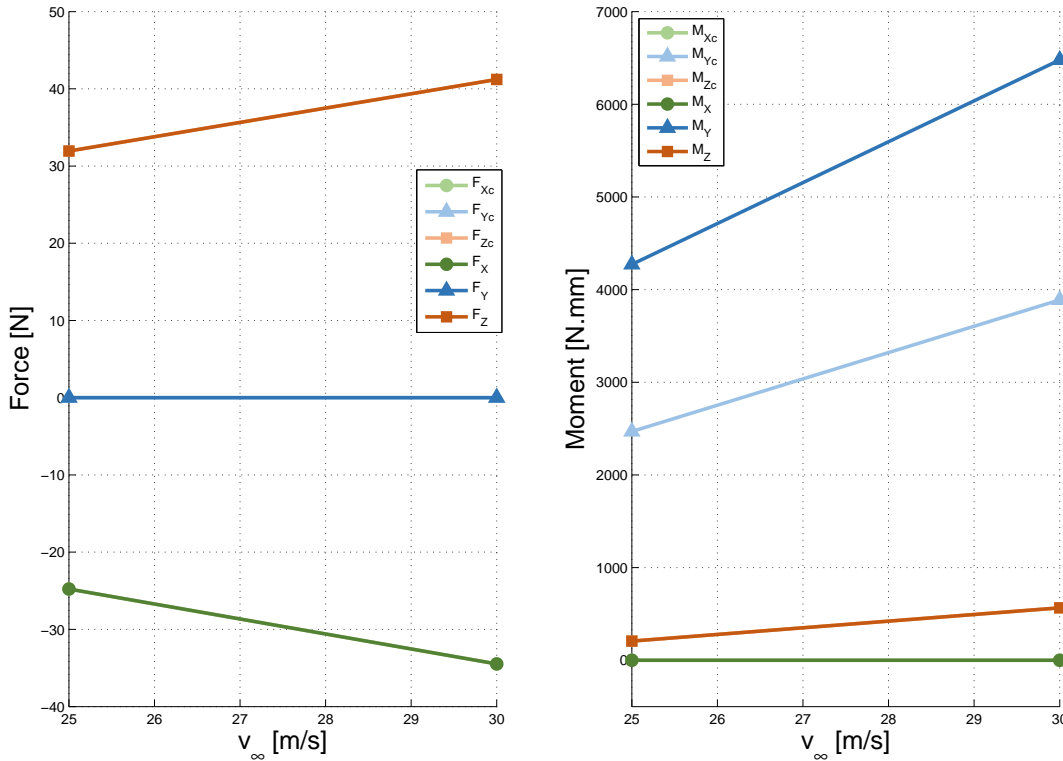


Fig. C.30: Case 4 – transformation of the reference coordinate system

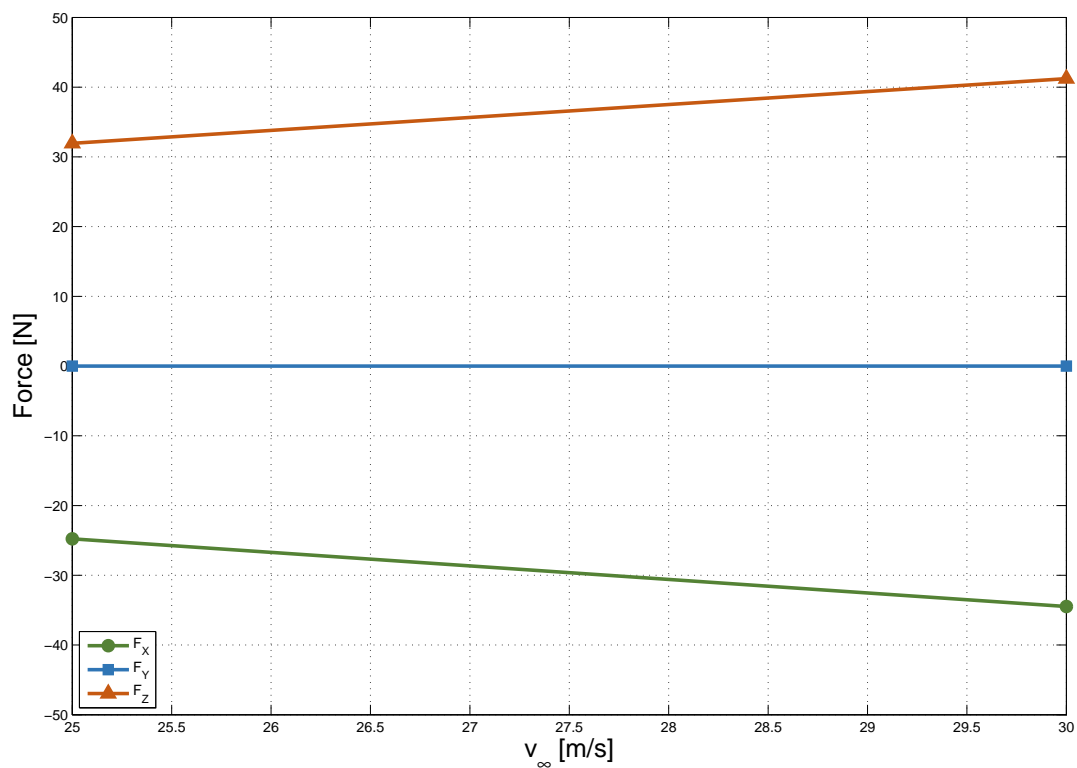


Fig. C.31: Case 4 – resulting forces acting on the model

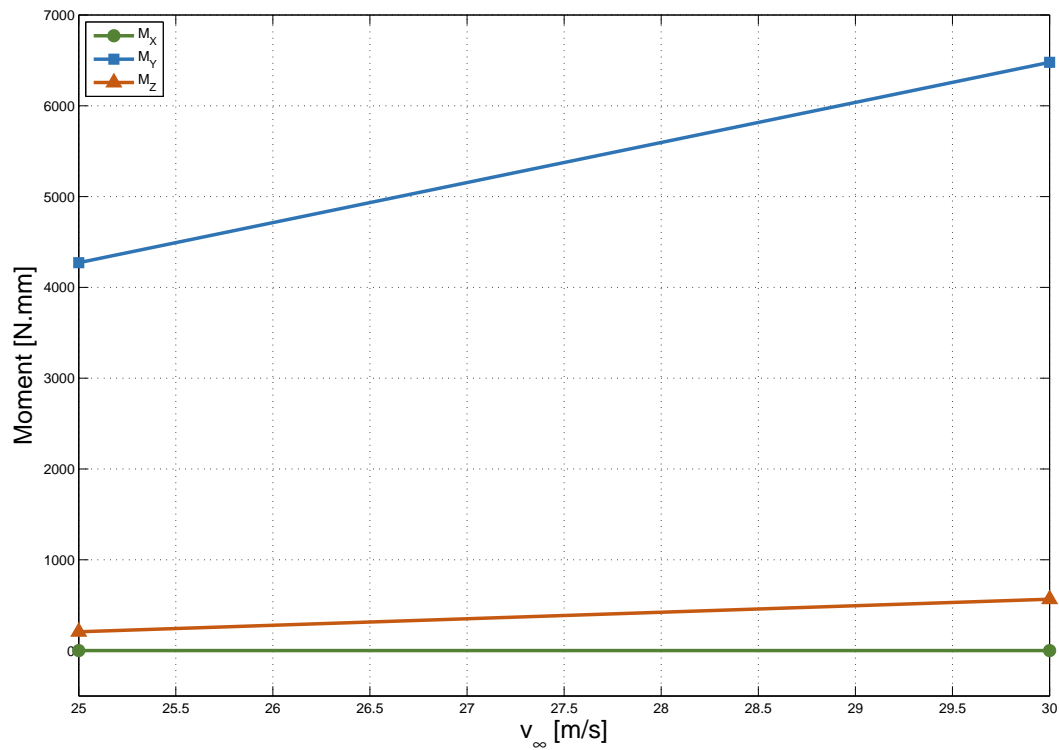


Fig. C.32: Case 4 – resulting moments acting on the model

C Aerodynamic load evaluation

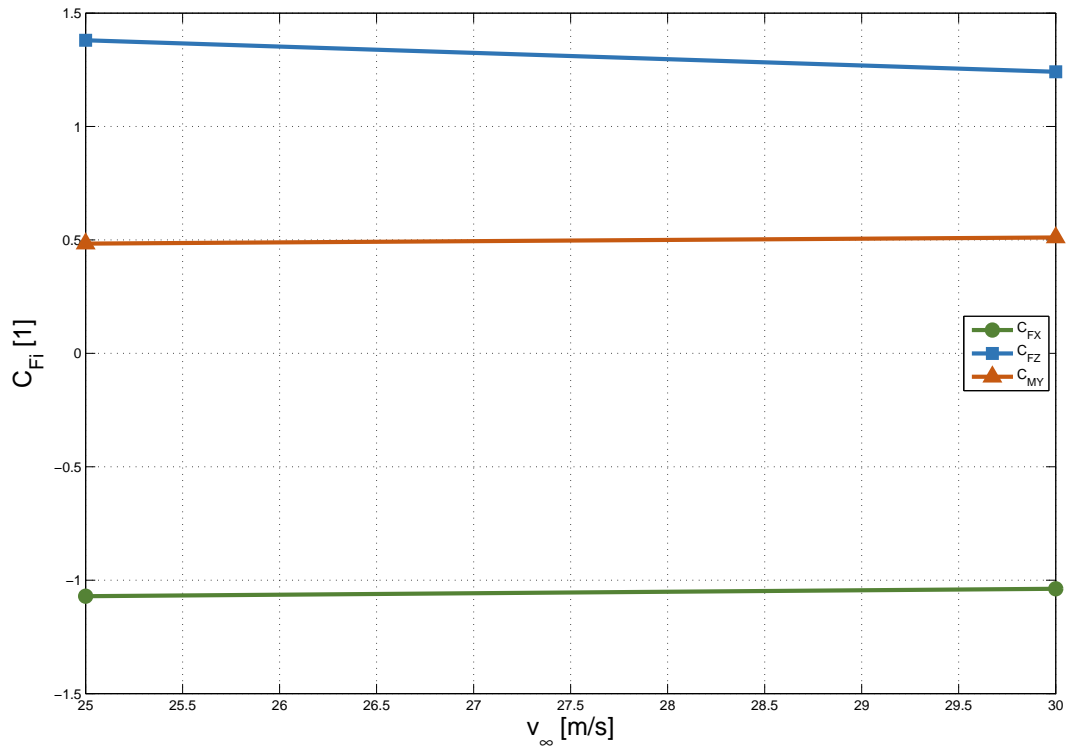


Fig. C.33: Case 4 – resulting aerodynamic coefficients of the model